Spectral Characterization of the Herschel SPIRE Photometer

Locke Dean Spencer

B.Sc. Engineering Physics, University of Alberta, 2003

A Thesis
Submitted to the School of Graduate Studies
of the University of Lethbridge
in Partial Fulfilment of the
Requirements of the Degree

Master of Science

Department of Physics
University of Lethbridge
Lethbridge, Alberta, Canada

Spectral Characterization of the Herschel SPIRE Photometer

Locke Dean Spencer

Approved:

Dr. David A. Naylor, Supervisor, Department of Physics — Date

---

Dr. Steve Patitsas, Department of Physics — Date

Dr. René Boeré, Department of Chemistry — Date

Dr. Mike Smith, External Examiner — Date

Dr. James Thomas, Chair, Thesis Examination Committee — Date

Dedication

"That which we persist in doing becomes easier, not that the task itself has become easier, but that our ability to perform it has improved."

Ralph Waldo Emerson

To my parents, *Kevin and Sharon Spencer*, who's love and example of hard work and dedication has been a constant inspiration to me.

Abstract

Spectral Characterization of the Herschel SPIRE Photometer

by

Locke Dean Spencer

Master of Science in Physics

University of Lethbridge

The European Space Agency's Herschel Space Observatory is comprised of three cryogenically cooled instruments commissioned to explore the far infrared/submillimetre universe. The Spectral and Photometric Imaging REceiver (SPIRE) is one of Herschel's instruments and consists of a three band imaging photometer and a two band imaging spectrometer. Canada is involved in the SPIRE project through provision of instrument development hardware and software, mission flight software, and support personnel.

This thesis discusses Fourier transform spectroscopy (FTS) and FTS data processing. A detailed discussion is included on FTS phase correction, with results presented from the optimization of an enhanced Forman phase correction routine developed for this work. This thesis discusses the design, verification, and use of the hardware and software provided by Dr. Naylor's group as it relates to SPIRE verification testing. Results of the photometer characterization are presented. The current status of SPIRE and its future schedule is also discussed.

Acknowledgements

First, I need to thank David Naylor for giving me such a wonderful opportunity to work on the SPIRE project with such a talented group at the University, and for placing such high trust and confidence in me. Thank you for everything you have taught me, and for your sense of humour which has kept all of this work enjoyable. I am especially grateful for the countless hours proofreading my thesis. I also am indebted to Margaret Tahic, Ian Chapman, Trevor Fulton, Peter Davis, Brad Gom, and John Lindner for their help in the editing process.

I need to thank Ian Chapman for introducing me to Dr. Naylor and his group and persuading me to do a M.Sc. at the U of L. I also need to thank Ian for being so supportive throughout the entire process.

I would like to thank Matt Griffin, Bruce Swinyard, Tanya Lim, Samuel Ronayette, Ken King, Marc Ferlet, Sunil Sidher, Dave Smith, Steve Guest, Judy Long, Alan Pierce, Mike Trower, Peter Ade, Asier & Mercedes Aramburu, Sarah Leeks, Peter Hargrave, Adam Woodcraft, Bruce Sibthorpe, along with the remainder of the SPIRE team in the UK and Europe for their support and training while I was staying in the UK. I would also like to especially thank Samuel and Tanya for their friendship (as well as the car-pool service) without which my time at RAL would have been a lot more difficult.

I would also like to thank Trevor Fulton, Ian Chapman, Peter Davis, Kris Dyke, Andres Rebolledo, and Brad Gom for their assistance in various aspects of computer programming and data processing.

For all of their assistance in electronics and hardware support, I wish to thank Greg Tompkins, Ian Schofield, and Brad Gom.

For their reference letters I would like to thank Dr. David Naylor, Dr. Robert Fedosejevs, Dr. Matt Griffin, Dr. Keramat Ali, Dr. Tanya Lim, and Peter Davis.

I am very grateful for the assistance of Dr. Steve Patitsas, Dr. René Boeré, Dr. Mike Smith, and Dr. Jim Thomas as members of my supervisory committee.

I am also incredibly grateful for my relatives in the UK, most of which did not know me at all before I arrived, but still received me as if I had known them for years. Thank you Luke & Cynthia, Lilian, David & Jeanette, Aunty Irene, Aunty Kathlene, Eric & Doris, Stanley, and Carol & Mike. It was such a great opportunity to get to know the family across the pond.

I also wish to thank Professor G.R. Davis, now Director of the James Clerk Maxwell Telescope, for negotiating and securing approval for Canada's participation in the SPIRE project. This work would otherwise not have been possible.

This research has been funded in part by NSERC, the CSA, PPARC, and CIPI.

Contents

List of Tables

List of Figures

List of Abbreviations

AIG	astronomical instrumentation group	1.4, 1.5, 6.2, 6.3, 8.1, 8.4
AIV	assembly integration verification	6.2, 6.3, 6.8
AR	anti-reflective optical coating	3.5
BSM	beam steering mirror	1.3
CHSSSC	Canadian Herschel SPIRE science steering committee	1.4
CQM	SPIRE cryogenic qualification model	1.3, 1.4, 3.7, 3.8, 5.3, 5.5, 6.3, 6.4, 6.8, 6.9, 7.1, 7.2, 7.5–7.7, 8.1, 8.2, G
CSA	the Canadian space agency	1.1
CSL	Centre Spatial de Liège	7.6
DCU	detector control unit	6.3
DPU	digital processing unit	6.3
EGSE	electrical ground support equipment	6.3
EM	electromagnetic	1.2
eNB	extended Norton-Beer apodization functions[1]	4.8
ESA	the European space agency	1.1, 1.2, 1.4, 1.5, 6.2, 6.3, 8.4
FFT	fast Fourier transform algorithm developed by Cooley and Tukey[2]	2.2, 2.10, 3.2
FIR	far Infrared radiation	6.2, 6.3, 6.8, 7.11, 8.3
FPU	SPIRE focal plane unit	7.6, 8.3
FTS	Fourier transform spectrometer/spectroscopy	1.3, 1.5, 2.1, 2.2,

		2.6–2.11, 3.1–3.3, 3.5, 3.7, 4.2, 4.3, 5.3–5.6, 6.2, 6.5, 7.4, 8.1
FWHM	full width at half maximum	2.10, 4.7–4.9, 5.1, 5.4, 5.5, E, F-2
GUI	graphical user interface	4.2, 5.3
HIFI	Herschel Heterodyne Instrument for the Far Infrared	1.1, 1.2, 8.3
HR	high resolution	7.5, 7.7
HSO	Herschel Space Observatory	1.1, 1.2, 8.4
HST	Hubble Space Telescope	1.2
ICC	instrument control centre	1.4, 8.2
IDL	Interactive Data Language[3]	3.7, 4.9, 5.3, 6.6
iFTS	imaging Fourier transform spectrometer/spectroscopy	2.9, 5.6
ILS	instrumental line shape	2.10, 3.5–3.7, 4.7, 4.8, 5.4–5.6, 6.6, 6.8, 6.9, 8.2, E
IR	Infrared radiation	3.6, 5.5
IRAS	Infrared Astronomical Satellite	8.4
ISO	Infrared Space Observatory	1.2, 8.4
JAXA	Japanese Aerospace Exploration Agency	8.5
JCMT	James Clerk Maxwell telescope	1.4
JPL	jet propulsion laboratory	6.6
JSSA	joint subcommittee for space astronomy	1.4
LAN	local area network	6.3
LR	low resolution	7.5, 7.7, 7.10
MKS	metres-kilograms-seconds units	G
NTD	neutron transmutation doped	7.3
OPD	optical path difference	2.5–2.7, 2.10, 3.2–3.5, 3.7, 4.2, 4.3, 4.6–4.8, 5.4, 7.5, B, E
PACS	the Herschel photoconductor array camera and spectrometer	1.1, 1.2, 8.3
PCF	phase correction function	3.6, 4.4, 4.6–4.8,

		4.10, 5.2, 5.4–5.6, 8.1
PLW	SPIRE photometer long wavelength array	1.3, 5.5, 6.4, 6.7, 7.4, 7.5, 7.8, 7.10, 7.11, 8.3, G
PMW	SPIRE photometer long wavelength array	1.3, 5.5, 6.4, 8.3
PSO	position synchronized output signal	6.3
PSW	SPIRE photometer short wavelength array	1.3, 5.5, 6.4, 8.3
RAL	Rutherford Appleton Laboratory	1.4, 3.7, 5.3, 5.5, 6.2, 6.3, 6.5, 6.8
RJ	Rayleigh-Jeans	G
RMS	root mean square	3.7, 4.9
S/N	signal-to-noise ratio	2.7, 2.9, 2.10, 3.5, 3.6, 4.4, 4.9, 5.4, 6.5, 6.6, 7.5, 7.7, 7.8, 7.10
SCOS	spacecraft operating system	6.3
SLW	SPIRE spectrometer long wavelength array	1.3, 5.5, 6.4, 7.11, 8.3
SPIRE	Spectral and Photometeric Imaging Receiver	1.1–1.5, 3.1, 3.5–3.8, 5.3, 5.5, 6.1–6.3, 6.5–6.9, 7.1, 7.2, 7.5, 7.7, 7.9, 7.11, 8.1–8.5, G
SSW	SPIRE spectrometer long wavelength array	1.3, 5.5, 6.4, 7.11, 8.3
TFTS	test facility FTS (see chapter 6)	1.3–1.5, 3.5, 3.7, 4.5, 5.5, 5.6, 6.1–6.9, 7.4, 7.5, 7.7, 7.8, 8.1, 8.2, G
TFTS-CS	TFTS control server	6.3, 6.8
UV	ultra violet radiation	3.6
ZPD	zero optical path difference	2.6, 2.10, 3.2, 3.3, 3.5, 4.2, 4.5, 4.8, 5.4, 6.3, 6.5, 6.7, 6.9, 8.2

Chapter 1

Introduction

1.1 Overview

The Spectral and Photometric Imaging REceiver (SPIRE) is one of three instrument payloads on the European Space Agency's (ESA) Herschel Space Observatory (HSO), i.e. Herschel. Herschel is an ESA cornerstone mission scheduled for launch in August 2007. Herschel consists of three instruments which will be used to study the far-infrared/submillimetre universe. The three instruments are the Spectral and Photometric Imaging Receiver (SPIRE), the Photoconductor Array Camera and Spectrometer (PACS), and the Heterodyne Instrument for the Far Infrared (HIFI). Canada, through Dr. Naylor of the University of Lethbridge and his research group, is contributing to SPIRE. Dr. Naylor's group, with funding from the Canadian space agency (CSA), is supplying personnel and expertise, mission flight and instrument development software and hardware, and flight software to the SPIRE effort. The work presented in this thesis details my contributions to this project which includes SPIRE software and hardware development, and participation

in instrument level testing.

1.2 ESA's Herschel space observatory

The main scientific objectives of the Herschel Space Observatory are spectroscopy of star forming regions and stellar evolution in our own and nearby galaxies, and deep extra-galactic and galactic imaging surveys[4]. The Infrared Space Observatory (ISO), Herschel's precursor, operated between 2 and 240 μm with great success[5]. Herschel, however, will study celestial bodies over the 60 to 670 μm wavelength range in the relatively unexplored far infrared and submillimetre part of the electromagnetic (EM) spectrum. This frequency range is inaccessible from Earth because of atmospheric absorbtion (see section 6.4). Thus, the HSO will close the gap between the infrared and radio portions of the EM spectrum[6].

Herschel has been designed with the experience gained from the ISO mission. In order to reduce the effect of the infrared radiation from the Herschel instruments on the received signal, they will be cooled inside a cryostat (i.e. 300 $mK - < 6\ K$). With its 3.5 m diameter primary mirror[7], Herschel will be the largest imaging space telescope ever built. In comparison, the Hubble Space Telescope (HST) has a 2.4 m diameter primary mirror. Also, by virtue of its large primary mirror, which is passively cooled to $\sim$80 K, and its more sensitive detectors, Herschel will be able to detect objects considerably fainter and with higher spatial resolution than ISO.

To ensure an unimpeded view, Herschel will be located $\sim$1.5 million kilometres from the Earth on the opposite side from the sun, at the second Lagrangian point (L2)[8]. Herschel's remote orbit and cryogenic payload, which precludes any servicing mission, re-

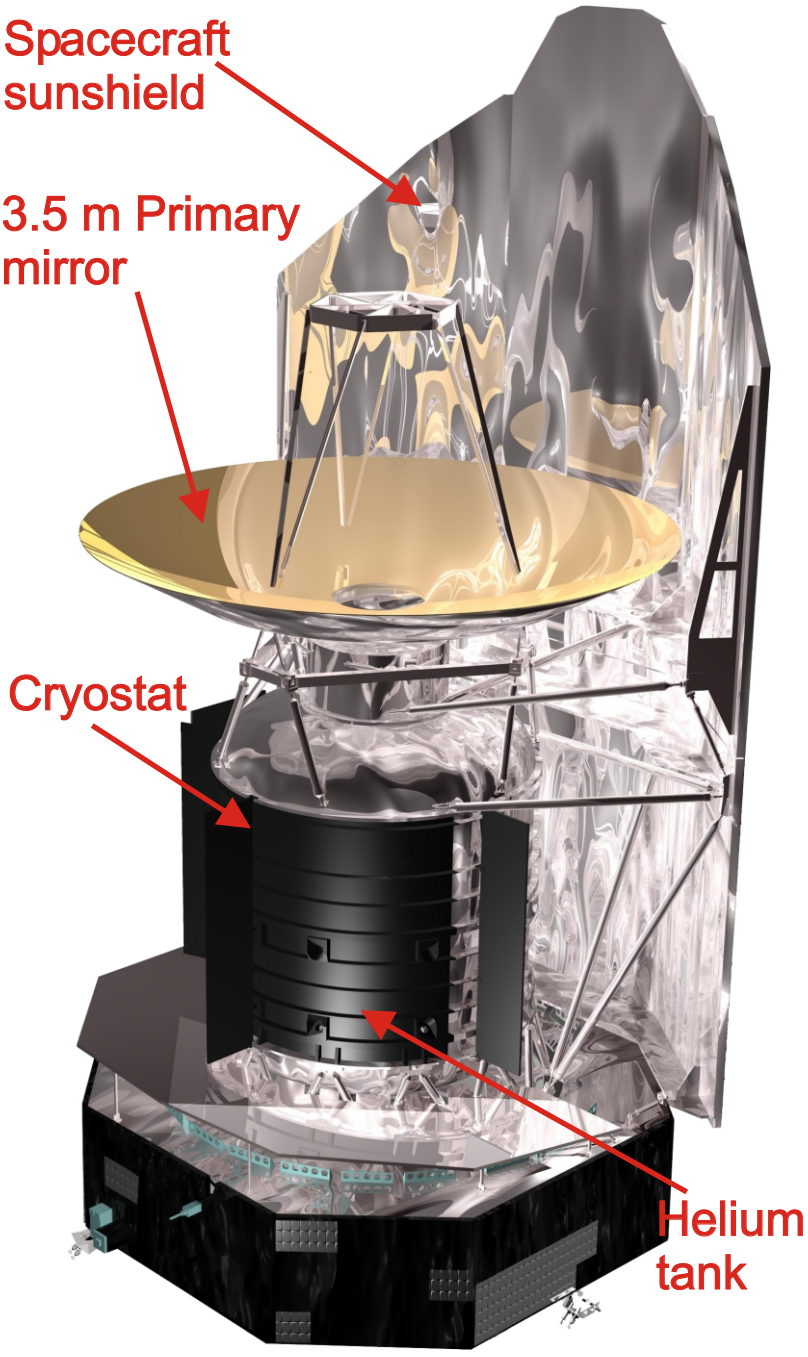

Figure 1.1: A model of the Herschel Space Observatory. The SPIRE, PACS, and HIFI instruments are all housed in Herschel's cryostat. The total payload height and diameter are ∼7.5 and 4.0 m, respectively. Fully loaded with liquid Helium, launch mass is expected to be ∼3,250 kg. Image courtesy of ESA.

quires rigorous instrument development testing and characterization as there will be no opportunity for hardware repairs or modifications once Herschel is launched.

1.3 SPIRE

The SPIRE science program consists of two primary themes: extragalactic and galactic surveys. The goal of the SPIRE extragalactic deep survey is to cover a large area of sky to a depth that is at the confusion limit for galaxies. For the Galactic Survey, SPIRE will survey nearby molecular clouds to detect complete samples of prestellar, protostellar, and young-stellar objects. SPIRE must be sensitive enough to detect faint objects, covering a large area in a reasonable time, while having sufficient dynamic range to simultaneously measure bright sources. SPIRE consists of a three band imaging photometer and a 2 band imaging spectrometer, both cooled in the Herschel cryostat. This section will describe the SPIRE photometer and spectrometer.

1.3.1 SPIRE 3-band imaging photometer

The photometer channels are centred at 250, 363, and 517 μm (40, 27.5, and 19.3 cm^{-1}, respectively) with a resolving power ($\frac{\sigma}{\Delta\sigma}$) of 3. The three bands are referred to as the photometer short wavelength (PSW), photometer medium wavelength (PMW), and photometer long wavelength (PLW), respectively. The field of view is observed simultaneously in all three bands through the use of fixed dichroic beam-splitters. The field of view for the photometer is 4 x 8 arcminutes, the largest achievable given the location of the SPIRE field in the Herschel focal plane and the size of the unvignetted field of view for the telescope

[9]. Modulation can be provided either by a beam steering mirror (BSM) in the instrument or by drift-scanning the telescope across the sky. The sensitivity of the photometer will be limited by thermal emission from the telescope. The photometer integrates all light within the spectral bandpass of the photometer channel indiscriminately. Therefore, it is important to know the spectral response across the channel. The University of Lethbridge test facility FTS (TFTS) was identified as a key piece of test equipment to identify the spectral responsivity of the SPIRE photometer bands.

A physical diagram of the SPIRE photometer is shown in figure 1.2. As part of this thesis work, I was heavily involved in evaluating the performance of the PLW array ($\sim$18 - 24 cm^{-1}) which was tested during the SPIRE cryogenic qualification model (CQM) test campaign.

1.3.2 SPIRE 2-band imaging spectrometer

The SPIRE Fourier transform spectrometer (FTS) is of the Mach-Zehnder variety[11], containing two novel broadband intensity beamsplitters[12]. One of the input ports is for the astronomical source while the other contains a calibration source which is expected to null the telescope emission. The two output ports contain detector arrays covering the ranges 200 - 325 μm and 315 - 670 μm (50 - 30.8 cm^{-1} and 31.7 - 14.9 cm^{-1}, respectively). These bands are referred to as the spectrometer short wavelength (SSW) and spectrometer long wavelength (SLW) bands, respectively. The spectral resolution is variable in the range 0.04 to 1.00 cm^{-1}. The field of view for the FTS is circular with a diameter of 2.6 arcminutes. Figure 1.4 shows a physical diagram of the SPIRE spectrometer. A block diagram of the SPIRE spectrometer is shown in figure 1.5. The TFTS was designed to have a higher

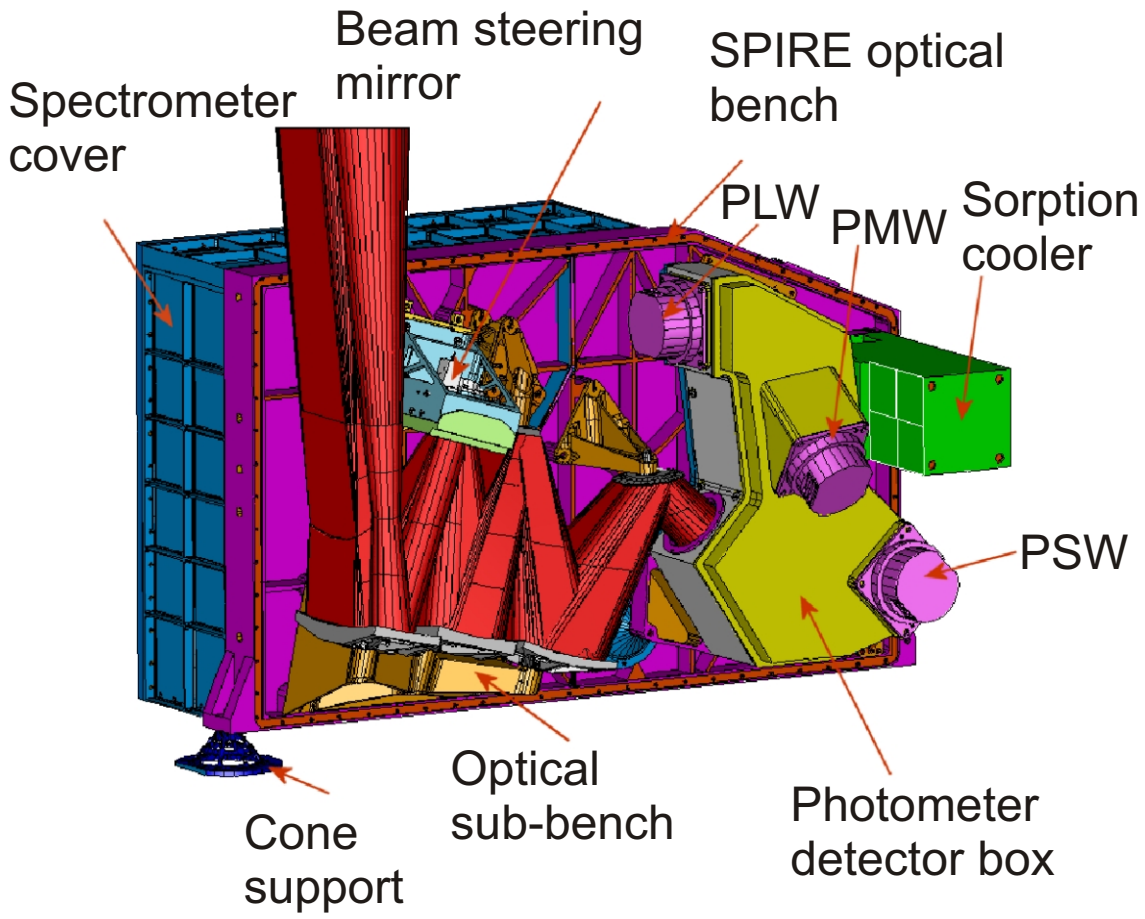

Figure 1.2: Physical diagram of the SPIRE photometer. Image courtesy of the SPIRE Design Description Document[10].

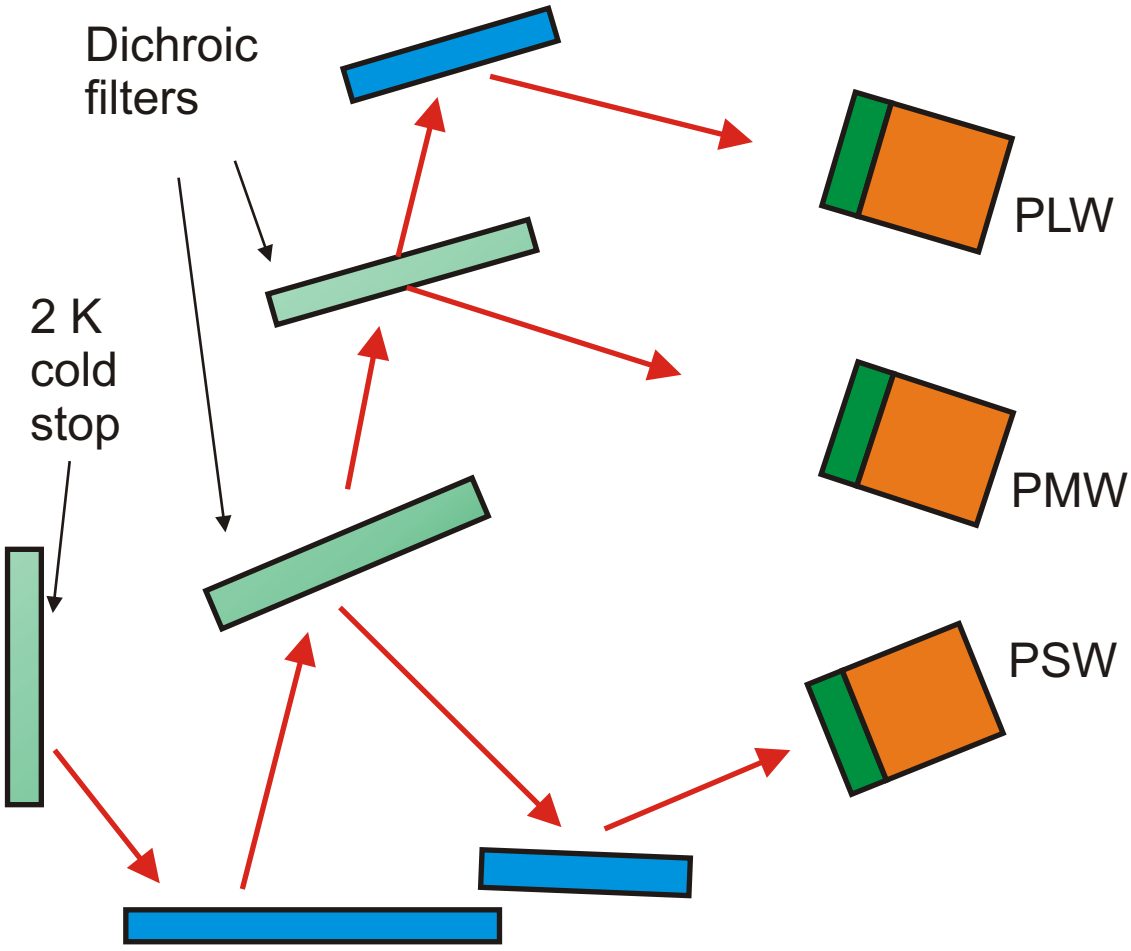

Figure 1.3: A block diagram of the photometer detector box (see figure 1.2).

spectral resolution than the SPIRE FTS so that it could fully characterize the spectral performance of this instrument.

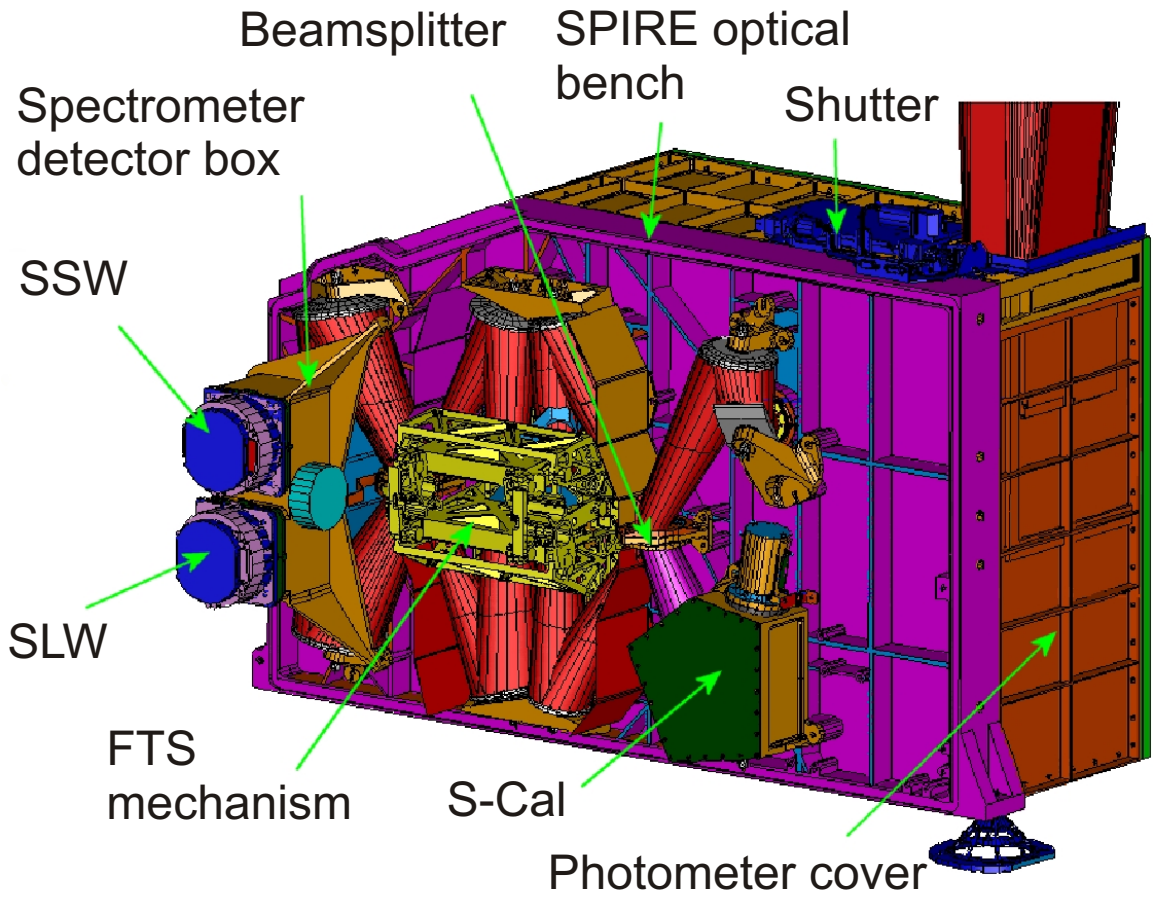

Figure 1.4: A simplified diagram of the SPIRE spectrometer. Image courtesy of the SPIRE Design Description Document[10].

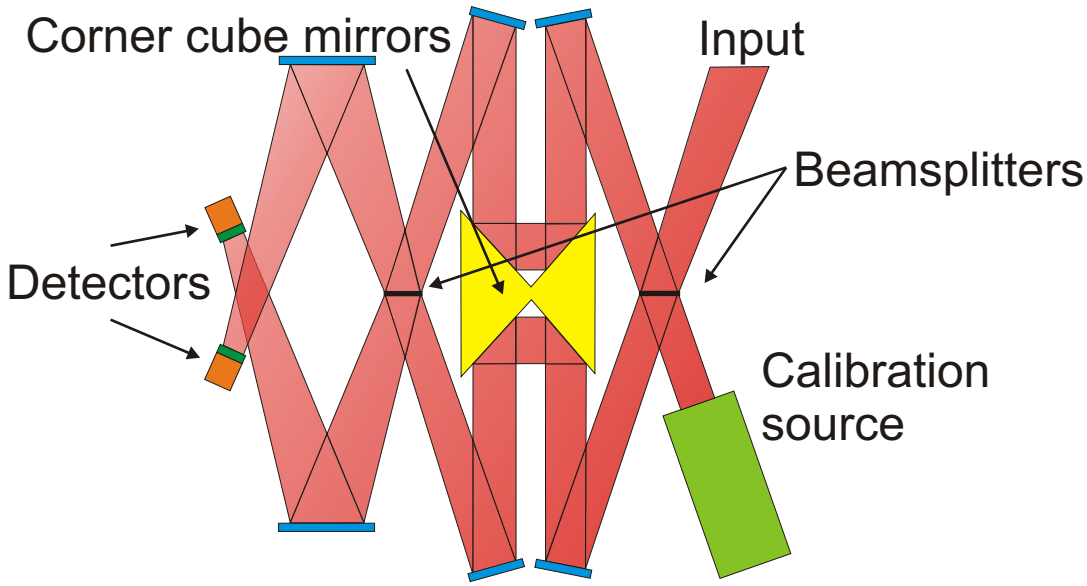

Figure 1.5: A block diagram of the SPIRE FTS including S-Cal (the spectrometer calibration source).

1.4 Canada's involvement in SPIRE

Canada's involvement in the SPIRE project was initiated by Dr. Gary Davis (then of the University of Saskatchewan) who championed a role for Canada in this European Space Agency endeavor. In November 1999, the Joint Subcommittee for Space Astronomy (JSSA) formally recommended that Canada join the SPIRE project. Two Canadian contributions to SPIRE were identified in the original proposal:

1. a cryogenic shutter mechanism for the instrument; and

2. personnel for the SPIRE instrument control centre (ICC).

In return for these contributions, Canada was allocated six positions on the SPIRE science team: one as a Co-Investigator (Dr. G.R. Davis (University of Saskatchewan)) and five as Associate Scientists; these individuals formed the Canadian Herschel SPIRE science steering committee (CHSSSC).

In August 2002, Dr. Davis took on the position as Director of the James Clerk Maxwell telescope (JCMT) on Mauna Kea, Hawaii and ESA realized that a Herschel wide cryogenic shutter was required, thus making the SPIRE shutter redundant. Dr. David Naylor of the University of Lethbridge assumed the lead role for Canada in the SPIRE project and the Canadian contributions were redefined as:

1. a test facility Fourier transform spectrometer for SPIRE instrument development and flight support testing,

2. instrument development and flight software, and

3. personnel for the SPIRE ICC.

This thesis discusses the TFTS designed and built by Dr. Naylor's astronomical instrumentation group (AIG) for use in the spectral characterization of SPIRE. I have assisted in the development of all of the contributions in the list above, including: development of the SPIRE TFTS before delivery to the Rutherford Appleton Laboratory (RAL) in August 2003, development of SPIRE instrument development software in preparation for CQM instrument testing, and service as ICC personnel from January to June 2004 while CQM testing was underway.

1.5 Summary

Accurate characterization of the Herschel instruments is critical due to the fact that the Herschel spectral band is relatively unexplored, and the cryogenic payload and remote orbit of the Herschel telescope preclude any servicing missions. Detailed information regarding the progress of Herschel/SPIRE is found in the literature [4,6,9,13-24]. This thesis discusses the TFTS, designed and built by Dr. Naylor's AIG, for use in the spectral characterization of SPIRE. Chapter 2 discusses the science of Fourier transform spectroscopy (FTS). Chapters 3, 4, and 5 discuss FTS data processing techniques; in particular, the process of phase correction is addressed in detail. Chapter 6 discusses the TFTS built by Dr. Naylor's group at the University of Lethbridge as a Canadian contribution to ESA's Herschel mission. Chapter 6 also discusses how the TFTS was used in SPIRE characterization and performance testing. The TFTS, in conjunction with the SPIRE flight spare, will serve as ground support test equipment during the flight phase of the Herschel mission. Finally, chapter 7 discusses verification testing of the SPIRE cryogenic qualification model and

chapter 8 presents conclusions and future work. Several papers have resulted from this thesis work [13, 15, 25, 26].

Chapter 2

Fourier Transform Spectroscopy and FTS Data Processing

2.1 Overview

Fourier transform spectroscopy (FTS) has gained an appreciable following in astronomy as a spectroscopic technique to maximize input flux utilization with broad spectral coverage and variable spectral resolution[27]. This chapter gives an overview of Fourier transform spectroscopy and its underlying mathematical principles. Fourier series and integrals are introduced. A description of a classical Michelson interferometer is included. The chief advantages of FTS are reviewed including the Jacquinot and Fellgett advantages. FTS limitations such as noise, sampling, and natural apodization are also discussed.

2.2 Brief history

A technique for analyzing periodic functions was developed by Jean Baptiste Joseph, Baron de Fourier[28, 29] (1768-1830), which is now known as *Fourier's Theorem* [30]. Fourier's theorem was well ahead of its time and it was not until much later that it became appreciated as a powerful analytical tool. In fact, Fourier had difficulty getting his results published [31, p. 187].

Fourier transform interferometry was initiated in 1880 when Dr. Albert A. Michelson invented the interferometer[32, 33, 34] and realized the basic concepts of Fourier transform spectroscopy[35, 36], although it was not exploited due to the lack of computational power as well as extremely poor detector sensitivity at the time[37, 38, 39]. Michelson invented a mechanical analog computer (called a harmonic analyzer[40]) capable of performing Fourier transforms of about 80 data points, but this was not extensively used for Fourier transform spectroscopy. Michelson measured 'visibility curves'[41] with his eye and made crude estimates of the spectrum. The Michelson interferometer is described later in section 2.6 of this chapter.

The first interferogram (see section 2.6) was recorded in 1911 by Rubens and Wood[42] where a microradiometer was used to record the signal. The Fourier transform of the interferogram was not calculated, but rather the spectrum was estimated and the interferogram of the estimated spectrum was compared to the measured interferogram. Fellgett was the first to apply the Fourier transform to interferograms numerically in 1958 and was also the first to recognize the multiplex advantage of FTS spectrometers (see section 2.9)[43]. In 1960, Jaquinot was the first to realize the throughput advantage of an FTS over

other spectrometers (see section 2.8)[44]. The first application of FTS to astronomy was published in 1969 by Janine & Pierre Connes[45]. An important development in analysis of FTS data was the fast Fourier transform (FFT) algorithm, developed by Cooley and Tukey in 1965[2], which was introduced to Fourier spectroscopy by Forman[46] in 1966.

2.3 Fourier series

Fourier's theorem states that a periodic function, $f(z)$, of period Z_o, can be expressed as a series of harmonic functions whose periods are integral submultiples of Z_o (i.e. Z_o, $Z_o/2$, $Z_o/3$, etc.). The mathematical form of the Fourier Series representation is given by:

$$f(z) = \frac{a_o}{2} + \sum_{n=1}^{\infty}(a_n \cos(n\omega_o z) + b_n \sin(n\omega_o z)), \tag{2.1}$$

where

$$\omega_o = \frac{2\pi}{Z_o}, \tag{2.2}$$

is the fundamental frequency and the functions $\cos(n\omega_o z)$, and $\sin(n\omega_o z)$ form a set of mutually orthogonal basis vectors. The constants a_o, a_n, and b_n are determined using the following relations (see appendix A for further details):

$$a_o = \frac{2}{Z_o}\int_{z_1}^{z_1+Z_o} f(z)dz, \tag{2.3}$$

$$a_n = \frac{2}{Z_o}\int_{z_1}^{z_1+Z_o} f(z)\cos(n\omega_o z)dz \qquad n = 1, 2, 3, \ldots , \tag{2.4}$$

and,

$$b_n = \frac{2}{Z_o}\int_{z_1}^{z_1+Z_o} f(z)\sin(n\omega_o z)dz \qquad n = 1, 2, 3, \ldots . \tag{2.5}$$

By introducing negative values of n into equation 2.1 and expressing it in exponential form (see appendix A for further detail), the expression becomes:

$$f(z) = \sum_{n=-\infty}^{\infty} d_n e^{in\omega_o z}, \tag{2.6}$$

where

$$d_n = \frac{1}{Z_o} \int_{z_1}^{z_1+Z_o} f(z) e^{-in\omega_o z} dz. \tag{2.7}$$

The amplitudes of the spectral components are split between positive frequencies (positive n), and negative frequencies (negative n).

2.3.1 Dirichlet conditions

Functions must adhere to certain conditions in order for the Fourier series to exist (weak Dirichlet condition) and be convergent (strong Dirichlet conditions). These conditions are called the Dirichlet conditions[47, 48]. The weak Dirichlet condition states that in order for a function, $f(z)$, to have a Fourier series:

- $f(z)$ must be absolutely integrable over one period,

$$\text{i.e. } \int_{Z_o} |f(z)| dz < \infty. \tag{2.8}$$

If a function $f(z)$ satisfies the weak Dirichlet condition, the existence of a Fourier series is guaranteed, but the series may not converge at every point. Similarly, if a function has an infinite number of maxima or minima in one period, then the function contains an appreciable number of components of frequencies approaching infinity. Thus, for a convergent Fourier series, in addition to the weak Dirichlet condition, the strong conditions

must be met. The strong Dirichlet conditions state that, in order for a function to have a convergent Fourier series:

- $f(z)$ must have a finite number of extrema in one period,
- $f(z)$ must have a finite number of finite discontinuities in one period.

Any periodic waveform that can be generated in the laboratory satisfies strong Dirichlet conditions, and hence possesses a convergent Fourier series.

2.4 Fourier integrals

As the limits of the Fourier series extend closer to infinity, and the spacing between harmonic frequencies decreases, the Fourier series representation (equation 2.6) can be replaced by the Fourier integral representation as follows:

$$f(z) = \int_{\sigma=-\infty}^{\infty} F(\sigma) e^{i2\pi\sigma z} d\sigma, \tag{2.9}$$

where the expression is known as the inverse complex Fourier transform[49, 50]. In this case, optical path difference (OPD), i.e. z (cm), and wavenumber, σ (cm^{-1}), are used as reciprocal Fourier transform variables. Another common Fourier transform pair of variables is time (t), measured in seconds, and frequency (ν), measured in Hz. The term $F(\sigma)$ is given by

$$F(\sigma) = \int_{-\infty}^{+\infty} f(z) e^{-i2\pi\sigma z} dz, \tag{2.10}$$

and is known as the forward complex Fourier transform. The complex Fourier transform can be expressed in terms of sine and cosine transforms as follows:

$$\begin{aligned} f(z) &= \int_{\sigma=-\infty}^{\infty} F(\sigma) e^{i2\pi\sigma z} d\sigma \\ &= \int_{-\infty}^{+\infty} \frac{a(\sigma)}{2} \cos(2\pi\sigma z) d\sigma + \int_{-\infty}^{+\infty} \frac{-i^2 b(\sigma)}{2} \sin(2\pi\sigma z) d\sigma \qquad (2.11) \\ &= \int_{-\infty}^{+\infty} \frac{a(\sigma)}{2} \cos(2\pi\sigma z) d\sigma + \int_{-\infty}^{+\infty} \frac{b(\sigma)}{2} \sin(2\pi\sigma z) d\sigma, \end{aligned}$$

where

$$F(\sigma) = \frac{a(\sigma) - ib(\sigma)}{2}, \qquad (2.12)$$

and the Fourier coefficients, $a(\sigma)$ and $b(\sigma)$, are given by:

$$a(\sigma) = 2 \int_{-\infty}^{+\infty} f(z) \cos(2\pi\sigma z) dz, \qquad (2.13)$$

and

$$b(\sigma) = 2 \int_{-\infty}^{+\infty} f(z) \sin(2\pi\sigma z) dz. \qquad (2.14)$$

Inspection of equations 2.13 and 2.14 shows that under certain symmetry conditions these coefficients are trivial. For example when the function $f(z)$ is even, $b(\sigma) = 0$ for all σ and its Fourier transform will contain only cosine terms, which are themselves even functions. In the same way, when the function $f(z)$ is odd, $a(\sigma) = 0$ for all σ, and its Fourier transform will contain only sine functions, which are odd functions. Equations 2.9 and 2.10 are referred to as Fourier transform pairs [50].

2.5 Parseval's theorem

Parseval's theorem[28, 51], as applied to Fourier series, states that the energy in a finite signal (or energy per period for a periodic signal, or power for an infinite signal) is

the same when calculated in either reciprocal Fourier domain (e.g. time and frequency, or OPD and wavenumber). The signal energy, E_f, for a signal $f(z)$ (finite) is defined as:

$$E_f = \int_{-\infty}^{+\infty} |f(z)|^2 dz = \int_{-\infty}^{+\infty} |F(\sigma)|^2 d\sigma. \tag{2.15}$$

The energy of the signal $f(z)$ results from energies contributed by all of the spectral components of the signal, $F(\sigma)$. The total signal energy is the area under $|F(\sigma)|^2$ or $|f(z)|^2$ from $-\infty$ to $+\infty$. Consider a small band $\Delta\sigma(\sigma_o)$ (where $\Delta\sigma \to 0$), centred at frequency σ_o. The energy ΔE_f of the spectral component in this band is the area of $|F(\sigma)|^2$ under the band $\Delta\sigma$:

$$\Delta E_f(\sigma_o) = |F(\sigma_o)|^2 \Delta\sigma. \tag{2.16}$$

The total signal energy is the sum of all such energy bands in the spectrum. Therefore, $|F(\sigma)|^2$ is the energy spectral density, that is energy per unit bandwidth; consequently, $F(\sigma)$ is the signal spectral density, that is signal per root unit bandwidth.

2.6 The Michelson interferometer

The simplest form of FTS is a Michelson interferometer[30, 38, 52], as is shown in figure 2.1. The Michelson interferometer operates on the principle of amplitude division and interference of light. The path that light travels through a Michelson interferometer is summarized as follows (see figure 2.1):

1. Light from a source enters the interferometer (and is collimated by a lens or mirror if required) resulting in a plane wave.

2. The resulting plane wave is then split (ideally into two equal amplitude waves) by the beamsplitter.

3. These waves travel and reflect off of the FTS mirrors (one fixed (3a) and one movable (3b)) and are directed back on themselves towards the beamsplitter.

4. The reflected beams are recombined at the beamsplitter, where two resultant beams are formed, one traveling back to the source and the other one to the detector.

5. The optical detector records the interference of the combined beams of light, resulting in an intensity variation that depends on the phase difference between the recombined beams.

Interference is accomplished by the light in each path of the interferometer traveling a different number of cycles due to the OPD between the two paths. Different amounts of optical path traveled correspond to different phases upon recombination, and therefore different levels of interference as the OPD changes. When the OPD is zero, all frequency components exhibit zero phase difference and constructive interference occurs simultaneously for all wavelengths; this position of the FTS moving mirror is referred to as the position of zero path difference (ZPD).

The variation of optical path difference by the motion of the moving mirror from one limit, through the point of ZPD, to the other limit constitutes a scan (e.g. $-L \rightarrow ZPD \rightarrow +L$). The optical signal recorded by the detector for the duration of a scan is called an interferogram.

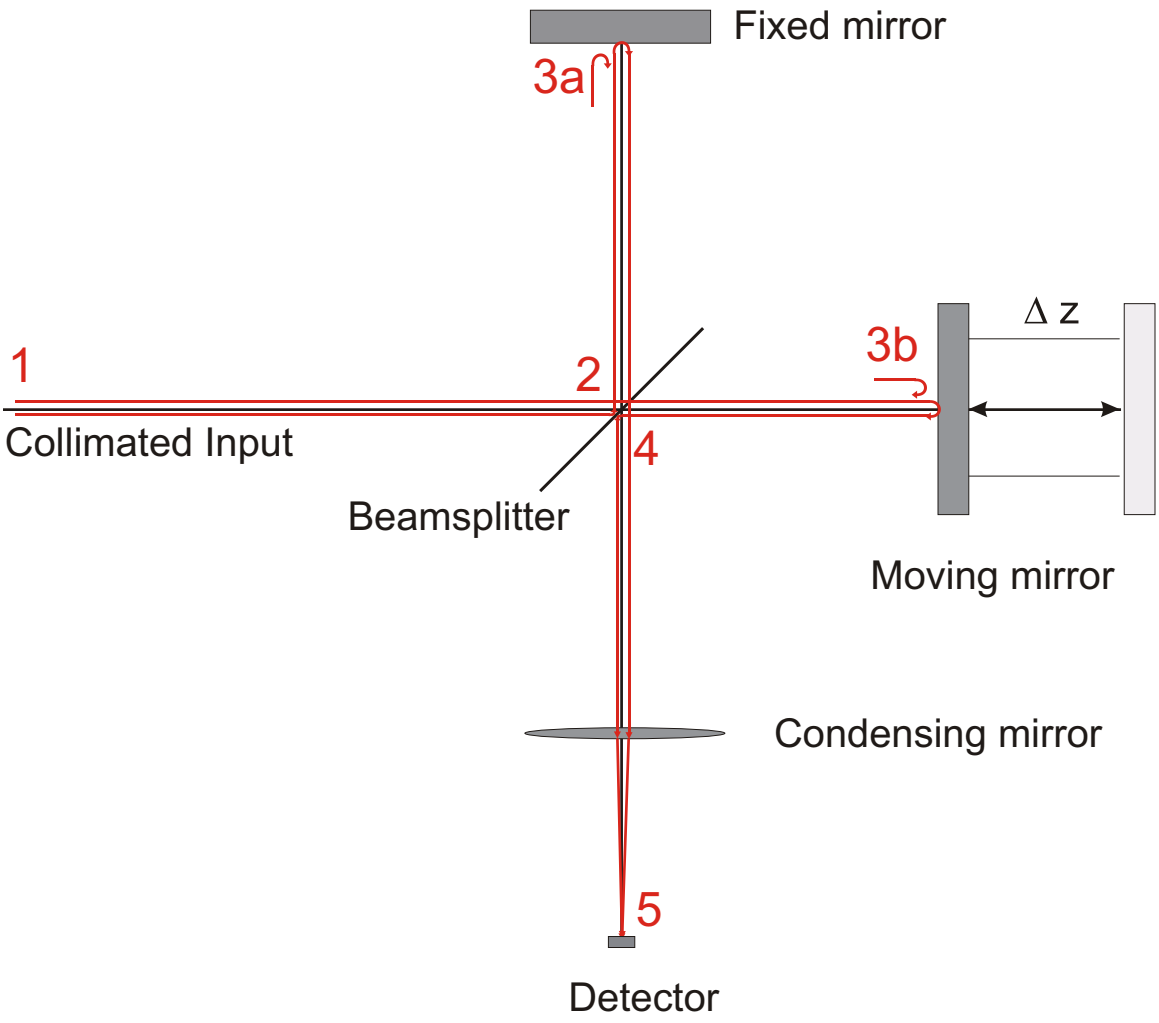

Figure 2.1: Diagram of a classical Michelson FTS[30].

All FTS interferometers have two input ports and two output ports. Each of the two ports on the Michelson interferometer is doubly occupied by both an input and an output port.

The relationship between the interferogram and spectrum is most easily explained using a monochromatic source; the extension to general spectral sources is straightforward.

2.6.1 Monochromatic sources

Consider a monochromatic beam of frequency σ_o entering the interferometer. The input beam is divided in two by the beamsplitter. The electric fields describing these two beams, starting in phase at the point just prior to the beamsplitter, can be written as:

$$\begin{aligned} E_1(z_1) &= E_0 e^{i\phi} r_m r_b t' e^{-i2\pi\sigma_o z_1} \\ E_2(z_2) &= E_0 e^{i\phi} r_m r_b t' e^{-i2\pi\sigma_o z_2}, \end{aligned} \tag{2.17}$$

where E_0 is the amplitude of the incident electromagnetic wave of angular frequency $\omega = 2\pi\sigma_o$, ϕ is the phase of the monochromatic wave at the beamsplitter, r_m is the amplitude reflection coefficient of each mirror, r_b is the amplitude reflection coefficient of the beamsplitter, t' is the amplitude transmission coefficient of the beamsplitter, and z_1 and z_2 are the lengths of the optical paths traveled by the two beams, respectively. The total electric field at the detector is given by adding the two individual electric fields from equation 2.17

$$E_T = E_1 + E_2 = E_0 e^{i\phi} r_m r_b t' (e^{-i2\pi\sigma_o z_1} + e^{-i2\pi\sigma_o z_2}). \tag{2.18}$$

The interferometer detector measures optical intensity rather than electric field. The total intensity measured at the detector is defined as the square of the magnitude of the total

electric field[38] and is given as follows:

$$I(z_1 - z_2) = |E_T|^2 = 2E_0^2 R_m R_b T(1 + \cos(2\pi\sigma_o(z_1 - z_2))), \tag{2.19}$$

where $R_m = r_m^2$ is the reflectance of the mirrors, $R_b = r_b^2$ is the reflectance of the beamsplitter, and $T = t'^2$ is the transmittance of the beamsplitter. In the case of an ideal interferometer, the beamsplitter reflects and transmits 50 % of the incident light and the interferogram can be expressed as:

$$I_0(z) \propto B(\sigma)(1 + \cos(2\pi\sigma_o z)), \tag{2.20}$$

where z is the OPD which was expressed as $z_1 - z_2$ in equation 2.19, $B(\sigma)$ is the spectrum ($E_0^2(\sigma) \propto B(\sigma)$), and σ_o is the frequency in wavenumbers (cm^{-1}) of the monochromatic source. The interferogram is seen to be composed of a constant (DC) term and a modulation term, which is given by the cosine function. In the monocromatic example, the spectrum $B(\sigma)$ is only nonzero at frequencies $\pm\sigma_o$ and is zero elsewhere.

2.6.2 Polychromatic/broad sources

When the spectral source contains more than one frequency, the resultant interferogram is the superposition of the interferograms for each frequency, i.e.

$$\begin{aligned} I_0(z) &\propto \int_{-\infty}^{+\infty} B(\sigma)(1 + \cos(2\pi\sigma z))d\sigma \\ &\propto \int_{-\infty}^{+\infty} B(\sigma)d\sigma + \int_{-\infty}^{+\infty} B(\sigma)\cos(2\pi\sigma z)d\sigma. \end{aligned} \tag{2.21}$$

It is customary to neglect the constant ($\int_{-\infty}^{+\infty} B(\sigma)d\sigma$) component and express the interferogram as:

$$I(z) \propto \int_{-\infty}^{+\infty} B(\sigma)\cos(2\pi\sigma z)d\sigma. \tag{2.22}$$

This is the cosine Fourier transform of the source spectrum $B(\sigma)$. The spectrum can be recovered by the inverse cosine Fourier transform of the interferogram:

$$B(\sigma) \propto \int_{-\infty}^{+\infty} I(z)\cos(2\pi\sigma z)dz. \tag{2.23}$$

As discussed earlier, when the inverse cosine Fourier transform of an interferogram is taken, in addition to the positive frequency spectrum $B(\sigma)$, the negative frequency spectrum $B(-\sigma)$ is produced.

The interferogram, $I(z)$, and spectrum, $B(\sigma)$, are Fourier transform pairs. $B(\sigma)$ and $I(z)$ are ideally real valued, allowing the interferogram and spectrum to be related using the cosine Fourier transform:

$$I(z) = 2\int_{0}^{+\infty} B(\sigma)cos(2\pi\sigma z)d\sigma, \tag{2.24}$$

and

$$B(\sigma) = 2\int_{0}^{+\infty} I(z)cos(2\pi\sigma z)dz. \tag{2.25}$$

$B(\sigma)$ is the spectrum formulated as a function of wavenumber, and $I(z)$ is the interferogram as a function of OPD. The even symmetry of $I(z)$ and the extension of $B(\sigma)$ to include negative frequencies ($B(-\sigma) = B(\sigma)$), allows the $2\int_{0}^{+\infty}$ integration limit on the cosine Fourier transforms in equations 2.24 and 2.25 to be interchangeable with the integration limit of $\int_{-\infty}^{+\infty}$:

$$I(z) = \int_{-\infty}^{+\infty} B(\sigma)cos(2\pi\sigma z)d\sigma, \tag{2.26}$$

and

$$B(\sigma) = \int_{-\infty}^{+\infty} I(z)cos(2\pi\sigma z)dz. \tag{2.27}$$

More generally, the interferogram and spectrum may be expressed using complex Fourier transforms[37]. The inverse complex Fourier transform is expressed as:

$$I(z) = \int_{-\infty}^{+\infty} B(\sigma) e^{+i2\pi\sigma z} d\sigma, \tag{2.28}$$

and the forward complex Fourier transform is expressed as:

$$B(\sigma) = \int_{-\infty}^{+\infty} I(z) e^{-i2\pi\sigma z} dz. \tag{2.29}$$

The complex Fourier transforms shown in equations 2.28 and 2.29 can be separated into sine and cosine Fourier transforms. The inverse transform is separated as

$$\begin{aligned} I(z) &= \int_{-\infty}^{+\infty} B(\sigma) e^{+i2\pi\sigma z} d\sigma \\ &= \int_{-\infty}^{+\infty} B(\sigma) cos(2\pi\sigma z) d\sigma \quad + i \int_{-\infty}^{+\infty} B(\sigma) sin(2\pi\sigma z) d\sigma, \end{aligned} \tag{2.30}$$

and the forward transform is separated as

$$\begin{aligned} B(\sigma) &= \int_{-\infty}^{+\infty} I(z) e^{-i2\pi\sigma z} dz \\ &= \int_{-\infty}^{+\infty} I(z) cos(2\pi\sigma z) dz \quad - i \int_{-\infty}^{+\infty} I(z) sin(2\pi\sigma z) dz. \end{aligned} \tag{2.31}$$

The even symmetry of $B(\sigma)$ can be exploited to express the interferogram as a cosine Fourier transform:

$$\begin{aligned} I(z) &= \int_{-\infty}^{+\infty} B(\sigma) cos(2\pi\sigma z) d\sigma \qquad + 0 \\ &= 2 \int_{0}^{+\infty} B(\sigma) cos(2\pi\sigma z) d\sigma. \end{aligned} \tag{2.32}$$

In the non-ideal (asymmetric) case the cosine (equation 2.25) and complex (equation 2.29) Fourier transforms are not equivalent. If uncorrected, the interferogram asymmetries lead to the introduction of phase errors in the spectrum. Phase correction is needed to re-symmetrize the interferogram and recover the correct spectrum. Phase correction will be discussed in detail in chapter 3.

2.7 FTS observing modes

There are two modes to record interferograms using an interferometer: step and integrate, and rapid-scan. The step and integrate mode involves stepping precise amounts of OPD and waiting for a prescribed period of time for the optical detector to integrate signal. Step and integrate mode requires some form of signal modulation such as a chopper combined with a lock-in amplifier to separate the signal from the DC/low frequency noise. Improvements in signal-to-noise ratio (S/N) are obtained through increasing the integration time per step.

Alternatively, rapid-scan mode, developed by Mertz[53, 54], involves moving the FTS translation stage at constant velocity and sampling both the optical signal and stage position in uniform increments of OPD. The mirror velocity can be selected such that the interferogram fringes provide signal modulation[37]. The ac modulated signal can be processed for spectral filtering and electronic noise reduction before the spectrum is computed. S/N improvements are found through repeating scans and averaging either interferograms or spectra, rather than slowing down the mirror velocity which would reduce the fringe modulation.

For a Michelson interferometer in rapid-scan mode, the OPD, z, as a function of time, t, and optical speed, v, is given by:

$$z = vt. \tag{2.33}$$

Equation 2.20 reveals that the angular frequency relating to any particular spectral contribution to the interferogram, i.e. σ_o, is derived from the term $\cos(\omega z) = \cos(2\pi\sigma_o z)$. Since the mirror is moving in time, the electrical detector signal modulation is observed as a func-

tion of time rather than position. Thus, the observed interferogram electrical oscillation frequency will be related to both the moving mirror velocity and the maximum spectral frequency (see equation 2.43). In the rapid scan mode an external source of signal modulation (e.g. a chopper) is not required, therefore the entire signal is exposed to the detector at all times. Thus, for a given scan time, T, the detector is exposed to the interference signal for time T in rapid scan mode while the detector is only exposed to the interference signal for a time $\frac{T}{2}$ in step-and-integrate mode. Rapid-scanning measurements are more resilient to source fluctuations than step-and-integrate measurements as individual interferograms are recorded in a short time interval. Individual interferograms deemed unacceptable (e.g. a scan encountering a cosmic ray event) can be discarded without affecting the remainder of the measurement, whereas a corrupted integration step in step and integrate data collection affects the entire measured spectrum.

2.8 The Jacquinot advantage

The throughput of an FTS is defined as the product of the area of the input light beam A (m^2) and the solid angle Ω (sr) contained within the beam; this quantity is also known as the étendue or light-grasp. The controlling factor for the throughput is usually the most expensive component of the spectrometer; in the case of an FTS this is typically the beamsplitter. All interferometers possessing circular symmetry (eg. FTS or Fabry Perot interferometers) have significantly higher throughput or optical efficiency, compared with dispersive spectrometers such as grating spectrometers, where the real component of the throughput is determined by the narrow entrance and exit slits. The high throughput of

the FTS is known as the Jacquinot advantage[44]. As will be shown in section 2.10.4, while in principle one can increase the throughput by increasing the divergence angle within the FTS this results in a natural apodization of the interferogram, which limits the maximum attainable resolution. Hence, there is a trade-off between attainable resolution and signal intensity.

2.9 The Fellgett advantage

The multiplex advantage[43] of an FTS, also known as the Fellgett advantage, is due to the exposure of an interferometer to all spectral components of a signal at all times. To illustrate the Fellgett advantage an example comparing an FTS with a dispersive spectrometer is given. In a dispersive spectrometer[30] only a narrow range of wavelengths are measured at a given instant. By comparison, in an FTS all source wavelengths are incident on the detector at all times. This leads to a multiplex advantage also known as the Fellgett advantage.

Suppose a spectrum is measured between σ_1 and σ_2 with a resolution $\delta\sigma$ (cm^{-1}). The number of spectral elements, M, in the band is given by

$$M = (\sigma_2 - \sigma_1)/\delta\sigma. \tag{2.34}$$

If a grating spectrometer is used then each small band of width $\delta\sigma$ can be observed for a time $\frac{T}{M}$ where T is the total time required to scan the full spectrum. The integrated signal received in a small band $\delta\sigma$ is proportional to $\frac{T}{M}$. If the noise is random and does not depend on the signal, then the signal noise should be proportional to $\sqrt{\frac{T}{M}}$. Therefore, the

S/N for a grating spectrometer is [37]:

$$S/N_G \propto \sqrt{\frac{T}{M}}. \tag{2.35}$$

An FTS measures all wavelengths at all times. Therefore the integrated signal in a small band $\delta\sigma$ is proportional to T (rather than $\frac{T}{M}$) and the signal noise is proportional to $\sqrt{T}$. Thus, for an interferometer, the S/N is[37]:

$$S/N_I \propto \sqrt{T}. \tag{2.36}$$

If the grating and FTS spectrometers have identical (or at least comparable) throughput then the ratio of the S/N for the two instruments can be written as:

$$\frac{S/N_I}{S/N_G} = \sqrt{M}. \tag{2.37}$$

Since M is the number of spectral elements of width $\delta\sigma$, equation 2.37 indicates that the interferometer has a much higher S/N than a grating spectrometer. Moreover, it should be noted that due to the narrow entrance and exit slits of a grating spectrometre[30], the throughput of an FTS is typically two orders of magnitude larger than a grating spectrometer, which leads to an even greater increase in S/N.

Advances in detector array technology allow grating spectrometers to observe entire spectral ranges simultaneously; however, the FTS can use the same detector arrays to simultaneously observe many spatial components of the source (i.e. imaging FTS (iFTS)) so the gain is retained [37].

The Multiplex advantage is lost when the signal noise is proportional to the square root of the source intensity (i.e. photon noise) as the ratio of FTS and grating spectrometer S/N approaches unity. The Jacquinot advantage (section 2.8) is not lost during photon

noise limited measurements, however, so the FTS still holds an advantage over the grating spectrometer.

2.10 FTS design issues

The analysis presented in section 2.6 for determining the spectrum from the interferogram involve integrating the OPD from $-\infty$ to $+\infty$. In practice, interferograms cannot be measured out to infinity in either direction of OPD, but to a finite maximum OPD, L. As a result, the spectral resolution achieved is not infinite, but rather finite and is given by:

$$\Delta\sigma = \frac{1}{2L}, \tag{2.38}$$

where L is the maximum optical path difference and $\Delta\sigma$ is the spacing between elements in the spectrum. Thus the resolution of an FTS interferometer is variable depending on the OPD length L selected for an interferogram. A consequence of the finite truncation of the interferogram is a sinc function convolved across the spectrum in the reciprocal Fourier domain[37]. Thus, FTS interferometer spectra have an inherent sinc instrumental line shape (ILS).

2.10.1 Phase

Asymmetries in interferograms cause the calculated spectrum to be complex valued. Thus, interferogram asymmetries are observed in spectra as phase. The determination of the spectral phase, $\phi(\sigma)$, is as follows:

$$\phi(\sigma) = \arctan(\frac{B_i(\sigma)}{B_r(\sigma)}), \tag{2.39}$$

where B_r is the real component of the spectrum and B_i is the imaginary component of the spectrum. FTS instrument design and data processing must account for asymmetries in the interferogram and will be discussed in greater detail in chapter 3.

2.10.2 Noise

Optical noise consists of photon noise and source noise. Photon noise is due to statistical fluctuations in the rate of arrival of photons. If n photons are measured in a given time period, the photon noise level is proportional to $\sqrt{n}$. Source noise arises from periodic and random variations in source intensity over time. The random component of source noise typically varies as $1/f$ in the frequency domain[38].

Electrical noise sources can be categorized as Johnson noise, phonon noise, shot noise, and flicker noise[55]. Johnson noise, also known as white noise, has a flat spectral profile. Phonon noise is produced by vibrations and temperature fluctuations in the detectors (e.g. bolometers) and the thermal connection to the detector heat sinks[55, 56]. Shot noise results from time-dependent fluctuations in electrical current caused by the quantized electron charge, and is well known to occur in solid-state devices such as tunnel junctions, Schottky barrier diodes, and p-n junctions. Flicker noise has a $1/f$ frequency profile, similar to random optical source noise. The shot and flicker noise produced in the detector contacts is difficult to model, and is measured as excess noise in the detector signal.

Ideally, an FTS is designed such that all noise is reduced to the point where photon noise dominates through alignment and proper choice of detectors, optics, and readout electronics. Noise should affect the real and imaginary domains of the spectrum equally. Therefore, the noise found in the real portion of the spectrum is less than that in the entire

(i.e. complex) spectrum. Random noise levels are reduced through improving interferometer stage metrology and signal S/N. The random noise contribution to the interferogram can never be completely removed but can be minimized through FTS design and data processing techniques (see chapter 5).

2.10.3 Nyquist and Sampling

The Nyquist sampling theorem[57, 58] states that a signal may be perfectly reconstructed if the data sampling frequency is twice that of the highest spectral content of the signal being sampled. Other conditions on the Nyquist sampling theorem are similar to convergence requirements in a Fourier series and are given in section 2.3.1. For the sampling of an interferogram, the OPD sampling interval must satisfy the following criteria:

$$\Delta z \leq \frac{1}{2\sigma_{band}}, \tag{2.40}$$

where Δz is in cm and σ_{band} is the spectral bandwidth of the signal (in cm^{-1}). For spectra including zero frequency as the lowest portion of the band, σ_{band} is equivalent to σ_{max}, the highest spectral frequency component (cm^{-1}). Inversely, the maximum observable or Nyquist frequency, σ_{nq}[1] in cm^{-1}, is given in terms of interferogram OPD sampling interval by the relation:

$$\sigma_{nq} = \frac{1}{2\Delta z} \qquad cm^{-1}, \tag{2.41}$$

where Δz is the optical sampling interval in cm.

In essence, an interferometer is simply an effective method of bringing the unobservable high frequencies of light down to observable acoustic frequencies by exploiting the

[1]The distinction between σ_{nq} and σ_{max} is this: σ_{nq} is the highest frequency that the spectrometer is capable of observing while σ_{max} is the highest frequency (or band if zero frequency is not required) that is actually present in the spectrum.

principle of interference. Assuming that the spectrum is not under-sampled (i.e. no aliasing) then, for a rapid scan FTS, the highest modulation frequency found in an interferogram, ν_{max} (Hz), is related to the highest spectral frequency, σ_{max}, as follows:

$$\nu_{max} = v_{OPD}\sigma_{max} \qquad Hz, \tag{2.42}$$

where v_{OPD} is the speed of the translation stage in optical path difference.

For example, an optical source of 0.1 cm wavelength ($\lambda = 0.1$ cm, $\sigma = 10\text{cm}^{-1}$) has a frequency of 300 GHz. A Michelson interferometer with a translation stage moving at 1 cm_{opd}/s will modulate the 300 GHz oscillation down to 10 Hz (equation 2.42). This is a frequency reduction on the order of 10^{11}.

It is common practice to measure the interferogram in equal increments of optical path difference, which allows use of the FFT algorithm. The FFT algorithm[2] computes the discrete Fourier transform of N data points on the order of $N \log_2 N$, as compared to a time scale on the order of N^2 for the discrete Fourier transform algorithm. The FFT algorithm requires at least one unique data point at ZPD(see figure 3.2). Failure to sample the exact position of ZPD correctly results in phase errors in the spectrum which will be discussed in chapter 3.

Stage Velocity

In rapid-scanning observation mode, interferometer mirror stage velocity is limited by the detector roll-off frequency[59]. For a Michelson interferometer, the relationship between the maximum spectral frequency (σ_{max}), the stage velocity, and the detector roll-

off frequency (ν_{max} in Hz) is given by

$$\sigma_{max} = \frac{\nu_{max}}{v} \qquad (cm)^{-1} \tag{2.43}$$

where v is the optical linear stage velocity in cm/s.

2.10.4 Natural apodization

In the case of a point source located at a focus of a lens which feeds an interferometer, the resulting collimated beam has no divergence and thus the overlap of the recombined beams from the interferometer is independent of OPD. In reality, however, all interferograms suffer from some degree of distortion due to the divergence of radiation within the interferometer. In a real interferometer the entrance aperture has a finite size which means that a beam entering the interferometer is divergent and the overlap between the recombined beams depends upon OPD; this leads to the phenomenon known as natural apodization.

Consider light entering an interferometer's entrance aperture at an angle α away from the optical axis (see figure 2.2). Where the on-axis OPD is simply z, the off-axis OPD is $z\cos(\alpha)$ instead. The resulting interferogram intensity is determined by integrating over the solid angle Ω. For a monochromatic source, the interferogram is determined as follows:

$$\begin{aligned} I(z) &\approx \int_0^{\Omega} \cos(2\pi\sigma_o z[1-\frac{\alpha^2}{2}])d\Omega' \\ &\approx \int_0^{\Omega} \cos(2\pi\sigma_o z[1-\frac{\Omega'}{2\pi}])d\Omega' \\ &\approx \Omega sinc(\frac{\sigma_o z\Omega}{2\pi})\cos(2\pi\sigma_o z(1-\frac{\Omega}{4\pi})). \end{aligned} \tag{2.44}$$

Two simplifications are incorporated into the above expression. Firstly, the small angle

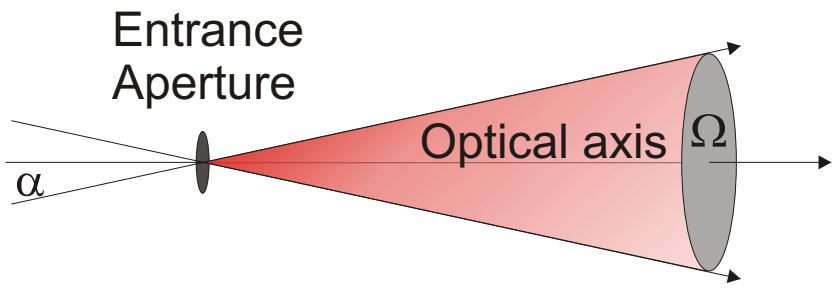

Figure 2.2: Diagram of off-axis light due to a finite sized entrance aperture on an FTS.

approximation (i.e. $\cos(\alpha) \approx 1 - \frac{\alpha^2}{2}$) and secondly, a circular aperture at the focus of a collimating mirror has solid angle $\Omega = \pi\alpha^2$. Equation 2.44 shows that the measured interferogram is different from the ideal interferogram (equation 2.26 change in the cosine term as well as a multiplication by a sinc function.

There are two effects on the interferogram/spectrum caused by the finite entrance aperture of a non-ideal interferometer:

- the interferogram envelope is multiplied by a sinc function, and
- there is both an OPD and wavenumber scale change.

The scale change in OPD and wavenumber can be expressed as $z' = z(1 - \frac{\Omega}{4\pi})$ and $\sigma' = \sigma(1 - \frac{\Omega}{4\pi})$.

The multiplication of the interferogram by a sinc function is equivalent to convolving the spectrum with a rectangular function. For a monochromatic source at frequency σ_o, the spectral line appears to be at σ_o for the on-axis signal, but for the most oblique rays with the shortest OPD ($z' = z\cos(\alpha)$) the spectral line will be shifted to $\sigma_o(1 - \frac{\Omega}{2\pi})$. Thus the observed line will be centred at $\sigma_o(1 - \frac{\Omega}{4\pi})$ and will have a width increase of $\frac{\Omega\sigma_o}{2\pi}$.

Therefore, spectral resolution greater than $\frac{\Omega\sigma_o}{2\pi}$ cannot be achieved as the rectangular convolution has broadened all spectral features. Resolving power of an interferometer is given as:

$$R = \frac{\sigma}{\Delta\sigma}. \tag{2.45}$$

The limit on spectral resolution can be related to resolving power as follows:

$$\begin{aligned} R &\leq \frac{\sigma}{\frac{\sigma\Omega}{2\pi}} \\ R &\leq \frac{2\pi}{\Omega}, \end{aligned} \tag{2.46}$$

where the inequality above is known as the Jacquinot criterion[38]. The Jacquinot criterion prescribes an upper limit on both the resolution of an interferometer and the size of the entrance aperture (and hence the maximum off-axis angle).

There is also a component of natural apodization due to the finite scan range of actual FTS interferometers. Essentially, an infinite interferogram is multiplied by a finite rectangular function of width $\pm L$. This is equivalent to convolving the spectrum with a sinc function (with full width at half maximum (FWHM) $\sim \frac{1.207}{L}$). Thus the natural ILS of an FTS with a collimated input is a sinc function. The natural ILS of an FTS without a collimated input is a sinc function convolved with a rectangular function.

2.11 Conclusions

This chapter has introduced the mathematics behind the operation of an FTS. The classical Michelson FTS design was introduced and the Jacquinot and Fellgett advantages

of the FTS have been explored. Limitations of the FTS have also been explored in areas such as natural apodization, sampling, noise, symmetry, resolution, finite travel, and finite aperture size. The FTS, with its simple optomechanical design, broad spectral coverage, high throughput and variable resolution make it a choice spectrometer for measurements of weak astronomical signals at submillimetre wavelengths.

Chapter 3

Phase Correction

3.1 Overview

In Fourier transform spectroscopy, measured interferograms are likely to contain phase errors. When operating an FTS in single-sided operation (section 3.2), as is the case for the Herschel SPIRE spectrometer, it is necessary to phase correct the interferograms to obtain accurate spectra. The Herschel SPIRE spectrometer contains two beam-splitters; both of which are expected to have a non-linear, perhaps unique, phase response. This chapter will discuss sources of phase errors and two phase correction methods introduced by Mertz[60] and Forman[61].

3.2 Terminology

There is considerable discrepancy in the literature regarding the terminology associated with FTS interferograms. The terminology used in this work is defined here for

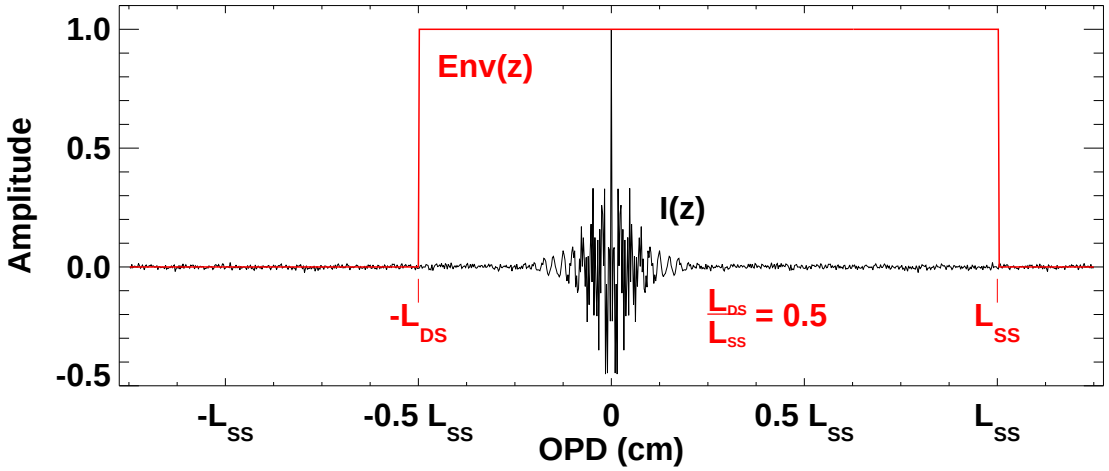

Figure 3.1: The interferogram of a spectrum containing a broad Gaussian emission line on which are superimposed several Gaussian absorption features and a random noise component. Also shown is the envelope function, $Env(z)$, in red. If $L_{DS} = 0$ then the resulting interferogram is one-sided, if $\frac{L_{DS}}{L_{SS}} = 1$ then the interferogram is double-sided, and if $\frac{L_{DS}}{L_{SS}} < 1$ then the interferogram is single-sided.

clarity, and will be used extensively throughout this and the remaining chapters. Unless explicitly stated, all values with units of distance are stated in terms of optical path difference. Figure 3.1 illustrates an interferogram of a spectrum containing a broad Gaussian emission line on which are superimposed several Gaussian absorption features. The figure is used to define the terms double-sided, single-sided, one-sided, and envelope function.

An interferogram, although theoretically of infinite length, is recorded over a finite range of optical path difference determined by the length of the translation stage of the FTS instrument (see figure 2.1). The term $I_\infty(z)$ is used to denote a theoretical interferogram with values over the optical path range $z \in (-\infty, +\infty)$. An actual interferogram can be considered to be the product of $I_\infty(z)$ and an envelope function, $Env(z)$:

$$I(z) = I_\infty(z) \times Env(z). \tag{3.1}$$

The value of the envelope function over the interval $z \in [-L_{DS}, L_{SS}]$ is as follows:

$$Env(z) = \begin{cases} 1 & z \in [-L_{DS}, L_{SS}] \\ 0 & \text{elsewhere.} \end{cases} \tag{3.2}$$

The interval $[-L_{DS}, L_{SS}]$, with $z = 0$ marking the location of ZPD, defines the finite interval over which the interferogram is actually measured in practice. To distinguish between the terms one-sided, single-sided, and double-sided the ratio of $\frac{L_{DS}}{L_{SS}}$ is used. The interferogram is one-sided for

$$\frac{L_{DS}}{L_{SS}} = 0, \tag{3.3}$$

single-sided for

$$0 < \frac{L_{DS}}{L_{SS}} < 1, \tag{3.4}$$

and double-sided for

$$\frac{L_{DS}}{L_{SS}} = 1. \tag{3.5}$$

The FFT algorithm[2] requires both positive and negative OPD interferogram data at the same resolution to calculate a complex Fourier transform. A one-sided interferogram known to be symmetric may, in principle, be *butterflied* in order to provide the FFT algorithm with the required negative OPD information. The process of butterflying an interferogram involves setting the interferogram values of negative OPD equal to the corresponding positive OPD values. This is only accurate if the interferogram is of even symmetry, as is ideally the case:

$$I(-z) = I(z). \tag{3.6}$$

The resulting spectrum of the butterflied, one-sided interferogram will have the same resolution as a double-sided interferogram of the same length (i.e. $\frac{L_{DS}}{L_{SS}} = 1$). This, of course,

neglects any phase errors propagated by the butterflying process which ignores any asymmetry in the original single-sided interferogram.

3.3 Introduction

The finite amount of stage travel in FTS instruments may be allocated towards two reciprocal applications. Stage travel may be used for higher spectral resolution (one-sided interferogram) or it may be used for providing phase information (double-sided interferogram). The idea of measuring a one-sided interferogram was first introduced by J. Connes in 1970[62]. In many cases, the phase information provided by a double-sided interferogram may be highly over-resolved as phase is typically slowly varying[54, 61, 63]. An ideal interferogram will contain identical information on both sides of the ZPD position. Theoretically, therefore, the spectrum can be uniquely recovered with an interferogram starting at ZPD (one-sided interferogram). However, in practice, a single-sided interferogram is measured in such a way that at least a small amount in the negative OPD region is recorded in order to characterize the phase. This phase information can then be used to correct the asymmetry in the high resolution one-sided interferogram. For a translation stage of fixed length, this leads to a trade-off between the length of the double-sided interferogram used to determine the phase information, and the one-sided interferogram used to achieve higher spectral resolution.

There are several causes of phase errors in Fourier transform spectrometers. The most common type of phase error arises from not precisely sampling the ZPD position of the interferogram, thereby producing a linear phase error in the spectral domain. Nonlinear

phase errors can arise from such things as: dispersion in the beam-splitter/compensator, electronic amplifier frequency response, detector time constants, and misalignment in mirrors. Random phase errors may be the result of: noise in the optical/electronic signal, and variations in the position and velocity of the translation stage. If left uncorrected, upon Fourier transformation the resulting phase errors will introduce artifacts into the final spectrum[39].

Phase contributions can be categorized as systematic, variable, and random. Systematic effects can in principle be calibrated and removed in post-processing. Variable and random phase require attention at the level of an individual interferogram. The following sections discuss phase correction as a technique used to correct for the asymmetry in single-sided interferograms.

3.4 Theory

The above contributions to phase, $\phi(\sigma)$, can be combined and expressed within the inverse complex Fourier transform, resulting in an asymmetric interferogram:

$$I_{asymmetric}(z) = \int_{-\infty}^{+\infty} B(\sigma) e^{i\phi(\sigma)} e^{+2\pi\sigma z} d\sigma. \tag{3.7}$$

The Fourier transform of a real, non-symmetric function results in a complex function with even and odd symmetry for the real and imaginary components, respectively[31]. An interferogram with spectral phase errors will be real but non-symmetric. The complex Fourier transform (equation 2.29) of an interferogram with asymmetry/phase errors will

result in a complex valued spectrum:

$$\begin{aligned}\int_{-\infty}^{+\infty} I_{asymmetric}(z)e^{-i2\pi\sigma z}dz &= B(\sigma)e^{i\phi(\sigma)} \\ &= B_r(\sigma) + iB_i(\sigma),\end{aligned} \tag{3.8}$$

where $B_r(\sigma)$ and $B_i(\sigma)$ represent the resultant real and imaginary components of the spectrum, respectively. The real and imaginary components are products of the actual spectrum, and a phase term, as shown below:

$$B_r(\sigma) = B(\sigma)cos(\phi(\sigma)) = \int_{-\infty}^{+\infty} I_{asymmetric}(z)cos(2\pi\sigma z)dz, \tag{3.9}$$

$$iB_i(\sigma) = iB(\sigma)sin(\phi(\sigma)) = -i\int_{-\infty}^{+\infty} I_{asymmetric}(z)sin(2\pi\sigma z)dz. \tag{3.10}$$

Due to the asymmetry of $I_{asymmetric}(z)$ (equation 3.7), the positive ($\int_0^{+\infty}$) and negative ($\int_{-\infty}^0$) frequency components of the sine Fourier transform do not cancel out as they do for the ideal, symmetric interferogram (equation 2.32). As a consequence of this, butterflying a one-sided interferogram without phase correction will result in spectral errors.

Ignoring any noise contributions, the original spectrum from an asymmetric interferogram may be recovered by taking the absolute value of the real and imaginary components (equations 3.9 & 3.10):

$$B(\sigma) = |B(\sigma)| = [B_r(\sigma)^2 + B_i(\sigma)^2]^{\frac{1}{2}}. \tag{3.11}$$

Two problems are associated with the absolute value method. Firstly, the interferogram needs to be double sided so that the complex Fourier transform may be taken (equation 2.29 rather than equation 2.25). Secondly, we have so far assumed that all of the detector output is modulated source radiation but there will also be noise included in the signal (see sections 2.10.2 & 3.5.4). Taking the absolute value of the real and imaginary components

of the spectrum brings all of the noise out of the imaginary domain into the real. This results in an undesirable increase in the spectral noise level by a factor of $\sqrt{2}$. Moreover, a positive valued noise floor is introduced due to the negative noise being inverted to become positive[64].

Any signal can be expressed as the sum of an even and an odd function[31]. Equation 3.12 shows the asymmetric interferogram separated into its constituent even and odd components:

$$I_{asymmetric}(z) = I_{even}(z) + I_{odd}(z). \tag{3.12}$$

Ideally, a single-sided interferogram is symmetric. This assumed symmetry allows both positive and negative OPD interferogram values to be known even though up to one half of the interferogram need not be measured. This is equivalent to performing the cosine Fourier transform (equation 2.25). However, in practice, when $I_{asymmetric}(z)$ is assumed to be symmetric and the cosine Fourier transform is performed, spectral errors in lineshape, line centre, amplitude, etc. are introduced. Equation 3.13 illustrates the output of the cosine Fourier transform (equation 2.25) when it is used on an asymmetric interferogram:

$$\begin{aligned} 2\int_0^{+\infty} I_{asymmetric}(z)cos(2\pi\sigma z)dz &= 2\int_0^{\infty}[I_{even}(z) + I_{odd}(z)]cos(2\pi\sigma z)dz \\ &= 2\int_0^{\infty} I_{even}(z)cos(2\pi\sigma z)dz \\ &\quad +2\int_0^{\infty} I_{odd}(z)cos(2\pi\sigma z)dz \\ &= B(\sigma)cos(\phi(\sigma)) + 2\int_0^{\infty} I_{odd}(z)cos(2\pi\sigma z)dz \\ &\neq B(\sigma) \end{aligned} \tag{3.13}$$

The correct spectrum ($B(\sigma)$) is not only multiplied by a phase dependent component ($cos(\phi(\sigma))$), but there is another term ($2\int_0^{\infty} I_{odd}(z)cos(2\pi\sigma z)dz$) added to the spectrum.

The added term is related to the odd-symmetry component of the interferogram, $I_{odd}(z)$. Thus, the degree of spectral degradation caused by the non-zero phase depends strongly on the nature of the asymmetry of the interferogram itself. The difference between $B(\sigma)$ and the output of equation 3.13 is as follows:

$$\begin{aligned} B(\sigma) - 2\int_0^{+\infty} I_{asymmetric}(z)\cos(2\pi\sigma z)dz \quad &= \quad B(\sigma)[1-\cos(\phi(\sigma))] \\ &\quad -2\int_0^{+\infty} I_{odd}(z)\cos(2\pi\sigma z)dz \\ \text{and, using the approximation described below,} \quad &\approx \quad -2\int_0^{+\infty} I_{odd}(z)\cos(2\pi\sigma z)dz. \end{aligned} \tag{3.14}$$

The approximation used in equation 3.14 is based on the small angle approximation and is as follows:

$$\cos(\phi(\sigma)) \approx \sqrt{1-\phi(\sigma)^2} \approx 1. \tag{3.15}$$

It is important to note that, although $\int_{-\infty}^{+\infty} I_{odd}(z)cos(2\pi\sigma z)dz = 0$ due to orthogonality, the last term in equation 3.14, $2\int_0^{\infty} I_{odd}(z)cos(2\pi\sigma z)dz \neq \int_{-\infty}^{+\infty} I_{odd}(z)cos(2\pi\sigma z)dz$ and is thus non-zero. If the phase is small, allowing the small angle approximation, then the difference between $B(\sigma)$ and the spectrum produced by equation 3.13 is limited to that related to $I_{odd}(z)$. Small phase implies that $I_{odd}(z)$ will also be small, and thus the resulting spectral errors may be negligible. If this is not the case, however, then phase correction is essential to recover accurate spectra.

3.5 Phase Errors

In practice, the total phase error can be considered to be the summation of several components:

$$\phi(\sigma) = \phi_{DC} + \phi_{Lin}(\sigma) + \phi_{NL}(\sigma) + \phi_R(\sigma). \tag{3.16}$$

There can exist a DC phase offset, ϕ_{DC}, due to sources such as inverting amplifiers and high pass filters in the detector readout electronics. A linear phase error, $\phi_{Lin}(\sigma)$, arises from not precisely sampling the location of ZPD. A nonlinear phase component, $\phi_{NL}(\sigma)$, may arise from electronic signal processing or any nonlinear optics such as a dispersive beamsplitter or optical filter. When there is a quadratic or higher order σ term in the phase then the interferogram can be described as *chirped* and a point of stationary phase (equation 3.19) will not exist[39]. In general there will also be a random component, $\phi_R(\sigma)$ attributable to noise. These phase components will be discussed in detail.

The extension of phase into the negative frequencies utilizes the odd-symmetry relation:

$$\phi(-\sigma) = -\phi(\sigma), \tag{3.17}$$

unlike the extension of the spectrum into negative frequencies which utilizes the even-symmetry relation (equation 3.6). Sheahen[65] discusses numerical errors resulting from a phase discontinuity at $\sigma = 0$ cm^{-1} if $\phi(0) \neq 0$. This discontinuity involves the limits:

$$\begin{aligned} \lim \phi(\sigma)_{\sigma \to 0^-} &= -\phi(0), \qquad \text{and} \\ \lim \phi(\sigma)_{\sigma \to 0^+} &= \phi(0). \end{aligned} \tag{3.18}$$

Discontinuities in one domain have effects in the reciprocal domain and will be discussed in greater detail in section 4.4.

3.5.1 Phase offset - ϕ_{DC}

There is typically electronic amplification in the data collection system of FTS detectors. In addition to the 180^o phase shift of an inverting amplifier, electronic amplifiers (both inverting and non-inverting) typically have a complex frequency response. The same holds true for electrical filters which are typically used in conjunction with electronic amplifiers[59]. Ideal in-band phase/amplitude response for an amplifier/filter is flat. Chebyshev type filters typically have a flat phase response at the cost of a rounded amplitude response. This flat phase response is ideal for reducing electronics-based interferogram phase errors. Conversely, Butterworth and Bessel type electronic filters have a flat amplitude response but a nonlinear phase response. Electronic filter and amplifier behavior is well understood[66, 59] and resulting phase errors can be minimized.

3.5.2 Linear phase errors - ϕ_{Lin}

Linear phase errors arise from incorrect sampling of the interferogram ZPD location. The interferogram OPD shift property is useful in explaining linear phase error and is illustrated in table B.1, where the variable z_o is used to express the point of stationary phase (ideally ZPD). If there is an error in the location of ZPD, or ZPD has not been sampled, then there will be a linear phase in the spectrum. A symmetric, continuous interferogram may be sampled such that the resultant discreet interferogram will not be symmetric. Two unique sampling conditions will ensure that a discreet interferogram does not lose its symmetry. As is outlined in figure 3.2, the sampled interferogram will be symmetric if the ZPD point is sampled exactly, or if the ZPD point lies exactly between two sample points. The

former sampling condition will have no linear phase error while the latter, although still symmetric, will have linear phase error ($\phi(\sigma_{nq}) = \pi$)[1]. The latter symmetric mode is called even-extension symmetry[67] and contains the same information with one less data point as the other symmetric sampling mode. This memory savings may seem small but potentially allows significant memory/computation savings for large interferogram arrays such as those generated by imaging FTS, e.g. SPIRE[9] and SCUBA-2[27].

If the ZPD is not measured exactly on a sampled data point, then the spectral phase will have a linear variation with frequency. Connes[39, 68] discussed the effect of an error in the choice of the ZPD point on the instrumental line shape. Connes' considers only linear phase error due to ZPD missampling. The linear form of the phase is related to the point of stationary phase as follows:

$$\phi_{Lin}(\sigma) = 2\pi z_o \sigma. \tag{3.19}$$

If ϕ_{Lin} varies linearly with wavenumber, then the interferogram is symmetric about the point where $z = z_o$ which is known as the point of stationary phase.

Unless an accurate fiducial marker is used to determine ZPD, such as that produced by an interferogram of a broadband optical source, a linear phase error will generally be present in all measured interferograms and should be removed in order to minimize spectral errors. The extent of this error depends on the translation stage sampling interval, Δz. A finer sampling interval will allow the interferogram to be sampled closer to ZPD and thus reduce the magnitude of the linear phase error. Figure 3.3 illustrates the sloped phase resulting from a linear sampling shift in the interferogram. Correcting an interferogram for

[1] σ_{nq} is the Nyquist frequency

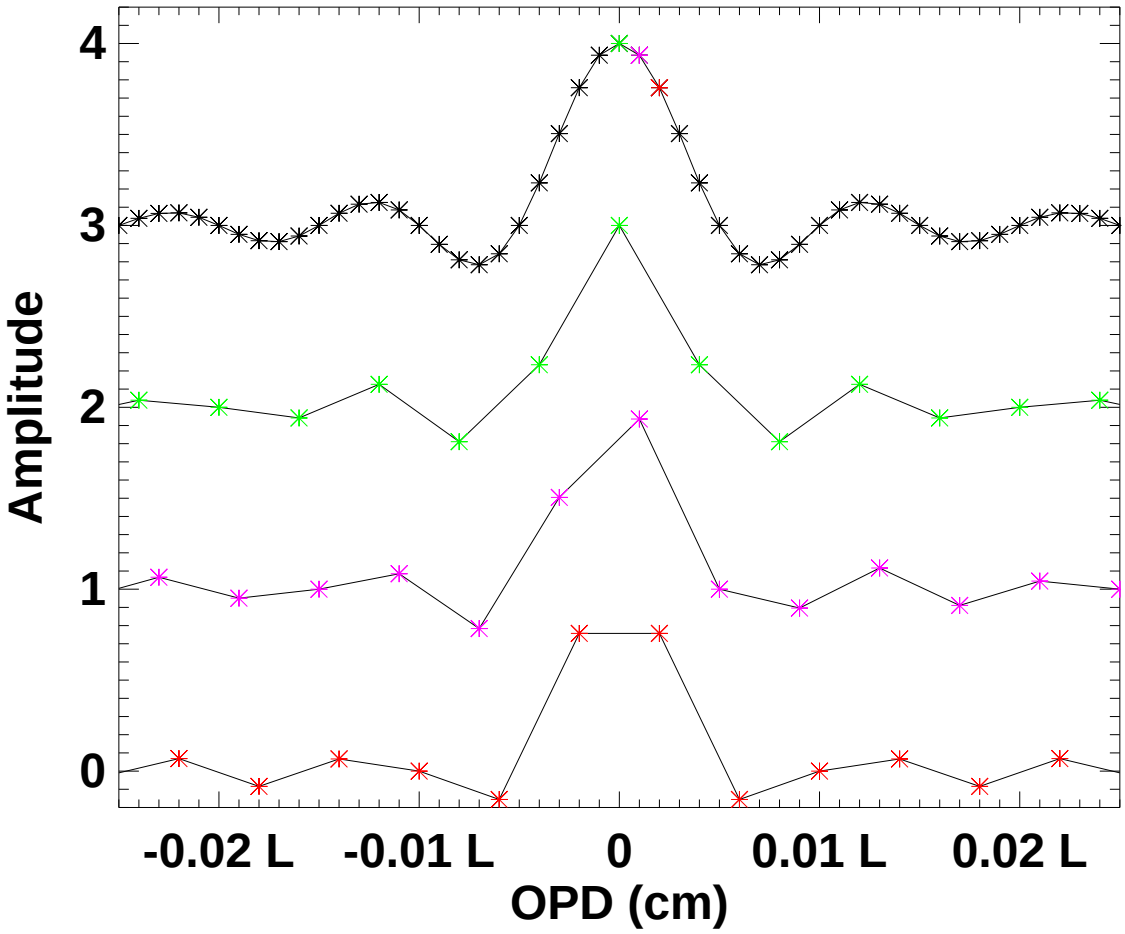

Figure 3.2: Linear shifts of the uniform sampling of an interferogram. The top function shows the original interferogram prior to sub-sampling (4x). The function immediately below (green) shows a symmetric sampling scheme including ZPD. Below that (purple) is an asymmetric sampling of the originally symmetric interferogram. The bottom (red) shows the even-extension symmetric sampling (ZPD is exactly between two sample points). The graphs have been offset for clarity.

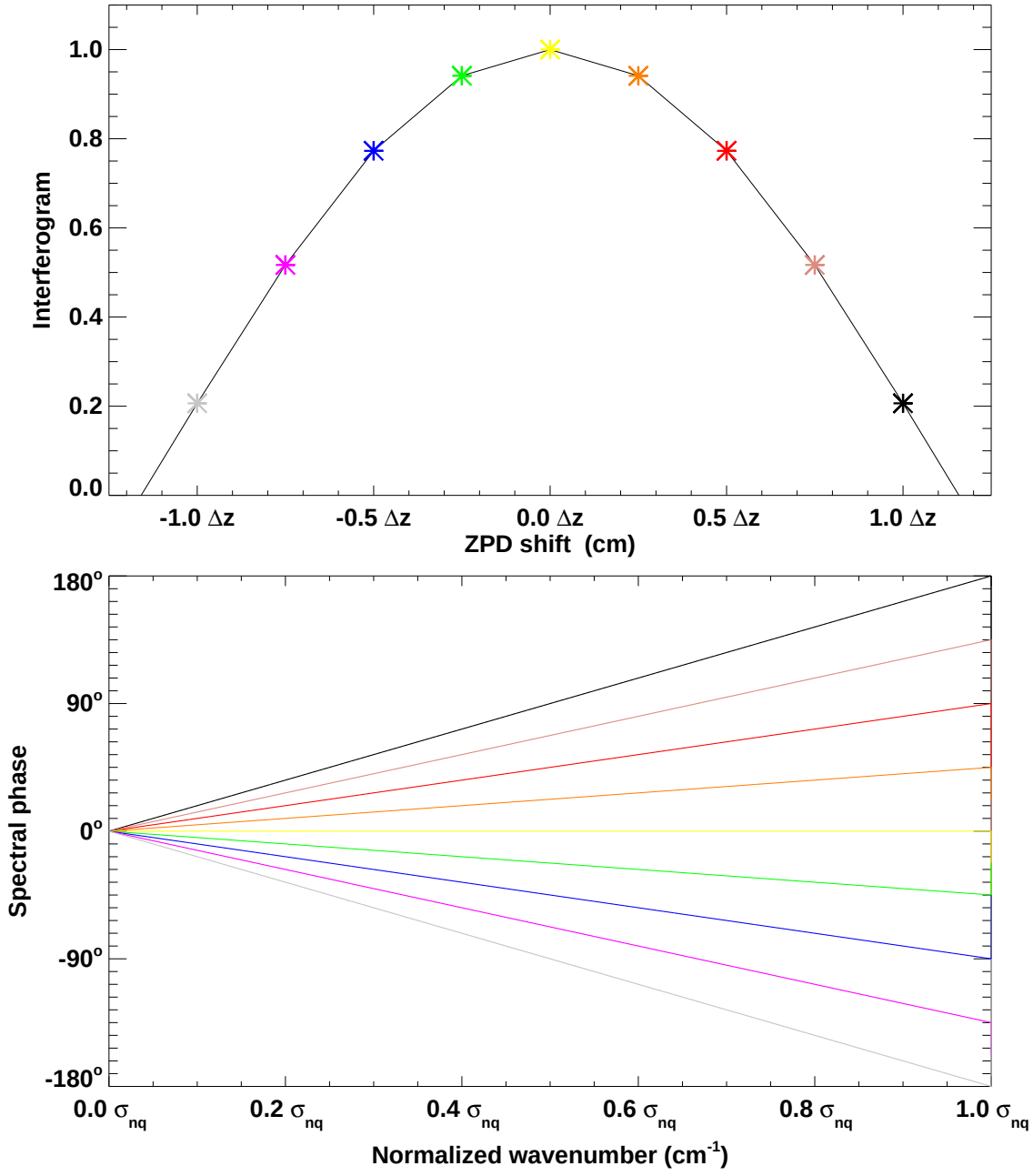

Figure 3.3: The resultant linear phase error due to ZPD sampling shift. In each case the interferogram is sampled uniformly, however the location of the data point closest to ZPD is shifted, resulting in a linear phase with slope proportional to the corresponding ZPD shift. A shift of zero results in a slope of zero, while a shift of one sample point results in a phase shift of 180^o at σ_{nq}.

linear phase error is generally straightforward and leaves minimal residual linear phase in the spectrum[38].

3.5.3 Non-linear phase errors - ϕ_{NL}

Several factors may contribute towards nonlinear phase in FTS spectra[30]. Dispersion in the beamsplitter substrate often contributes nonlinear phase. In a normal dispersive medium, higher frequencies (shorter wavelengths) appear delayed in time or trail the lower frequencies (longer wavelengths)[69]. This results in a chirped interferogram as shown in figure 3.4. By use of a phase compensating plate in the appropriate arm of the interferometer (figure 3.5) it is possible to minimize the $\phi_{NL}(\sigma)$ component introduced by the beamsplitter.

Dispersion can be described empirically by the Cauchy equation[30]:

$$n(\lambda) = C_1 + C_2\lambda^{-2} + C_3\lambda^{-4} + \cdots + C_m\lambda^{-2(m-1)}, \tag{3.20}$$

where $n(\lambda)$ represents the index of refraction of the dispersive medium, and the C_m terms are empirical constants. Typically, only the low order terms are included. Since the index of refraction may also be expressed as a function of σ, the beamsplitter will respond differently to different frequencies, potentially causing chirping in the interferogram. An example of nonlinear phase due to beamsplitter dispersion for the TFTS beamsplitter is shown in figure 3.6.

Dispersion compensator plates can be used to minimize the nonlinear phase. Figure 3.5 illustrates the use of an optical compensating plate in a classical Michelson interfer-

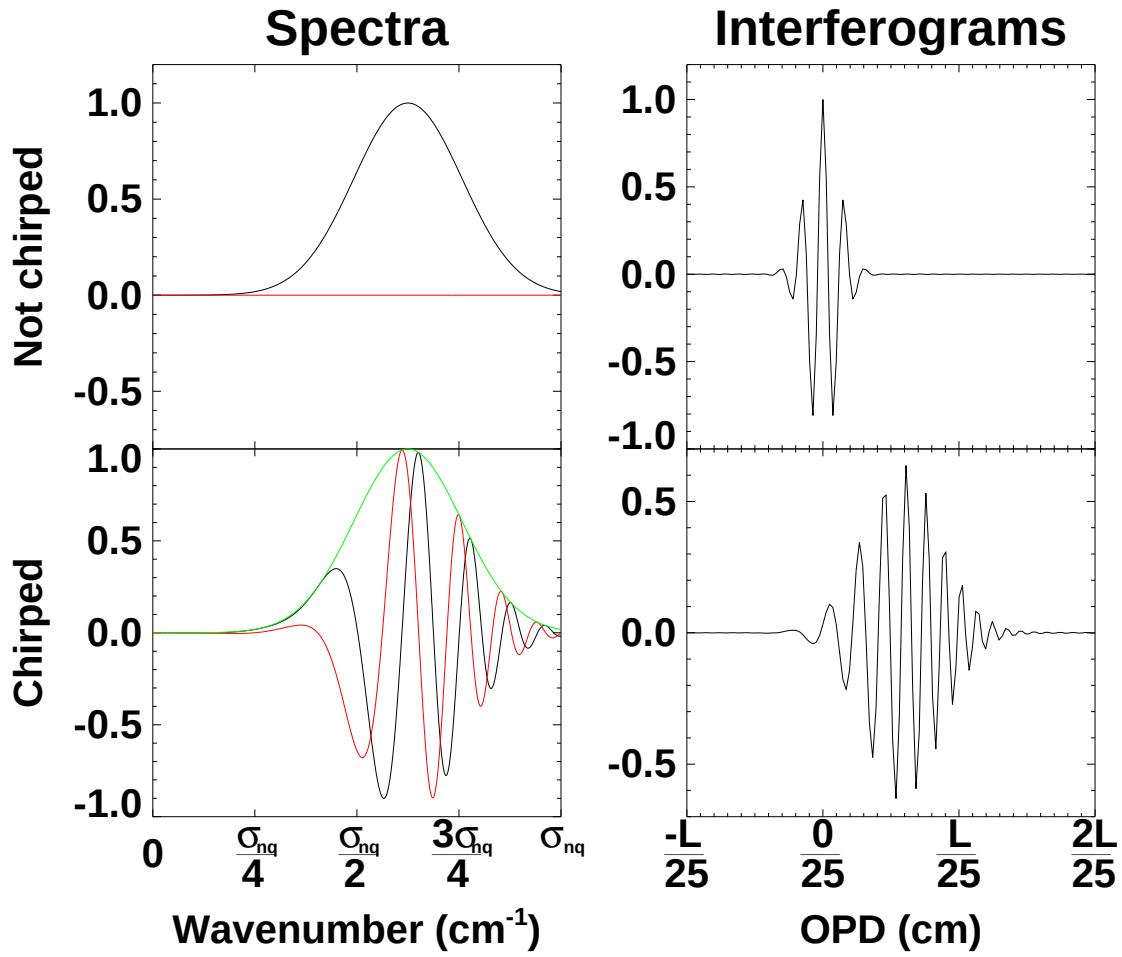

Figure 3.4: The resultant chirping from a non-linear spectral phase error. The top row shows the original non-chirped spectrum/interferogram and the bottom row shows the chirped case. The left column shows the spectra, with the real component in black, the imaginary component in red, and the absolute value shown in green (chirped case only). The right column shows the interferograms. The chirped phase has both a linear and quadratic component. The chirped interferogram has no point of stationary phase (equation 3.19). For both interferograms the location of ZPD is 0 cm. L represents the maximum OPD.

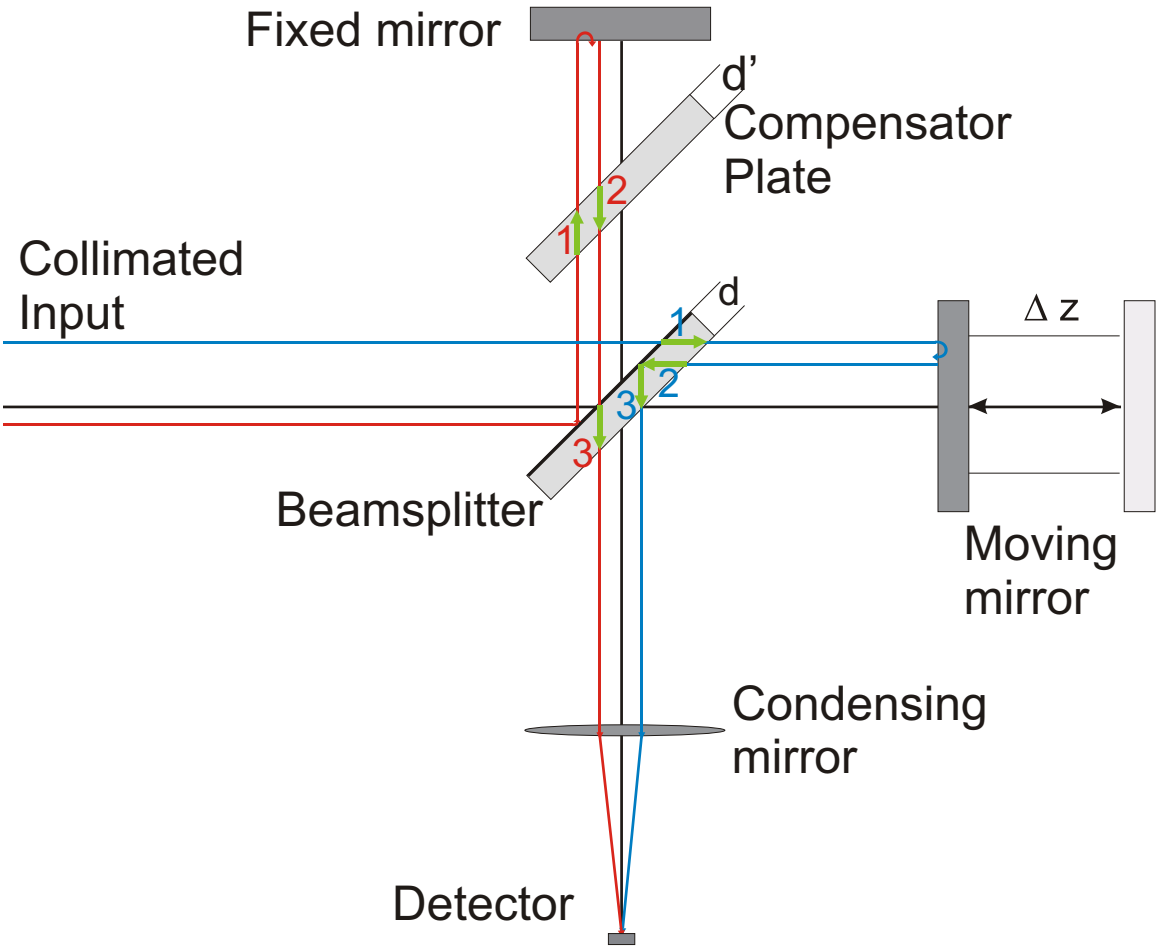

Figure 3.5: A compensator plate may be used in the fixed beam path of a Michelson interferometer in order to correct OPD errors resulting from the difference between the fixed and moving mirror paths of an interferometer. Without the compensator plate, the red path would only pass through the beamsplitter once, while the blue path passes through the beamsplitter three times. The beamsplitter is reflective on the upper left side, and the substrate thickness is labeled on the figure as d. The thickness of the compensator plate is labeled as d'. The difference between d and d' is referred to as η in equation 3.21. The non-reflective side of the beamsplitter and both sides of the compensator may be coated with an anti-reflection coating to reduce undesired reflections. Phase error will result from compensator mismatch.

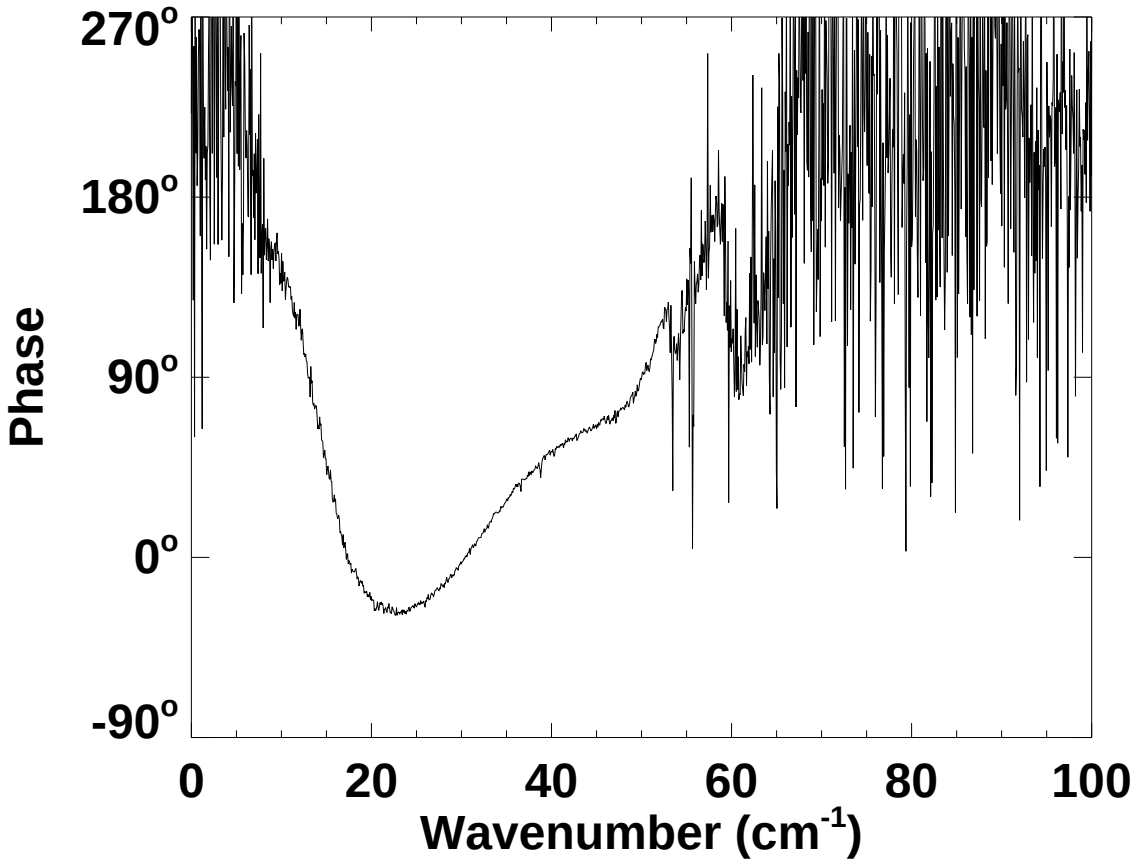

Figure 3.6: A measure of the $\phi_{NL}(\sigma)$ dispersive phase of the TFTS beamsplitter. The phase was determined by averaging several linear phase corrected interferograms of a 1300 K Blackbody source measured with the SPIRE TFTS (chapter 6). The phase as shown is the result of two data sets from different detectors (both used with the TFTS) being merged together to cover a window including the entire SPIRE band. Below 7 cm^{-1} and above 55 cm^{-1} the phase is undetermined because of low S/N.

ometer. Sheahen indicates that optical compensation errors can result in a constant phase offset at best, and often a frequency dependant phase as well[70]. Optical compensation is also done at the cost of optical efficiency and throughput[37, p. 125]. Learner[64] discusses nonlinear phase as the result of an optical mismatch when a compensator plate is used. In this case, the phase takes the form:

$$\phi(\sigma) = 2\pi\sigma[n(\sigma) - 1]\eta, \tag{3.21}$$

where $n(\sigma)$ is the refractive index of the material, and η is the mismatch in thickness (cm_{opd}). For constant index of refraction, this turns into a linear phase error, but for a dispersive medium this remains nonlinear, provided that $\eta \neq 0$. FTS mirror misalignment may also cause nonlinear phase errors. Kunz and Goorvitch[71] describe how the combined effect of a converging beam of light and a translation stage mirror misalignment in a Michelson interferometer produce interferogram asymmetries. Each effect considered separately leads to a symmetric interferogram with reduced modulation intensity, however the combined effect also causes asymmetry in the interferogram. Schröder and Geick[72] discuss how an angular misalignment in the moving mirror of a Michelson interferometer may lead to interferogram asymmetry if the beamsplitter is not at the focal plane (as is usually the case), or if the source is not collimated. Usually the beam is collimated with the residual divergence as minimal as possible to satisfy the Jaquinot criterion[37] (see equation 2.46). Goorvitch[73] has also shown misalignment of the moving mirror in a Michelson interferometer to cause a nonlinear phase error:

$$\phi_{NL}(\sigma) = -\arctan(\frac{\pi D\alpha\sigma}{\sqrt{2}(f/)})^2, \tag{3.22}$$

where D is the distance from the fixed mirror to the focus, α is the mirror misalignment angle (radians), and $f/$ is the f number of the radiation traversing the FTS instrument. For $(\frac{\pi D\alpha\sigma}{\sqrt{2}(f/)})^2 < 1$, as is also a requirement to minimize interferogram power loss[71] due to a mirror misalignment in an FTS instrument with converging light, the nonlinear phase relation simplifies to become quadratic:

$$\phi_{\mathrm{NL}}(\sigma) = -(\frac{\pi D\alpha\sigma}{\sqrt{2}(f/)})^2. \tag{3.23}$$

For the SPIRE TFTS (chapter 6) the values of D and $f/$ are 66.3 cm and 2.33, respectively. For example, using the above equation it can be shown that the angular misalignment on the TFTS mirror must be kept within $0.005^o, 0.003^o, 0.003^o, 0.004^o$, and 0.002^o for the PLW, PMW, PSW, SLW, and SSW bands, respectively to have residual phase no greater than 1^o. Mirror alignment becomes more critical for higher frequencies as one would expect for any nonlinear function. Figure 3.7 illustrates the theoretical non-linear phase resulting from a varying TFTS mirror misalignment. As discussed earlier, electronics and filters may also introduce asymmetries into an interferogram, and thus introduce a non-zero phase component into the spectrum. Also, a symmetric interferogram may be recorded asymmetrically due to the frequency dependance of the response function of the detector and the electronic system[65].

Non-linear phase errors may create the illusion of spectral features where there are none[70]. Failure to correct for the nonlinear phase terms leads to line position shift as well as an asymmetric ILS[74, 64]. $\phi_{NL}(\sigma)$ is significantly more difficult to correct for than ϕ_{DC} and ϕ_{Lin}. It is important to minimize sources of $\phi_{NL}(\sigma)$ where possible, and to be aware of the residual $\phi_{NL}(\sigma)$ where it is not possible to remove. The SPIRE FTS is expected to

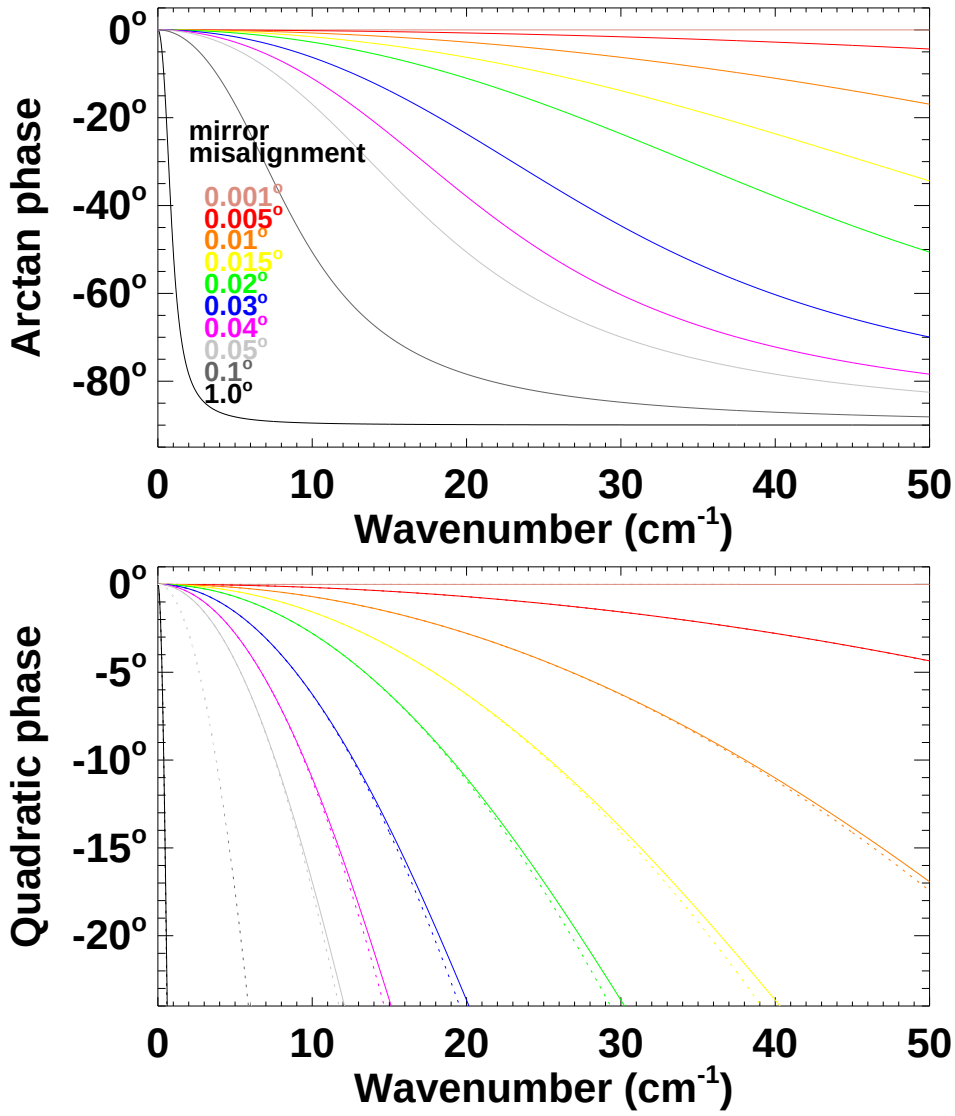

Figure 3.7: The effect of varying mirror misalignment on $\phi_{NL}(\sigma)$ for the SPIRE TFTS (equations 3.22 and 3.23). The upper plot shows the calculations using equation 3.22 without the simplifying assumption. The lower plot shows the curves from the upper plot (solid) in addition to the quadratic phase curves (broken) resulting from the power loss minimization restriction $((\frac{\pi D\alpha\sigma}{\sqrt{2}(f/)})^2 < 1)$.

have nonlinear phase[2] (figure 3.6) which will require phase correction prior to quantitative spectral analysis. However, the TFTS nonlinear phase is systematic and therefore remains constant for the instrument (see section 4.5). Calibration measurements of the nonlinear phase allows the residual nonlinear phase of the TFTS to be minimized in post-processing.

3.5.4 Random phase errors - ϕ_R

An interferogram ($I(z)$) consists of two key measurements, optical signal (I) and OPD (z). The optical signal can be affected by both optical and electrical noise while the optical path measurement can be affected by mechanical vibrations and electrical noise. Noise is discussed in detail in section 2.10.2. Interferogram noise will propagate into the spectrum, which will in turn introduce noise into the phase. Phase uncertainty is related to spectral uncertainty by the inverse of the spectral amplitude ($\delta\phi(\sigma) = \frac{\delta B(\sigma)}{|B(\sigma)|}$, see appendix D). Therefore, phase uncertainty is greatest in regions of low spectral amplitude.

An ideal FTS will be designed such that all noise levels are reduced to the point where photon noise dominates. Random noise should affect the real and imaginary domains of the spectrum equally. Therefore, phase correction has the potential of affecting the spectral noise due to the redistribution of the spectrum between the real and imaginary domains. Random noise levels are reduced through improving interferometer stage metrology and optical signal S/N. Slowly varying phase information is typically within the centreburst[38] (i.e. ZPD) region of the interferogram where S/N is the highest. The random noise contribution to phase, $\phi_R(\sigma)$, can never be completely removed but can be minimized through FTS design and data processing techniques (see chapter 5).

[2]According to TFTS verification measurements (section 6.5)

3.6 Phase correction methods

Phase correction is the technique of correcting asymmetric interferograms[38]. In principle, to correct the phase, the phase distorted spectrum ($B(\sigma)e^{i\phi(\sigma)}$) must be multiplied by the reciprocal of the phase ($e^{-i\phi(\sigma)}$):

$$B(\sigma) = [B(\sigma)e^{i\phi(\sigma)}]e^{-i\phi(\sigma)}, \tag{3.24}$$

however this is more complicated in practice as every spectral data point only has corresponding phase information if the interferogram used to generate the spectrum is double-sided. Since phase is expected to be slowly varying, phase correction methods have been developed to extract low resolution phase information from the double-sided portion of the interferogram to correct the higher resolution spectrum obtained from the one-sided portion of the interferogram.

The essential result of any phase correction procedure is to restore the spectral energy from the imaginary domain back to the real, leaving only the undesired imaginary noise behind. In the spectral domain, this rotation of energy to the real domain from the imaginary is accomplished with a multiplication by the reciprocal phase function (equation 3.24). In the interferogram domain, this corresponds to a convolution (table B.1) by the appropriate function known as the phase correction function (PCF) (equation 3.31). This section will discuss both the multiplicative (Mertz[54]) and the convolution (Forman[46, 61, 75]) phase correction methods.

3.6.1 The Mertz Method

In Mertz phase correction[54] the initial step is the determination of the double-sided phase (equation 2.39). The spectrum from the single-sided interferogram is of a higher resolution than that of the phase information provided by the double-sided interferogram. A combination of zero filling and linear interpolation is used to determine the phase at the required resolution[76]. Apodization of the double-sided interferogram is recommended, and in his original paper, Mertz suggested that a triangular type of apodization[77] (figure E.1) be used on the double sided interferogram although this is now regarded as far from optimal[78]. The Mertz method found favour through its elegant simplicity decades ago when computer capabilities were significantly less than they are today and multiplication was much preferred to convolution[60].

The single-sided interferogram needs to be appropriately weighted to ensure that each point of optical retardation is equally accounted for. Multiplying an apodizing function with an interferogram is equivalent to convolving the corresponding spectrum with the Fourier transform of the apodizing function (more on apodizing in section 4.8). The Fourier transform of the apodizing function is known as the ILS[38].

Unequal weighting of interferogram points results in deviations in the ILS from the ideal sinc profile (see section 2.10.4). Ideally all of the points that are doubly accounted for would be weighted equally, and the weighting of the remaining points would be twice that of the doubly accounted points. This is not practical, however, as the weighting function would then have discontinuities at $\pm L_{DS}$. To address this discontinuity problem a linear weighting with value of 0 beginning at $-L_{DS}$ and ending with a value of 1 at $+L_{DS}$ within

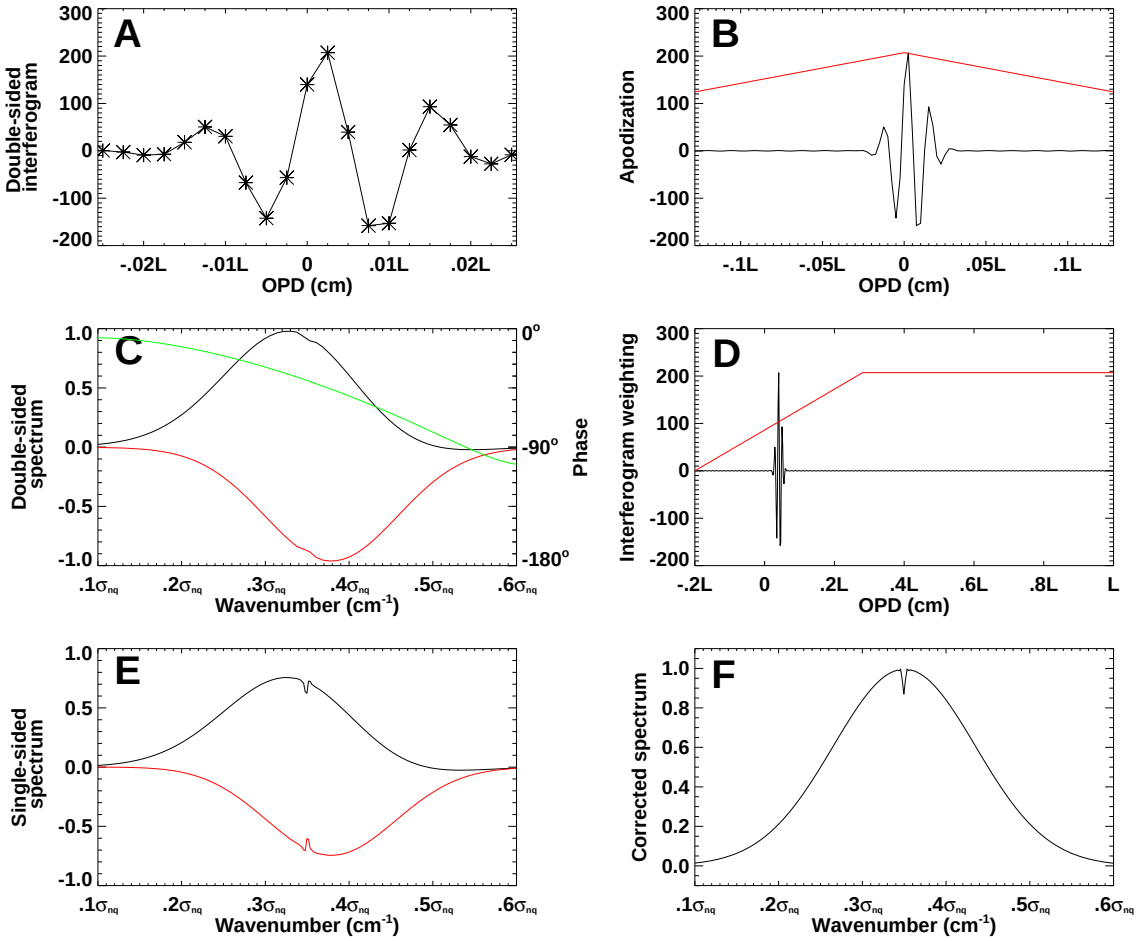

Figure 3.8: Mertz phase correction involves a narrow double-sided interferogram (A) , suitably apodized (B), to obtain a low resolution spectrum (real - black, imaginary - red) and phase (green) (C). The phase is interpolated and used to generate a multiplicative correction function. The full interferogram is weighted (D) to obtain the uncorrected high resolution spectrum (E). The real component of the complex multiplication of $e^{-i\phi(\sigma)}$ and E result in the corrected spectrum (F). In all spectral plots, black is the real component, and red is the imaginary.

the double-sided window is used instead of the flat amplitude of $\frac{1}{2}$ (see figures 3.9 & 3.10). This also ensures that each point receives the appropriate weighting without having an abrupt discontinuity at $+L_{DS}$.

The linear weighting scheme is based on the assumption of a symmetric interferogram. Phase correction is fundamentally necessary because interferograms are not symmetric and therefore this assumption is problematic. Chirped interferograms are not symmetric and thus the linear weighting scheme devised to overcome the discontinuity problem is not the best solution. Other methods to have appropriate weighting, avoid function/derivative discontinuities, and to equally weight an asymmetric double-sided interferogram use curved (e.g. cosinusoidal) sections between the flat regions as is shown in figure 3.9. Examples of various Mertz envelope weighting functions, $Env_{Mertz}(z)$, with their corresponding complex $ILS(\sigma)$ functions are shown in Figures 3.9 & 3.10.

3.6.2 The complex line shape of the Mertz method

As shown in figures 3.9 & 3.10, the Fourier transform of $Env_{Mertz}(z)$ can be expressed in terms of real and imaginary components:

$$ILS_{Mertz}(\sigma) = ILS_{real}(\sigma) + iILS_{imaginary}(\sigma), \tag{3.25}$$

where $ILS_{real}(\sigma)$ is symmetric and $ILS_{imaginary}(\sigma)$ is antisymmetric. $Env_{Mertz}(z)$ multiplied with the interferogram is equivalent to convolving $ILS_{Mertz}(\sigma)$ with the spectrum as follows (see section 4.8):

$$Env_{Mertz}(z) \times I(z) \Leftrightarrow [ILS_{real}(\sigma) + iILS_{imaginary}(\sigma)] * B(\sigma). \tag{3.26}$$

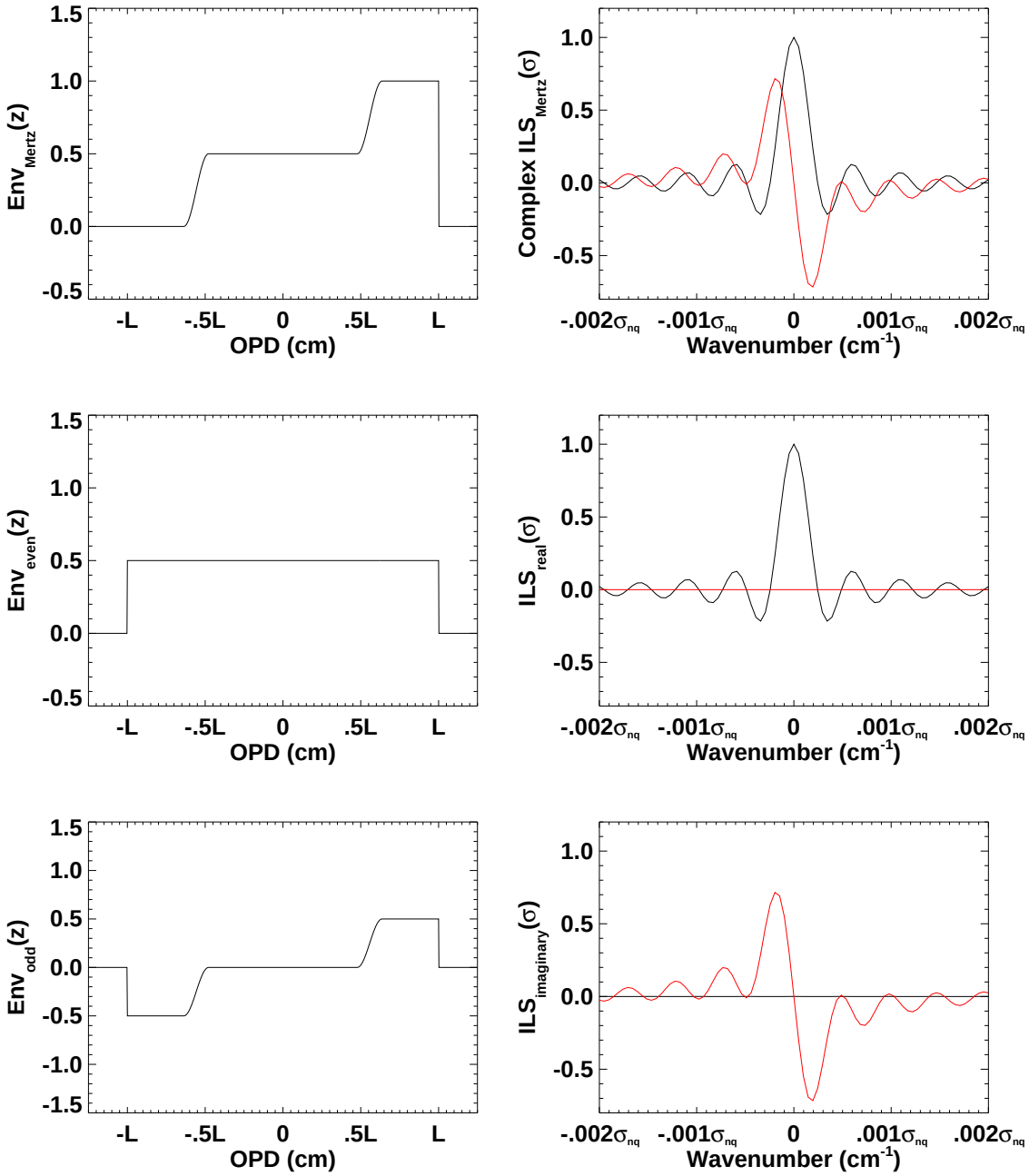

Figure 3.9: A typical weighting function used in the Mertz method of phase correction. The central region is doubly accounted for and as such each point is weighted by 0.5. $Env_{Mertz}(z)$ can be broken up into an even ($Env_{even}(z)$) and an odd ($Env_{odd}(z)$) component as is shown. The ILS of the even component is exactly a sinc function and the ILS of the odd portion is entirely imaginary. The transition between weighting levels is done with a sinusoidal function to ensure no discontinuities in both the function and its derivative. The real components of the spectra are shown in black and the imaginary components are shown in red.

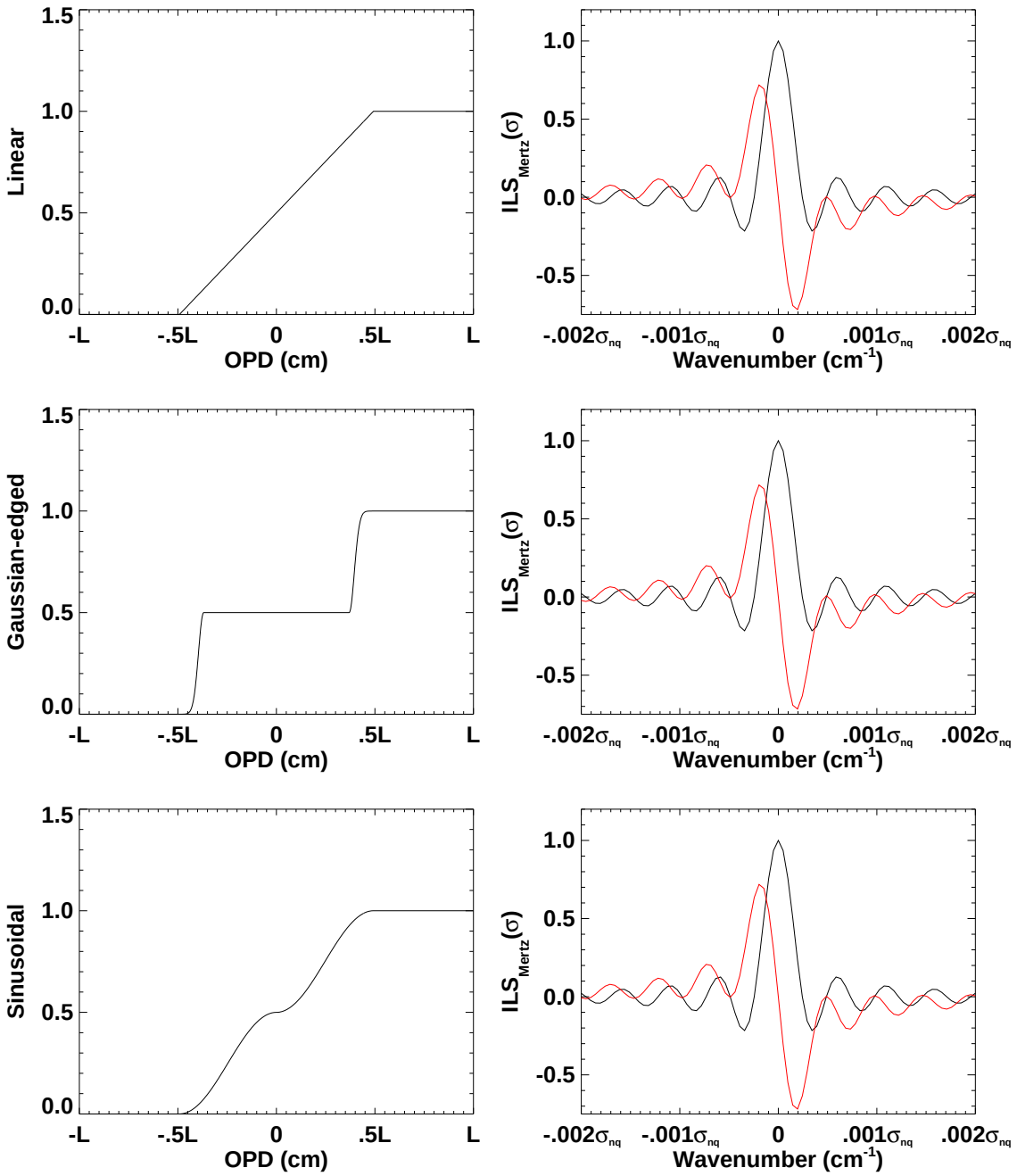

Figure 3.10: Other potential weighting functions for the Mertz method. First is shown the linear function proposed by Mertz, second is a function with Gaussian transition curves, and third is shown wide sinusoidal curves in the double-sided portion of the interferogram. The even portion of all of the weighting functions results in a real valued sinc spectral ILS. The real components of the spectra are shown in black and the imaginary components are shown in red.

In this equation $\Leftrightarrow$ represents the Fourier transform pair (see appendix B) and convolution is denoted by $*$ (see appendix C). Since an ideal interferogram has a wholly real spectrum; the real part of the convolution, $ILS_{real}(\sigma) * B(\sigma)$, gives the required spectrum, and the imaginary part can be discarded. For even a small residual phase error in the spectrum, $\phi_{residual}(\sigma)$ (expressed in radians), the imaginary part can no longer be completely ignored. The spectrum, $B(\sigma)$, which only has a real component, is observed[3] to be complex valued due to the residual phase (ignoring the ILS convolution for now):

$$B_{obs}(\sigma) = B(\sigma)e^{i\phi_{residual}(\sigma)}, \tag{3.27}$$

and using the small angle approximation (equation 3.15) can be expressed as:

$$\begin{aligned} B_{obs}(\sigma) &= B(\sigma)e^{i\phi_{residual}(\sigma)} \\ &= B(\sigma)cos(\phi_{residual}(\sigma)) + iB(\sigma)sin(\phi_{residual}(\sigma)) \\ &\approx B(\sigma) + i\phi_{residual}(\sigma)B(\sigma). \end{aligned} \tag{3.28}$$

Therefore, $B(\sigma)$ is recovered by taking the real portion of $B_{obs}(\sigma)$, however equation 3.28 neglected the ILS convolution that also affects the observed spectrum. Equation 3.29 does take the ILS convolution into account. The combination of residual phase and an imaginary portion to the ILS results in the real portion of $B_{obs}(\sigma)$ being different from the expected $B(\sigma) * ILS_{real}(\sigma)$. Since the ILS width should be fairly narrow, $\phi_{residual}(\sigma)$ should be relatively constant over the instrument profile. This allows the real part of the Mertz

[3]The subscript $_{obs}$ is used to differentiate the observed spectrum, $B_{obs}(\sigma)$, from the actual spectrum, $B(\sigma)$.

spectrum to be expressed as:

$$\begin{aligned} Re[B_{obs}(\sigma)] &= B(\sigma) * ILS_{real}(\sigma) - [\phi_{residual}(\sigma)B(\sigma)] * ILS_{imaginary}(\sigma) \\ &\approx B(\sigma) * [ILS_{real}(\sigma) - \phi_{residual}(\sigma)ILS_{imaginary}(\sigma)] \\ &\neq B(\sigma) * ILS_{real}(\sigma). \end{aligned} \tag{3.29}$$

The difference between the expected and observed real spectrum is

$$[\phi_{residual}(\sigma)B(\sigma)] * ILS_{imaginary}(\sigma).$$

It is important to note that within this additional term, $ILS_{imaginary}(\sigma)$ is of odd symmetry so the effective ILS is distorted. The added term involving the asymmetric instrument function displaces and distorts all the observed lines by an amount proportional to the residual phase error[64]. Thus the ILS no longer has the ideal sinc profile, but has an added asymmetric contribution.

The above expressions show asymmetric ILS even with residual phase assumed to be small enough to allow the small angle approximation (equation 3.15) and to be slowly varying. If $\phi_{residual}(\sigma)$ is not small or slowly varying, then the simplifying assumptions are no longer valid and the resulting Mertz ILS is even more complicated and distorted from the ideal[76, 79, 80].

3.6.3 The Forman Method

In this method, also known as the symmetrization-convolution method[61, 76], the short double-sided portion of the interferogram is used to calculate the phase spectrum at low resolution (equation 2.39). The resulting phase spectrum is then used to generate a

phase correction function (PCF) given by:

$$PCF(z) = \int_{-\infty}^{+\infty} e^{-i\phi(\sigma)} e^{+2\pi\sigma z} d\sigma. \tag{3.30}$$

Convolution of the PCF with the original interferogram results in a symmetric interferogram:

$$I_{symmetric}(z) = I_{asymmetric}(z) * PCF(z). \tag{3.31}$$

The fundamental phase determination used in the Forman method is similar to the Mertz method, however, the two methods now proceed along different paths. The Forman method utilizes the equivalence of the multiplication/convolution Fourier transform pair (see table B.1). Rather than multiply the high resolution spectrum by the reciprocal of the phase, $e^{-i\phi(\sigma)}$, the original interferogram is convolved with the PCF. Forman argues that prior to the calculation of the PCF, mathematical bandpass filtering can be added into the data processing at no extra processing or information cost[61]. The PCF may also be apodized in order to minimize the introduction of spectral artifacts, which are caused by discontinuities at the boundaries of the PCF being convolved through the interferogram. Forman developed his own apodization function[61, 39] (see appendix E) for the PCF apodization.

Forman also discussed repeating the convolution more than once to further improve the spectral correction. Theoretically, however, if the phase correction convolution function was determined correctly the first time, one convolution should be sufficient to phase correct the interferogram (see section 4.2).

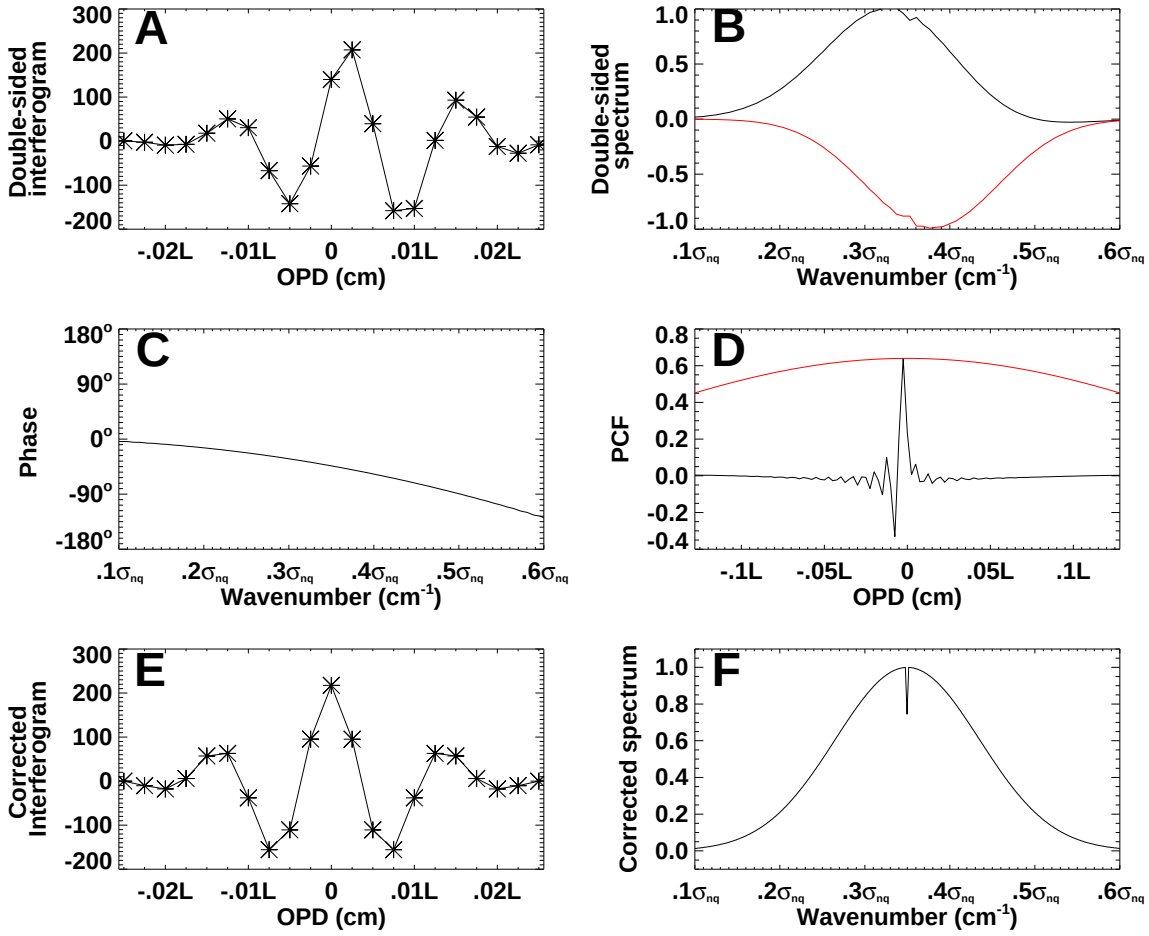

Figure 3.11: The Forman phase correction method involves a narrow double-sided interferogram (A), used to obtain low resolution amplitude (B) and phase (C) spectra. The phase correction function (D) is generated from the phase (equation 2.39) and convolved with the original single-sided interferogram to generate the phase corrected interferogram (E). D also shows the PCF apodization function (red) which Forman developed (equation E-4). The corrected high resolution spectrum (F) shows a broad Gaussian continuum with an unresolved absorption line. In all spectral plots, black and red show the real and imaginary components, respectively.

3.6.4 Phase correction of emission line spectra

Phase correction of emission line spectra is similar to continuum and absorption spectra phase correction, but is complicated by the fact that the phase uncertainty is inversely proportional to spectral amplitude[64]. Therefore phase information is only present in a spectrum where there is non-zero amplitude, which is more prevalent with a continuum present. There are two main limitations to phase determination in emission spectroscopy. First is the limited S/N, second is the availability of suitable reference lines. One method that is commonly used to determine the instrumental phase involves using a strong continuum source. With correction of systematic phase from instrument calibration measurements, the only additional correction required on each individual interferogram is linear, which is fairly straightforward with even a relatively low number of emission lines. SPIRE will not have phase determination issues due to lack of continuum because of the prevalence of broad spectral emission in the sub-mm Infrared (IR) band. Phase correction of emission line spectra becomes an issue for higher frequencies such as ultra violet (UV) spectroscopy where continuum emission is not typically present[81].

Two related problems occur in the phase correction of emission spectra that are not usually significant for absorption spectra. The first is that reliable phase information is only present within strong emission lines. The second problem is that there are mechanisms that introduce false phase data such as ghosting effects. As long as the phase determination of an emission spectrum is done properly, the remainder of the phase correction is similar to absorption/continuum phase correction methods.

3.6.5 Other approaches to phase correction

There are other methods of phase correction which have found a more limited use than the Mertz and Forman based methods. For example, precise line shape error minimization is a different approach to phase correction which only requires one-sided interferograms. Other methods use different means of phase error identification. These methods will not be discussed here, but are discussed in the literature[65, 70, 74, 82, 83].

3.7 Comparison of the Mertz and Forman methods

The fundamental equivalence between the Mertz and Forman method lies in the convolution/multiplication Fourier transform pair (see appendix B and table B.1). Both phase correction methods are equivalent to the first order[84], however secondary effects vary. Both phase correction methods were introduced at a time when computer processing capabilities were far more primitive than they are today. As a result, the relative simplicity of the spectral multiplication utilized in the Mertz method gained favour over the complicated interferogram convolution found in the Forman method. As FTS instruments and data processing capabilities have advanced through the years, the advantages of the simplistic Mertz phase correction have lost ground over the versatility of the Forman phase correction method.

3.7.1 General comparisons

In order to illustrate the differences between the Mertz and Forman phase correction methods, both methods have been used to correct the same interferograms. The input

spectra are composed of a broad Gaussian emission line with an unresolved Gaussian absorption feature superimposed. Two basic types of phase error, both linear and quadratic, are introduced to distort the interferograms. All of the processing parameters were kept identical to ensure a valid comparison. The spectral output of each method as well as the difference from the input spectrum is shown in figure 3.12.

Phase Error type		Forman		Mertz	
		Linear	Quadratic	Linear	Quadratic
Continuum	Amplitude	0.41 %	0.42 %	1.24 %	0.95 %
	Line centre	0.0016 %	0.0012 %	0.0015 %	-0.0599 %
	Line width	-0.12 %	-0.12 %	-2.54 %	-2.53 %
Unresolved	Amplitude	24.7 %	24.7 %	61.7 %	61.6 %
	Line centre	-0.027 %	-0.027 %	-0.027 %	-0.027 %
	Line width	2.19 %	2.19 %	22.39 %	22.37 %

Table 3.1: Comparison of the spectral feature errors from the Mertz and Forman methods of phase correction with linear and quadratic phase error. Errors are represented as percentages of the model parameters for the zero-phase spectrum. The errors on the amplitude of the unresolved absorption line are significantly larger than any of the other parameters. This is primarily due to the nature of the unresolved line and the fact that the spectrum is only discretely sampled. The Forman method preserves the lineshape significantly better than the Mertz method as is shown in figure 3.13.

To quantitatively evaluate the phase correction methods, an Interactive Data Language (IDL)[3] procedure was written to fit the spectrum to a theoretical one containing a broad Gaussian continuum and an unresolved (sinc) absorption line centered at the same frequency. In this analysis the line amplitude, centre, and width for both the Gaussian and unresolved lines were free parameters. The minimization of χ^2 in this six-dimensional space was used to determine the parameters for the best model fit. The phase corrected spectra as well as the modeled fit spectra for the Mertz and Forman methods with linear and quadratic phase error are shown in figure 3.13. The resulting errors in amplitude, line

centre, and line width are shown in table 3.1.

Both the linear and the chirped (quadratic phase) interferograms are corrected better by the Forman method than by the Mertz method. The point of stationary phase (z_o), about which the interferogram symmetry is expected to lie, is shifted for an interferogram with linear phase and does not exist for a chirped interferogram. The unequal weighting of the double-sided interferogram in the Mertz method (figure 3.10) weights the positive OPD region of the interferogram with more confidence than the negative OPD region. This will introduce artifacts into the Mertz spectrum (and ILS) because of the lack of symmetry of an interferogram with phase errors. This is evidenced by the fact that Mertz line centre error is comparable to Forman line centre error, however other spectral errors (with a stronger connection to the ILS) are significantly larger for the Mertz correction than for the Forman correction (table 3.1).

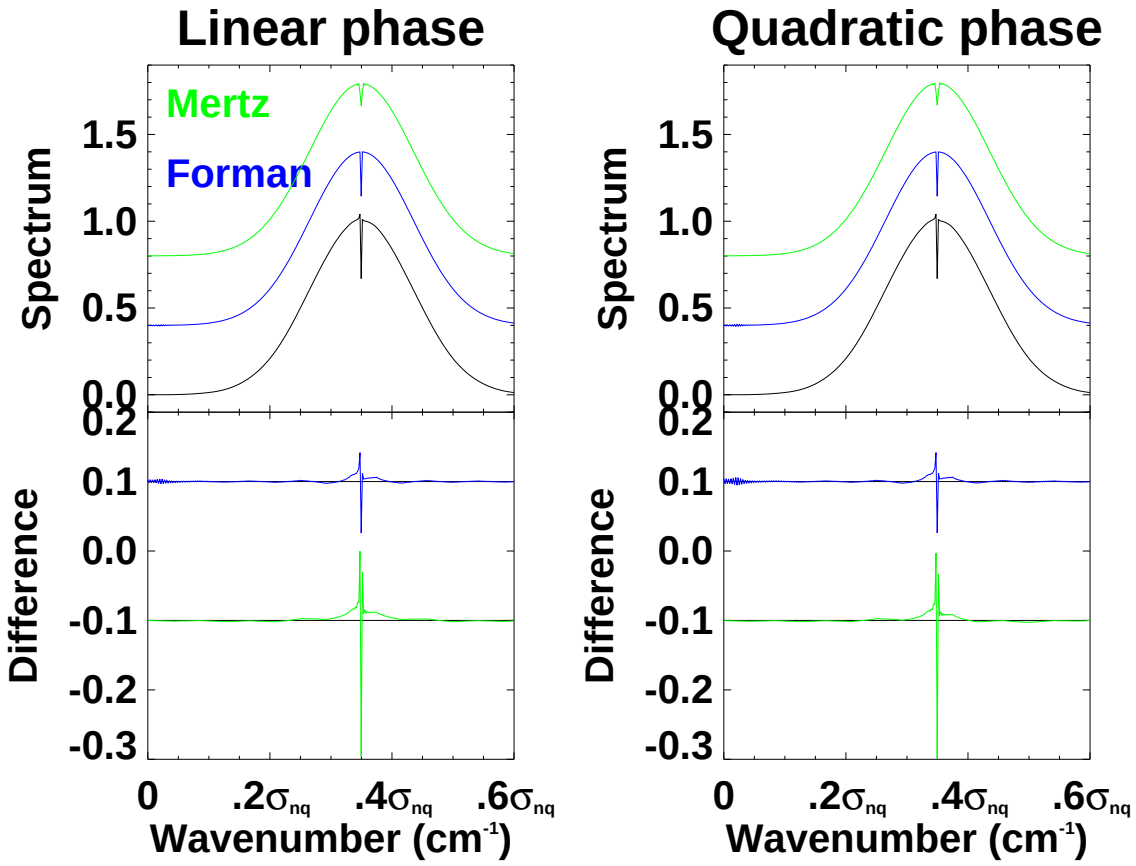

Figure 3.12: Spectra resulting from the Mertz and Forman phase correction methods on data with linear and quadratic phase. The zero-phase spectrum is shown in black, with the Forman spectra shown in blue and the Mertz spectra shown in green. Below each spectral plot is a plot showing the difference from the phase corrected spectrum and the zero phase spectrum. The Forman difference plots are shown in green while the Mertz difference plots are shown in blue. The graphs have been offset for clarity.

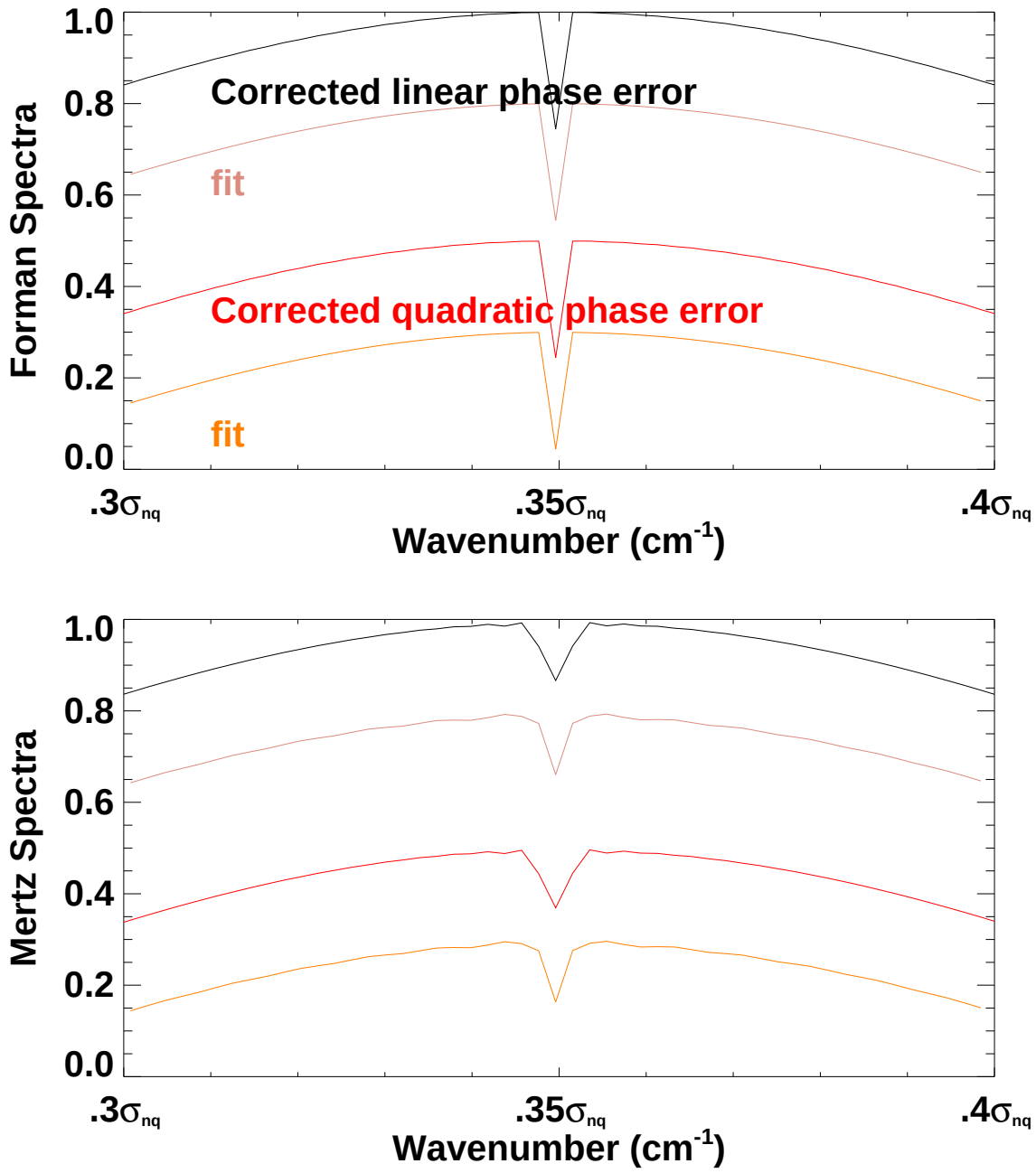

Figure 3.13: Output spectrum from the Mertz and Forman methods compared to the least squares fit. From top to bottom (in colours black, brown, red, orange), the curves shown are spectrum (corrected for linear phase error), fit (of the spectrum immediately above), spectrum (corrected for quadratic phase error), and fit (of the spectrum immediately above). The Forman results are shown in the top figure while the Mertz results are shown in the bottom figure. Note the reduced amplitude of the unresolved absorption line in all the Mertz spectra. The data illustrated here is the same as is illustrated in figure 3.12.

3.7.2 Comparisons for SPIRE instrument verification

The effect of both phase correction methods on the modeled spectra for SPIRE ground testing is also important. Details of the SPIRE ground testing and CQM model verification will be discussed elsewhere (chapter 7), however, a simple spectrum including a blackbody radiation source, atmospheric transmission, beamsplitter phase, optical filter profile, and mirror efficiency has been generated to assist in the preparation of data processing software[15]. In order to evaluate the performance of both methods of phase correction, output spectra are generated and compared to a zero-phase spectrum of the same model data. The spectra and differences are shown in figure 3.14. Application of the phase correction techniques discussed in this chapter applied to the optimization of SPIRE data processing is found in chapter 5.

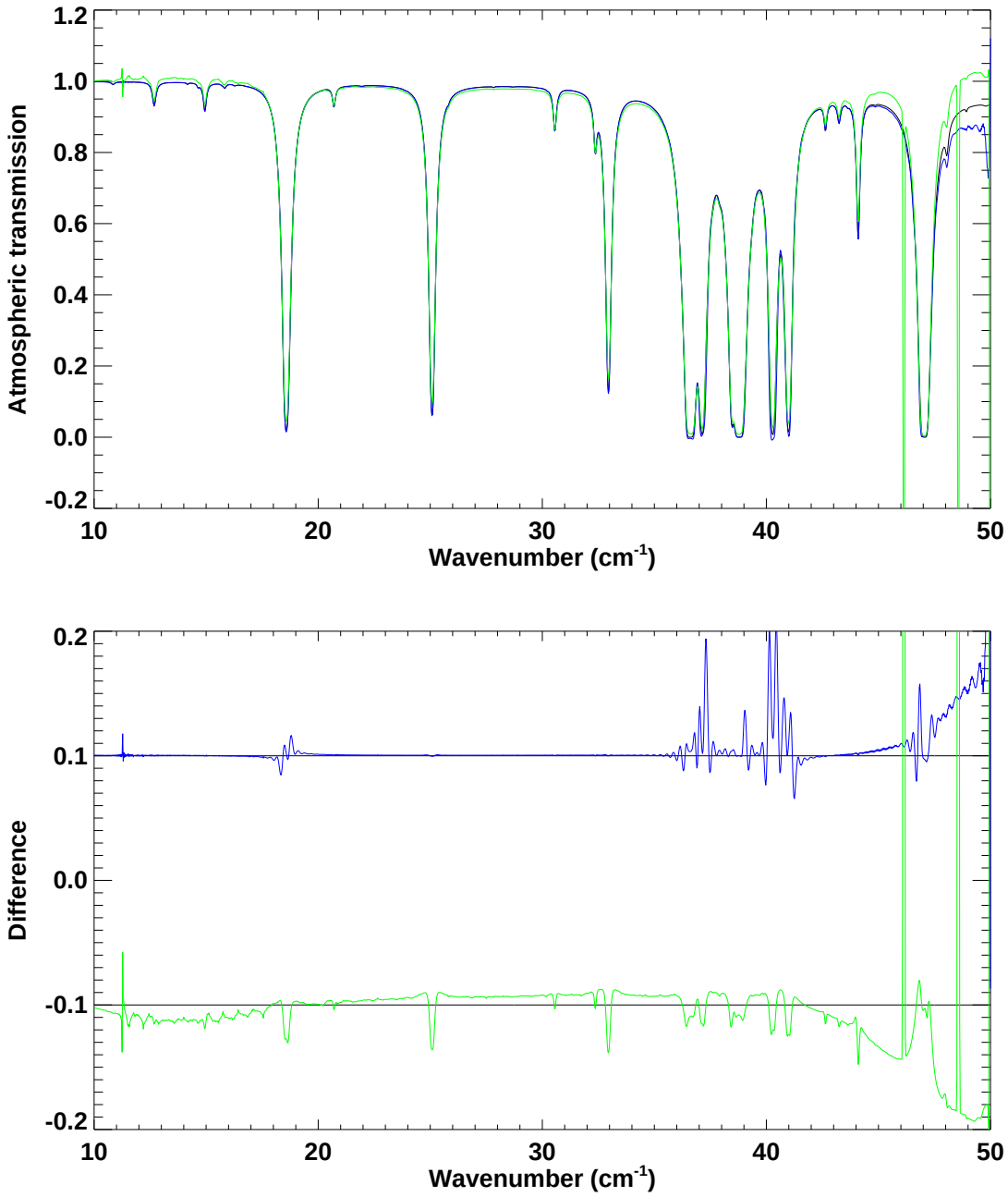

Figure 3.14: A model atmospheric transmission spectrum for the SPIRE ground test facility at RAL. The atmospheric beampath length is 5m, with temperature 290 K and 1013 mbar pressure. Double-sided and single-sided resolution are at 0.07 and 0.014 cm^{-1} respectively, comparable to the capabilities of the SPIRE TFTS (chapter 6). The Forman and Mertz methods are shown in blue and green, respectively. The differences (below) are offset for clarity. The in-band RMS error of the Mertz method is an order of magnitude larger than that of the Forman method (0.12 vs. 0.02).

3.8 Conclusions

Phase errors can be systematic, variable, and random. Whenever possible, systematic phase can be minimized and calibrated at the instrument level. Nonlinear phase errors are typically both systematic and difficult to correct for and thus should be minimized, with residual nonlinear phase recorded with calibration measurements. The most common variable phase error is linear, which is easily corrected.

The Forman phase correction method has been shown to perform better than the Mertz method, as is illustrated in section 3.7. Chase discovered that for a comparable number of points the residual errors were less for the Forman method than for the Mertz method[76]. There are situations when the Mertz method will suffice, however, the quality of the resultant spectrum will be greater if the Forman method of phase correction is used. An enhanced version of the Forman method is discussed in chapter 4. Several sources in the literature cite the advantages of the Forman method over the Mertz method.[61, 62, 39, 76, 79, 84] For these reasons, a Forman based method (see chapter 4) has been selected to correct the phase errors in the SPIRE/CQM verification test campaign.

Chapter 4

Enhanced Forman Phase Correction

Contents

4.1 Overview

As discussed in the previous chapter, the Forman method of phase correction is superior in performance to other phase correction methods. There are, however, limitations to the Forman method, which may be overcome by enhancing the functionality of the

basic Forman method. The enhanced Forman phase correction developed in this thesis is discussed in this chapter. Also discussed is the effect of residual phase on the spectrum.

4.2 Introduction

The finite amount of stage travel in FTS instruments may be allocated towards two reciprocal applications, i.e. double-sided and single-sided interferogram measurement. Stage travel may be used for higher spectral resolution (one-sided interferogram) or it may be used for providing phase information (double-sided interferogram). In many cases, the phase information provided by a double-sided interferogram may be highly over-resolved as phase is typically slowly varying. An ideal interferogram has a phase of zero at all frequencies and will contain identical information on both sides of the ZPD position. Theoretically, therefore, the spectrum can be uniquely recovered with an interferogram starting at ZPD (one-sided interferogram). However, in practice, a single-sided interferogram is measured (with $0 < \frac{L_{DS}}{L_{SS}} < 1$, see section 3.2) where at least a small amount in the negative OPD region is recorded in order to characterize any phase present. This phase information can then be used to correct the asymmetry in the high resolution one-sided interferogram. For a translation stage of fixed length, this leads to a trade-off between the length of the double-sided interferogram used to determine the phase information, and the one-sided interferogram used to achieve higher spectral resolution.

The Forman phase correction method is widely regarded as being superior to other methods[61, 62, 39, 76, 79, 84, 26] and forms the basis of the analysis presented in this thesis. The basic processing steps of the Forman method are discussed in section 3.6.3 and outlined

in figure 3.11. In this thesis, the Forman phase correction procedure has been enhanced in order to better utilize the phase correction advantages it provides. These enhancements include better choice and application of apodization functions, a range of methods of fitting the phase, and flexibility in the choice of the lengths of both the double-sided interferogram and the phase correction function. The added flexibility enables tailoring of the phase correction procedure to the specific data being corrected for, and allows the minimization of spectral resolution loss while maintaining accurate phase correction. The steps of the enhanced Forman phase correction used in this thesis are summarized in figure 4.1. A graphical user interface (GUI) used to illustrate the function of the enhanced Forman phase correction is shown in figure 4.2.

Brault[78] offers 5 recommendations for phase correction:

1. Accurately determine ZPD to reduce linear phase error.

2. Apodization of the double-sided interferogram alone is not sufficient for phase noise reduction, double-sided phase should also be *smoothed* by fitting it to a function or to a model.

3. Measure as much of the double-sided interferogram as possible; phase errors become fully resolved if $\frac{L_{DS}}{L_{SS}} = 1$.

4. Avoid use of the Bartlett (triangular) apodization function. More optimum apodization functions are available (see section 4.8).

5. Significant variation of scan parameters will help isolate systematic from data processing errors.

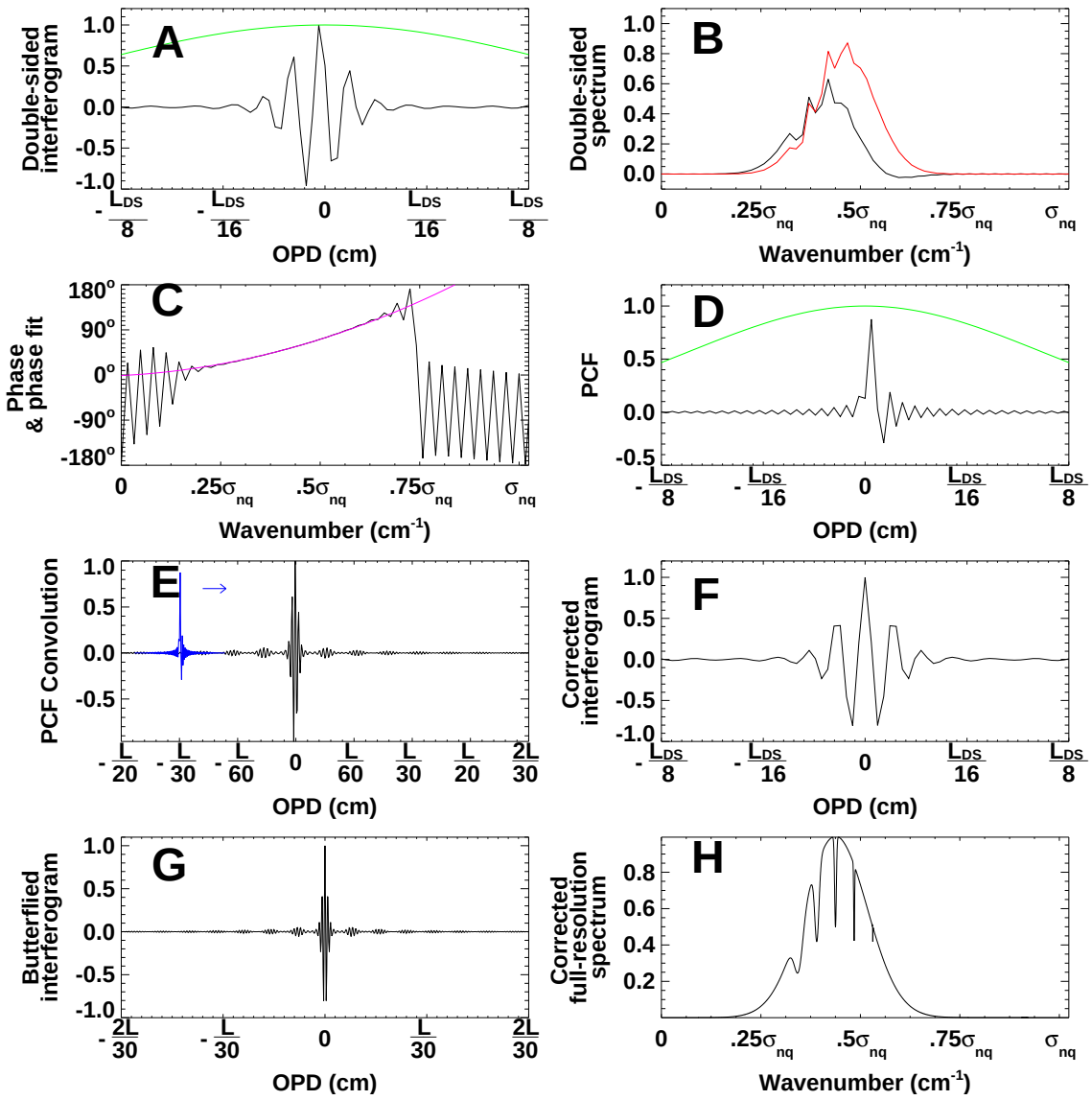

Figure 4.1: The enhanced Forman phase correction method involves a narrow double-sided interferogram (A), used to obtain low resolution amplitude (B) and phase (C) spectra. Also shown is a low-order polynomial fit of the phase (violet). The phase correction function (D) is generated from the polynomial fitted phase (equation 2.39) and convolved (blue) with the single-sided interferogram (E) to generate the phase corrected interferogram (F). The corrected interferogram (F) is butterflied (and apodized if desired) (G) to obtain the full resolution spectrum (H). The final high resolution spectrum (H) shows a broad Gaussian emission line with Gaussian absorption features of varying widths. In all plots, black and red show the real and imaginary components, respectively, and green is used for apodization.

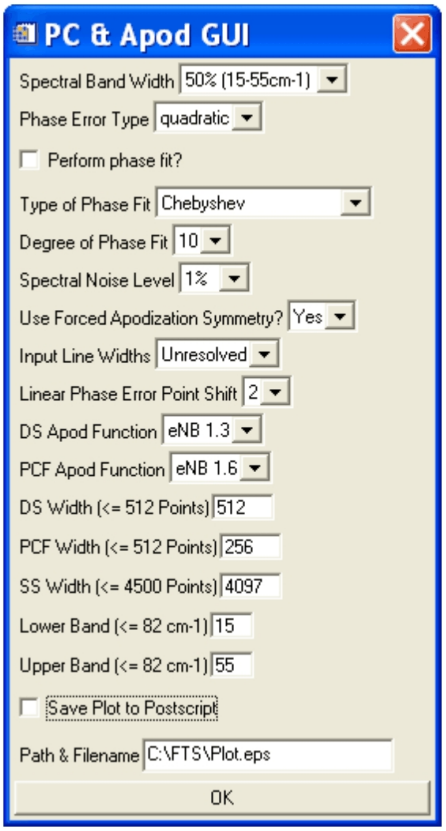

Figure 4.2: This GUI illustrates the variety of parameters that can be controlled in assessing the performance of the phase correction method.

While we agree with points 1,2,4, and 5, it is point 3 that deserves special consideration. If one can phase correct interferograms by measuring a single-sided ($\frac{L_{DS}}{L_{SS}} < 1$) rather than a double-sided ($\frac{L_{DS}}{L_{SS}} = 1$) interferogram a resolution loss is reduced. The goal then becomes to measure only as much of the double-sided interferogram as is necessary, and thus minimize spectral resolution loss. This chapter will explore the minimum double-sided interferogram length required to achieve adequate phase correction.

4.3 The double-sided interferogram

The amount of doublesidedness in an interferogram, i.e. the ratio $\frac{L_{DS}}{L_{SS}}$, is an important factor in FTS instrument design and data acquisition. The translation stage OPD that is dedicated to double-sided measurement is taken from that which could have been used for single-sided interferogram measurement (i.e. $L_{total} = L_{SS} + L_{DS}$). An increase in L_{DS} must either be accompanied by a reduction in L_{SS} or an increase of L_{total}; neither of which may be possible or feasible. Therefore the double-sided length of an interferogram becomes an important parameter in instrument design. For example, an L_{DS} greater than necessary limits the attainable spectral resolution, while a lower amount will provide insufficient phase information to allow adequate phase correction.

It is well recognized that the amount of double-sidedness required is driven largely by the nature of the spectrum under investigation. For example, a spectrum having a bandwidth of 10% of the Nyquist frequency would require an interferogram of at least 40 points double-sided to guarantee at least 2 in-band phase measurements, sufficient to perform a linear phase correction; a quadratic phase correction would require 3 phase measurements

within the band, in turn requiring a double-sided interferogram of at least 60 points.

4.4 Phase

Once the phase has been determined using the double-sided portion of the interferogram (equation 2.39), it is common practice to compute a fit (e.g. polynomial or Chebyshev) to the derived phase, weighted by the intensity of the corresponding spectrum. Ideally, the uncertainty in phase is inversely proportional to the magnitude of the spectrum (see appendix D), thus the phase fit is weighted by the spectral S/N. The type and degree of the phase fit is variable. The phase fit reduces noise contributions to the phase correction.

The phase uncertainty outside of the spectral band is greater due to the low spectral amplitude. As a result, special attention to how the phase fit handles the out of band phase is required. The most important aspect of the out of band phase values used in phase correction is the functional form of the out of band phase. There should be a smooth transition between the band edge and the spectral limits (i.e. 0 to σ_{low} and σ_{high} to σ_{nq}, cm^{-1}). Sharp transitions, discontinuities, and periodicities in the phase fit have deleterious effects on the interferogram upon convolution of the PCF.

4.5 Systematic phase correction

Some phase errors (e.g. those due to dispersive elements) are instrument specific and therefore can be determined a priori from the spectra of calibration sources. Other phase errors vary on a scan by scan basis (e.g. scan direction dependent instrument response and ZPD sampling), which calibration data cannot account for. A combination of high spectral

resolution external calibration data and low resolution interferogram measurement allows for the efficient correction of phase errors.

With systematic phase previously corrected for in an interferogram, interferogram-specific phase errors are typically low-order (i.e. linear) and do not require a high $\frac{L_{DS}}{L_{SS}}$ ratio in order for an accurate phase correction[26]. Therefore, there is potentially a great savings in the required double-sided interferogram length through combining systematic phase correction with a linear one. This dual phase correction approach allows both the reduction of spectral errors and the retention of higher spectral resolution within the single-sided interferogram.

The systematic phase correction used in processing TFTS data is described in section 6.5.

4.6 The phase correction function (PCF)

The PCF is determined by the inverse Fourier transform of the phase (equation 3.30). Thus the PCF length cannot exceed that of the double-sided interferogram. However, the requisite length of the PCF in order to perform the phase correction may be smaller than the double-sided interferogram. The number of points (i.e. length) of the PCF, like the double-sided interferogram length, is also an important consideration[26]. As will be emphasized in greater detail in section 4.7, convolution will distort both edges of the interferogram array, resulting in a truncated single-sided interferogram. A PCF that is longer than required will result in an unnecessary reduction in spectral resolution.

In essence, PCF convolution effectively redistributes energy throughout the inter-

ferogram in order to make it symmetric[26]. The range over which interferogram signal may be redistributed is determined by the length of the PCF as interferogram energy may only be redistributed at most by the length of the PCF kernel. In the spectral domain, the PCF length corresponds to the phase resolution. A PCF length that is too short implies insufficient phase resolution to correct the spectrum. A short PCF may not be able to redistribute the energy over a broad enough range to correct the interferogram, while a PCF that is overly wide may unnecessarily reduce spectral resolution. Therefore the length of the PCF function is an important element of phase correction.

Brault has suggested that the double-sided interferogram be as long as possible[78], but this comes at the cost of high spectral resolution. In the worst case this resolution cost is a factor of two as the OPD needed to generate the double-sided interferogram is not available for single-sided interferogram measurement.

Forman cited improvements upon multiple convolutions of the interferogram with the same PCF convolution kernel[61]. A possible explanation for the first convolution not properly correcting the interferogram is that the PCF function is not long enough for the interferogram content to be appropriately redistributed by the convolution. It is found that there is no benefit in applying multiple convolutions within the enhanced Forman approach used in this work, provided that the PCF has sufficient length. Rather than take an iterative approach with a narrow convolution function it is better to increase the PCF length in order to properly symmetrize the interferogram after the first convolution. In other words, correcting the spectrum once with sufficient phase resolution is much better than attempting to correct the spectrum multiple times with insufficient phase resolution

(recall $\Delta\sigma_{phase} = \frac{1}{2L_{DS}}$).

4.7 Convolution vs. resolution

The spacing between data points in a spectrum, $\Delta\sigma$, is given by the relation $\Delta\sigma = \frac{1}{2L}$ (equation 2.38). Standard resolution criteria dictates that in order to distinguish two spectral features, the spacing between them must also be $\Delta\sigma$. There are other resolution criteria (e.g. Sparrow, derivative, etc.) that only require a smaller separation which are discussed in the literature[38, 39]. Apodization however, be it natural apodization (section 2.10.4) or introduced in the data processing (section 4.8), produces spectral line broadening and with it a decrease in resolution. For apodization resulting from the interferogram being finite in length, the FWHM of an unresolved line is 1.207 rather than 1.0. Thus, the minimum spectral resolution for separable spectral features, rather than the ideal minimum stated above, becomes:

$$\Delta\sigma = \frac{1.207}{2L}, \tag{4.1}$$

where L is the maximum OPD. Other apodizations broaden the ILS to an even greater extent as is shown in table 4.1 and figure 4.4. To determine the available spectral resolution associated with a given apodization function, use the number in the second column of table 4.1 (FWHM of ILS) in equation 4.1 in place of 1.207 (the FWHM of the sinc function). In practice, resolution of the final spectrum (one-sided) must be sufficient for the spectral features under investigation in order to allow quantitative spectral analysis.

In addition to the resolution loss due to the one-sided OPD length being reduced, there is another more subtle form of resolution reduction. The convolution used to correct

the interferogram asymmetries also reduces spectral resolution. An example of this is illustrated with rectangular functions in figure 4.3. The original rectangular function loses the rectangularity of the edges as a rectangular kernel is convolved with it. Also shown on figure 4.3 is the resulting ILS caused by the convolution edge distortion along with the difference between the resulting ILS and the ideal sinc ILS. This distortion can only affect the edges of the interferogram by an amount equal to half of the PCF length on each side. Thus a longer PCF will result in greater interferogram edge distortion which in turn results in greater resolution loss. To remove this convolution based interferogram edge distortion, the interferogram needs to be truncated at the edges prior to where the edge distortion commences. The full resolution spectrum is obtained from the one-sided portion of the interferogram, so the edge distortion on the negative OPD portion of the interferogram does not affect the final resolution. Therefore, the phase correction convolution reduces spectral resolution by an amount equal to half of the PCF length.

4.8 Apodization

Sidelobe ringing in the spectral ILS can be reduced/minimized by a mathematical process known as apodization[38, 39, 85, 86, 87, 88, 89]. Apodization essentially applies a weighting function to the interferogram to reduce the amplitude of ILS sidelobes (at the cost of broadening the line width). Unresolved spectral features are accompanied by characteristic 'ringing' throughout the spectrum due to the sinc nature of the ILS which is caused by the finite length of an interferogram. The amplitude of the sinc sidelobes can be reduced at the cost of a broadened spectral line. Certain apodizing functions are more

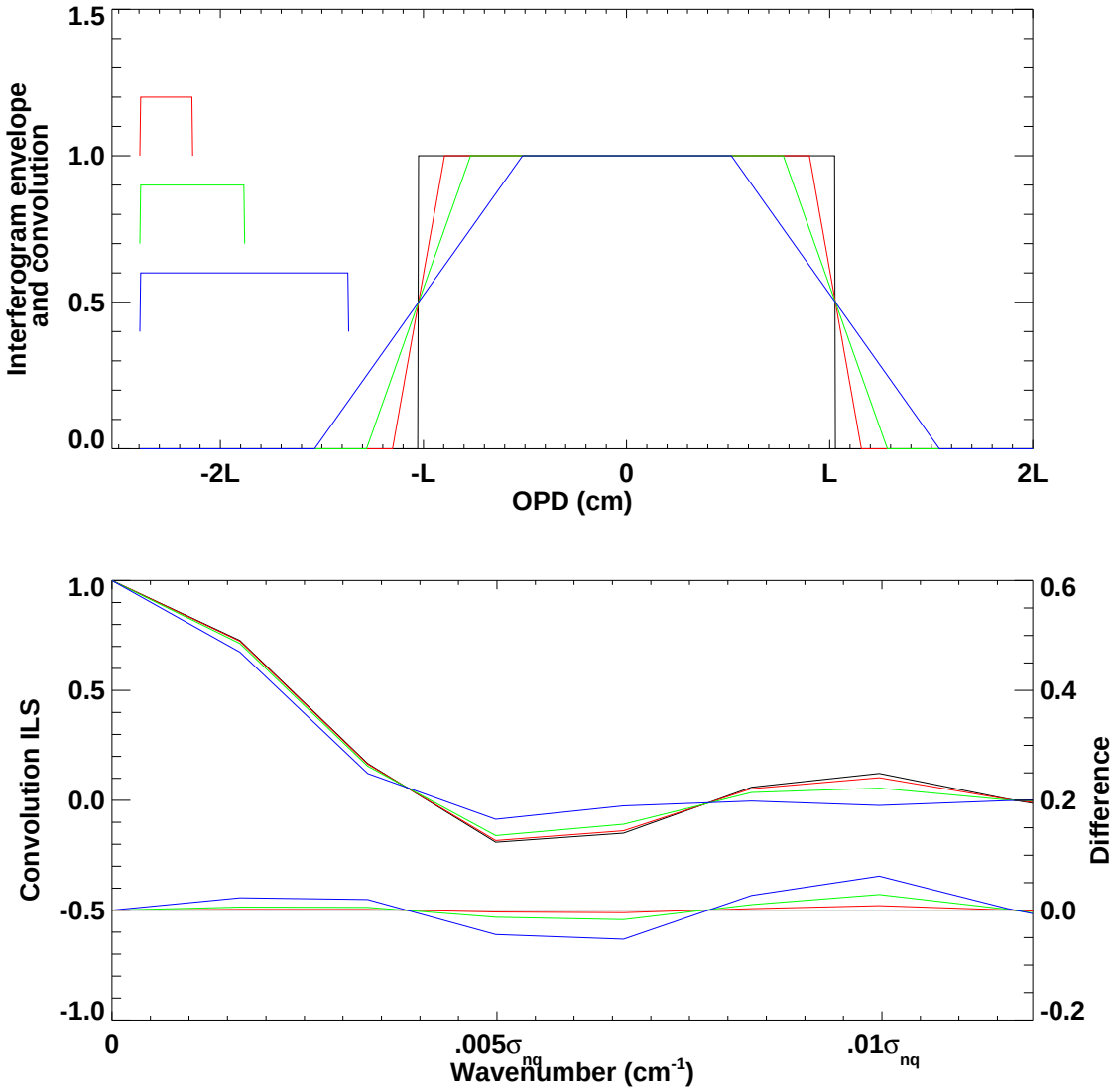

Figure 4.3: The effect of convolution on ILS. The upper figure illustrates the convolution of a rectangular function by rectangular convolution kernels of various widths. The lower figure illustrates the ILS associated with each of the post-convolution rectangular functions above. Also shown in the lower figure is the difference between the sinc ILS and the distorted ILS caused by the convolution, offset by -0.5 for clarity. Rectangular envelope functions are used here to illustrate the main point, but depending on the convolution kernel form, this ILS may change. The only way to ensure that the convolution distortions do not affect the spectrum is to truncate the convolution edges from the interferogram.

Apodization function	FWHM of ILS	Normalized FWHM	largest sidelobe amplitude	sidelobe reduction (%)
Unapodized	1.20	1.00	−0.217	0.00
eNB[a] 1.1	1.32	1.10	−0.0963	55.6
eNB 1.2	1.44	1.20	−0.0550	74.6
eNB 1.3	1.57	1.30	−0.0272	87.4
eNB 1.4	1.69	1.40	−0.0138	93.6
eNB 1.5	1.81	1.50	−0.00674	96.9
eNB 1.6	1.93	1.60	−0.00275	98.7
eNB 1.7	2.05	1.70	−0.00129	99.4
eNB 1.8	2.17	1.80	−0.00055	99.7
eNB 1.9	2.29	1.90	−0.00028	99.8
eNB 2.0	2.41	2.00	−0.00010	99.9
NB[b] weak	1.44	1.20	−0.0581	73.2
NB medium	1.69	1.40	−0.0142	93.4
NB strong	1.93	1.60	0.00373	98.2

[a] extended Norton-Beer
[b] Norton-Beer

Table 4.1: Table comparing the ILS FWHM and sidelobe reduction of the various apodizing functions[1, 90]. The normalization is done with respect to the unapodized sinc ILS.

efficient than others and consequently broaden the spectral features to a different degree. Section E and figure E.1 illustrate a variety of traditional apodizing functions and their associated ILSs.

The Norton-Beer apodizing functions have been optimized for a known minimal spectral broadening/sidelobe amplitude reduction relationship[1, 87, 88]. These extended Norton-Beer (eNB) apodization functions, along with their associated ILSs are shown in figure 4.4 and are the primary apodization functions used in this work. Figure 4.4 also shows the three original Norton-Beer apodizing functions (NB-W,M,S) for comparison. Table 4.1 illustrates the FWHM of the ILS for the apodization functions shown in the figure.

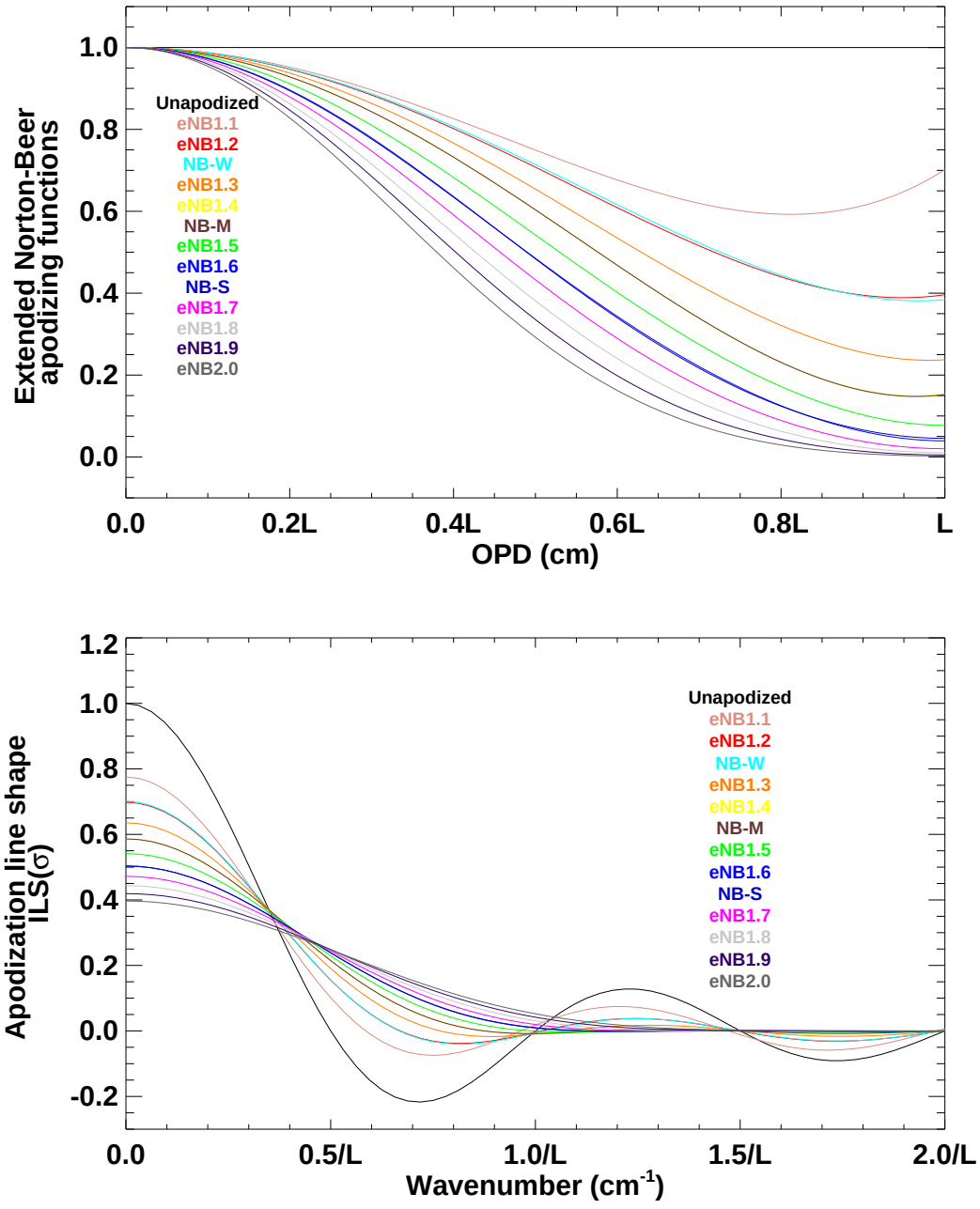

Figure 4.4: The extension of the Norton-Beer apodization functions to known/desired line broadening. The ILS has been extended in steps of 0.1 from 1.1 to 2.0 of the natural line width[1, 90].

Apodization of the double-sided interferogram may be performed in order to reduce the effect of narrow spectral features on the continuum used to generate the phase. Unresolved spectral features are observed to include sinc features[90] with oscillating sidelobes potentially distorting the spectral continuum. Apodization will broaden the spectral line itself but reduce the sinc sidelobe structure affecting the continuum, thus decreasing uncertainty in the spectrum. Since phase uncertainty is proportional to spectral uncertainty, apodization of the double-sided interferogram therefore has potential to increase the accuracy of the phase determination by reducing sidelobe oscillation if the phase is smooth/slowly varying.

The PCF is generated using equation 3.30, with the phase fit, $\phi_{fit}(\sigma)$, used in place of the measured phase $\phi(\sigma)$ (equation 2.39). The PCF may also be apodized prior to convolution. There are two main reasons for PCF apodization. Firstly, a PCF with discontinuities such as non-zero edges can introduce discontinuities into the interferogram, which will in turn produce artifacts in the spectrum. Apodization of the PCF will reduce the amplitude of the edges of the PCF in order to reduce the discontinuous convolution effect. Apodization functions which taper down to zero at the PCF limits are expected to be better suited for this. Secondly, PCF apodization will emphasize the slowly varying nature of the phase as higher resolution features contained in the far limits of the PCF wings are de-emphasized.

Apodization inherently requires some form of symmetry to the data being apodized, ideally that it is symmetric about OPD = 0 cm. If the interferogram has a linear or higher order phase shift, the location of ZPD will not be at OPD = 0 cm. Therefore the

apodization itself, if not properly centered, will introduce a phase error to the spectrum. One of the enhancements added to the enhanced Forman phase correction used in this work is the ability to re-center the apodization to be symmetric about any arbitrary (user/software specified) point rather than the OPD = 0 cm point. Figure 4.5 illustrates the importance of symmetric apodization.

Apodization of the double-sided interferogram and PCF is possible without broadening the ILS of the final spectrum from the one-sided interferogram. The choice of intermediate phase correction apodizations does not place any limits on the apodization of the one-sided interferogram, and thus does not directly affect the ILS of the one-sided spectrum.

4.9 Spectral Error Analysis

In order to evaluate the performance of the phase correction routine, a set of benchmark measurements is required. In this work, the spectral parameters used to determine the effectiveness of phase correction are spectral line amplitude, centre, width, and area; the latter being a combination of amplitude and width. The errors in retrieving these parameters from a processed interferogram/spectrum are used to indicate the quality of phase correction.

Spectral parameter reduction is done in the same fashion for each case to allow for unbiased spectral comparisons. For sections 5.4 & 5.5, the parameters used to generate the input spectrum are available and are used for comparison with the post-processing result. To evaluate the phase correction methods quantitatively, an IDL[3] procedure was written to fit the spectrum to a theoretical one containing the model spectral features. This routine

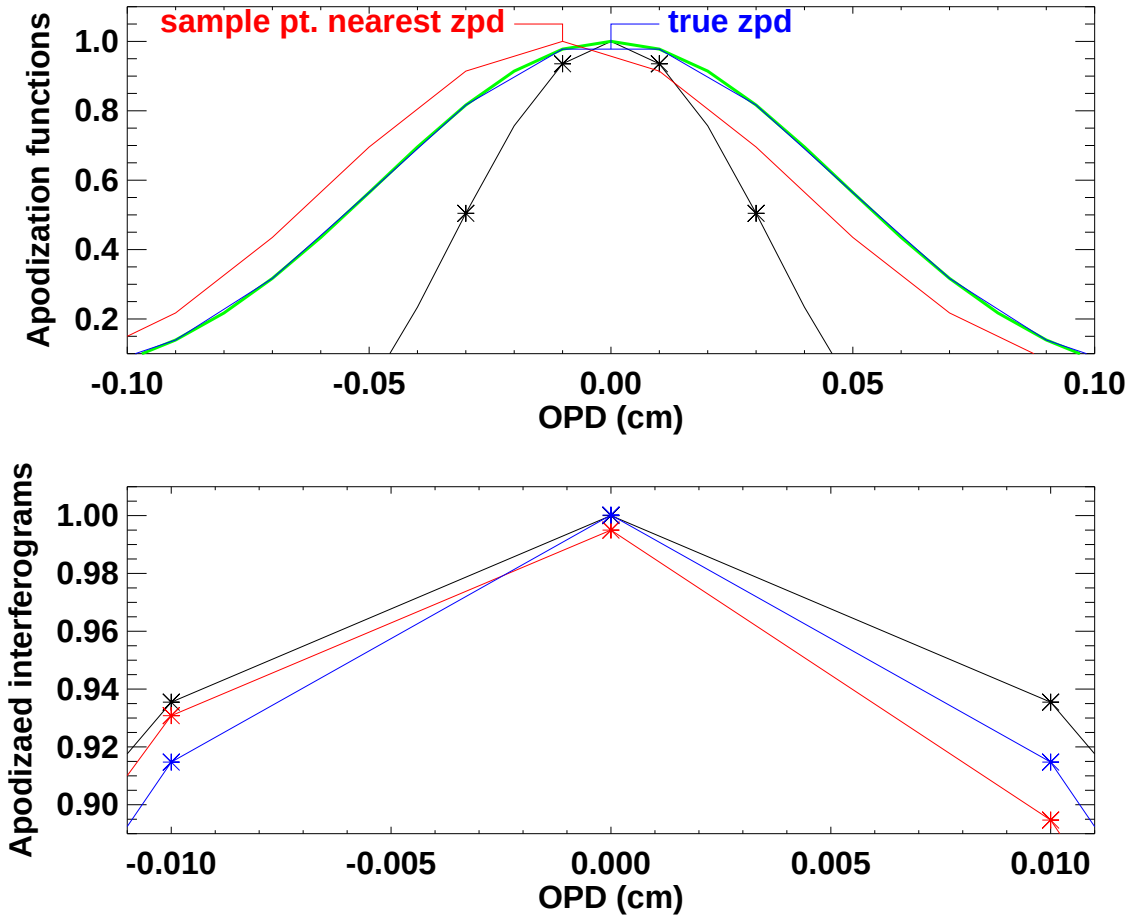

Figure 4.5: Apodization symmetry about the true ZPD point rather than the closest sampled point to ZPD. The top figure shows a sinc function as an interferogram, sub-sampled by a factor of 2 such that the actual ZPD point is not sampled, with the apodization of the sinc function before sub-sampling shown in green. The sub-sampled apodization symmetric about the closest sample point to ZPD is shown in red while the sub-sampled apodization with true symmetry about ZPD is shown in blue. The lower figure shows the apodized interferograms (red and blue) superimposed on top of the unapodized interferogram (black).

uses the expected line-shape for each feature and performs a minimum χ^2 analysis[91] with the spectral properties as free parameters.

4.9.1 Line Centre Error

The effect on line amplitude and width (and consequently area) due to processing is primarily related to apodization (see section 4.8) and residual phase (see section F-3). Figure 5.5 illustrates the effect of apodization on the FWHM, amplitude, and area error of a spectral feature. Apodization may also introduces a shift in line centre as is described in section 2.10.4. Line centre error is also influenced by other factors such as phase error and spectral noise.

The relationship between $\delta\sigma(\sigma_o)$, and the spectral S/N can be expressed as[78]:

$$\delta\sigma \propto \frac{W}{\sqrt{N_W}(S/N)} \tag{4.2}$$

where W is the width of the line and N_W is the number of statistically independent data points in the line. The ratio of line centre error for two different values of S/N, 1% noise and n% noise, for example, will vary linearly with the S/N.

A case study was performed in order to verify that the errors measured with the IDL spectral fitting routine match that expected from theory. Using the input spectra described in section 5.4, one hundred thousand spectra were created with varying levels of random noise. These spectra were processed with a spectral fit performed in order to obtain the error in the line centre. The line centre errors were averaged for each noise level[1] with the results shown in figure 4.6. There is a linear relationship between the line centre error,

[1] 0.1% increments over a 10% region starting at 1%, with 1000 spectra at each RMS noise increment.

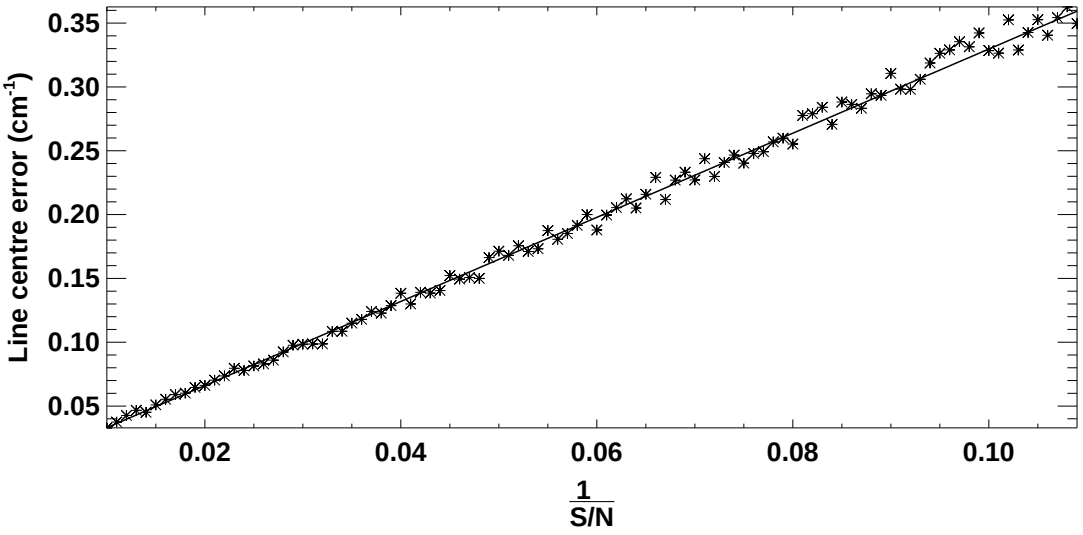

Figure 4.6: The relation between resolved line centre error and the spectral S/N ratio. The expected relationship is a $\frac{1}{S/N}$ dependence as is observed[78].

$\delta\sigma$, and $\frac{1}{S/N}$ as is expected.

4.9.2 Effect of phase correction on spectrum

Ideally, phase is slowly varying and the net result of phase correction is equivalent to a slowly varying function ($e^{-i\phi(\sigma)}$) multiplied with the original spectrum. Also, it is expected that the phase fit/model will be reasonably accurate, leaving only small residual phase errors. There are no mathematical limits on $\phi(\sigma)$, however $e^{-i\phi(\sigma)}$ is limited to the range $[-1, 1]$ in both the real and imaginary domains. Thus, neglecting the consideration of noise effects, the phase corrected spectrum can never be greater in magnitude than the zero residual spectrum.

As a result, line amplitude and width are expected to be more prone to err in

ϕ_{max} (^{o})	$\frac{\delta Amplitude}{Amplitude}$	$\frac{\delta FWHM}{FWHM}$	$\frac{\delta Area}{Area}$	$\frac{\delta Line\ centre}{FWHM}$
0.1	$[-10^{-4}$, 0.00]	$[-10^{-4}$, $10^{-4}]$	$[-10^{-4}$, $10^{-4}]$	$[-10^{-5}$, $10^{-5}]$
1.0	[-0.01 , 0.00]	[-0.01 , 0.01]	[-0.03 , 0.01]	[-0.003 , 0.003]
5.0	[-0.38 , 0.00]	[-0.37 , 0.38]	[-0.75 , 0.38]	[-0.095 , 0.095]
10.0	[-1.51 , 0.00]	[-1.49 , 1.56]	[-3.01 , 1.56]	[-0.382 , 0.382]

Table 4.2: Expected error ranges for spectral parameters based on residual phase errors as determined by equation 4.3 (see appendix F).

the negative direction as it is more likely for amplitude and width to be reduced rather than increased. Line area is also expected to decrease rather than increase for the same reason. Spectral parameter error also is significantly related to the line profile itself and the accuracy of the phase correction. The expected parameter error ranges due to uncorrected residual phase are as follows:

$$\begin{aligned}
\frac{\delta Amplitude}{Amplitude} &\in [\cos(\phi_{max}) - 1, 0], \\
\frac{\delta FWHM}{FWHM} &\in [\frac{\cos(\phi_{max}) - 1}{2 - \cos(\phi_{max})}, \frac{1 - \cos(\phi_{max})}{2\cos(\phi_{max}) - 1}], \\
\frac{\delta Line\ centre}{FWHM} &\in [\frac{\cos(\phi_{max}) - 1}{2(1 + \cos(\phi_{max}))}, \frac{1 - \cos(\phi_{max})}{2(1 + \cos(\phi_{max}))}], \\
\frac{\delta Area}{Area} &\in [\frac{-(3 - \cos(\phi_{max}))(1 - \cos(\phi_{max}))}{2 - \cos(\phi_{max})}, \frac{1 - \cos(\phi_{max})}{2\cos(\phi_{max}) - 1}].
\end{aligned} \tag{4.3}$$

For further explanation on how the parameter error ranges are derived see appendix F. Table 4.2 illustrates the expected range of parameter errors assuming a maximum residual phase, ϕ_{max}, as given in the first column of the table.

Overall spectral degradation will be caused by other factors as well as residual phase and will be limited by the dominant spectral degradation contribution (ideally photon noise). Once phase correction error has been reduced to below the dominant source of

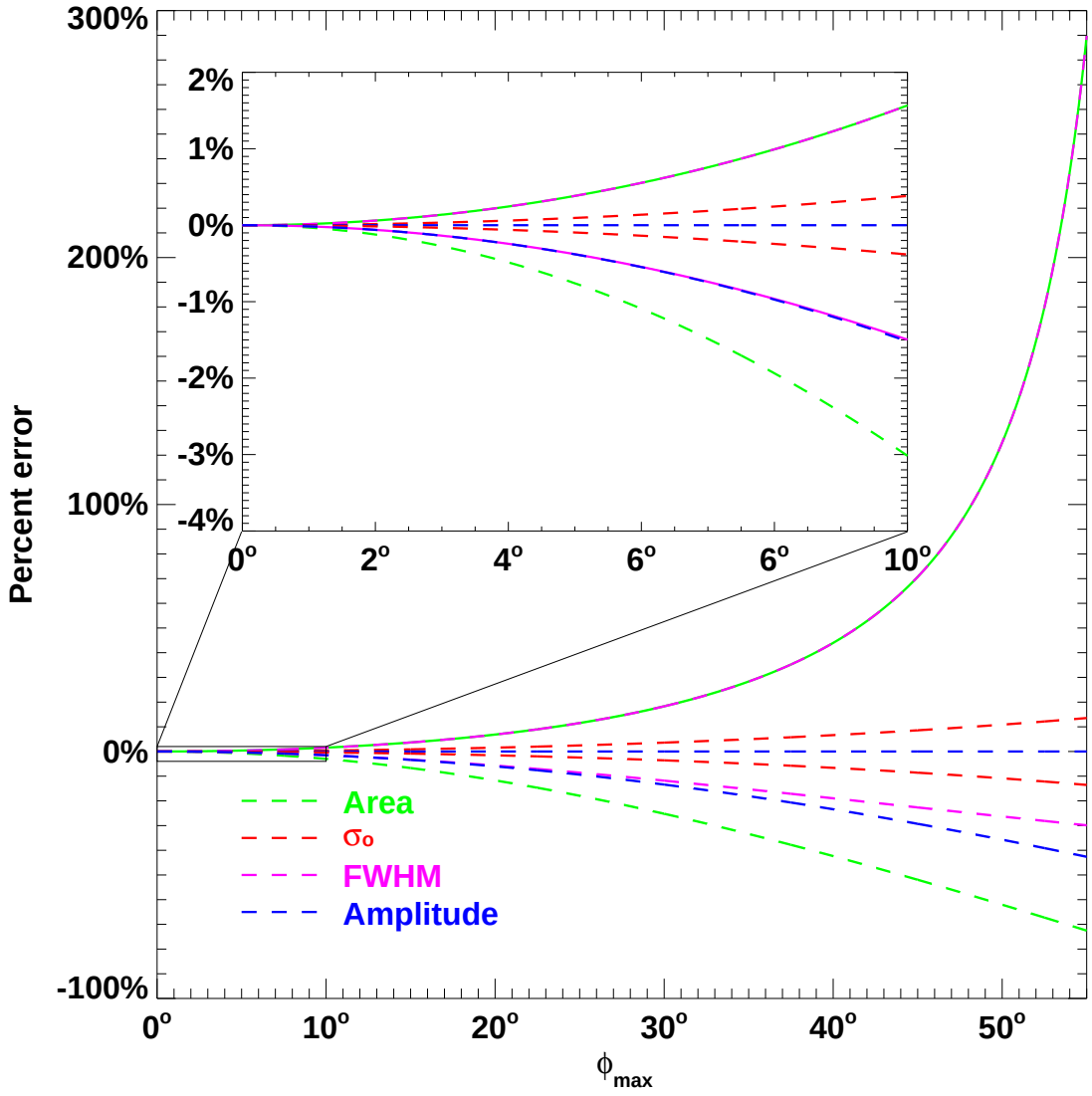

Figure 4.7: Positive and negative spectral parameter error ranges resulting from residual spectral phase. The approximations used are described in appendix F.

Processing feature	Original	Enhanced
Phase fit	no	optional
Spectral band-pass filter[a]	optional	optional
Variable convolution width	no	optional
PCF apodization	Forman apodization	optional, variety of apodizations
Apodization centre shift	no	optional
Iterative	optional	optional, not recommended

[a] see section 3.6.3

Table 4.3: A comparison of the processing options within the original and enhanced Forman phase correction methods.

error then further phase correction improvements are less likely to produce significant error reductions.

4.10 Conclusions

An enhanced Forman phase correction routine has been developed. This method allows better choice and application of apodization functions, a range of methods of fitting the phase, and flexibility in the choice of the lengths of both the double-sided interferogram and the PCF. Table 4.3 compares the processing features of the original and the enhanced Forman phase correction methods. This method of phase correction is used in the following chapter to investigate the optimization of single-sided phase correction.

Chapter 5

Phase Correction Optimization

Contents

5.1 Overview

Optimizing the parameters used in phase correction minimizes both the residual spectral errors and the associated resolution reduction. This chapter is focussed on the optimization of processing parameters for the enhanced Forman phase correction discussed in the previous chapter for both a general spectroscopic application and for the SPIRE/CQM ground testing case. Certain aspects of phase correction optimization may be generalized while others depend on the detailed nature of the spectrum under study. This section will review general phase correction optimization principles and introduce a software tool which has been developed by the author for instrument and application specific phase correction optimization.

The software tool generates spectral error surfaces for line amplitude, width, area, and centre. The error surfaces presented in this thesis are colour coded for clarity. Red represents the error in line amplitude, expressed as a percentage of the line amplitude. Green represents the error in line FWHM, expressed as a percentage of the line FWHM. Blue represents the error in area, expressed as a percentage of the line area. Finally, yellow represents the error in line centre expressed as a percentage of the one-sided spectrum resolution element ($\Delta\sigma$).

5.2 Introduction

The main goal of phase correction optimization for a given spectrum is an idea of the interplay between various parameters of the phase correction routine. The main questions relating to phase correction should be as follows:

- How much double-sidedness is required in an interferogram in order to phase correct accurately?
- What apodization (if any) should be used on the double-sided interferogram?
- How should the phase required to correct the interferogram be determined?

  i.e. What type of fit/model should be used?
- How long should the PCF convolution kernel be?

  i.e. What is the required phase resolution?
- What apodization (if any) should be used on the PCF?
- How has the phase correction changed the properties of the spectrum?
- How does the phase correction depend on the nature of the spectrum?

The answers to these questions cannot be both specific and universal. It is possible, however, to understand the principles and general trends involved, and also study unique cases as is done in section 5.5.

5.3 IDL optimizing tool

A software tool was developed in order to assist in the understanding and parameter selection of the phase correction of FTS data for several astronomy projects[26]. The phase correction optimizing tool consists of two main components, each comprised of several programs, procedures, and functions. The first of these is the phase correction routine itself

which is based upon processing options outlined in section 4.2. Figure 4.2 illustrates the GUI version of the phase correction program, outlining the several processing options.

The second component of the optimizing tool is the error surface generating tool. Due to the vast number of possible combinations of processing options in the phase correction, there are potentially billions of possible unique spectral outputs (depending on L_{DS}, L_{SS}, Δz, etc.). The analysis of these spectra yields the retrieved spectral feature parameters. The comparison of these parameters with the known model input parameters (amplitude, centre, width, area, pressure, humidity, temperature, etc.) results in a multi-dimensional error matrix. In addition to the error from the expected parameters, the tool also has the capability of showing the χ^2 goodness of fit surface for the phase fit of each phase correction processing iteration. The error surface generating tool allows the selection of two processing parameters (e.g. double-sided interferogram length and apodization) and an error type (e.g. line centre error) to generate a three dimensional error surface. These surfaces can can be used to study trends and patterns in the relationship between the processing parameters and the error parameter selected. An example of the error surface generating GUI is shown in figure 5.1 and examples of the surfaces generated using the tool are found in figures 5.5, 5.6, 5.8, 5.11, and 5.13.

Several multidimensional minimization routines are available[66, 92, 93], and could be used to find the exact set of phase correction parameters for a known input spectrum; however, this is not the purpose of this study. Once the exact input spectrum becomes unknown as is the case in astronomy, the optimal phase correction parameters for one case may not be the optimal parameters for another case. For this reason, the end result of the

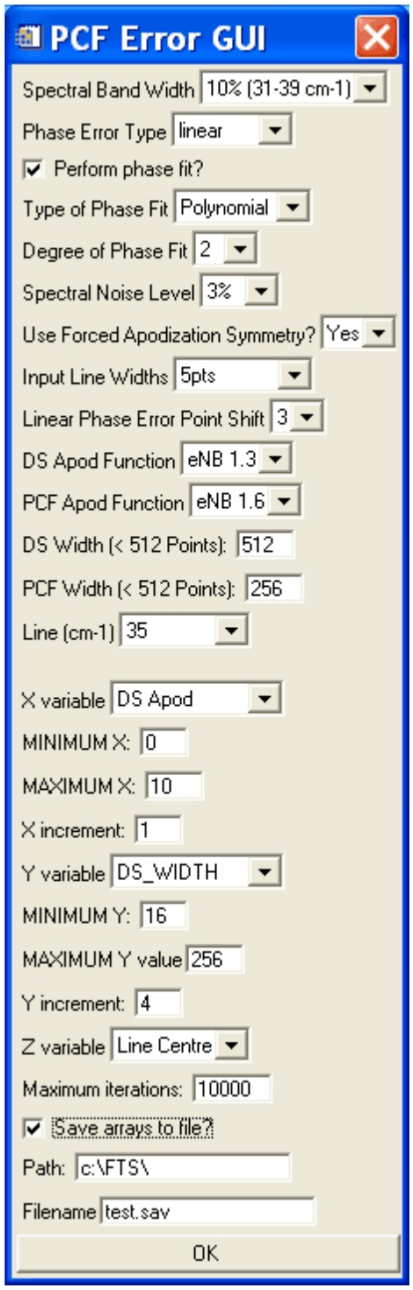

Figure 5.1: The error surface generation GUI used in the phase correction and multivariate error optimization routines. There are roughly 250 billion combinations of input and processing variations.

phase correction optimization is not an exact set of parameters for one specific interferogram, but rather a more general set of parameters for a series or family of interferograms such as those from a specific FTS instrument observing similar sources. This chapter illustrates the use of the IDL phase correction optimization software for two test cases. The first case consists of spectra containing Gaussian features of a variety of amplitudes, widths, and line centres. The second case is tailored to assist in the SPIRE/CQM verification tests and consists of a spectrum including the blackbody source, atmospheric absorption, and other optical components relevant to the ground test facility for SPIRE at RAL (see chapters 6 & 7 for more details).

5.4 Optimization for Gaussian spectral features

This study is the first of two introduced in section 5.3. This study uses a variety of input spectra, consisting of linear combinations of Gaussian emission and absorption lines of different amplitudes and widths. Linear and quadratic phase error has been introduced, and, to bring realism to the spectra, white noise, ranging from 0%-10% root mean square, has been included. The input spectra are summarized in figure 5.2. Overall there are a total of approximately 2^{10} different input interferograms (2 (continuum) x 6 (absorption width) x 2 (linear/quadratic phase error) x 4 (sampling pt. shift) x 11 (noise levels)) for the Gaussian feature phase correction minimization test case. In addition to the variation on the input parameters discussed above, there are approximately 2^{21} combinations of unique phase correction processing parameters (25 (DS apodizations) x 500 (DS widths) x 25 (PCF apodizations) x 500 (PCF widths) x 3 (phase fit) x 4 (apodization symmetry)).

The spectral line fitting software determines the line amplitude, centre, and width for each spectral feature synchronously. Thus, for the spectra of this section, with a broad Gaussian emission feature and five narrow Gaussian absorption features there is an 18 dimensional minimization parameter space to be minimized.

5.4.1 Gaussian Optimization Results

With over 2^{31} possible combinations of input and processing parameters, the parameter space is too large to show a comprehensive evaluation of every possible combination of phase correction. Rather, a sample of the optimization tools' capabilities is shown. The FTS instrument itself should narrow the choice of parameters significantly. The software tool should then be useful in further investigation of the best data processing scheme.

The level of interferogram double-sidedness, or in other words the value of the ratio $\frac{L_{DS}}{L_{SS}}$ (section 3.2), is dictated by the desired resolution of the double-sided spectrum required in order to accurately determine the phase. The phase resolution determines the ability of the PCF convolution to correct the interferogram. For a linear phase correction, two in-band phase measurements are required in order to perform a linear fit. This translates to a double-sided interferogram of at least 40 data points for a 10 % spectral band.

The double-sided interferogram apodization may also play a role in the phase determination accuracy, depending on the nature of the spectrum. The importance of apodization of the double-sided interferogram is in the minimization of ILS sidelobe amplitude, which allows a more accurate phase determination, unless of course there are real phase features which are 'hidden' by the apodization.

A spectrum with unresolved features will experience an improvement in the phase

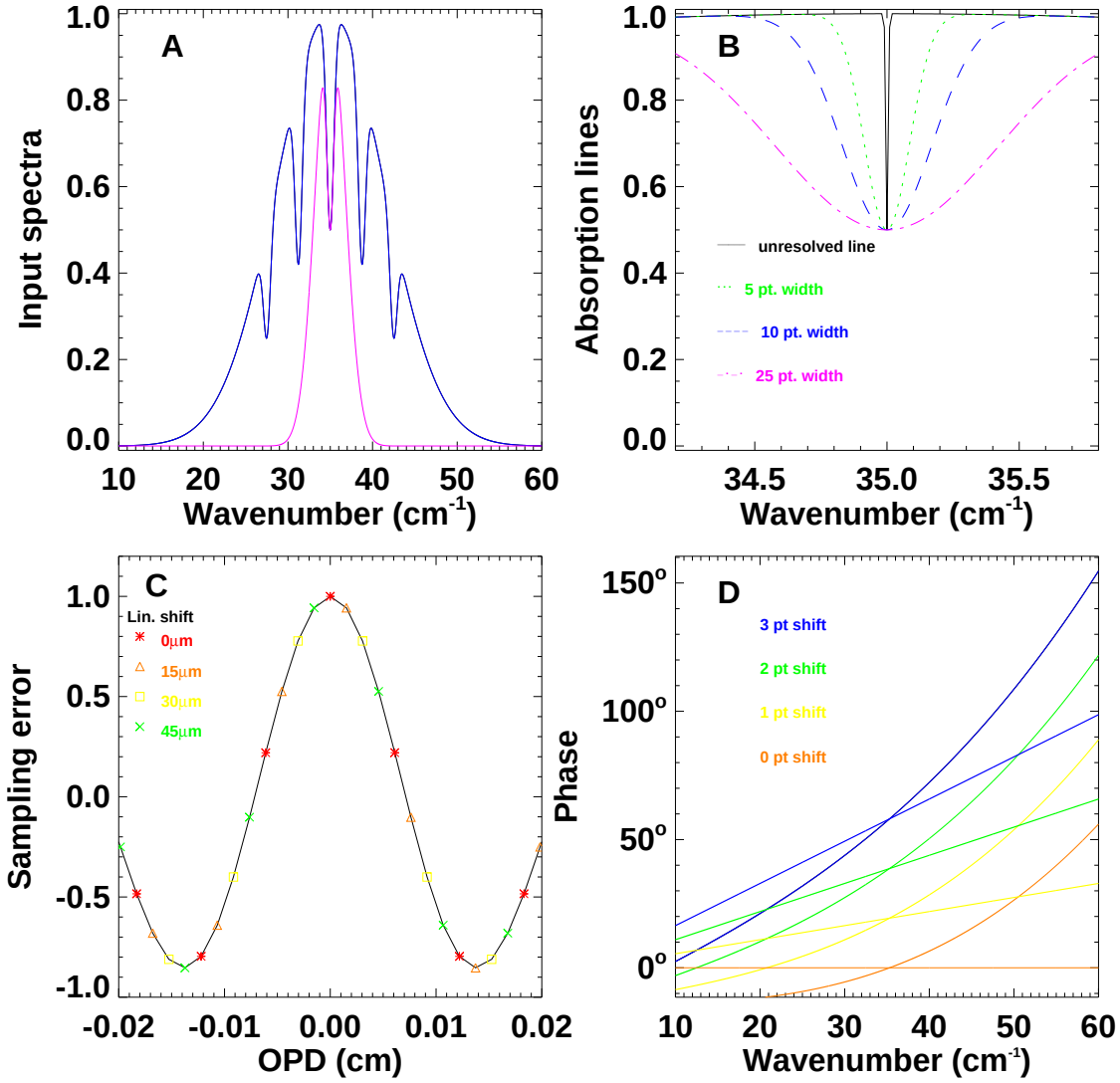

Figure 5.2: Input spectra used for the Gaussian phase correction optimization case study. (A) Broad (blue) and narrow (purple) band input spectra. (B) Absorption line widths. The narrow band spectrum only has one absorption line at the peak of the continuum while the broad-band spectrum has five absorption lines evenly spaced. (C) Sampling used to generate linear phase errors. (D) Phase introduced into the spectrum.

determination with double-sided interferogram apodization due to the reduction in sidelobe amplitude. Conversely, a spectrum with higher resolution, such that the spectral features are resolved, will not require double-sided interferogram apodization because there will not be any sinc sidelobes present if all features are resolved. Figure 5.3 illustrates the resulting phase for both apodized and unapodized double-sided interferograms with linear phase error. This figure illustrates how the phase difference between the apodized and unapodized cases is significantly greater for the unresolved spectral feature than it is for the resolved spectral feature.

The level of apodization required to accurately determine phase depends both on the nature of the spectrum and the resolution available. Apodization is required for accurate phase determination of unresolved spectral features. Since it is not expected that spectral features will be resolved in the double-sided spectrum, phase determination using the double-sided interferogram will typically benefit from double-sided interferogram apodization.

The phase can be used as is to generate the PCF, or a fit of the phase can be produced. The phase fit, if done properly, will include the slowly varying components of the double-sided phase, without the noise that is included in the double-sided phase itself due to the noise in the spectrum. Thus, similar to apodizing, a phase fit will produce better phase correction results than the original phase. However, if the double-sided phase is a quadratic or higher order function, and only a linear phase fit is performed, then the phase correction results are likely to be better using the actual phase (with an apodization on the PCF) rather than a phase fit.

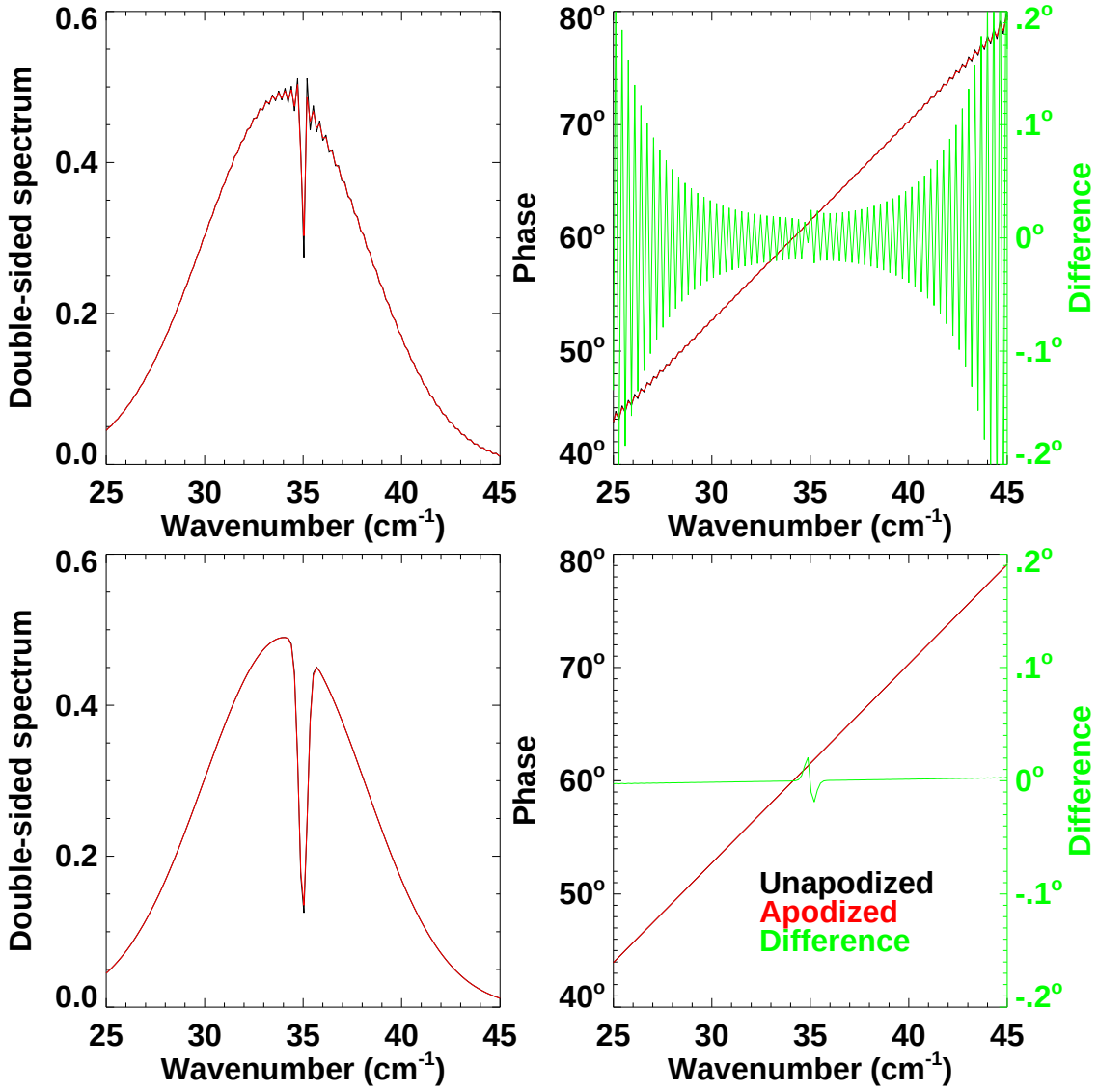

Figure 5.3: Unapodized (black) and apodized (red) spectra of unresolved (top) and resolved (bottom) spectral features. Also shown is the difference (green) between the unapodized and apodized phase. The unresolved spectral feature has a FWHM of $\Delta\sigma$ (i.e. 1 data point) in the original spectrum and the FWHM of the resolved spectral feature is $5\Delta\sigma$ (i.e. 5 data points).

The majority of the non-linear phase characteristics are likely to be systematic. Therefore, a study of the specific spectrometer instrumentation (using calibration spectra, for example) should in principle allow determination of the instrument specific PCF. If an instrument specific PCF is available, then it is recommended to perform two phase corrections, one for the systematic effects which do not change at all for interferograms from the same observation, and another for linear phase error which is likely to be different for each individual interferogram because of ZPD sampling errors. In practice, the two phase corrections can be performed simultaneously, only requiring one convolution.

The selection of the PCF length and apodization is assisted by the nature of the phase and thus the level of energy re-distribution required to re-symmetrize the interferogram. A PCF that is longer than required for symmetrization through convolution will unnecessarily reduce spectral resolution. An overly narrow PCF does not have sufficient phase resolution and thus will not symmetrize the interferogram properly, leaving residual phase distortions in the final spectrum.

PCF apodization ensures that the value of the PCF at both positive and negative limits is zero, and thus discontinuities are not convolved through the interferogram. Therefore the apodization selected should have zero amplitude at the kernel edges, and also should not significantly alter the central region of the PCF as this will affect the interferogram symmetrization in the PCF convolution.

In figure 5.4, the 100 point PCF is non-zero at the positive OPD kernel edge, indicating that the available length for interferogram redistribution is insufficient. The 256 point PCF in figure 5.4 has zero amplitude at both positive and negative OPD edges

and thus has sufficient length. The 1280 point PCF also has zero amplitude kernel edges; however, the spectral error is greater then the minimally sufficient PCF case. The 1280 point PCF has a significant resolution loss compared to the 256 point PCF case. In this case the absorption feature goes from resolved (256 point PCF) to unresolved (1280 point PCF) due to the convolution resolution reduction.

Figures 5.5 & 5.6 show the effects of various combinations of double-sided interferogram and PCF apodizations on the line centre, FWHM, amplitude, and area. As expected, apodization of the double-sided interferogram causes a slight decrease in amplitude, a slight increase in FWHM, area is unaffected, and line centre decreases.

The largest source of error becomes the limiting factor in FTS spectral analysis. Typically, detector noise limited errors are the goal. Once phase related errors are smaller than other errors, such as noise, then any further phase correction improvements are shadowed by the larger source of error. In order to have noise limited line centre error, a rule of thumb to determine the requirement on residual phase error ($\delta\phi$) from the available S/N[78] is given by Brault as follows:

$$\delta\phi < \frac{1}{S/N}. \tag{5.1}$$

For example, $\delta\phi$ must be less than 10^{-2} radians to make full use of a spectrum with a S/N of 100.

Earlier in this section some questions were posed about the general process in determining phase correction parameters. They are addressed now as follows:

- How much double-sidedness is required in an interferogram?

  Phase resolution is an important consideration in the required double-sided length

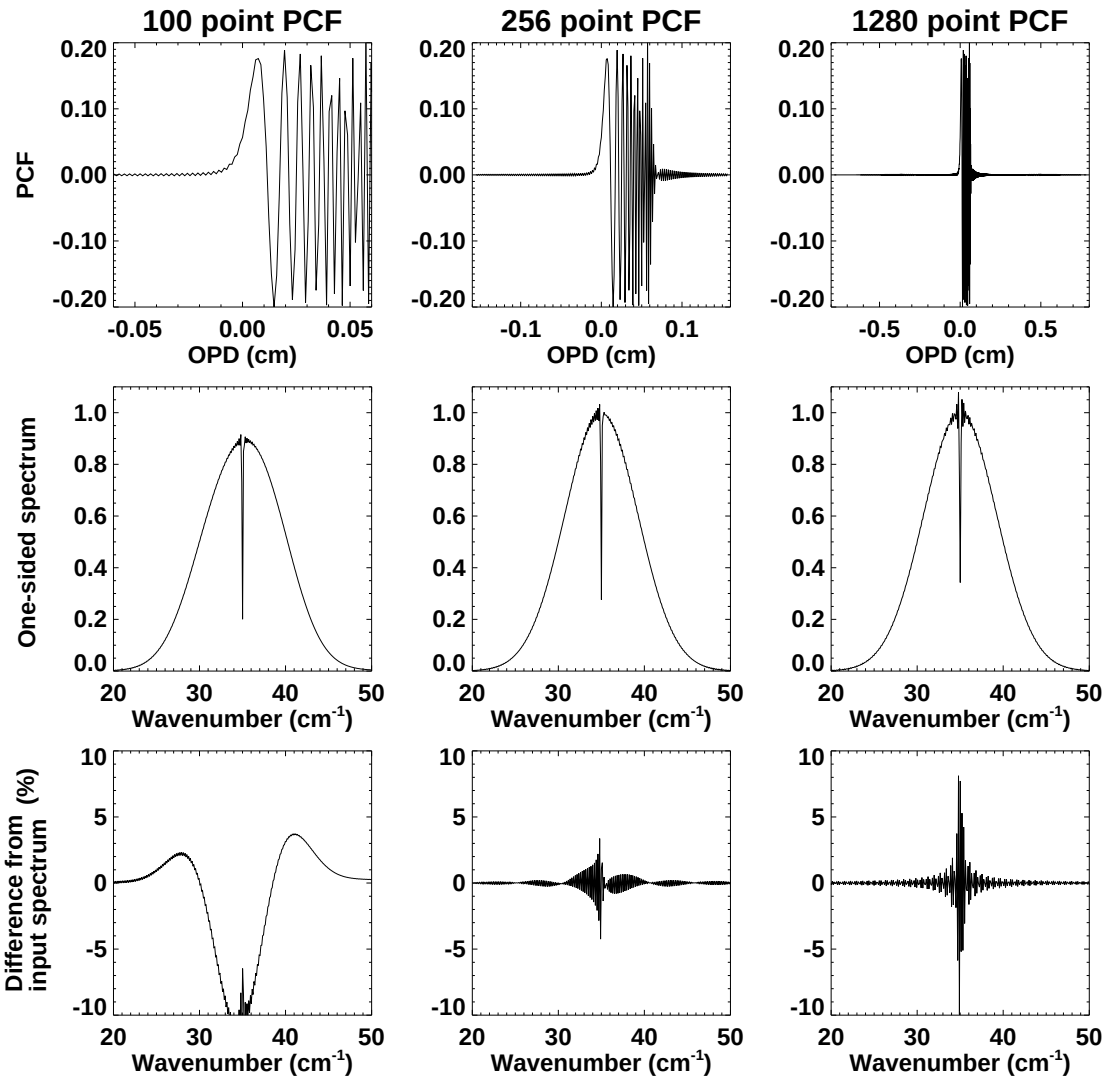

Figure 5.4: Insufficient (left column), sufficient (centre column), and excess (right column) PCF convolution kernel length. The input data are identical for each case, with the only processing difference being the number of data points in the PCF kernel (100 pts. - left, 256 pts. - centre, 1280 pts. - right). The final spectra have all been zero-padded up to the same resolution. The first row illustrates the same PCF convolution kernel, but truncated to the various widths. The central row illustrates the full resolution (Forman phase corrected, one-sided) spectrum resulting from each of the phase corrections. The bottom row illustrates the difference between the full resolution output spectrum and the original input spectrum. There is a trade-off between the quality of phase removal and the spectral resolution.

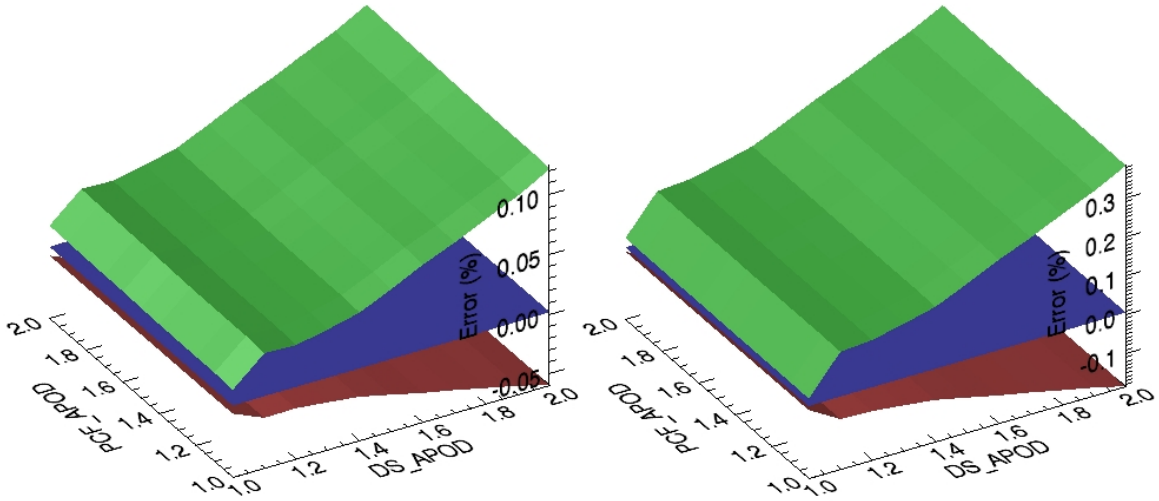

Figure 5.5: Error in line amplitude (red), width (green), and area (blue) as a function of double-sided interferogram and PCF apodization for both wide-band (left) and narrow-band (right), 10 point resolved, spectral input.

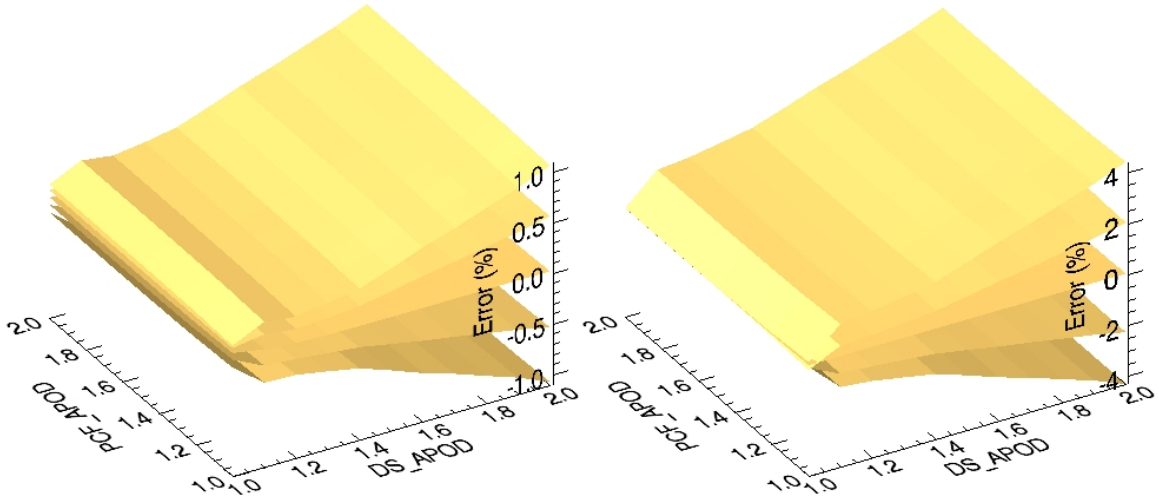

Figure 5.6: Line centre error vs. apodizations; shown for wide-band, 10 point resolved, spectral input, 256 pt. interferogram (left) and 128 pt. interferogram (right). Surfaces shown represent lines centred at 42.5, 38.75, 35, 31.25, and 27.5 cm^{-1} from top to bottom (see figure 5.2). With all other parameters equal, errors are smaller for the higher phase resolution (left). Spectral background plays a role in line centre error as all lines shown are identical with the exception of background profile.

of an interferogram. A quadratic phase fit will require a minimum of three in-band phase measurements. For a 50 % band, the double-sided interferogram must then be at least 12 points in order to provide sufficient phase resolution. A third order polynomial will require four phase measurements, etc. The phase resolution requirement must be met in order for the double-sided spectrum to provide an accurate measure of the phase.

- What apodization (if any) should be used on the double-sided interferogram?

  If S/N is high and the spectral features are resolved with the available L_{DS} then no double-sided apodization is necessary. This is not typically the case however.

  The required double-sided apodization is dependent on the nature of the spectrum under investigation. For unresolved double-sided spectral features given the L_{DS} available, the degree of double-sided apodization will necessarily depend on the degree of resolution required in order to resolve the spectral feature (i.e. an apodization broadening the line by a factor of 2 is required for a line of width $\frac{\Delta\sigma}{2}$).

- How should the phase be determined? (i.e. What type of phase fit/model should be used?)

  As Brault[78] has suggested, a functional or model fit is recommended. A model approach is recommended for a dual systematic/linear phase correction approach. For a single phase correction any modeled phase must have the ability to include a linear phase component. The degree of phase fit required depends on the phase response of the FTS instrument and support equipment/electronics.

- How long should the PCF convolution kernel be?

  The PCF kernel should be long enough to have minimal amplitude at the edges. As is shown in figure 5.4, a PCF kernel that is longer than necessary will reduce resolution more than required.

- What apodization (if any) should be used on the PCF?

  If it is not possible to have minimal amplitude edges to the PCF convolution kernel, then apodization is desirable. Significant apodization reduces the ability of the convolution to symmetrize the interferogram and thus residual phase errors are expected to be larger. If the functional/model fit to the phase was not performed then PCF apodization may also serve to reduce phase/PCF noise that would have been removed with a functional or model phase fit.

- How has the phase correction changed the properties of the spectrum?

  Ideally the phase correction has accounted for all phase and thus perfected the output spectrum. Due to errors in phase determination, phase fitting, and convolution, as well as sources of noise, residual phase errors may result. Spectral errors resulting from residual phase should be less than spectral errors resulting from no phase correction. The effect of residual phase on spectral parameters depends on the magnitude and structure of the residual phase itself (see section 4.9.2) For the underlying mathematics behind this analysis reader is referred to appendix F.

- How does the phase correction depend on the nature of the spectrum?

  The phase correction depends on the nature of the spectrum in several ways. Req-

uisite phase resolution, and consequently double-sided interferogram and PCF length as well as PCF apodization, is determined by the phase itself. The nature of the phase also determines the desired phase fit/model (e.g. polynomial, Chebyshev, etc.). Spectral feature resolution determines the required double-sided apodization. An understanding of the behaviour of the FTS instrument and source used for observations will improve phase correction accuracy.

5.5 Optimization for Herschel SPIRE CQM testing

The previous section included a general summary of phase correction optimization. In order to gain an estimate of the optimized data processing parameters required for the SPIRE CQM testing, a model of an expected spectrum was calculated. There is only one input spectrum used in this case, unlike the Gaussian minimization where there are $\sim 2^{10}$ input interferograms due to the generalized nature of the test case. The CQM model spectrum is illustrated in figure 3.14 and is introduced in section 3.7.2. This spectrum consists of a blackbody source at 1400 K, the non-linear beamsplitter phase (figure 3.6), atmospheric absorption for a 5m optical path (atmospheric conditions comparable to those at RAL), and the CQM/cryostat window/filter IR transmission profile. There are several spectral features over this band and each feature requires the amplitude, centre, width, and offset to be calculated in addition to continuum properties such as humidity, temperature, and pressure.

A fitting routine to fit all of the features across the entire band was constructed, yet the multivariable minimization required several minutes per spectrum. This minimiza-

tion processing time is not significant for a single spectral fit but becomes significant in developing error surfaces involving thousands of spectral minimizations. To illustrate the minimization of the spectral errors within a smaller processing time, the fitting routine is restricted to a narrow section of the band to minimize the number of spectral features requiring a best-fit. Since all of the spectral features have similar functional form (Lorentz dominated lineshape), the error minimization requirements should be similar across the band. Conveniently, the PLW band, (the band tested in the CQM test campaign) has only one spectral absorption feature (see figure 6.6). This feature has been isolated for the PLW minimization fit. The spectral fitting routine is composed of seven free parameters (line centre, temperature, pressure, self width, air width, line strength, and humidity). Other arrays of SPIRE (PMW, PSW, SLW, SSW) contain multiple absorption features and the spectral fitting routine required is significantly more complex and computationally intense as a result of this additional structure.

The number of unique combinations of processing steps possible in the CQM test case is slightly different than that in the Gaussian case as the lengths of the double-sided interferograms involved are different (and consequently the range in PCF lengths). There are approximately 2^{32} different unique combinations of processing parameters (25 (DS apodization) x 2000 (DS width) x 25 (PCF apodization) x 2000 (PCF width) x 2 (apodization symmetry)).

5.5.1 SPIRE optimization Results

There are five main choices required for the optimization of the phase correction involved with the SPIRE/CQM test campaign. The processing parameters needing opti-

mized are degree of phase fit, double-sided width and apodization, and PCF width and apodization.

Figure 5.7 illustrates the polynomial curve fitting to the TFTS phase. Although it appears that a 6th order polynomial is sufficient by examining the phase plots, the difference plot and error surface indicate a slight improvement with an 8th order polynomial. Figure 5.8 illustrates the line centre error with changing apodizations and degree of polynomial fit. Beyond a 10th order polynomial, the higher order polynomial terms affect the out of band phase significantly. The large amplitude of the out of band phase introduces artifacts into the PCF which then cause errors in the entire spectrum. The double-sided apodizations appear to have minimal effect because the double-sided interferogram resolution is sufficient to resolve the spectral feature, hence there are no sinc sidelobes present even without apodization.

Figure 5.9 illustrates various degrees of Chebyshev phase fitting to the TFTS phase. A 20th order or higher Chebyshev polynomial should be used for an accurate fit to the TFTS phase. The polynomial fit encounters problems with large amplitude out-of-band phase values as the polynomial degree increases. The Chebyshev fit does not encounter the same problem, as out-of-band phase is not handled by the Chebyshev fit and other methods are required to obtain an estimate for the out-of-band phase values to use in phase correction (see figure 5.12).

The absorption feature in the PLW array has a FWHM of ~ 0.4 cm^{-1} at the expected humidity for the CQM tests. In order for this feature to be resolved, a double-sided length (L_{DS}) of 1.47 cm (equation 4.1) is required. A FTS translation stage sampling

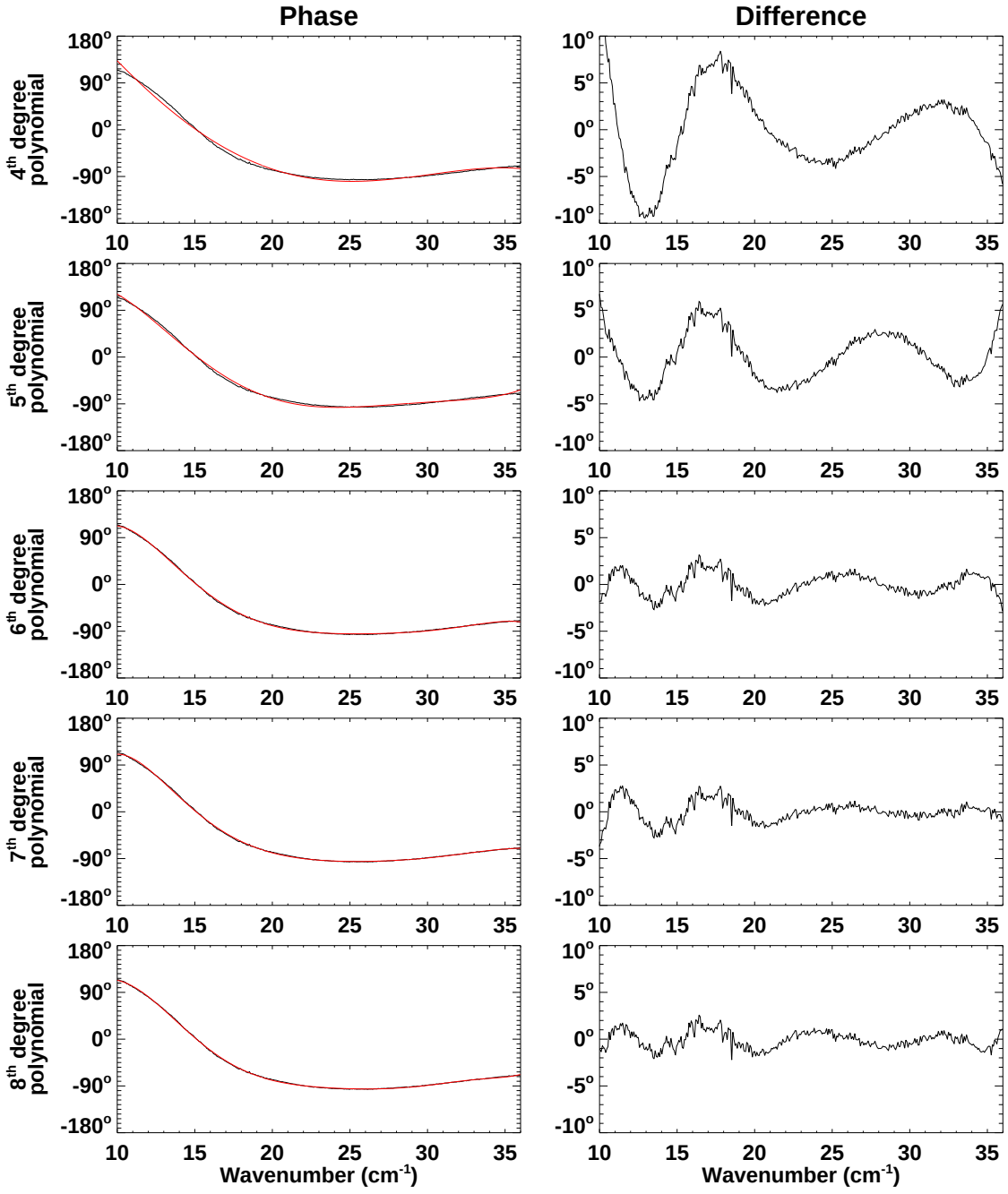

Figure 5.7: Varying degrees of polynomial fit used to determine minimum required polynomial fit of the TFTS non-linear phase. The spectral resolution of the phase is 0.0125 cm^{-1}.

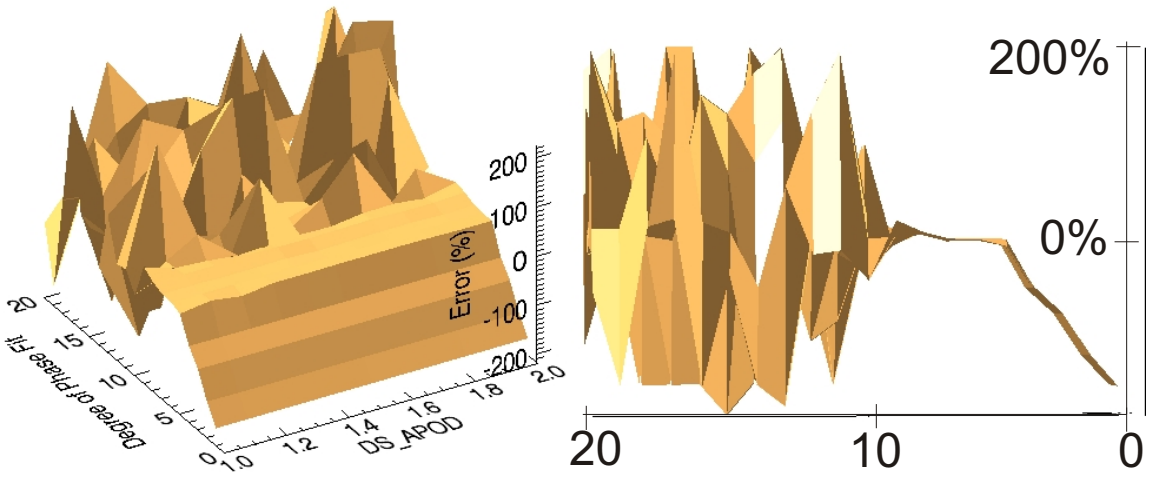

Figure 5.8: Line centre error vs. polynomial degree and double-sided interferogram apodization. Both images are different perspectives of the same surface. Errors are minimum for a polynomial of order 6-10. Polynomials of order greater than 10 have larger errors due to large amplitude out-of-band phase values (i.e. the polynomial fit only minimizes in-band errors) of the higher order terms, affecting the PCF convolution.

interval of 0.0050 cm_{opd} then dictates the required minimum of 586 points in the double sided interferogram in order to have the feature resolved. Figure 5.10 illustrates the double-sided interferograms of the model SPIRE CQM spectrum with double-sided widths of 256 and 1024 points[1]. The 256 point spectrum illustrates the ILS sidelobes characteristic of an unresolved spectral feature while the 1024 point spectrum feature is resolved. Figure 5.11 illustrates line centre error for changing double-sided width and apodization. Errors are significantly reduced once the double-sided width is sufficient for all of the spectral features to become resolved.

The PCF for the TFTS non-linear phase does not have zero-amplitude edges due to noise in the calibration measurements. The high amplitude central region of the PCF

[1]1024 points was selected rather than 586 in order to satisfy PCF length requirements and because it is a power of 2.

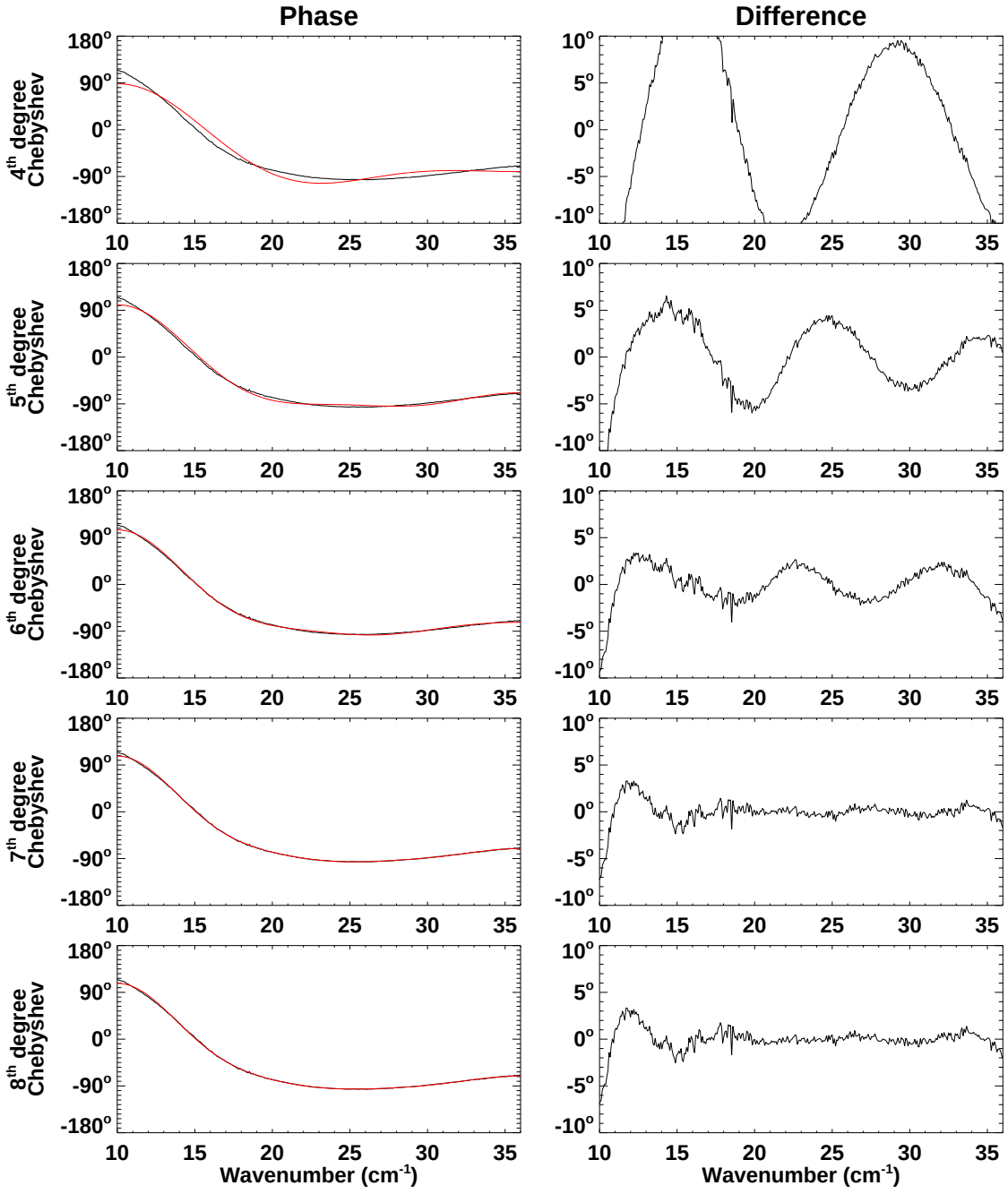

Figure 5.9: Varying degrees of Chebyshev fit used to determine required degree for phase fit of the TFTS non-linear phase. The spectral resolution of the phase is 0.0125 cm^{-1}.

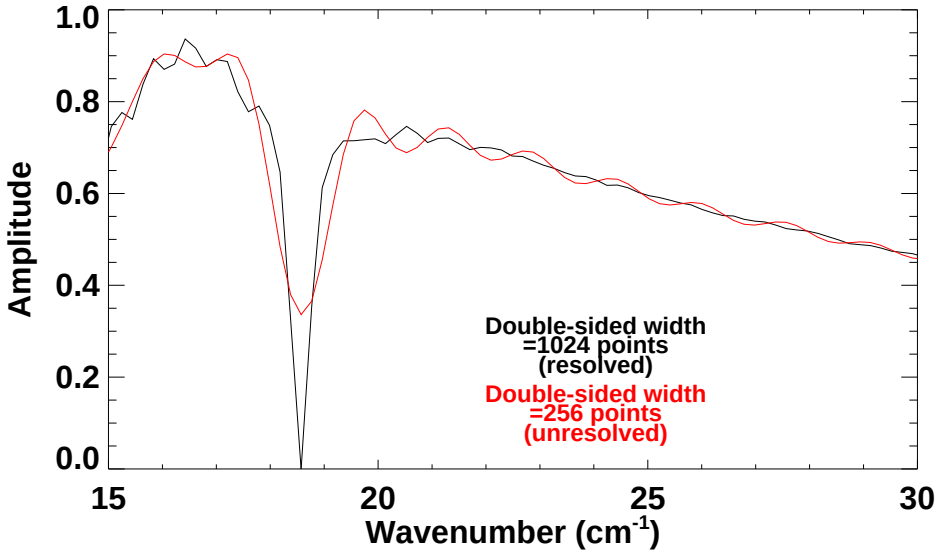

Figure 5.10: The SPIRE model uncorrected double-sided spectrum with a resolved (black) and unresolved (red) spectral feature. The unresolved spectrum results from a 256 point double-sided interferogram while the resolved spectrum results from a 1024 point double-sided interferogram. The spectral feature is an absorption line due to water vapour at 10% relative humidity.

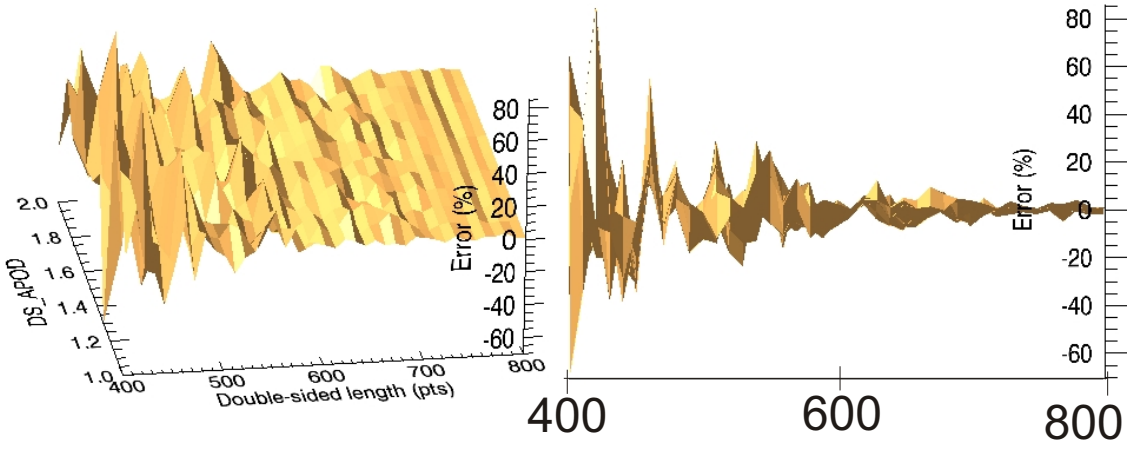

Figure 5.11: Line centre error vs. double-sided interferogram length and apodization for the PLW model spectrum. Both images are different perspectives of the same surface.

decreases to the noise floor approximately at the 2 cm_{opd} region of the PCF. This translates to a required PCF width of 800 points. The SPIRE PCF is shown in figure 5.12. Due to the nature of the phase itself, the PCF does not fall to zero amplitude at the edges. As a result of this, the choice of PCF width and PCF apodization in SPIRE FTS data processing is important. Some degree of apodization will be required in order to avoid the PCF convolution introducing discontinuities into the interferogram.

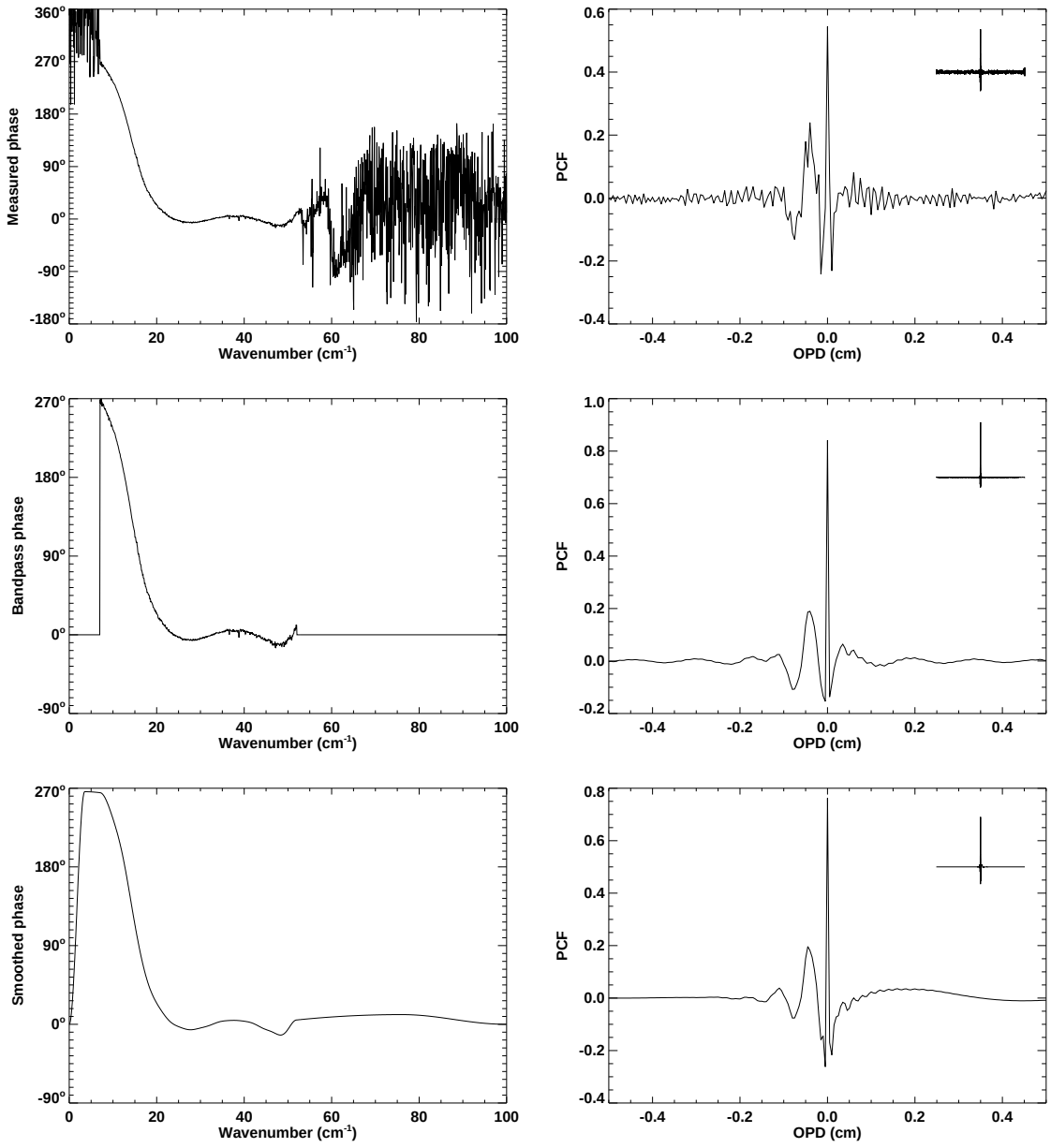

Figure 5.12: TFTS non-linear phase (left column) and the corresponding PCF (right column) as measured (top row), with out-of-band truncation/filtering (centre row), and with Chebyshev fit (bottom row). The Chebyshev fit data also incorporates smoothing in the out of band region to ensure zero phase and derivative discontinuities and zero amplitude at zero and Nyquist frequency. The PCF plots show the entire PCF in the upper right hand corner and the central region in the main window.

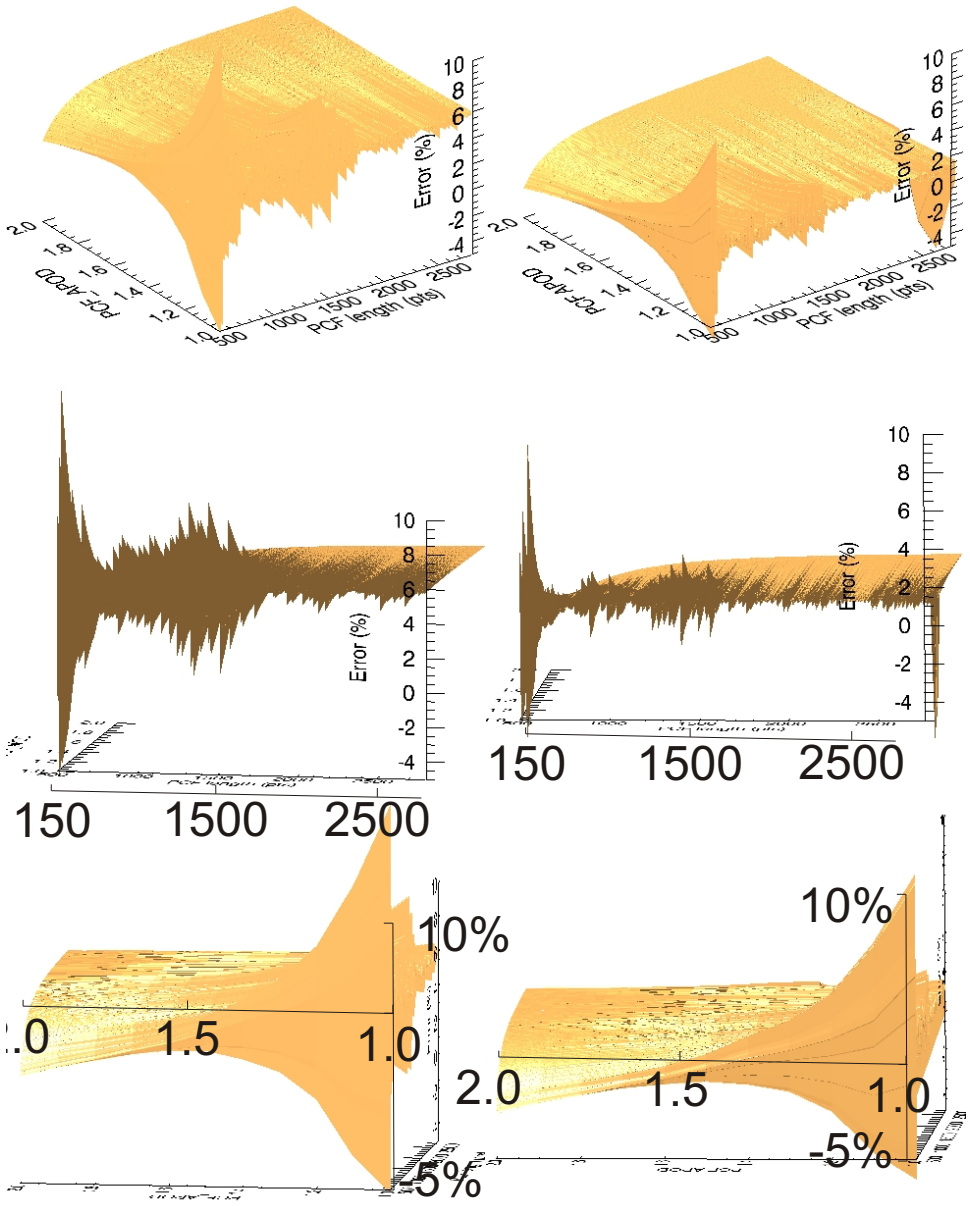

Figure 5.13: Line centre error vs. PCF length and apodization for the PLW band in the CQM model spectrum. The left column shows data for a polynomial phase fit of the 8th degree and the right column shows data for a Chebyshev phase fit of degree 20. Each column shows different perspectives of the same surface. The middle rows show error vs. PCF length. The bottom row shows error vs. PCF apodization. Shorter PCF lengths show greater error fluctuation with apodization, indicating that the PCF edge scaling is influencing the quality of the phase correction. As the PCF length is increased the PCF apodization has less of an effect on the error. The Chebyshev phase fit performs better than the polynomial fit.

5.6 Conclusions

A toolkit has been developed, written in IDL[3], to address the importance of various parameters in the phase correction process. The toolkit allows one to study the effects of length and apodization, as applied to both the interferogram and the PCF, on the retrieval of spectral line parameters. This toolkit may be customized for application specific FTS design or data processing pipeline development. It is proving to be useful as a tool to study the optimum parameters for phase correction in two iFTS projects (SPIRE[15] and SCUBA-2[27]). To a large measure the nature of the spectrum under investigation determines the optimum phase correction parameters.

As a result of the investigations discussed in this chapter, the following recommendations are suggested for phase correction optimization:

- Typically the required double-sided interferogram length is determined by the required phase resolution.
- Double-sided interferogram apodization is recommended if the double-sided spectrum contains unresolved features. The double-sided interferogram can be apodized without directly affecting the ILS of the one-sided spectrum.
- Non-linear phase is best corrected through instrument systematic phase calibration measurements.
- Non-linear calibration and linear phase correction can be performed synchronously, requiring only one convolution per interferogram.
- The length of the PCF convolution kernel should be sufficient to allow both edges to

approach zero. If this is not possible, PCF apodization should be employed to ensure limits of zero at the PCF edges.

- The residual phase (i.e. uncertainty in the phase measurement) can be determined through the double-sided spectrum uncertainty/noise.

- Optimal phase correction depends highly on the nature of the spectrum under study.

The TFTS phase calibration measurements greatly improved results over the individual interferogram non-linear phase fitting routines. With TFTS systematic phase calibration data used in parallel with linear phase correction, phase errors are removed from the spectrum allowing accurate spectral analysis as will be shown in chapter 6 through the TFTS verification testing.

Chapter 6

Test facility FTS for Herschel SPIRE instrument level testing

Contents

6.1 Overview

A test facility Fourier Transform Spectrometer (TFTS), with its broad spectral coverage and intermediate spectral resolution, was selected for the instrument-level testing and spectral characterization of SPIRE. The integration of the TFTS with the existing Ground Support Equipment of the Herschel/SPIRE test facility at the Rutherford Appleton Laboratory (RAL) imposed several mechanical, optical, electrical, and software constraints. This chapter describes the design and implementation of the TFTS. The TFTS will be used to evaluate spectral performance of the various models of the SPIRE instrument during development. In addition, it will continue to support ground based testing during the operational phase of the Herschel mission.

6.2 Introduction

Whilst the SPIRE instrument was being tested at an assembly integration verification (AIV) facility at RAL, a need was identified for a far Infrared (FIR) FTS. As the need for the TFTS was not addressed until after the AIV facility at RAL was already in place; restrictions were imposed upon the spectrometer design. Dr Naylor's astronomical instrumentation group (AIG) group at the University of Lethbridge was tasked to carry out the design, manufacture, assembly, testing and support of the SPIRE TFTS and associated control software for use during SPIRE calibration tests. This, combined with software and personnel contributions, is one of the chief Canadian contributions to ESA's Herschel mission. Delivery of the TFTS to the SPIRE test facility at RAL, Oxfordshire, UK, was time critical as it was required for the characterization of the SPIRE filters and bolometers. The

Figure 6.1: A picture of the TFTS during verification testing. The beamsplitter shown is used for optical alignment. A diagram of the TFTS with components labeled is shown in figure 6.2. The image is courtesy of the AIG.

TFTS was delivered fully functional and on schedule in the summer of 2003. Figure 6.1 is a picture of the TFTS during verification testing shortly before it was shipped to RAL.

6.3 TFTS design

Several performance requirements influenced the TFTS design. The baseline requirement of the TFTS is that it provide a resolution of 0.5 cm^{-1} (i.e., a resolving power greater than 1000 at 200 μm) and fit within tight mass and volume constraints. The goal was to produce the highest possible resolution within these constraints. These requirements fall into mechanical, optical, electrical, and software categories. Each of these categories is discussed in detail in this section.

6.3.1 Mechanical design

Figure 6.3 shows the SPIRE test facility layout. In addition to the bulky SPIRE cryostat, the laboratory includes a telescope simulator, molecular laser, and blackbody calibration source; all mounted on several large optical tables. Due to the TFTS's location near the edge of a large optical bench there were mass and volume constraints. The TFTS also needed to be in an enclosed space to allow humidity control in the beampath. The TFTS outline is shown in figure 6.2 and makes very efficient use of the space available.

6.3.2 Optical design

In order to test the SPIRE instrument it is necessary to simulate a beam identical to that provided by the Herschel telescope. This was accomplished by a telescope simulator constructed from four mirrors (three flat, one powered), three of which are motorized. These mirrors are significantly smaller than the Herschel primary mirror which is simulated (∼30 cm vs. 3.5m diameter). A point source located at the input of the telescope simulator can be focused on any detector by adjusting the motorized mirrors in such a way as to simulate the curved field of the Herschel telescope. The pupil mask, with image located 2.64 m from the SPIRE focal plane, reproduces the F/8.68 beam required by SPIRE. Thus any of the SPIRE bolometers can be illuminated by a point source similar to that provided by the Herschel telescope optics. The telescope simulator design is discussed in greater detail in Collins *et al*, 2003[21]. A block diagram of the SPIRE test facility including the telescope simulator is shown in figure 6.3, and a picture of the telescope simulator aligned with the TFTS is shown in figure 6.4.

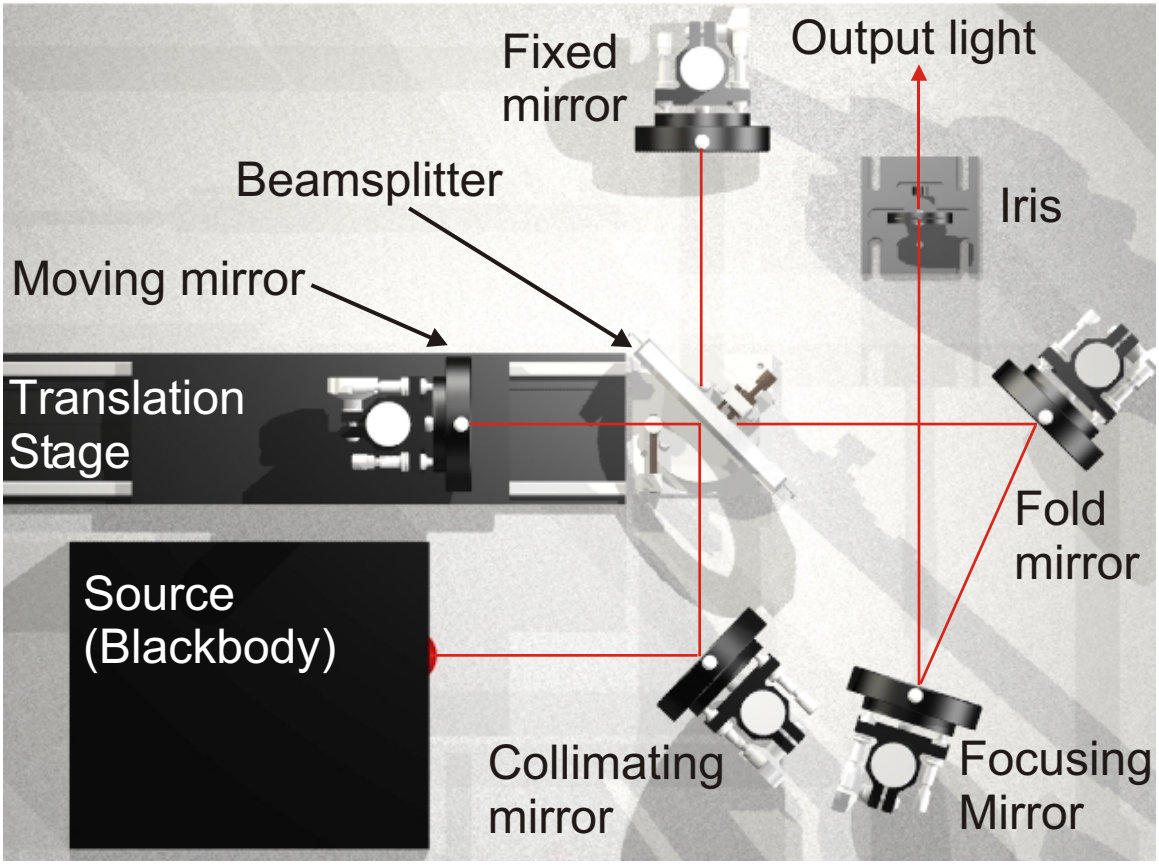

Figure 6.2: Herschel SPIRE qualification TFTS with Blackbody radiation source. The TFTS is in a sealed enclosure to allow humidity control. Dimensions are 1m x 0.75 m. Image courtesy of the AIG.

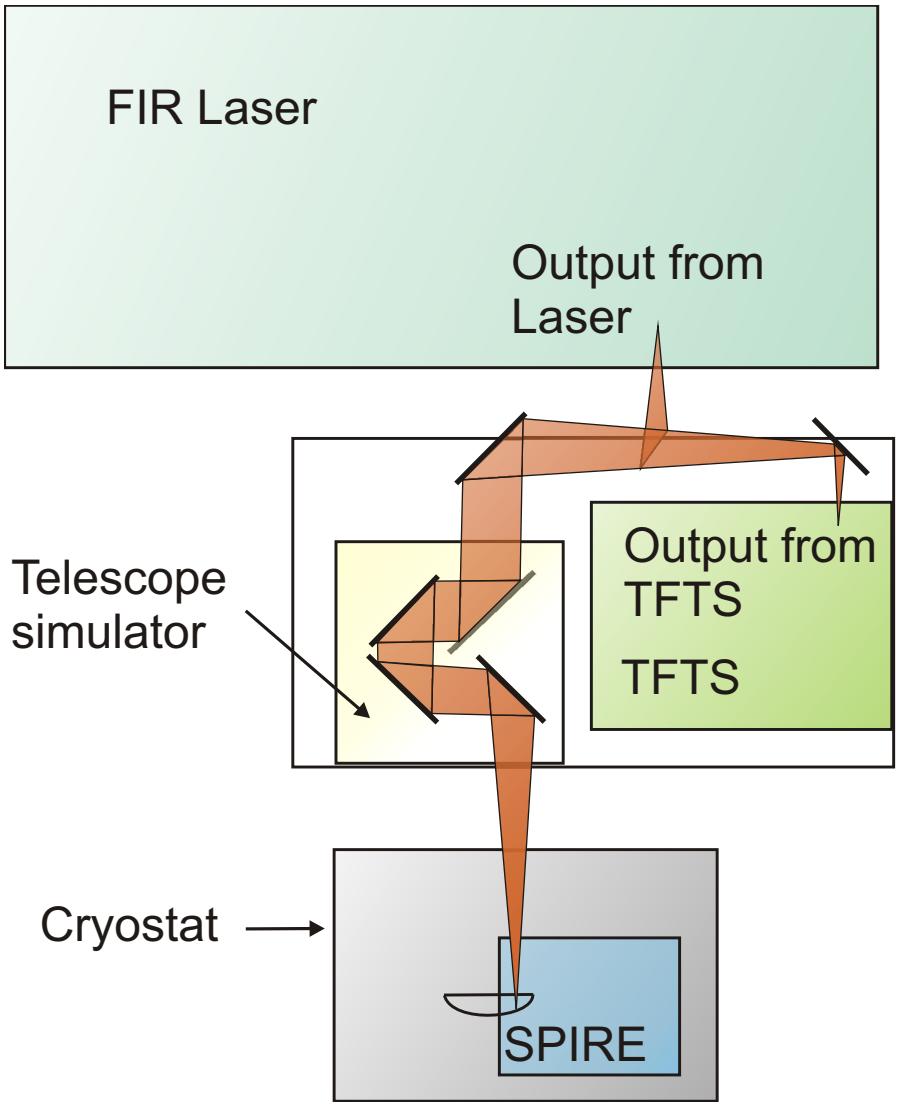

Figure 6.3: Herschel SPIRE AIV facility equipment diagram including TFTS. The optical path between the TFTS output port and the cryostat window are also in a sealed enclosure, which is pressurized with nitrogen gas and dry air to allow for humidity control. Optical input to the cryostat is toggled between the TFTS and the FIR laser by use of a flip-mount mirror. The area shown is approximately 3.5m x 4m.

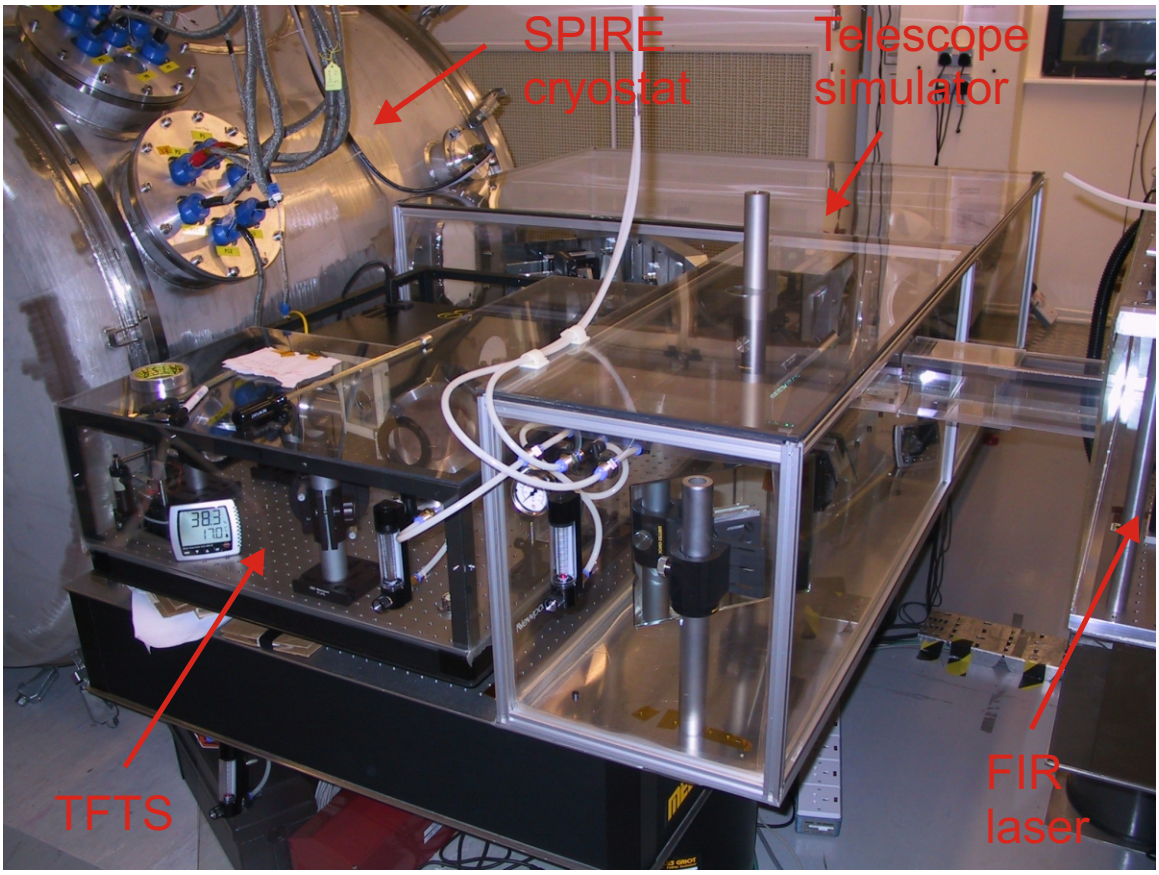

Figure 6.4: A picture of the SPIRE cryostat (back left) with the telescope simulator (back) and TFTS (front). The FIR laser is just to the right of the picture. Note that the humidity meter inside the TFTS enclosure reads 38 %. During normal operation the TFTS humidity is reduced to increase source transmission. Image courtesy of the Space Science Technology Dept. at RAL.

As shown in figure 6.2, the TFTS provides the telescope simulator with an F/8.68 beam by a series of powered mirrors. The blackbody source is located at the focus of an F/2.33 collimating mirror (off-axis parabolic, focal length 17.48 cm). The collimated beam enters the interferometer where it encounters the beamsplitter, and fixed and moving mirrors. The beam exits the interferometer and, after reflection off a plane mirror, is brought to a focus by an F/8 mirror (focal length 60 cm) which feeds the telescope simulator. An iris that is located at this focus provides a field stop for the radiation that is modulated by the interferometer. The use of an off-axis parabola, fold, and focal expansion mirrors makes the most of the limited surface area of the optical table.

The TFTS employs a broadband, high-efficiency, intensity beamsplitter[22] similar to that used in SPIRE[1]. Throughput is a factor of 2 higher than it would be for the traditional polarizing beam dividers as there is no sensitivity to the polarization of the incident radiation. Another feature of the TFTS is the beamsplitter mount, which allows for rapid beamsplitter exchange while preserving the alignment. During initial setup a thin Mylar beamsplitter is used for visible alignment of the interferometer itself, and also of the interferometer with the telescope simulator. The optical alignment of the TFTS and telescope simulator requires the alignment of fourteen optical components, a task made significantly easier working in the visible range.

6.3.3 Electronics design

For the TFTS/SPIRE system, the interferogram signal is recorded as a function of time, $I(t)$, and the time of the regular optical path difference intervals, $t'(z)$, is recorded

[1]The TFTS beamsplitter is an original version of the SPIRE beamsplitter.

independently. This is necessary as the TFTS uses the SPIRE optical detectors to measure interferograms while the TFTS translation stage is, by necessity, isolated from SPIRE. By combining $I(t)$ and $t'(z)$ it is possible to reconstruct $I(z)$ (spatial domain) and hence retrieve the spectrum, $B(\sigma)$ (spectral domain) using equation 2.29. The TFTS employs a precision linear motion translation stage which eliminates pitch and yaw errors associated with lead-screw type stages. The stage also provides positional information at the level of ± 10 nm by means of a non-contact linear encoder[94, 95] and multiplier option (AEROTECH model ALS135-200). The encoder position synchronized output signal (PSO) triggers time capture on the digital processing unit (DPU) electronics, whereby the time stamp is stored in a 64-slot, 32 bit FIFO.

The TFTS was designed primarily for a rapid-scan mode, in which the times at which the stage advances equal intervals of optical retardation are recorded, $t'(z)$, while the mirror scans at a constant velocity either towards or away from the beamsplitter (up and down scans, respectively). A counter which increments at the DPU clock frequency of 312.5 KHz, and is synchronized with the SPIRE instrument, is needed to allow for accurate interpolation.

$$\begin{matrix} I(t) \\ \\ t'(z) \end{matrix} \Rightarrow I(z) \tag{6.1}$$

Equation 6.1 illustrates the interpolation of the time sampled interferogram signal, $I(t)$, and the position sampled optical retardation times, $t'(z)$, to yield the interferogram, $I(z)$. The DPU clock signal is part of the SPIRE electronics. We were not allowed direct access to the clock signal and had to design a breakout box (see figure 6.5) in order to

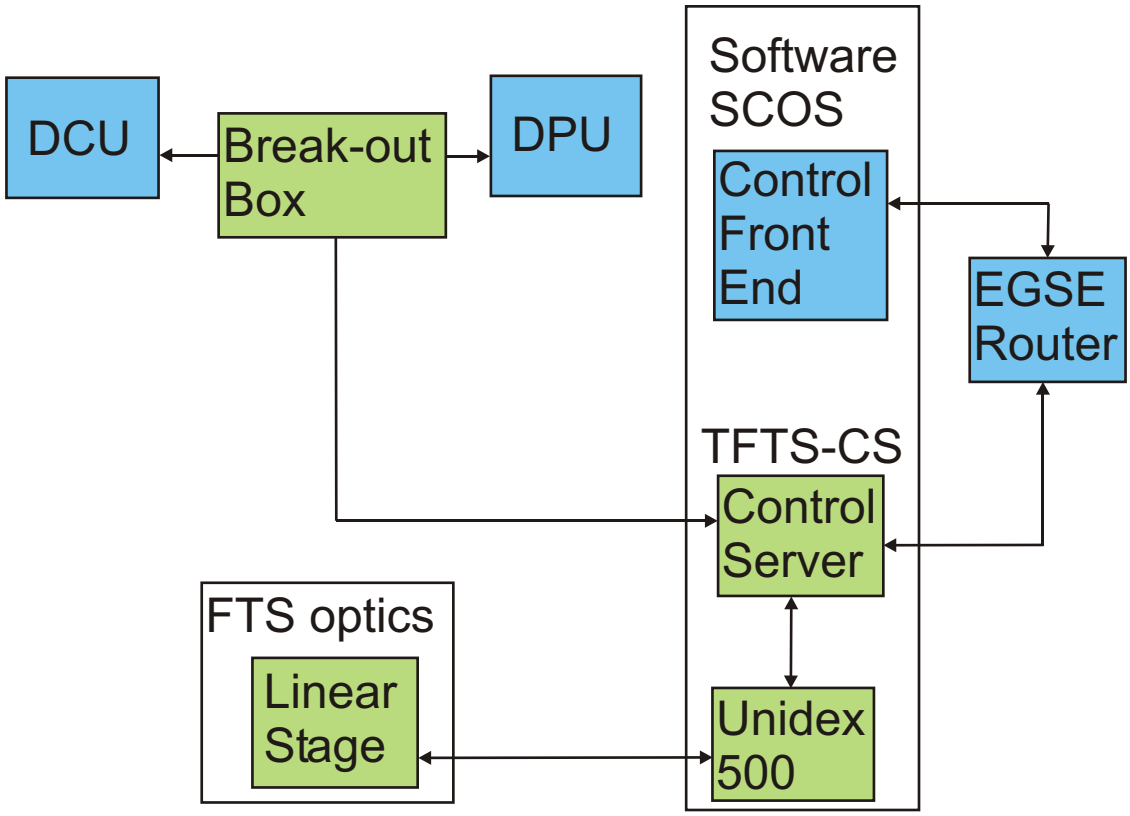

Figure 6.5: Block diagram outlining link between the TFTS, TFTS-CS, and SPIRE through the breakout box. The green boxes are part of the TFTS subsystem while the blue boxes are part SPIRE hardware and software subsystems, connecting the TFTS to SPIRE.

gain access to the clock signal. The breakout box provides an interface between the SPIRE detector control unit (DCU) and the DPU clock. The SPIRE and TFTS sections of the breakout box are electrically isolated from one another to ensure that malfunctions in the TFTS cannot adversely affect the SPIRE instrument.

In addition to the DPU clock pulses, the breakout box also recognizes global electronics resets which allow the two clock counters , t and t' (i.e. the bolometer readout clock counter and the TFTS stage clock counter) to be synchronized to within 100 ns, well below the packet time uncertainty for the bolometer readout of 1 μs[96].

The time synchronization provided by the breakout box should allow the TFTS to return the same ZPD position value independent of scan direction (i.e. towards and away from the beamsplitter). Section 6.7 shows that preliminary data analysis indicated that the ZPD location reported for both scan directions was not the same. The difference between up and down scan ZPD's is equivalent to an 80 ms time delay between reported bolometer signal values and stage position values. The cause of this difference has been identified and the exercise served as a useful check to ensure that the synchronization between the time sampled SPIRE bolometer signal and the TFTS stage position time was functioning correctly.

6.3.4 Software

The TFTS-CS is a Windows 2000 based network server application that configures, controls, and collects data from the TFTS. Communication via an Ethernet-based local area network (LAN) uses ESA's electrical ground support equipment (EGSE) data packet protocol. The TFTS-CS accepts instruction packets, executes the instructions con-

Parameter	Typical	Range
Input F Number	F/2.33	N/A
Output F number	F/8.68	N/A
Resolution	0.0125 cm^{-1}	0.0125 - 0.25 cm^{-1}
Physical Dimensions	1m x 0.75m x 0.3m	N/A
Nyquist Frequency[a,b]	100 cm^{-1}	10 - 50000 cm^{-1}
Mirror velocity	0.5 mm/s	0.01 - 5 mm/s
TFTS enclosure humidity[c]	6 %	1 - 30%
Blackbody Temperatures	1200^{o}C	150 - 1300^{o}C
Mass	∼100 kg	N/A

[a] see equation 2.41

[b] Depending on the detector used, the TFTS does not have a dedicated optical detector as it is designed to use the SPIRE detectors. The reported range is based on the translation stage capabilities assuming that the detector is not a limiting factor.

[c] with configuration at RAL at the time of CQM testing, the dry air enclosure setup has since been improved to allow humidities of ∼1%

Table 6.1: Summary of SPIRE Test FTS Capabilities

tained in the packets, and returns data packets if applicable. The software is event driven, and multi-threaded, to perform background operations simultaneously - such as scanning and housekeeping packet broadcasting. Specifically, separate threads of execution handle regular transmission of housekeeping packets as well as performing long-duration functions such as scans and table motion. Inter-thread communication is implemented with global variables, protected by critical section functions. Network activity, or button presses, trigger the TFTS-CS. Critical interfaces for the TFTS-CS are shown in figure 6.5 and include: EGSE router, spacecraft operating system (SCOS), and DPU counter electronics, all linked together through the breakout box, and external hardware specific to the TFTS which is responsible for the position and time capture.

Since there are 5 different arrays of detectors to be evaluated and characterized, the TFTS has been designed for flexibility. Variable scan speed, sampling rate, and maximum optical path difference enable a wide variety of spectral observation parameters (see table 7.1).

6.4 Test facility atmosphere

Significant obstacles to CQM testing are the atmospheric conditions outside of the cryostat. The chief obstacle caused by the atmosphere is the opacity in the SPIRE spectral band due to atmospheric water vapor. Figure 6.6 shows the atmospheric transmission of both the photometer (PLW, PMW, PSW) and spectrometer (SLW, SSW) bands for a 5m path at various relative humidities under laboratory conditions. This atmospheric model was generated by a radiative transfer model developed at the University of Lethbridge by one of Dr. Naylor's former graduate students[97]. Only the PLW array was available for CQM testing. The atmospheric transmission across the PLW band has fairly low opacity with a strong water absorption line at 18.578 cm^{-1}. This absorption line is useful for intensity and wavelength calibration. The high transmission region between 19 and 24 cm^{-1} provides higher signal-to-noise data which in turn allows reliable broadband phase correction. The PLW array is therefore seen to be a good choice for CQM testing because of these simple atmospheric properties. Figure 6.6 also illustrates the greater atmospheric opacity for wavenumbers above 36 cm^{-1}. Serious attempts at purging the atmospheric water vapour from the beampath will be required to reduce opacity to an acceptable level for CQM testing of the short wavelength arrays.

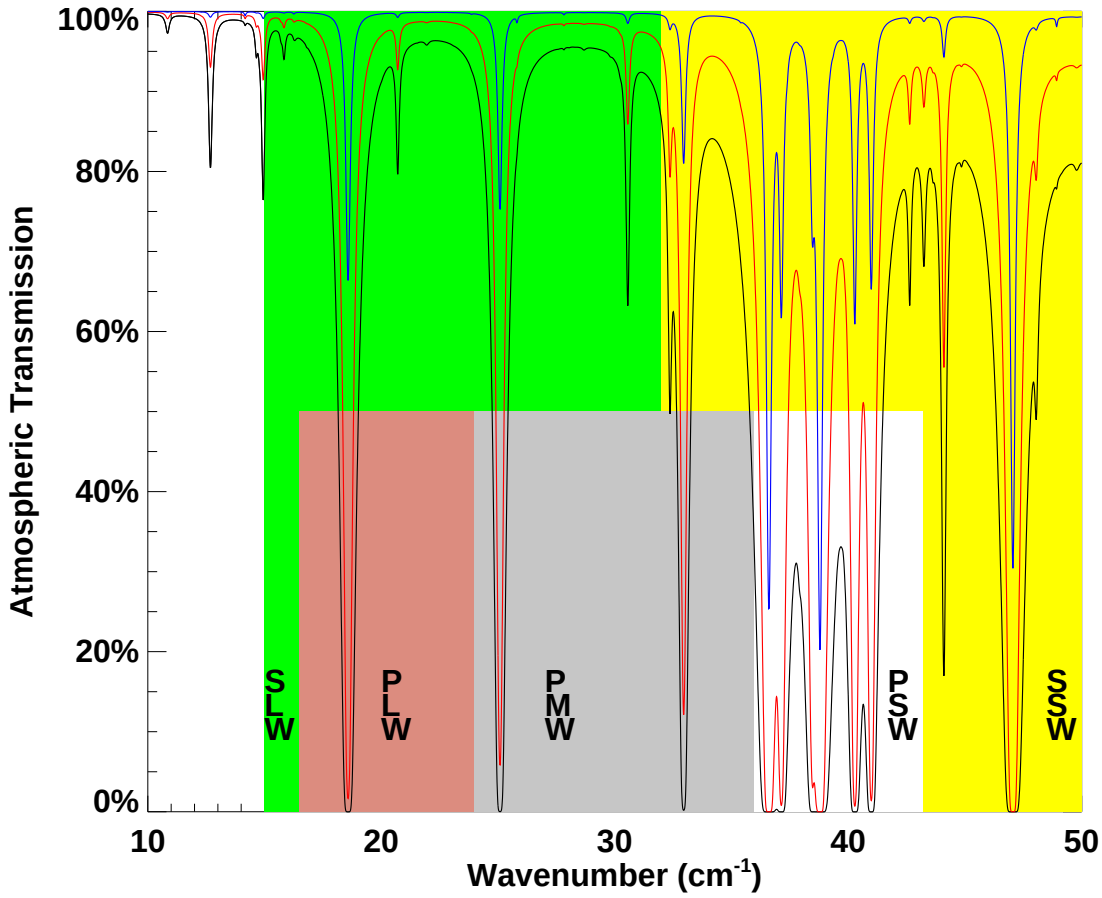

Figure 6.6: Atmospheric transmission at 17^{o}C and various relative humidities for the TFTS beampath of 5.0 m[97]. This table illustrates the difficulty in observing some of the SPIRE bands due to the humidity in the test facility environment, e.g. the PSW and SSW bands. Humidities shown are (top to bottom) 1%, 10%, and 30%. 30% is easily achieved, 10% is a challenge, and 1% is very difficult to achieve with the equipment configuration at the time of CQM testing. Changes have since allowed greater ease in beampath humidity reduction.

A dry air enclosure was built to surround the TFTS and dry nitrogen gas was pumped through the system to reduce the humidity. Another dry air enclosure was built around the telescope simulator for the same reason. The variety of tests within CQM test campaign required opening the enclosures periodically, so two separate enclosures minimize the increase in humidity while necessary equipment adjustments are performed. The enclosures are visible in figures 6.1 and 6.4.

6.5 TFTS phase

Preliminary data processing and analysis of TFTS verification data, including linear phase correction, revealed a need for non-linear phase correction as described in chapters 3 & 4. Equation 3.16 proposed that the phase calculated from an FTS interferogram may be expressed in terms of DC, linear, non-linear, and random components. It is further proposed that the TFTS phase function may be represented as a linear combination of three physical components: a component due to mis-sampling the position of ZPD, a systematic contribution due to the TFTS beamsplitter and a random contribution from other sources (e.g. noise, readout electronics). The overall measured phase can therefore be expressed as follows:

$$\phi(\sigma) = \phi_{\mathrm{Lin}}(\sigma) + \phi_{\mathrm{BS}}(\sigma) + \phi_{\mathrm{other}}(\sigma), \tag{6.2}$$

where:

- ϕ_{Lin} is the phase term arising from ZPD mis-sampling (see section 3.5.2),
- ϕ_{BS} is the contribution due to the beamsplitter,

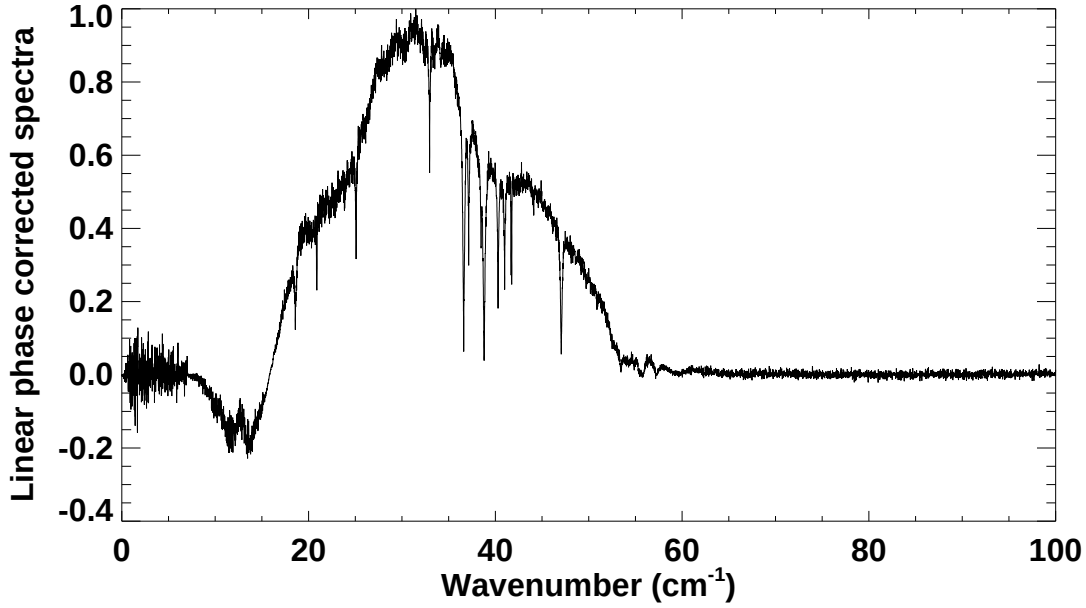

Figure 6.7: Spectrum resulting from the co-addition of 2216 linear phase corrected spectra from TFTS verification testing (see section 6.6). The spectrum shows a blackbody emission source at 800^oC and absorption lines from the TFTS beampath. The presence of non-physical negative intensities in the spectrum show that a residual phase errors exists. The phase corrected spectrum of the data shown here is found in figure 6.12.

- and ϕ_{other} is the contribution due to all other sources (dispersive optics, electronics, etc.).

While mis-sampling ZPD can contribute to the linear term, it is clear that only the beam-splitter contributes to the non-linear phase. Figure 6.7 illustrates co-averaged TFTS spectra with only linear phase correction.

For a signal contaminated by random noise (with S/N= S/N_1), averaging N such signals will improve the overall S/N as follows:

$$S/N_N = (S/N_1) \times \sqrt{N}. \tag{6.3}$$

The spectral phase is determined from the double-sided portion of the interferogram. Thus, averaging interferograms together should reduce the noise and hence decrease the uncertainty of the calculated TFTS phase. Since the linear phase error in each interferogram is not necessarily constant, directly averaging interferograms with a linear phase error will not be accurate. Figure 6.8 illustrates the double-sided phase resulting from the co-addition of 2216 linear phase corrected interferograms measured with the TFTS under similar conditions. As the phase is calculated by the arctangent of the spectrum, there is potential for discontinuous jumps of $\pm 2\pi$ (rad) in the phase. Originally, such a discontinuity was present in the data shown in figure 6.8 (near $\sigma = 13$ cm^{-1}), which is easily solved by the addition of the appropriate integer multiple of 2π radians to regions of the phase spectrum. Correction of phase discontinuity due to $\pm 2\pi$ rollover is difficult for low S/N as the actual point of discontinuity becomes more difficult to determine. Thus, it is preferred to average several interferograms and correct a rollover once rather than to correct several rollovers and then average phase because of the $\sqrt{N}$ reduction in noise.

After the TFTS was delivered to RAL, more scans were measured with a different detector to verify instrument design and performance. Similar interferogram averaging[98] revealed that the nonlinear phase was still present even with a different detector. The TFTS phase determined through the RAL TFTS verification tests is shown in figure 3.6.

The phase determined through measurements made at RAL differs from the Lethbridge measured phase by a linear component only. The linearity of the differences between the RAL and U of L phase functions, and the fact that the only element likely to lead to dispersion was the beamsplitter, provided compelling evidence that the observed systematic

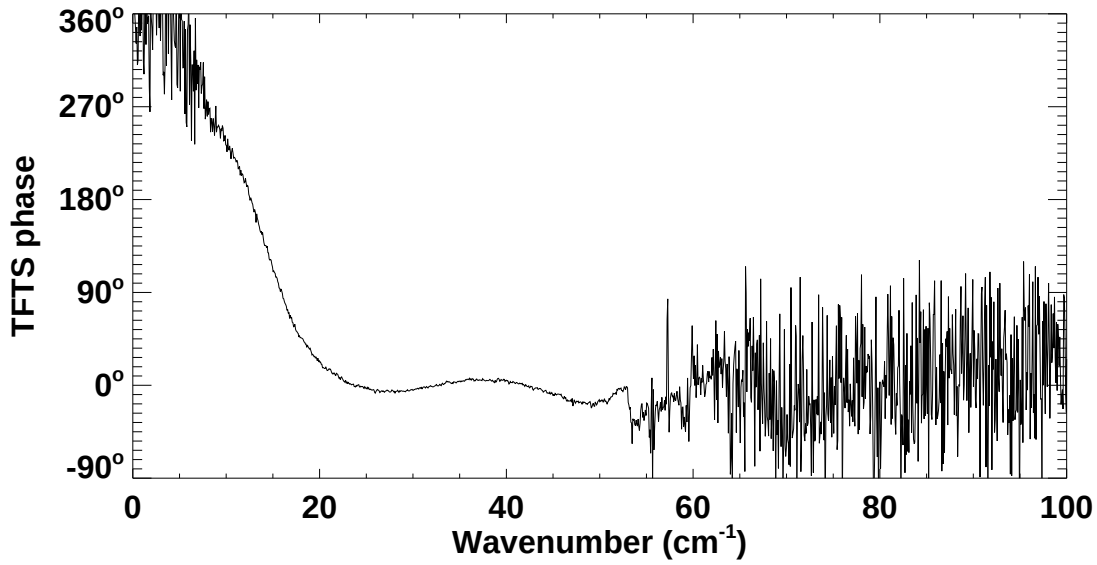

Figure 6.8: Non-linear phase of the TFTS beamsplitter as measured through TFTS verification testing in Lethbridge.

nonlinear phase was due to the beamsplitter.

The TFTS phase is useful in data processing to perform a systematic phase correction (see section 4.5) on all TFTS interferograms. The required double-sided interferogram length for each TFTS interferogram is dramatically reduced by the availability of the calibration data. Each interferogram will still need a linear phase correction, which can be performed in parallel with the systematic phase correction, but this requires very little phase resolution (i.e. double-sided interferogram length).

6.6 HCl gas cell

In order to verify the resolving power of the TFTS, a 22 cm long gas cell was filled with HCl at a pressure of $\sim$5 torr. The cell was placed between the TFTS output

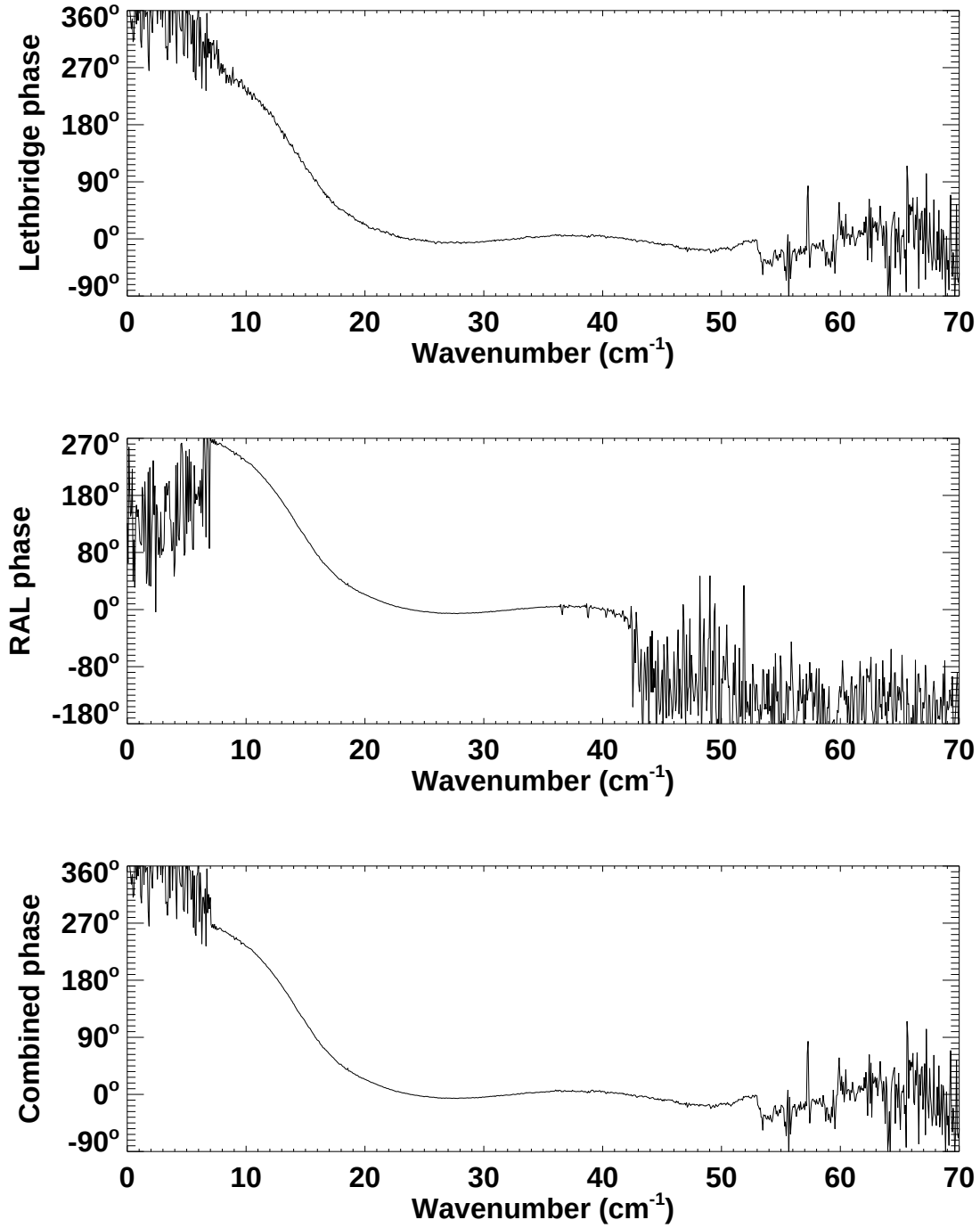

Figure 6.9: Both Lethbridge and RAL TFTS verification phase measurements combine to cover the entire SPIRE spectral band. The high frequency noise in the central figure (RAL measurement) is not centred about zero because of the need to remove the linear phase component from this measurement. This does not affect the averaging as no out of band data from this measurement is used.

and detector (see figure 6.10) and used to observe the absorption of two in-band rotational doublets. From the jet propulsion laboratory (JPL) molecular spectroscopy catalogue[99], the doublets are located at 20.87783 cm^{-1} and 20.84657 cm^{-1} (separation of 0.03126 cm^{-1}), and at 41.74434 cm^{-1} and 41.68157 cm^{-1} (separation of 0.06277 cm^{-1})[100]. Separation of the doublet lines corresponds to resolving powers greater than 665. Figure 6.10 illustrates the TFTS configuration used with the HCl gas cell in the beampath.

6.6.1 Molecular rotational spectroscopy

Rotational energy (E_{rot}) is related to the moment of inertia (I) as follows:

$$E_{rot} = \frac{1}{2} I \omega^2, \tag{6.4}$$

where ω is the angular velocity about the centre of mass. I and ω are related by the angular momentum (P) as follows:

$$P = I\omega. \tag{6.5}$$

For rotation in three dimensions, rotational energy can be expressed in two ways:

$$\begin{aligned} E_{rot} &= \frac{1}{2} I_x \omega_x^2 + \frac{1}{2} I_y \omega_y^2 + \frac{1}{2} I_z \omega_z^2, \\ \text{or} \quad &= \frac{1}{2}\left(\frac{P_x^2}{I_x}\right) + \frac{1}{2}\left(\frac{P_y^2}{I_y}\right) + \frac{1}{2}\left(\frac{P_z^2}{I_z}\right), \end{aligned} \tag{6.6}$$

where x, y, and z are orthogonal to each other. The components of I are given by:

$$I_x = \sum_i m_i (y_i^2 + z_i^2), \quad I_y = \sum_i m_i (x_i^2 + z_i^2), \quad I_z = \sum_i m_i (x_i^2 + y_i^2), \tag{6.7}$$

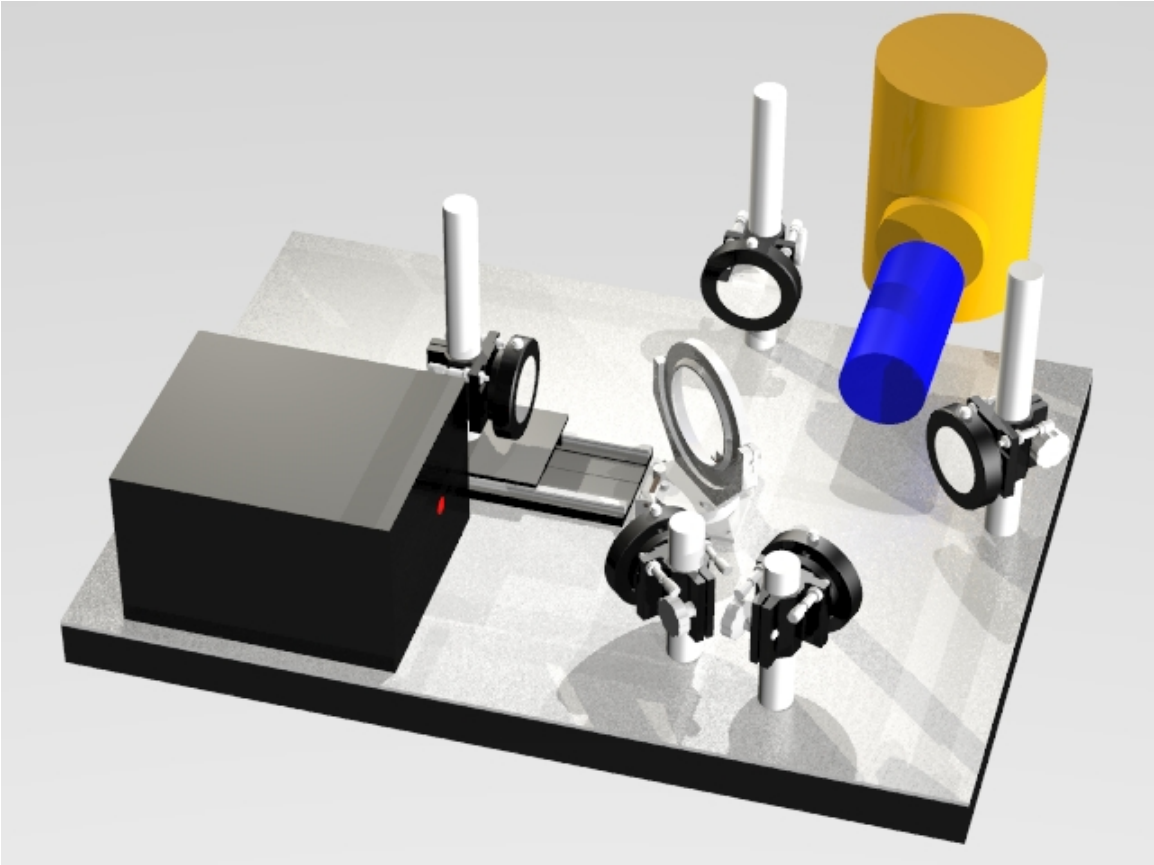

Figure 6.10: The TFTS with an HCl gas cell in the optical path. The HCl gas cell (∼5 torr HCl) was used to observe the absorption of the first two pure rotational transitions of HCl. The presence of both ^{35}Cl and ^{37}Cl isotopes causes a doublet to be observed for each rotational transition. The gas cell (blue), and detector (gold) are shown in addition to the other components labeled in figure 6.2. Image template courtesy of B. Gom.

where the origin is taken to be the centre of mass of the molecule. The m_i's are the masses of the individual atoms making up the molecule. The components of P are given by:

$$\begin{aligned} P_x &= \sum_i I_{x_i}\omega_{x_i} \\ &= \sum_i m_i(y_i^2+z_i^2)(\sqrt{\frac{v_{y_i}^2+v_{z_i}^2}{y_i^2+z_i^2}}) \\ &= \sum_i m_i\sqrt{(y_i^2+z_i^2)(v_{y_i}^2+v_{z_i}^2)}, \qquad (6.8) \\ P_y &= \sum_i m_i\sqrt{(x_i^2+z_i^2)(v_{x_i}^2+v_{z_i}^2)}, \\ P_z &= \sum_i m_i\sqrt{(x_i^2+y_i^2)(v_{x_i}^2+v_{y_i}^2)}, \end{aligned}$$

where components of velocity are represented by the v's. The total angular momentum can be expressed as:

$$P^2 = P_x^2 + P_y^2 + P_z^2. \qquad (6.9)$$

The HCl molecule is diatomic and can be approximated as a rigid rotor for low energy rotational transitions. With no unbalanced electronic angular momentum (Σ state[101]) and no nuclear coupling, the angular momentum arises wholly from end-over-end rotation[102]. For diatomic molecules in the $^1\Sigma$ state, the moment of inertia about the molecular bond axis is zero (i.e. $I_z = 0$), and equal for the moments of inertia for rotation in the plane orthogonal to the bond axis (i.e. $I_x = I_y = I$). The moment of inertia for rotation about the centre of mass in the plane orthogonal to the bond axis in a diatomic molecule is given in terms of the reduced mass (μ):

$$I = \mu R_o^2, \qquad (6.10)$$

where R_o is the separation between the two atoms along the bond axis, and the reduced

mass is given by[103]:

$$\mu = \frac{m_1 m_2}{m_1 + m_2}. \tag{6.11}$$

The Hamiltonian, $\mathcal{H}$, for the rigid rotor is expressed as:

$$\mathcal{H} = \frac{1}{2I}(P_x^2 + P_y^2) = \frac{P^2}{2I}. \tag{6.12}$$

Switching from the classical to the quantum domain, with the classical variables becoming quantum operators, it can be shown that P_z and P^2 have common eigenfunctions[104]:

$$P^2|J,M\rangle = \hbar^2 J(J+1)|J,M\rangle, \tag{6.13}$$

$$P_z|J,M\rangle = \hbar M|J,M\rangle, \tag{6.14}$$

where J and M are the rotational and magnetic quantum eigenvalues, respectively. It can be shown that the eigenvalues of J are integers such that $J = 0, 1, 2, \ldots$ and the eigenvalues of M are also integers such that $M = -J, -J+1, \ldots, J-1, J$. Selection rules for pure rotational energy level transitions require that $\Delta J = \pm 1$ and $\Delta M = 0$[102]. The rotational energy levels can be determined using the Hamiltonian operator ($\mathcal{H}$):

$$\begin{aligned} E_J &= \int \psi_{JM}^* \mathcal{H} \psi_{JM} d\tau \\ &= \langle J,M|\mathcal{H}|J,M\rangle \\ &= \frac{1}{2I}\langle J,M|P^2|J,M\rangle \\ &= \frac{1}{2I}\hbar^2 J(J+1), \end{aligned} \tag{6.15}$$

where the eigenfunctions (ψ_{JM} or $|J,M\rangle$) have been normalized. Thus the energy of absorption or emission lines corresponding to a purely rotational molecular transition ($|J+1,M\rangle \leftrightarrow |J,M\rangle$)can be expressed as:

$$E_{(J+1)\leftrightarrow J} = E_{J+1} - E_J = \frac{\hbar^2(J+1)}{I}. \tag{6.16}$$

Cl isotope	B (MHz)	σ (cm^{-1}) $J = 0 \leftrightarrow 1$	$\Delta\sigma$ (cm^{-1})	σ (cm^{-1}) $J = 1 \leftrightarrow 2$	$\Delta\sigma$ (cm^{-1})
35	312989.3	20.880399	0.031367	41.760797	0.062734
37	312519.12	20.849031		41.698063	

Table 6.2: The HCl rotational transitions found within the SPIRE band for both the ^{35}Cl and ^{37}Cl isotopes[99]. The closely spaced lines are used to verify the resolving power of the TFTS.

The equivalent frequency is given by:

$$\nu_{(J+1)\leftrightarrow J} = \frac{E}{h} = \frac{h}{4\pi^2 I}(J+1) = 2B(J+1) \qquad \text{MHz}, \tag{6.17}$$

or

$$\sigma_{(J+1)\leftrightarrow J} = \frac{E}{hc} = \frac{h}{4\pi^2 Ic}(J+1) = \frac{2B(J+1)}{c} \qquad \text{cm}^{-1}, \tag{6.18}$$

where $B = \dfrac{h}{8\pi^2 I}$, the rotation constant of the molecule[105]. The units of B are not consistent throughout the literature and are either given in MHz (equation 6.17), Hz, or cm^{-1} (equation 6.18).

The rotation constant is related to the reduced mass by:

$$B = \frac{h}{8\pi^2 \mu R_o^2}. \tag{6.19}$$

To first approximation, the bond length R_o does not change for different isotopes. Apart from the atomic mass difference (and hence reduced mass difference), molecules containing either of two isotopes behave similarly[106]. Table 6.2 compares the first two rotational transitions for the ^{35}Cl and ^{37}Cl isotopes, which are found in the SPIRE band. Figure 6.11 illustrates model spectra for the two rotational doublets used in the TFTS verification.

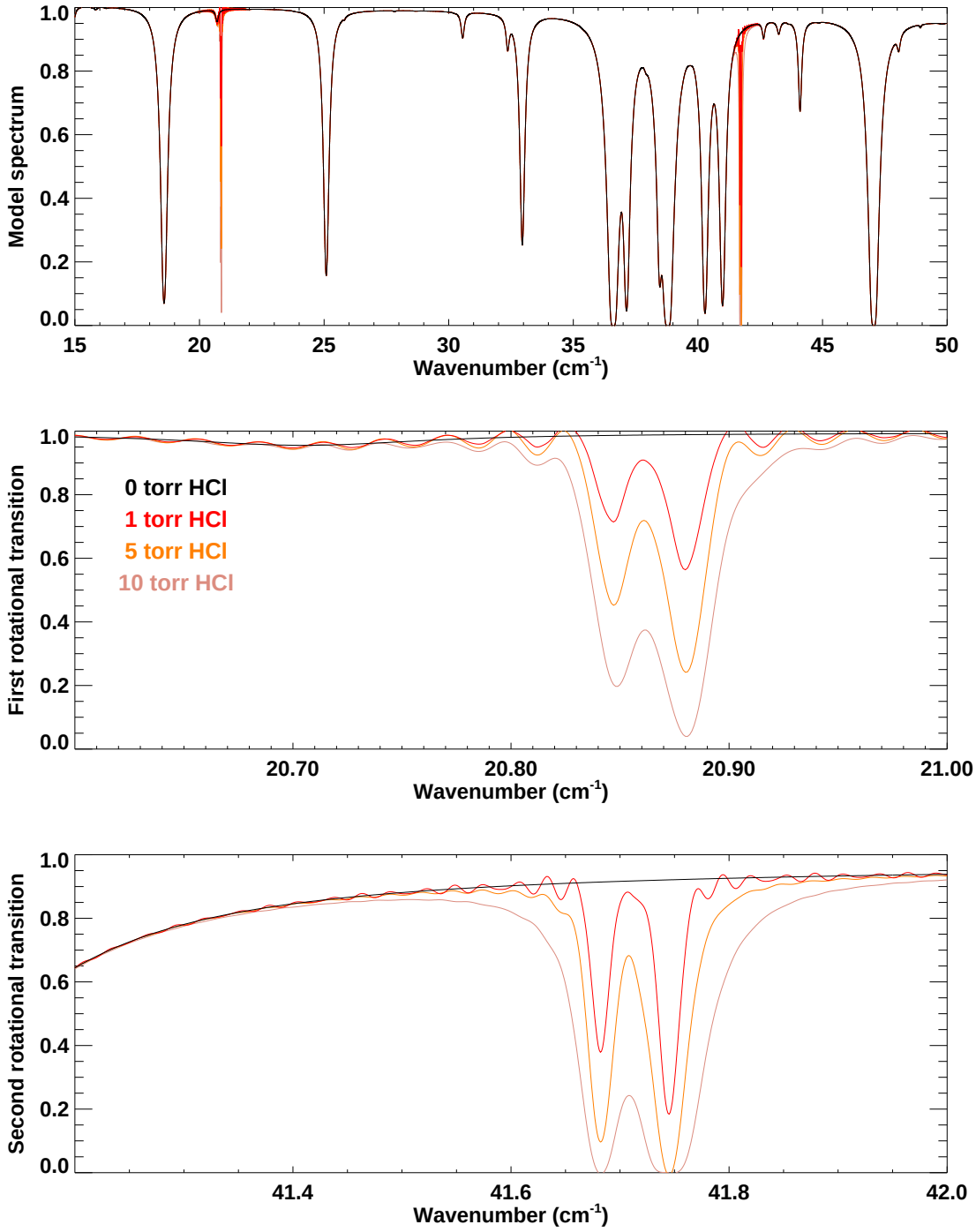

Figure 6.11: Model spectra for the HCl doublet absorption measured during TFTS verification testing. Spectra are shown for various pressures of HCl gas in the cell (see color legend on figure). The other absorption features are due to the atmosphere in the remainder of the optical path. The model spectra include the sinc ILS of the TFTS. These spectra were used to select the pressure of the HCl gas for the TFTS verification observations.

6.6.2 Analysis

As discussed in section 6.5, the HCl absorption interferograms required phase correction prior to the Fourier transformation used to generate high resolution ($\Delta\sigma = 0.015\text{cm}^{-1}$) spectra. Interferograms were recorded at the University of Lethbridge SPIRE laboratory between August 12th and 15, 2003. Scans were recorded with blackbody temperature of 800^oC, and HCl pressure of 1 - 10 torr within the gas cell. Over 2200 interferograms were recorded with the HCl cell in the optical path over the TFTS verification testing period. As is shown in figure 6.12, the S/N is too low to observe any spectral features in a single spectrum, and the 2216 interferograms which were co-added together were necessary in order to increase the S/N and allow quantitative spectral analysis.

The averaging of the 2216 interferograms increased the S/N in the interferogram[2] from ∼11 up to ∼540. S/N is expected to increase with the root of the number of averaged measurements, and since $11.5 \times \sqrt{2216} = 541.3$, this shows that the noise is random. Figure 6.13 illustrates the observed HCl doublet pairs.

Since the width of the HCl rotational transition lines is less than the resolution of the TFTS, the lines are expected to have a sinc line profile. In order to determine the line centres for each pair of doublets, an IDL least squares fitting routine was used to fit two sinc curves superimposed onto a flat background to the data. The measured line centres from the fitting routine are listed in table 6.3. Figure 6.13 illustrates the portions of the spectra that were used in the fitting routine.

[2]The S/N in the spectrum is approximately one tenth the S/N in the interferogram for the HCl spectra.

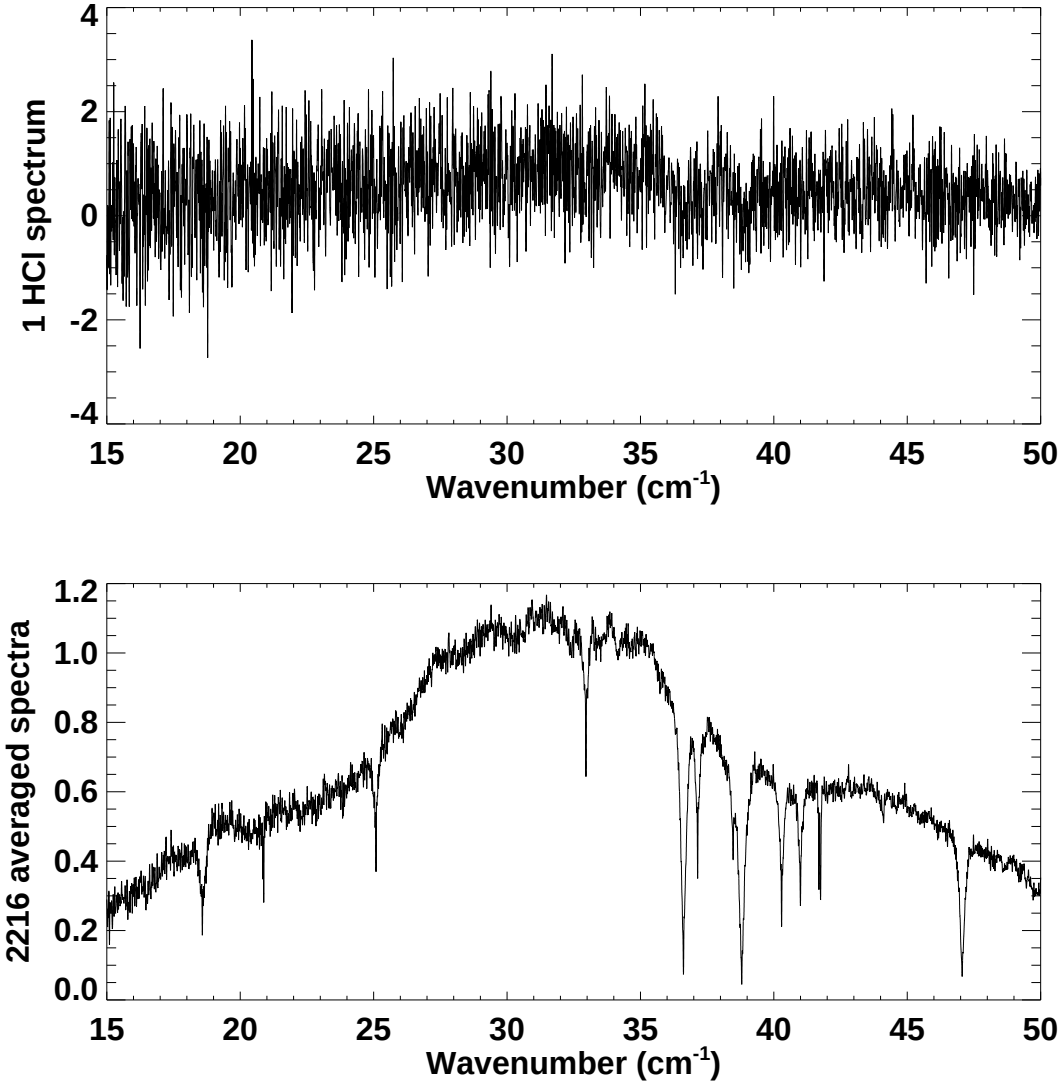

Figure 6.12: The observed HCl absorption spectra for the TFTS resolution verification testing. The upper figure shows an example of one measured spectrum. The S/N for the single spectrum ∼1 while the S/N for the averaged spectra is ∼50.

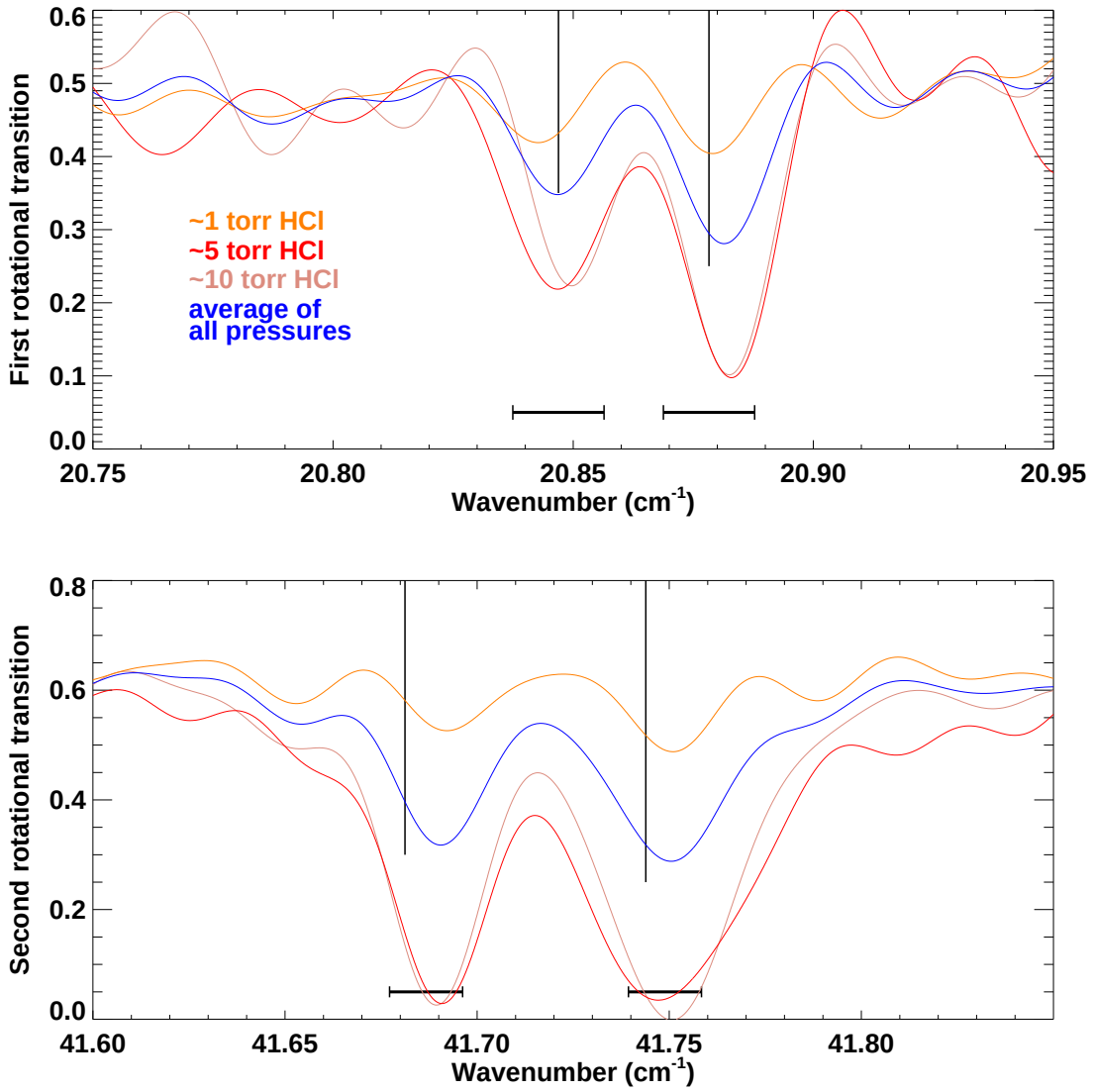

Figure 6.13: Measured rotational transition doublet pairs due to HCl gas absorption. The upper figure shows the absorption lines resulting from the $J = 0 \rightarrow 1$ transition and the lower figure shows the lines relating to the $J = 1 \rightarrow 2$ transition for $H^{35}Cl$ and $H^{37}Cl$. The solid vertical lines represent the theoretical line centres and the solid horizontal lines illustrate the width of the resolution element of each spectrum. The experimental and theoretical line positions lie within the same spectral resolution element. Transition selection rules are described in section 6.6.1.

Cl isotope	J	σ_{measured} $(\text{cm}^{-1})^{a}$	σ_{theory} $(\text{cm}^{-1})^{b}$
35	$1 \leftarrow 0$	20.8802 ± 0.0002	20.87828
37	$1 \leftarrow 0$	20.8491 ± 0.0002	20.84693
$\sigma_{35} - \sigma_{37}$	$1 \leftarrow 0$	0.0310 ± 0.0003	0.03135
35	$2 \leftarrow 1$	41.7501 ± 0.0002	41.74389
37	$2 \leftarrow 1$	41.6899 ± 0.0002	41.68121
$\sigma_{35} - \sigma_{37}$	$2 \leftarrow 1$	0.0602 ± 0.0003	0.06268

[a] Uncertainties are derived using equation 4.2

[b] There is not complete agreement with the empirical data and the theoretical frequency. The ranges listed in this column account for both empirical and theoretical expectations of frequency.

Table 6.3: Absorption line centres from the HCl rotation spectra

6.6.3 Results

The resolving power of the TFTS was measured to be greater than 665 at 21 cm^{-1}. This is equivalent to a resolving power of 1600 at 50 cm^{-1} and 475 at 15 cm^{-1}. The resolving power requirement for SPIRE is 1250 at 50 cm^{-1} and 370 at 15 cm^{-1}. The TFTS resolution exceeds that of SPIRE as is desired. The HCl lines were both of the correct separation, and at the correct location within the spectrum. The use of the HCl gas cell has shown both accurate and precise operation of the TFTS, and has been a useful tool in the TFTS verification testing.

6.7 Detector and stage synchronization

Preliminary data analysis indicated that the ZPD location differed for the up and down scans[15]; the difference being equivalent to an 80 ms time delay between reported bolometer signal values and stage position values. Since great lengths were undertaken

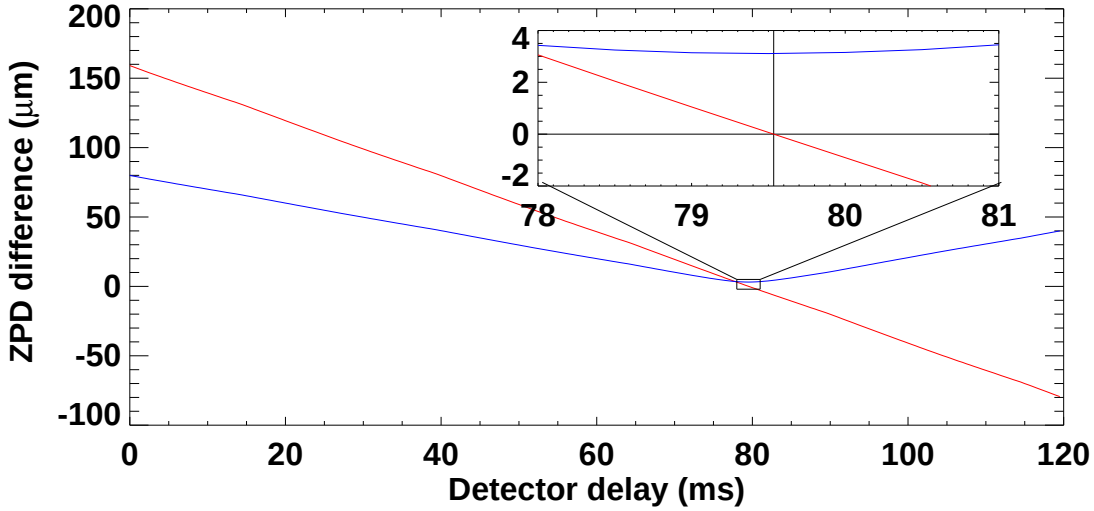

Figure 6.14: The constant time delay between up and down scans for the PLW bolometers using the TFTS. The difference between up and down scan ZPD positions is shown in red while the standard deviation of all ZPD values is shown in blue. The bolometer time delay is determined to be 79.5346 ms.

to synchronize the TFTS and SPIRE clocks (less than 100 ns) it was clear that some additional delay had not been accounted for. It was quickly realized that the time delay associated with the bolometer and detector electronics transfer function could be the cause. Using subsystem information provided by JPL[107] and LAM[108], the detectors and their electronics were modeled in Laplacian space to determine the impulse response function[109, 15, 110]. It is readily seen that the 80 ms delay observed (79.53 ms delay actually) agrees with the expected impulse response of the PLW array, thereby validating the SPIRE/TFTS clock synchronization. Pre-processing or linear phase correction will easily resolve any issues relating to timing delays between the two subsystems.

6.8 Laser in TFTS

The interferometric performance of the TFTS was validated using a molecular laser, a subsystem of the SPIRE test facility. Formic acid has a lasing transition at a wavelength of 432.65 μm. There are actually two closely spaced lines at 432.6324 μm[3] and 432.6665 μm[4] of similar strength[111, 112]; this separation (34.1 nm) is well below the resolution of the TFTS so a mean value was assumed). The molecular laser was filled to a pressure of $\sim$0.2 mbar of formic acid and pumped by the 9R20 line of CO_2. The CO_2 laser was operating in continuous flow mode with a pressure of $\sim$25 mbar. The optical power in the pump was on the order of $\sim$40 W. The molecular laser was tuned by adjusting the length of the resonant cavity. A pyroelectric detector was used to monitor the power of the infrared signal by means of a beamsplitter placed in the output path of the laser. A block diagram of the TFTS, FIR laser, telescope simulator, and SPIRE cryostat in the AIV cleanroom is shown in figure 6.3. A picture of the FIR laser is found in figure 6.15.

The laser beam was directed from the laser output towards the TFTS, and by means of a periscope mirror system, injected into the TFTS. A Golay cell[113] was placed inside the SPIRE test cryostat and viewed the TFTS through the cryostat window and telescope simulator. This Golay cell was then used to record an interferogram of the laser source. The pyroelectric detector provided automatic gain control of the interferogram signal by monitoring variations in the laser power output. The signal from both detectors was digitized and time stamped using a LabVIEW data acquisition system[114].

The TFTS translation stage is controlled by the TFTS-CS, which does not interface

[3] $\nu_6(J, K_a, K_c) : |33, 1, 33\rangle \rightarrow |32, 1, 32\rangle$
[4] $\nu_6(J, K_a, K_c) : |33, 0, 33\rangle \rightarrow |32, 0, 32\rangle$

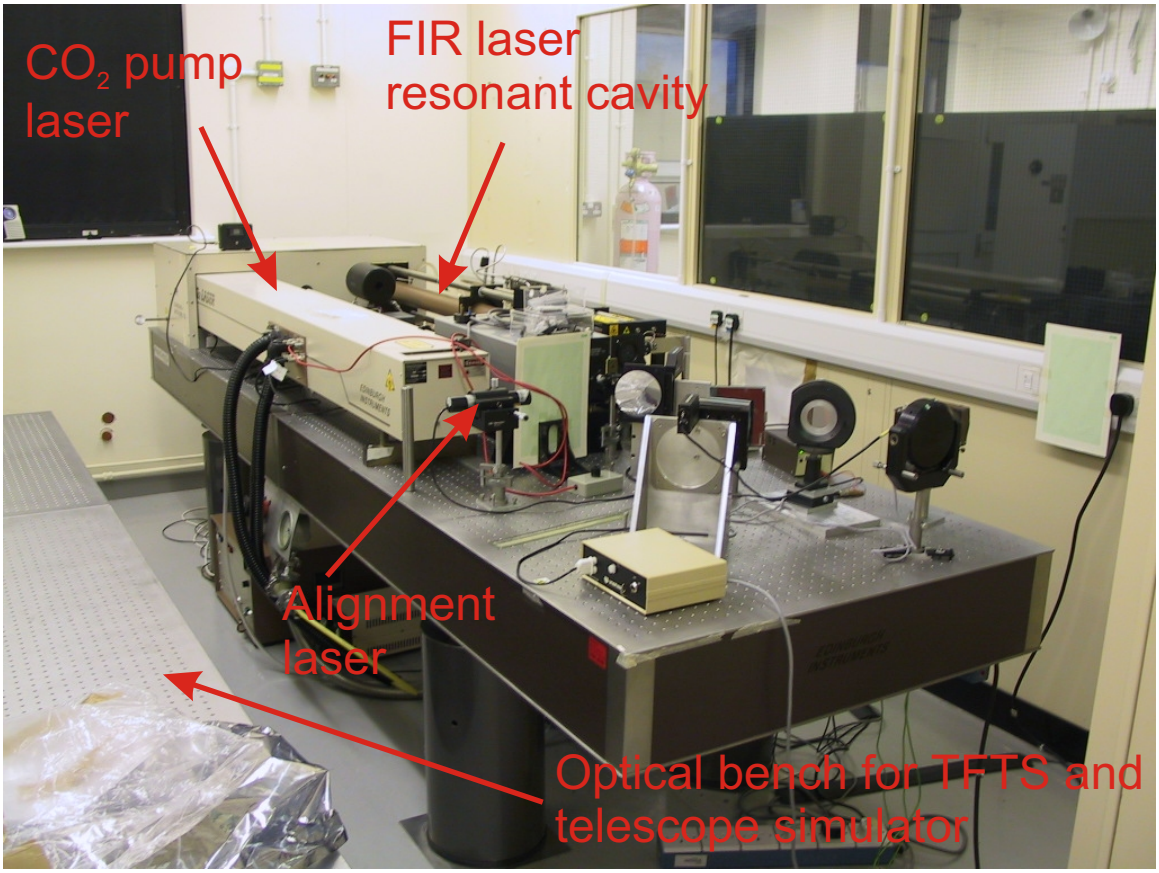

Figure 6.15: A picture of the SPIRE test facility FIR Laser. The laser is used in SPIRE verification testing. There are two possible output configurations for the laser. The principle configuration has the laser output light sent directly to the cryostat via the telescope simulator. This section describes a setup used to send the laser through the TFTS and then into the cryostat via the telescope simulator. Image courtesy of Space Science Technology Dept., RAL.

with the LabVIEW detector computer; therefore it was not possible to directly correlate TFTS stage position data with the time sampled interferogram data from the Golay cell. The TFTS stage control was operated in rapid scan mode at a constant velocity. The assumption of precise linearity of the TFTS stage motion control as well as the linearity of the LabVIEW time sampling was a necessary in order to obtain $I(z)$. The constant velocity profile of the TFTS translation stage was verified in pre-delivery TFTS verification testing. The assumed constant velocity and detector sampling is a potential source of error in the analysis, however the tests were carried out while the CQM model was undergoing vibration testing in another lab so the electronic interface that would normally serve to synchronize the detector and position data was not available. A more accurate line centre for the laser would likely have resulted had the proper equipment been available. Another source of error is the laser power fluctuations while the scans were being recorded.

Figure 6.16 shows the excellent agreement between the measured instrumental line shape and theoretical sinc line shape. With a knowledge of the sinc ILS it has been possible to determine the wavelength of the laser line to a small fraction of the resolution of the TFTS. The centre frequency of the laser was determined to be 23.12(3) cm^{-1} by use of a χ^2 sinc fit to the spectrum. Great accuracy in the wings of the $\sin(\sigma)/\sigma$ function validates the TFTS design and performance. This shows that the TFTS and telescope simulator are not apodizing the interferograms, nor are they introducing any significant distortions.

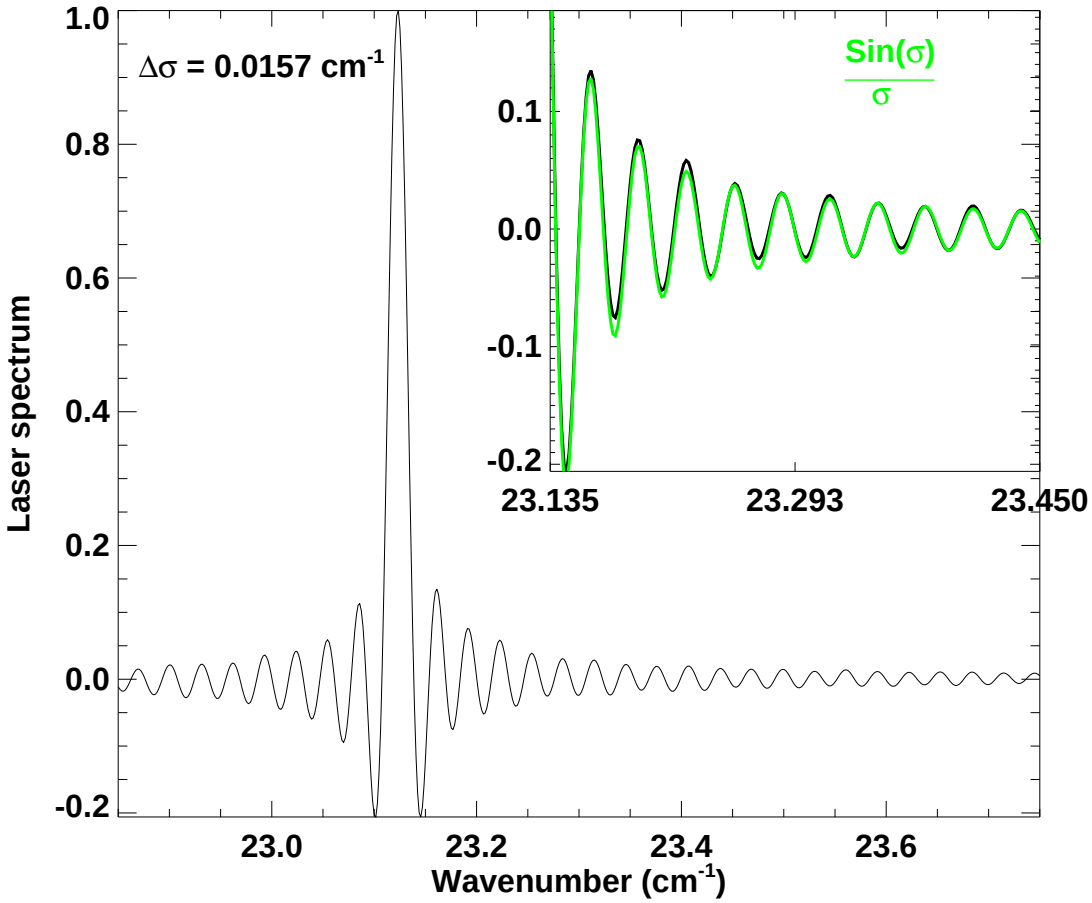

Figure 6.16: ILS of the TFTS, telescope simulator, and cryostat window obtained by propagating a laser through the test facility external to SPIRE. The inset shows a magnified comparison of the TFTS lineshape and classical $\sin(\sigma)/\sigma$ function (green).

6.9 Conclusions

One of the key Canadian contributions to the Herschel mission is the design, manufacture, assembly, testing and support of the SPIRE TFTS and associated control and data processing software for use during SPIRE calibration tests and during the Herschel mission. The TFTS performance has been characterized to allow for accurate characterization of the SPIRE instrument subsystems. The TFTS beamsplitter phase calibration measurements are necessary for the CQM data analysis discussed in the following chapter. HCl gas cell results illustrate that the TFTS has the resolution capability required for SPIRE. The electronic/software integration of the TFTS with the SPIRE test facility has been verified through the comparison of up and down scan ZPD locations. The laser spectrum measured by the TFTS proves that the TFTS ILS is the ideal sinc profile. The TFTS has proven to be an important component in the SPIRE instrument development.

Chapter 7

SPIRE CQM testing

Contents

7.1 Overview

As previously discussed, the Spectral and Photometric Imaging Receiver (SPIRE) is one of three instruments on the European Space Agency's Herschel mission. A detailed understanding of the SPIRE instrument is essential for a successful mission. In particu-

lar, it is important to characterize both the in-band spectral profile, and any out-of-band spectral leaks, which would severely degrade performance. This chapter will discuss the pre-vibration and post-vibration testing of the Herschel/SPIRE Cryogenic Qualification Model (CQM). Vibration testing is critical to the development of Herschel as the finished instrument (containing micron precision moving parts) will be launched cold (0.3 - 120 K) on an Ariane 5 rocket[115]. Pre-vibration testing revealed that the photometer long wavelength (PLW) array within the SPIRE CQM model was performing according to the required specifications. Post-vibration testing has shown no significant performance changes, and thus SPIRE development progresses towards the flight model testing phase. A detailed description of SPIRE and its subsystems is found in the SPIRE design description[10].

7.2 Introduction

The Spectral and Photometric Imaging Receiver (SPIRE) is one of Herschel's three focal plane instruments. SPIRE consists of a three band imaging photometer and a dual band imaging Fourier transform spectrometer. The SPIRE instrument is cooled to several temperature zones To achieve high sensitivity the SPIRE instrument has several temperature zones ranging from $\sim$0.3K to 120K; the detectors themselves operating at 0.3K[10, 19]. The important features of SPIRE are summarized in Table 7.1[20].

The combination of a low emissivity, passively cooled telescope, the total absence of atmospheric emission and a cryogenically cooled payload will allow sensitive photometric observations. SPIRE is designed to operate in the absence of an atmosphere, and the SPIRE instrument itself is inside an evacuated cryostat during testing to simulate space

Parameter	Photometer	Spectrometer
Spectral Bands (μm)	250, 363, 517	200 - 325, 315 - 670
Resolving Power	3	1000
Number of Pixels	43, 88, 139	19, 37
Field of View	4' x 8'	2.6' diameter

Table 7.1: Comparison of the Photometer and Spectrometer components of SPIRE.

flight conditions. Outside of the cryostat, however, ground testing occurs under atmospheric conditions. The test facility consists of a molecular laser to provide an accurate spectral line source and a blackbody source for band profiles. A spectrometer was identified as an additional piece of test equipment required to determine the spectral performance of SPIRE. The SPIRE test facility FTS(TFTS), with its broad spectral coverage, intermediate and variable resolution, intrinsic wavelength and intensity calibration, and simplicity of integration was designed for this task (see chapter 6).

Cold-vibration testing (see section 7.6), subjecting the instrumentation to accelerations up to 18× that due to gravity, is carried out to simulate the conditions the Herschel satellite will experience during launch. Pre-vibration tests provide a benchmark for comparison with post-vibration and future instrument testing. It is imperative that any performance changes due to vibration testing be characterized and understood to ensure that Herschel will operate within design specifications both before and, more importantly, after launch. Ground based testing of the SPIRE instrument poses challenges in simulating the space environment that gives SPIRE its observational advantages.

A multi-stage Helium cryostat cools SPIRE to the required temperatures[10]. CQM testing is comprised of two stages, pre-vibration testing, and post-vibration testing.

For information that discusses more general aspects of SPIRE CQM verification testing refer to Lim *et al*, 2004[13].

7.3 SPIRE detector arrays

The SPIRE detector arrays use spider-web bolometers and neutron transmutation doped (NTD) germanium thermistors (i.e. thermometers)[116]. The bolometers are coupled to the telescope by hexagonally close-packed single-mode conical feedhorns[20], providing diffraction-limited beams. Each of the arrays is cooled by a thermal strap from the ^{3}He cooler. A diagram of the photometer detector arrays is shown in figure 7.1. Further details on the detectors including the feedhorns and bolometers are found in references [117, 118, 119, 120, 121, 122, 123].

7.4 CQM model spectrum

To compare experimental observations with theory, a TFTS model spectrum was calculated. This model included a full radiative transfer[1] analysis of all optical components from the blackbody source, and the optical path through the TFTS and the telescope simulator to the entrance window of the cryostat. As mentioned previously, the atmospheric water vapour is a problem since it acts simultaneously as a source of absorption and emission in the optical path. This provided the impetus for enclosing the beampath and purging the water vapour with dry air and nitrogen gas, however, residual amounts of water vapour remain (see humidity reading on figure 6.4). The radiative transfer is further complicated

[1]The radiative transfer model used, known as ULTRAM, was developed at the University of Lethbridge by Ian Chapman[124].

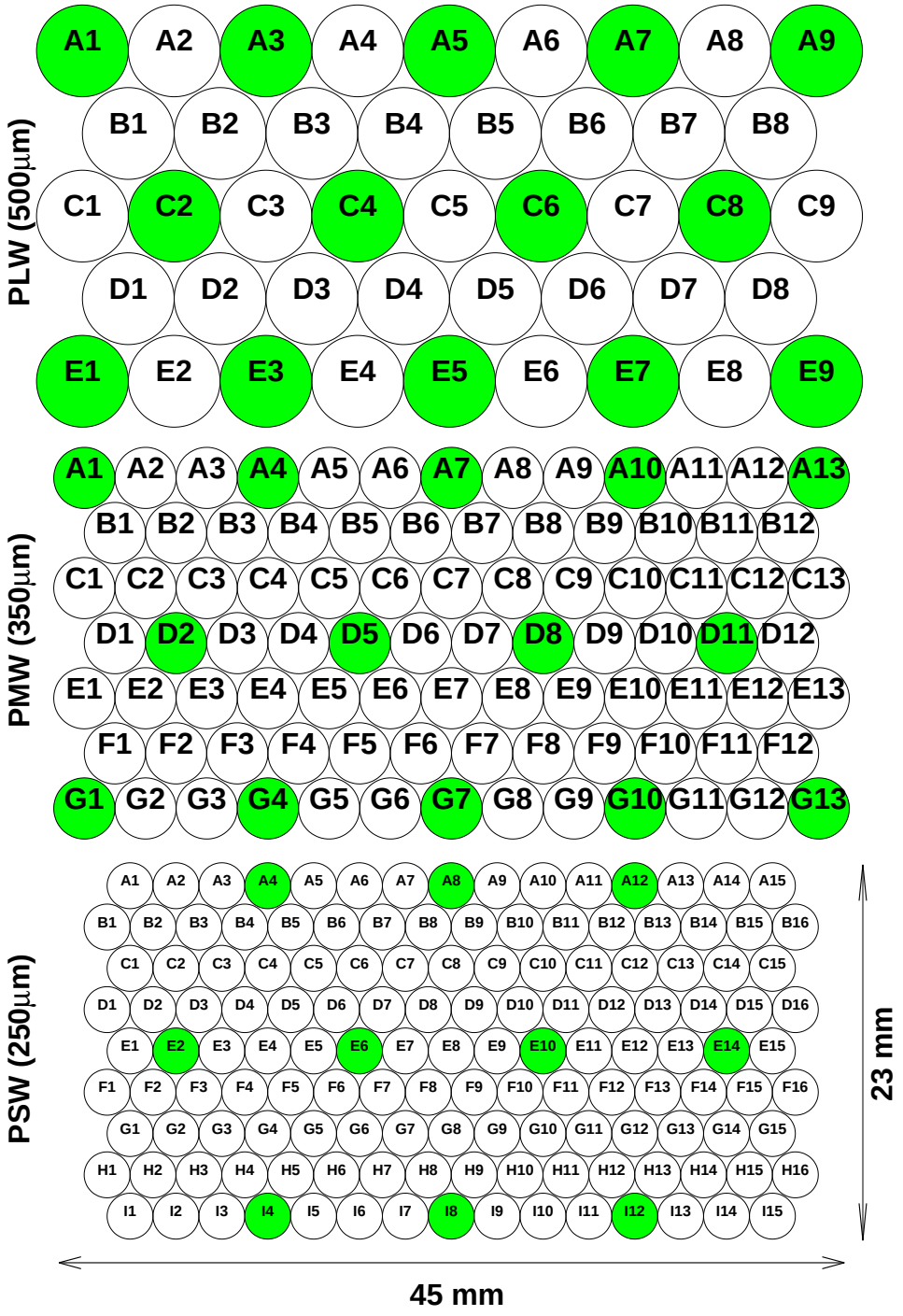

Figure 7.1: A diagram of the spire photometer arrays. The shaded pixels represent pixels that are co-aligned with those in the other photometer arrays.

by the fact that the second input port of the interferometer corresponds to one of the two outputs in the classical Michelson interferometer design; in this case the path from the cryostat window to the TFTS. The model also should include the FTS instrumental line shape. The sinc function is used (see section 2.10.4) in the case of the TFTS.

In addition to the atmosphere, there are six mirrors between the cryostat window and the TFTS that act as ambient sources of unknown emissivity. These sources are not expected to alter the shape of the spectral profile as measurements occur in the Rayleigh-Jeans region[125, 126] (see appendix G) and are normalized as part of the analysis. The effect of these sources is removed in differencing provided that scans of two different blackbody temperatures are available (see section 7.8), however, if scans are only available for one blackbody temperature then the Rayleigh-Jeans (RJ) approximation gains importance. Other detector calibration measures eliminate these uncertainties by using sources inside the cryostat[13]. Therefore, to a first approximation, it was assumed that the theoretical spectrum is given by the following relationship:

$$S = F\mathcal{R}\eta e^{-\tau} B_h \sigma A\Omega, \tag{7.1}$$

where F is the filter profile, $\mathcal{R}$ is the spectral responsivity, η is the combined optical efficiency of the external mirrors, B_h is the Plank function for the blackbody source (1200^oC), $e^{-\tau}$ is the atmospheric transmission, A is the detector area, and Ω is the detector solid angle. $A\Omega$ is expected to be proportional to λ^2 due to the single mode, diffraction limited, propagation[127]. The model spectrum for a 1200^oC blackbody source seen by the PLW array is shown in figure 7.3, which is based on the assumption that $\mathcal{R}$ is unity.

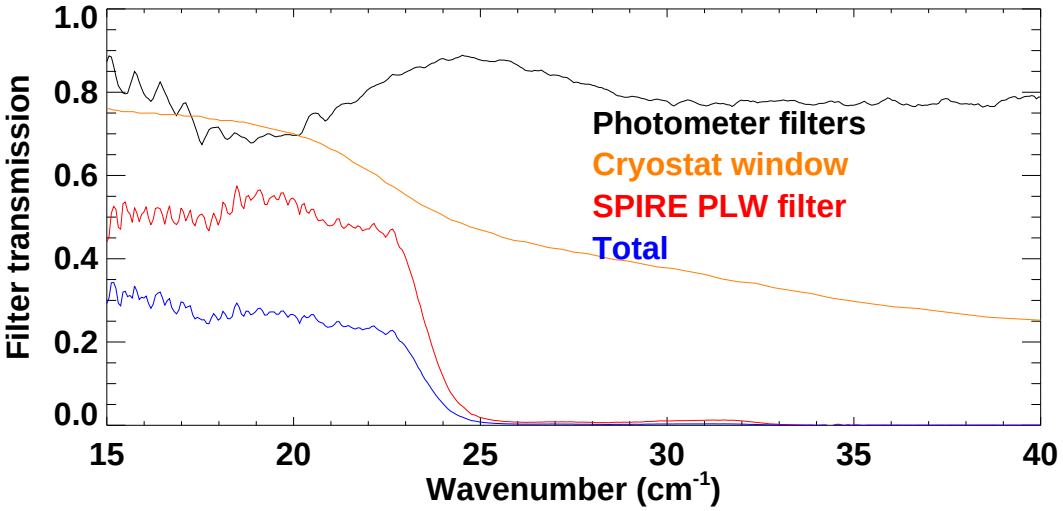

Figure 7.2: Transmission profiles of optical filters from the cryostat window to the PLW array. The low frequency cut-off of the PLW array is provided by the bolometer feedhorns and is not shown on this figure, but is expected to be very sharp. Data for this figure is courtesy of Astronomy Instrumentation Group, Cardiff University, UK.

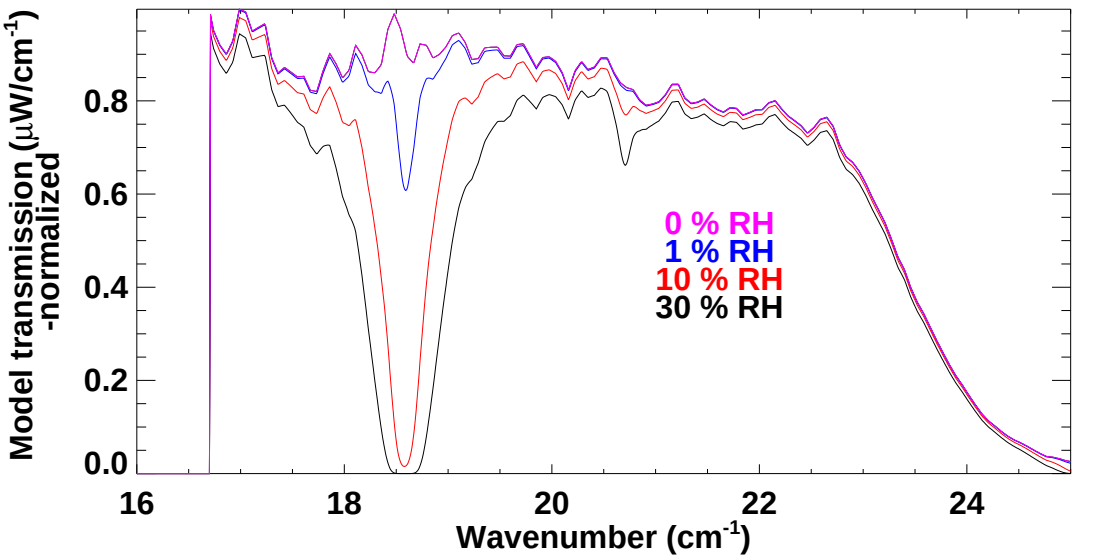

Figure 7.3: Model PLW spectrum from a diffraction limited blackbody radiation source at 1200^{o}C and various humidities in the optical beampath. This is calculated assuming a Spectral Responsivity of unity (see equation 7.1) and a sharp low frequency cut-off.

7.5 Pre-vibration test campaign

CQM testing involved the photometer PLW array. The atmospheric transmission across the PLW band has fairly low opacity with a single strong water absorption line at 18.578 cm^{-1}[128]. This absorption line is useful for intensity and wavelength calibration. The high transmission region between 19 and 24 cm^{-1} provides higher signal-to-noise data, which in turn allows reliable broadband phase correction. The PLW array is therefore seen to be a good choice for CQM testing because of these simple atmospheric properties.

A full week is required to cool the SPIRE instrument in its test cryostat down to its operating temperature; this process also requires monitoring 24 hours a day, and typically requires 1,000 L of Helium. (It also takes a week to heat the SPIRE instrument back up to room temperature once testing is completed.) During testing, the cryostat needs close monitoring and frequent helium refills (100 L of He and 50 L of liquid N_2 daily). Once cooled, the time available for the CQM testing is at a premium. Flexibility and efficiency are key to a successful CQM test campaign.

During CQM testing, TFTS parameter selection involved a compromise between different test goals. Four parameters relating to the TFTS are free to be manipulated to obtain the desired spectral properties: TFTS stage velocity, TFTS position sampling interval, hot blackbody temperature, and maximum optical path difference (OPD_{max}). Given the limited amount of time allotted for use of the TFTS within the CQM pre-vibration test campaign, the fundamental trade off lies between signal-to-noise and spectral resolution. In total 9 pixels were tested at a variety of scan speeds, resolutions, and blackbody temperatures. Observing parameters are shown in Table 7.2. The choices in setting these

parameters in the case of the PLW array are discussed below.

Interferogram S/N increases with blackbody temperature. As discussed in section 7.8, spectral measurements of the blackbody at two different temperatures, ideally widely spaced, are required to determine the spectral responsivity using equation 7.3. During the test campaign, the blackbody was operated at 1200^{o}C and 950^{o}C. This was a reasonable compromise in that both temperatures are well above ambient and yet a significant difference exists between them. To maximize the number of pixels that could be measured, it was decided to conduct low resolution (LR) and high resolution (HR) scans at two blackbody temperatures for the central pixel, and do LR scans at one blackbody temperature (1200^{o}C) on the other pixels to be tested (see table 7.2). This allows greater S/N and testing of a greater number of pixels in the time available.

The TFTS was one of several facility instruments used to evaluate the performance of SPIRE. A total of 3.5 hours of TFTS scans were recorded during the week-long pre-vibration CQM test campaign. The central pixel, C5, was tested the most comprehensively with four scan sets. The first set of scans consisted of thirty LR scans with the stage velocity, v, at 1.0 mm/s and the hot blackbody source set at 1200^{o}C. The second scan set was the same as the first except that the hot blackbody was set to 950^{o}C instead of 1200^{o}C. The third and fourth sets of C5 scans were each eight HR scans done at 1200^{o}C and 990^{o}C respectively with the stage velocity, v, at 0.5 mm/s. The LR C5 scans were done on the evening of the first day available for TFTS testing, and only after they were completed was it realized that the stage speed velocity was set too high. At this speed, it was realized that the fringe frequency of the interferograms (equation 2.42) lies too close to the bolometer

Pixel	Vel.[a](mm/s)	opd$_{max}$ (cm)	Δz (μm)	BB[b]Temp. (^{o}C)	R.H.[c](%)	Scan Pairs
A2	0.5	2	25	1200	7.8	6
A5	0.5	2	25	1200	7.8	6
A9	0.5	2	25	1200	7.0	6
C1	0.5	2	25	1200	10.0	6
C5	1.0	2	25	1200	10.5	60
C5	1.0	2	25	950	8.0	60
C5	0.5	34	25	1200	7.5	6
C5	0.5	34	25	990	8.7	6
C9	0.5	2	25	1200	5.6	6
E2	0.5	2	25	1200	12.0	6
E5	0.5	2	25	1200	6.0	6
E9	0.5	2	25	1200	6.0	6

[a] FTS translation stage velocity (optical path difference mm /s)
[b] Blackbody Radiation Source
[c] Relative Humidity

Table 7.2: TFTS tests performed during pre-vibration SPIRE CQM verification test campaign. For pixel location on the PLW array refer to figure 7.1.

roll-off frequency of 5 Hz. The stage velocity was subsequently reduced to 0.5 mm/s for all remaining scans. All of the other pixels were only scanned six times with a blackbody source at 1200^{o}C. Time did not allow scans at two temperatures, so the higher blackbody temperature was selected because it provided better S/N. Table 7.2 summarizes the tests performed during the pre-vibration CQM test campaign.

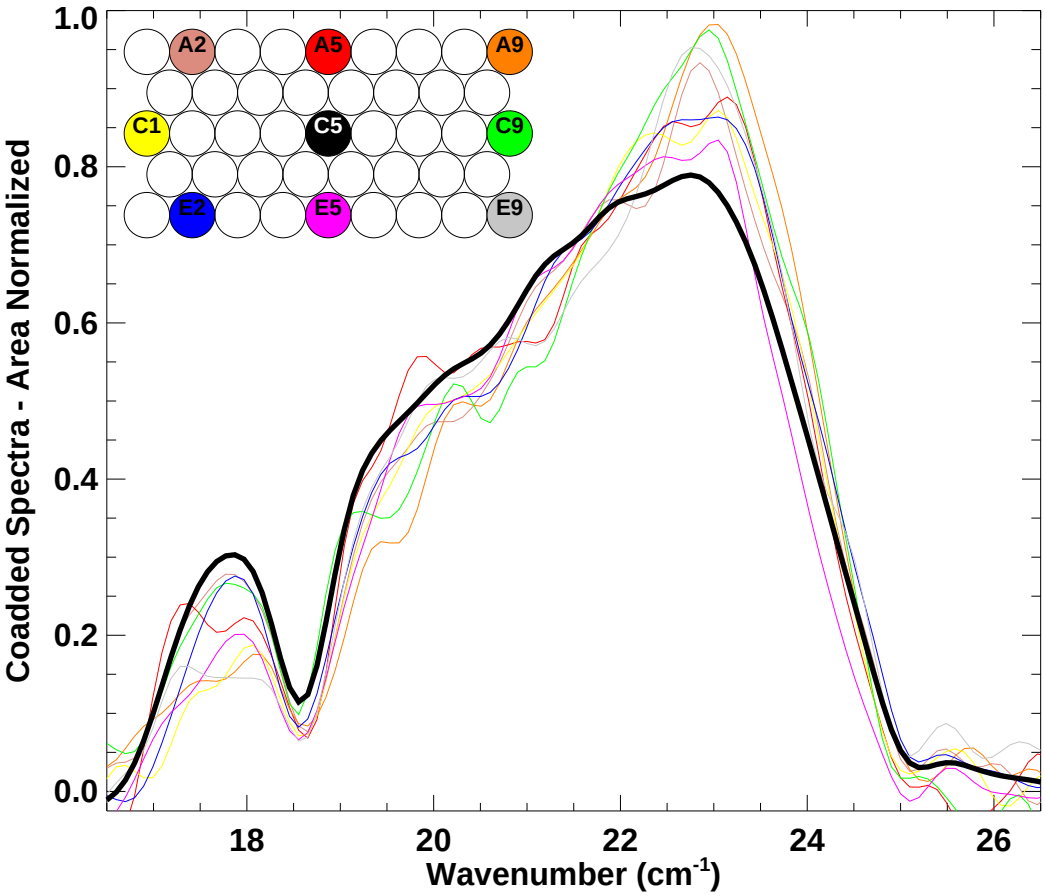

Figure 7.4: Observed (averaged) spectra from each pixel for the pre-vibration CQM test campaign. Spectra are normalized to pixel C5 by the area under the curve of each spectrum over the high S/N region.

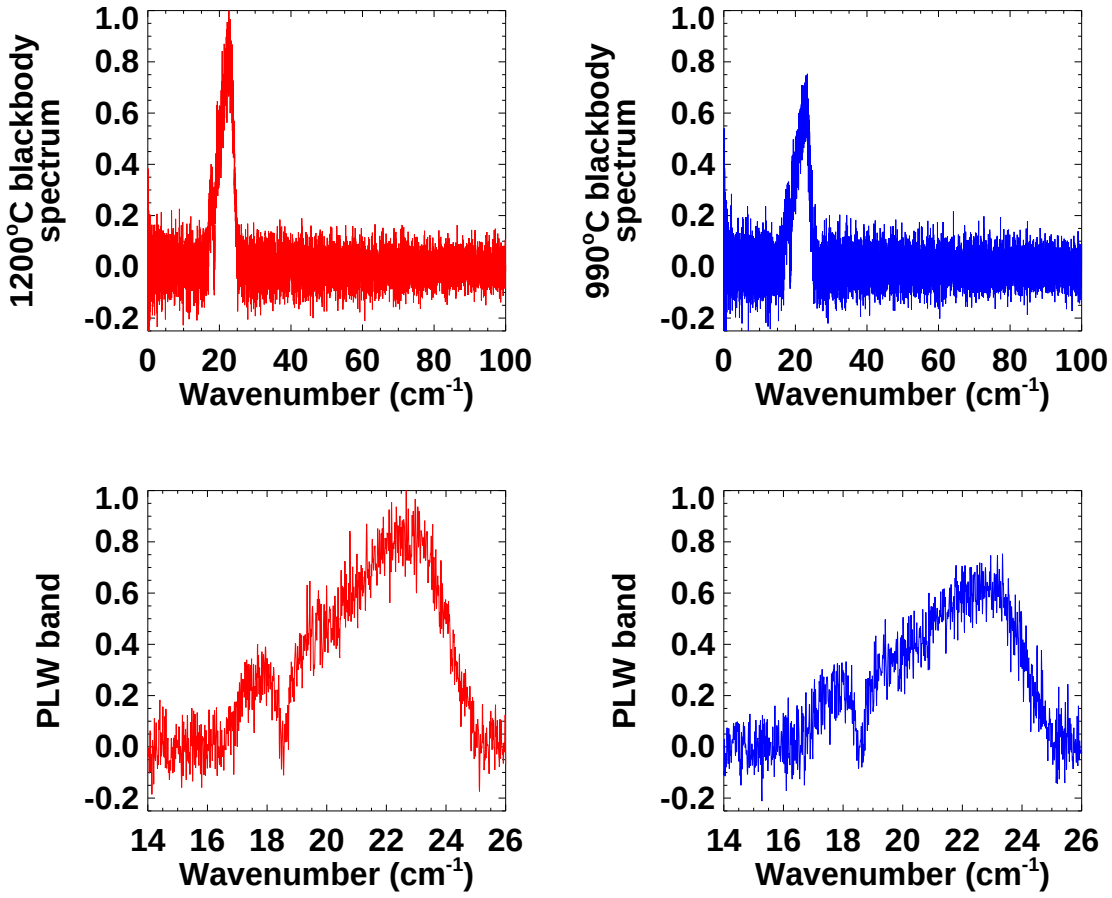

Figure 7.5: Co-added HR spectra of the hot blackbody source at 1200^{o}C (left) and 990^{o}C (right) and atmospheric absorption taken by the central pixel of the PLW array during pre-vibration testing.

7.6 Vibration testing

Following the pre-vibration CQM test campaign, the SPIRE focal plane unit (FPU) was subjected to cryogenic vibration tests at the Centre Spatial de Liège (CSL), Belgium. The CSL is capable of subjecting instrumentation to vibrations up to 150 g (i.e. 150× the acceleration due to gravity) over a frequency range of 5 - 3000 Hz and a temperature range of -268 - 120^{o}C[129], with cleanroom classifications ranging from 10000 - 100. This is the only facility in the world capable of performing launch simulation testing on a payload this large at cryogenic temperatures. The FPU was subjected to vibration testing, with accelerations up to 18 g at frequencies ranging from 10 - 1000 Hz (peak vibration amplitude was in the range of 100 - 200 Hz), at nominal operating temperatures (see section 7.2) for a period of several weeks to simulate the harsh environment that Herschel will experience during launch on an Ariane 5 rocket[115].

7.7 Post-vibration Test Campaign

The post-vibration test schedule is similar to the pre-vibration schedule, but probed some areas further[13]. The TFTS performance has been well established by pre-delivery verification testing and the pre-vibration CQM tests, so post-vibration testing was able to concentrate on investigations of SPIRE itself and verifying more pixels. In addition to the pixels tested in the pre-vibration test campaign, the post-vibration test will also observe performance of pixels B3, C4, D2, and D4 (see figure 7.1). Table 7.3 illustrates the number of low and high resolution interferograms measured in both phases of CQM testing.

The S/N on pixel B3 was particularly low (i.e. interferogram S/N was <2), so

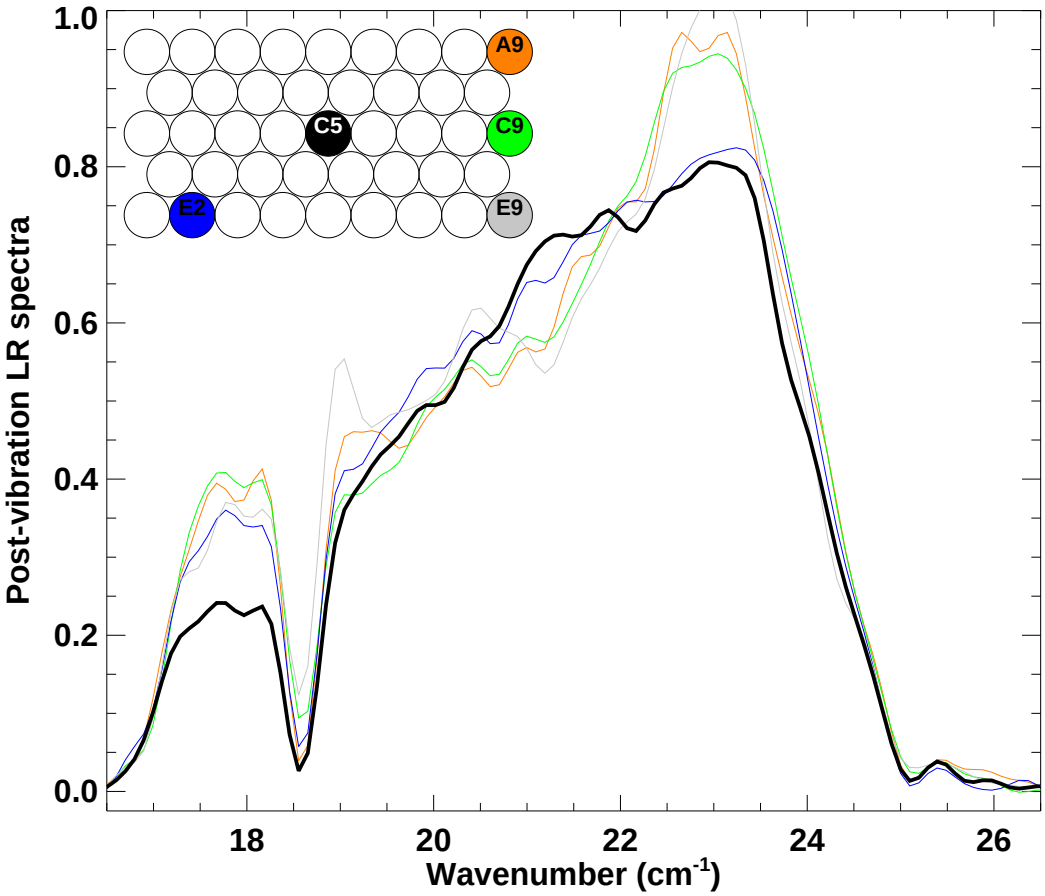

Figure 7.6: Observed (averaged) spectra from each pixel for the post-vibration CQM test campaign. Spectra are normalized to pixel C5 by the area under the curve of each spectrum over the high S/N region.

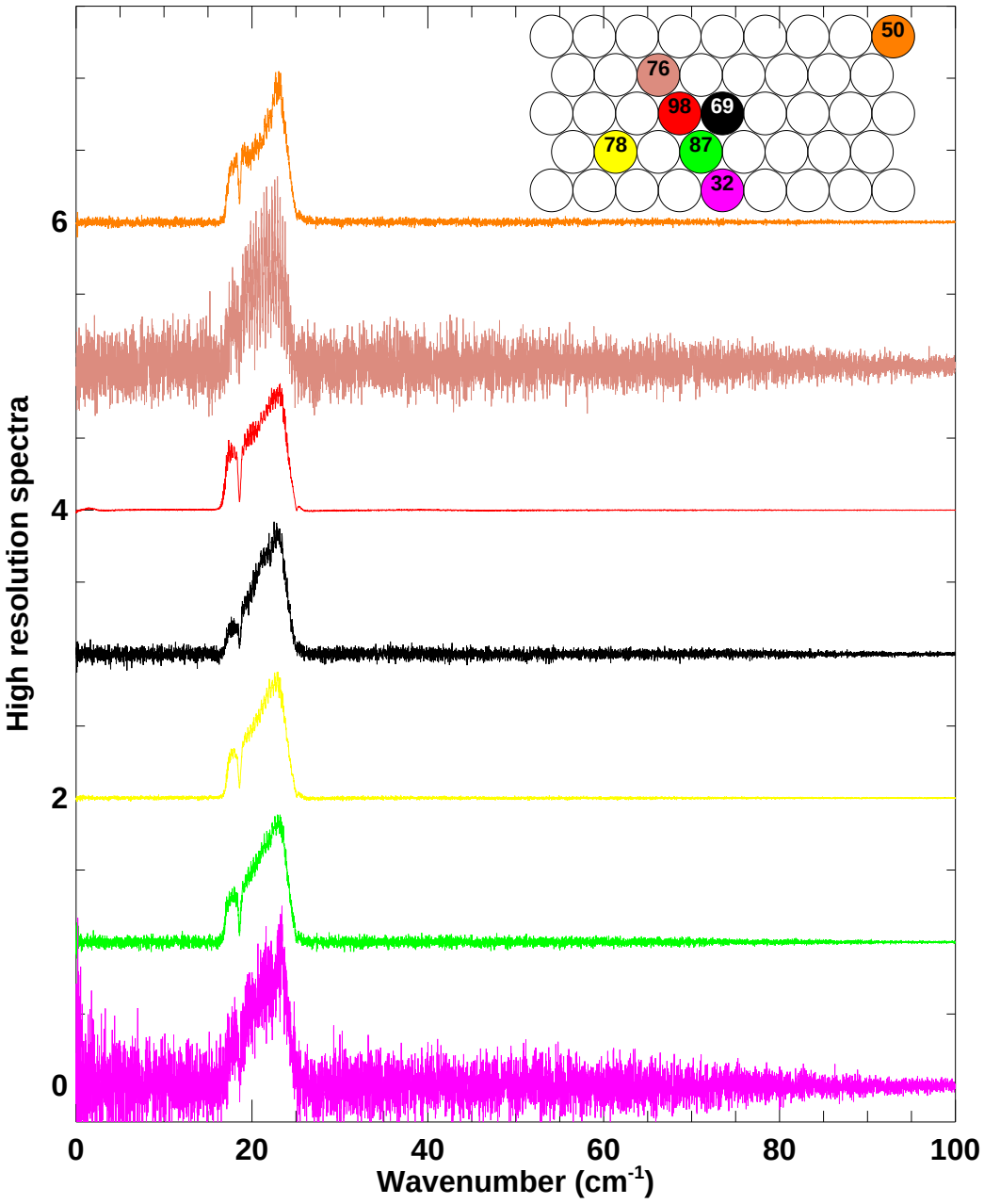

Figure 7.7: Observed HR spectra for post-vibration CQM test campaign. Instead of the pixel name in the legend box, the number of averaged spectra appears, i.e. 50 spectra were averaged for pixel A9. Note the lack of out-of-band spectral leaks.

Pixel	HR		LR	
	pre	post	pre	post
A2	0	0	6	0
A5	0	0	6	0
A9	0	50	6	40
B3	0	76	0	0
C1	0	0	6	0
C4	0	98	0	0
C5	15	69	120	80
C9	0	0	6	80
D2	0	78	0	0
D4	0	87	0	0
E2	0	0	6	39
E5	0	32	7	0
E9	0	0	6	40

Table 7.3: Comparison of the resolution and pixels observed for the pre and post vibration portions of CQM testing. Numbers listed are for the number of interferograms recorded.

the averaged spectra appear very noisy (see figure 7.7). This is amplified by the fact that the double-sided spectra are too noisy to accurately determine the linear phase error, and hence perform a phase correction. S/N for pixel E5 was also of poorer quality, but still sufficient for linear phase to be accurately determined. Even though there were less than half of the number of spectra to average than for B3, the E5 averaged spectrum has higher S/N because the phase correction algorithm was able to determine the linear phase. Without accurate phase correction, spectral averaging does not effectively increase S/N. This explains the artifacts in the co-added spectra (figure 7.7) and stresses the importance of phase correction.

While the HR scans were performed on pixel C4 there were also several other pixels exposed (i.e. A2-A6, B1-B4, and C2-C5) because the TFTS iris was fully opened to

a 2.5 cm diameter. The S/N is similar to or worse than the B3 scans (figure 7.7) and thus they are not worth presenting here.

7.8 Detector responsivity

In order to account for the self-emission term (see section 7.4) within the TFTS and telescope simulator, equation 7.1 is modified to include k as follows:

$$S = F\mathcal{R}\eta e^{-\tau}(B_h A\Omega - k). \tag{7.2}$$

The negative sign indicates this spectral contribution originates from the second input port of the Michelson interferometer. The mirror efficiency, η, is assumed to be 0.83 as it represents the reflectivity of six room temperature mirrors ($R \approx 0.97$ each). Assuming that all other variables such as relative humidity are constant, spectral responsivity, $\mathcal{R}$, can be determined by taking the difference between two spectra (equation 7.2) obtained at different blackbody temperatures as follows:

$$\begin{aligned} \text{for } S_1 &= \mathcal{R}F\eta e^{-\tau}[B_1 A\Omega - k] \\ \text{and } S_2 &= \mathcal{R}F\eta e^{-\tau}[B_2 A\Omega - k], \\ S_1 - S_2 &= \mathcal{R}F\eta e^{-\tau}[(B_1 A\Omega - k) - (B_2 A\Omega - k)] \\ \text{thus } \mathcal{R} &= \frac{S_1 - S_2}{F(\eta)(e^{-\tau})(A\Omega)[B_1 - B_2]}. \end{aligned} \tag{7.3}$$

Equation 7.3 is used to determine the spectral responsivity for the central pixel (C5) of the PLW array using the pre-vibration dual temperature spectra as shown in figure 7.8.

In order to measure as many pixels as possible, the remaining pixels of the pre-vibration tests and all of the pixel measurements for the post-vibration tests used only the

1200^{o}C blackbody temperature setting. It is not possible to solve for $\mathcal{R}$ using equation 7.3 with spectra from only one blackbody temperature. Thus, another spectral responsivity approximation is assumed which omits the unknown k because the 1200^{o}C blackbody S/N dominates any unknown spectral contributions:

$$\mathcal{R} = \frac{S}{F\eta e^{-\tau}[B_h A\Omega]}. \tag{7.4}$$

Using the spectral responsivity determined through the two temperature method, equation 7.3 can be solved for k. This unknown should represent the contributions to the spectra that are not accounted for in equation 7.1. The result of the calculation is shown in figure 7.9, with the flat room temperature blackbody source plotted in the background (green). The unknown spectral contribution, k, is seen to be essentially flat (over the regions of high S/N and thus will not change the profile of the spectral responsivity, as measurements occur in the Rayleigh-Jeans region (see appendix G). With spectra taken from two blackbody temperatures, any systematic contributions could be removed, be it constant or irregularly shaped. With only one blackbody temperature, however, the systematic contribution being flat simplifies the analysis.

7.9 Comparisons across PLW array

As seen in figures 7.8, 7.10, 7.11, and 7.12, the spectral responsivities from different pixels are in general agreement. The low and high frequency cutoffs are unvarying. Spectral profiles agree, however, the normalization factors are not fully understood. Also, the low frequency cut-off is more gradual than expected. This issue will be addressed in future SPIRE test campaigns.

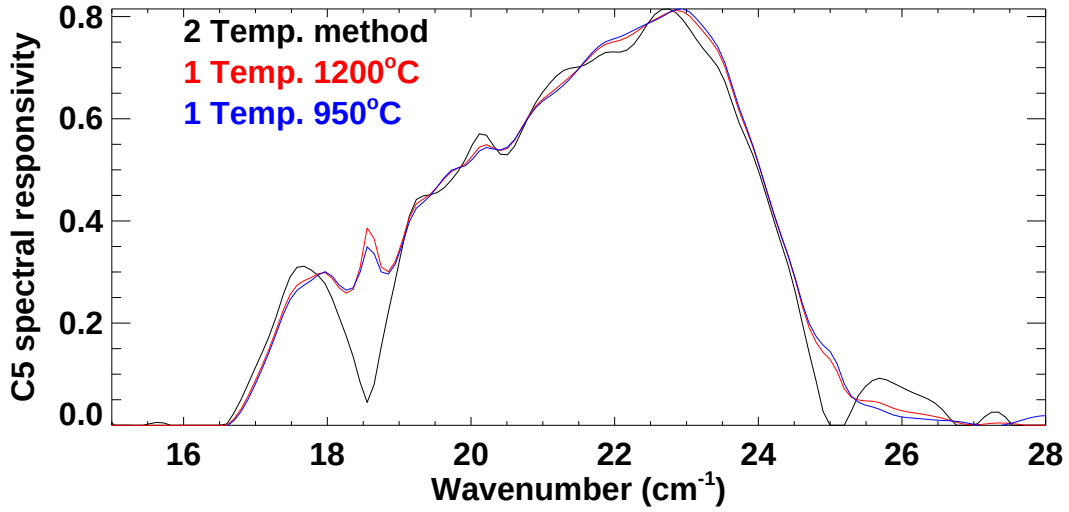

Figure 7.8: Both the two temperature determined (equation 7.3) and one temperature determined (equation 7.4) spectral responsivity for PLW pixel C5 as measured in pre-vibration testing. Humidity differences account for the difference at the region of the absorption feature.

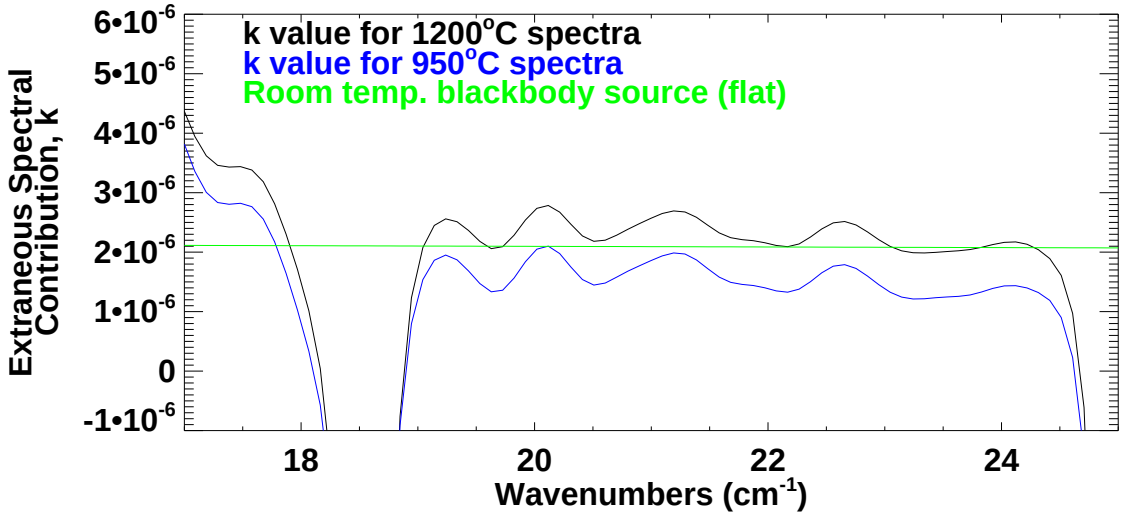

Figure 7.9: Extraneous spectral source as identified in equation 7.2 calculated with equation 7.3 using the spectral response for the central pixel also obtained from equation 7.3. Also shown is a room temperature blackbody source (flat).

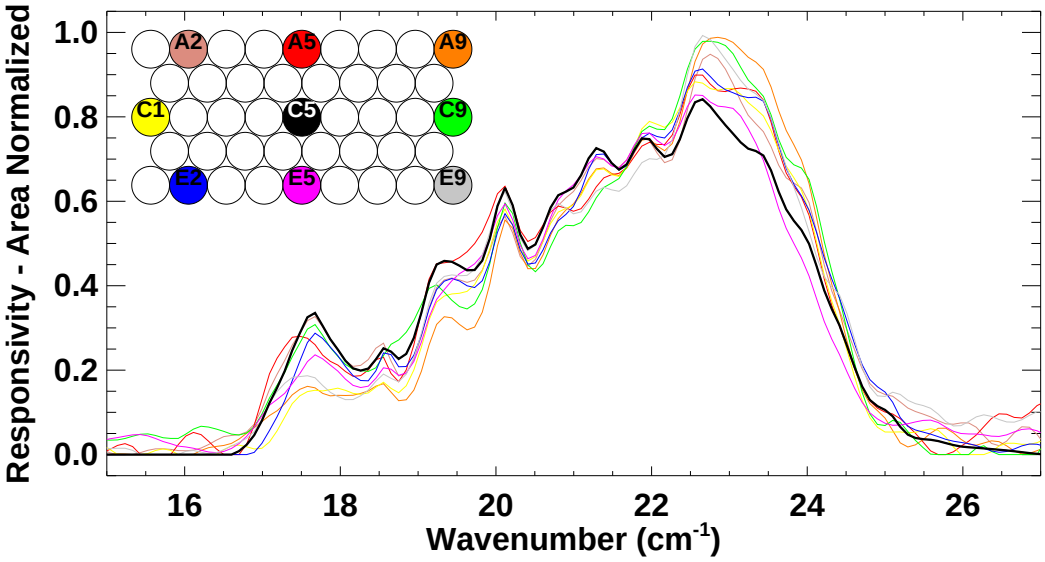

Figure 7.10: Spectral Responsivity for all pre-vibration tested pixels as determined by equation 7.4.

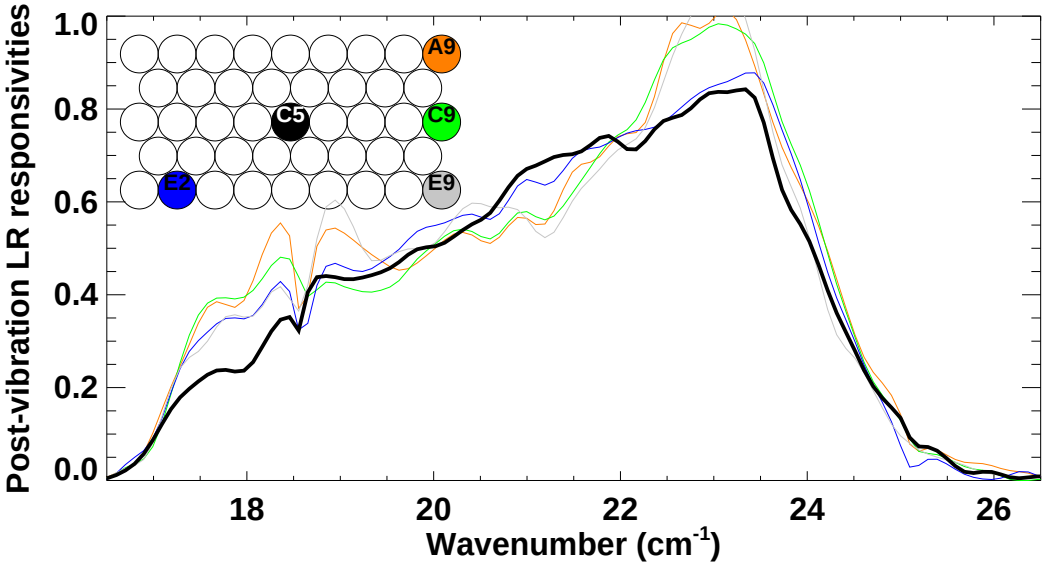

Figure 7.11: Post-vibration low resolution spectral responsivities (equation 7.4).

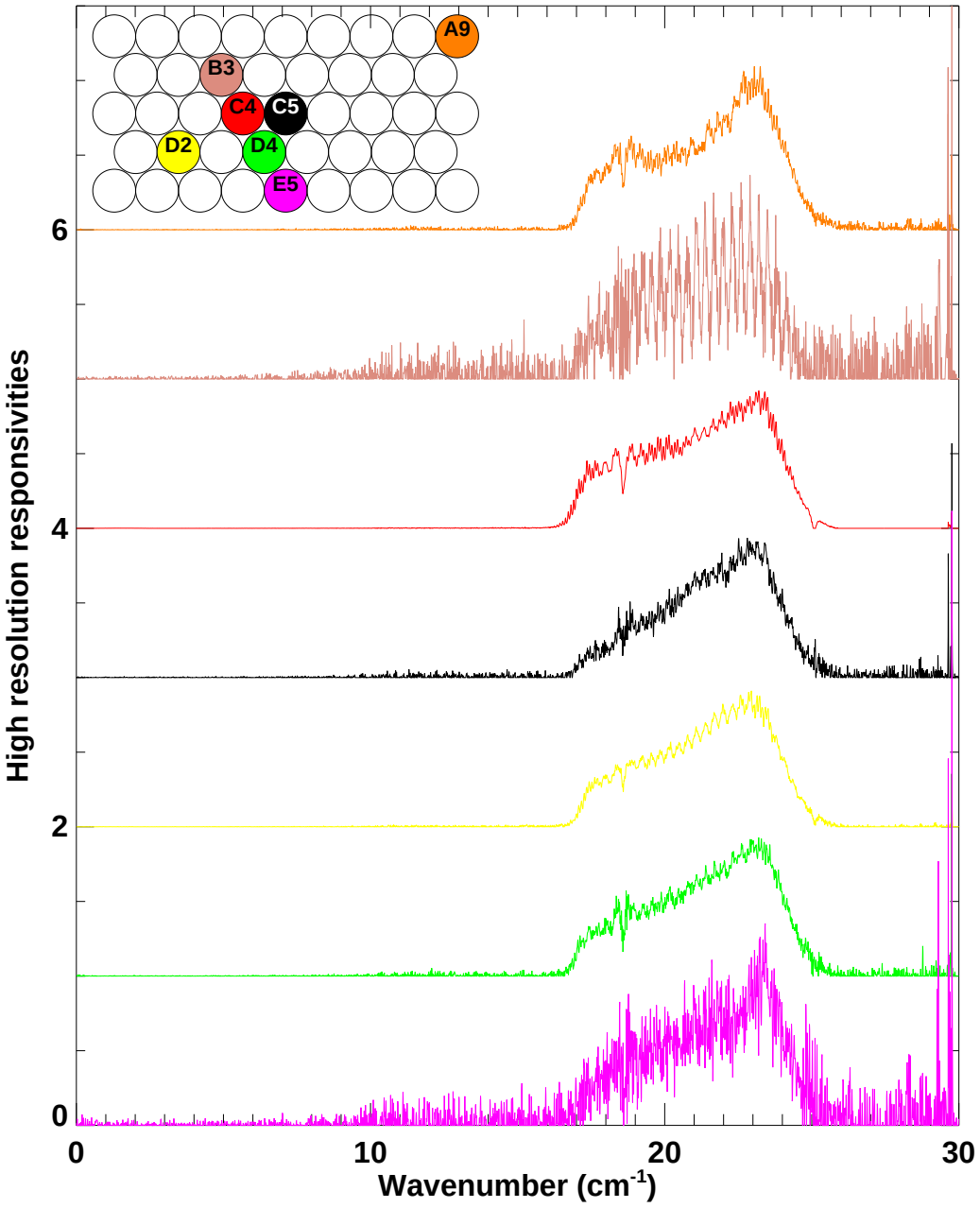

Figure 7.12: Post-vibration high resolution spectral responsivities (equation 7.4).

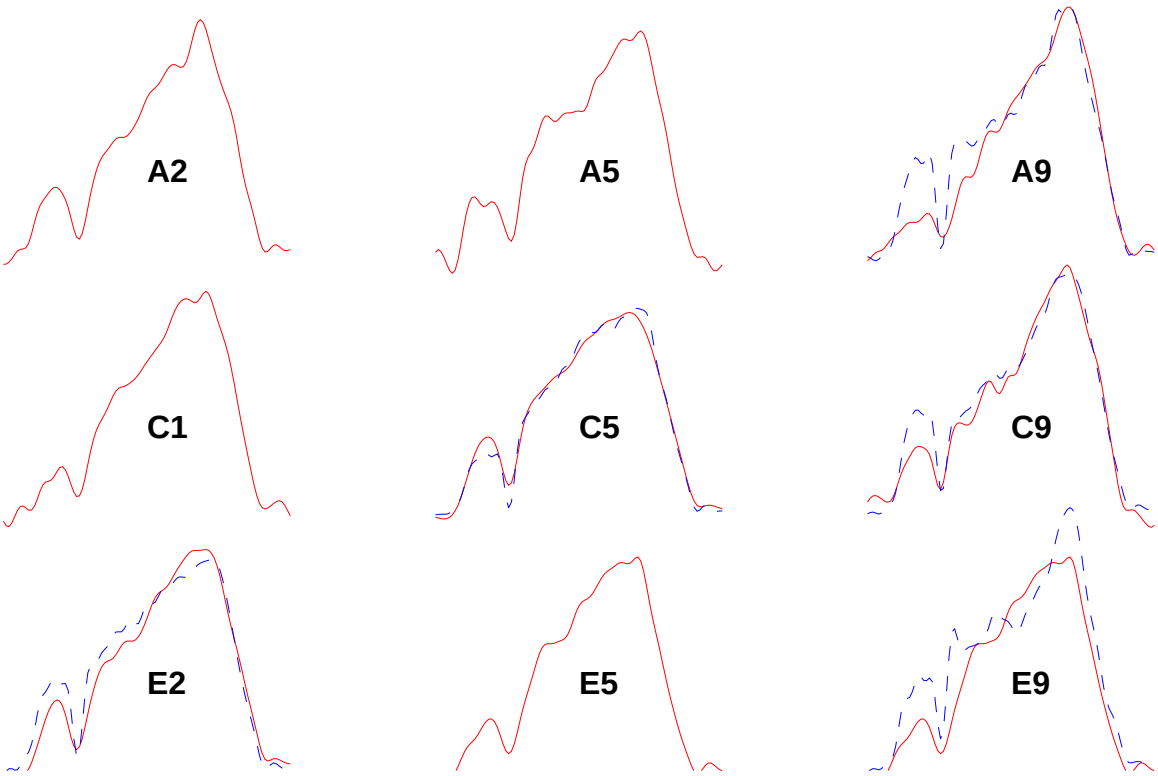

Figure 7.13: A comparison of pre and post vibration LR spectra. Pre-vibration spectra (red) are taken from figure 7.4 and post-vibration spectra (blue-dashed) are taken from figure 7.6. All spectra are area normalized as in the previous figures.

7.10 Pre/Post Vibration comparisons

Bearing in mind that the post-vibration testing allowed for significantly more scans (and hence better S/N), the PLW pixels were not observed to have significant performance variations between tests. Figure 7.13 compares the pre/post vibration LR spectra for those pixels tested in both campaigns.

7.11 Conclusions

The basic function of the PLW array within the SPIRE photometer has been verified. The operating range of the PLW array matches well with the design criteria. Furthermore, there is no evidence of any out-of-band spectral leaks. The shape of the PLW array spectral responsivity is not yet fully understood. The cause of this has not been determined, some factors associated with apodization or multiple reflections have been eliminated due to the tests performed with the FIR laser. The spectra of all pixels are in general agreement with each other, however, the profile shape and intensity variations are not yet fully understood. Furthermore, the experience gained testing the PLW array allows us to predict, with some confidence, the expected spectral profile from the testing of the two other photometer arrays which are also single-moded. Due to the broader bands involved in the two spectrometer arrays (SLW and SSW), spectral responsivity for the entire band may be different from the PLW array. Further study of the detector spectral profile will be conducted in future test campaigns.

The test Fourier transform spectrometer has proven to be a valuable piece of test equipment in the SPIRE test laboratory in identifying the spectral profile of the PLW array pixels.

Chapter 8

Conclusions and future work

Contents

8.1 Introduction

This thesis has discussed the TFTS, as used in the spectral characterization of SPIRE. This chapter summarizes results from work performed relating to FTS phase correction (as discussed in chapters 4 and 5), the SPIRE TFTS (chapter 6), and SPIRE instrument verification testing (chapter 7). Also discussed in this chapter is the current status of and future work relating to Herschel/SPIRE.

8.2 Phase correction

Phase errors can be systematic, variable, and random. Whenever possible, systematic phase can be minimized and calibrated at the instrument level, as was done for the SPIRE TFTS. Nonlinear phase errors are typically both systematic, and difficult to correct for, and thus should be minimized, with residual nonlinear phase recorded with calibration measurements. The most common variable phase error is linear, which is easily corrected.

An enhanced Forman phase correction routine has been developed[26]. This method allows better choice and application of apodization functions, a range of methods of fitting the phase, and flexibility in the choice of the lengths of both the double-sided interferogram and the PCF. Additionally, the enhanced phase correction method allows the user to input phase calibration data to be combined with a linear or other type of phase correction.

A toolkit has also been developed, written in IDL[3], to address the importance of various parameters in the phase correction process. The toolkit allows one to study the effects of phase correction input parameters (e.g. double-sided interferogram and PCF length, apodization, etc.) on the retrieval of spectral line parameters. To a large measure, the nature of the spectrum under investigation determines the optimum phase correction parameters. This toolkit may be customized for application specific FTS design or data processing pipeline development. It has proven to be useful as a tool to study the optimum parameters for phase correction of the SPIRE CQM verification data measured using the TFTS built by Dr. Naylor's AIG.

8.3 TFTS

One of the chief Canadian contributions to the Herschel mission is the design, construction, assembly, testing and support of the SPIRE TFTS and associated control and data processing software. The other key Canadian contribution is ICC support staff. I have assisted in fulfilling both of the main Canadian contributions to SPIRE leading up to and during SPIRE calibration testing through a six month field assignment on location at RAL in addition to remote efforts from the University of Lethbridge campus. Whilst the Herschel spacecraft is in flight, Canada will continue to support SPIRE through support staff and the TFTS will serve as ground testing support equipment.

The TFTS performance has been characterized to allow for accurate characterization of the SPIRE instrument subsystems. The TFTS beamsplitter phase calibration measurements are necessary for the CQM data analysis discussed in chapter 7. HCl gas cell results illustrate that the TFTS has the resolution capability required for SPIRE. The electronic/software integration of the TFTS with the SPIRE test facility has been verified through the comparison of up and down scan ZPD locations. The laser spectrum measured by the TFTS proves that the TFTS ILS is the ideal sinc profile. The TFTS has proven to be an important component in the SPIRE instrument development.

8.4 SPIRE

The basic function of the SPIRE PLW array has been characterized. The operating range of the PLW array matches well with the design criteria. Furthermore there is no evidence of any out-of-band spectral leaks. The experience gained testing the PLW array

allows prediction, with some confidence, of the expected spectral profile of the other two photometer arrays (PMW and PSW). The behaviour of the two spectrometer arrays (SLW and SSW) can be predicted with less confidence as there may be multi-mode issues due to the broader spectral bands involved.

The spectra of all pixels measured are in general agreement with each other, however, the profile shape and intensity variations are not yet fully understood. The cause of this has not been determined, however, some factors associated with apodization or multiple reflections have been eliminated due to the tests performed with the FIR laser. Further investigation is needed towards the cause of the PLW array low frequency cut-off profile. This will be addressed in flight model testing which is quickly approaching (i.e. late August 2005).

The test Fourier transform spectrometer has proven to be a valuable piece of test equipment in the SPIRE test laboratory in identifying the spectral profile of the PLW array pixels.

8.4.1 Current status

The most recent SPIRE consortium meeting took place on July 19 - 21, 2005 in Pasadena, California. The following items are taken from the proceedings of the consortium meeting:

- The current Herschel launch date of August 2007 is very aggressive. A delay of 6 months or more is likely in order to allow completion of instrument qualification and calibration.

HIFI and PACS will deliver later than SPIRE.

- The schedule for the remaining SPIRE flight model test campaigns has been laid out.

  Proto-flight model 2 testing begins August 2005.

  Some flight model subsystems are not available until early 2006.

  Cold vibration testing September - November 2005.

  Proto-flight model 3 testing January 2006.

  FPU delivery in February 2006.

  FPU delivery in May 2006 preferred. This delivery would still occur prior to delivery of HIFI and PACS.

- Preliminary flight model tests show that most instrument subsystems perform very well. There are, however, a few remaining open questions.

- As Herschel comes closer to launch, public outreach programs will grow.

- Specialist Astronomy Groups (SAGs) are making progress with matching telescope research proposals to the available guaranteed observing time.

Information on progress and the current status of SPIRE, including the Canadian contributions is found on the SPIRE Canada website[130].

8.5 Herschel

The fact that Herschel will bring far infrared and submillimetre observatory capabilities into space for the first time has an important consequence. When the ISO [5]

observing programmes were being planned, the data resulting from the all sky survey performed by the Infrared Astronomical Satellite (IRAS) [131] were available. With ISO one could thus plan to build on the IRAS observations.

Herschel, however, has no IRAS. To a certain degree it will need to be its own pathfinder, while benefitting from IRAS, ISO, Spitzer[132], and hopefully also from the yet to be conducted Japanese Aerospace Exploration Agency (JAXA) Astro-F all sky survey (expected launch in early 2006)[133]. The fact that Herschel observers will want to build on and follow-up their own observations put stringent timescale implications on being able to successfully process Herschel data in a timely manner, and thus by implication, on the calibration of Herschel instruments. To follow up on these observations, it is necessary not only to have the capability to process these data immediately, but it also must be possible to properly process and assess the data collected in the performance verification and science demonstration phases. Dr. Naylor's AIG is working towards providing resources for the SPIRE data processing centre and will thus play a key role in ensuring that the limited lifetime (3-5 years) of the Herschel Space Observatory will be best utilized.

Information about the HSO including its current status may be found on the ESA Herschel Science Centre home page[134]. Reference [4] includes a thorough overview of Herschel and its subsystems, including the current status and schedule (at the time of its publication). The current HSO schedule includes instrument and telescope flight model deliveries in early 2006, to be followed by spacecraft integration and extensive system level ground testing, leading to a 2007 launch.

8.6 Future work

I am continuing with the SPIRE project through a PhD program dealing with the flight model testing and characterization of SPIRE. This opportunity is timely since both the test and launch schedule of Herschel complements my PhD timeline. Since access to space flight hardware is limited, my PhD thesis will also focus on the development of an iFTS in Dr. Naylor's laboratory. This system will closely resembles the SPIRE iFTS and provide data comparable to that expected from SPIRE. It confers a significant advantage in that it can be used on a daily basis. This thesis has provided an invaluable introduction to Herschel/SPIRE. I am excited to be a part of this very ambitious project and am proud to be one of the scientists representing Canada in this international endeavor.

Appendix A

Fourier series supplement

Recall, that in approximating a signal $f(t)$ over the interval $[t_1, t_2]$ by a set of N real, mutually orthogonal signals $x_1(t)$, $x_2(t)$, ...,$x_n(t)$[31, pp. 222-224], i.e.

$$f(t) = \sum_{n=1}^{N} c_n x_n(t), \tag{A-1}$$

the error,

$$e(t) = f(t) - \sum_{n=1}^{N} c_n x_n(t), \tag{A-2}$$

is minimized when:

$$c_n = \frac{\int_{t_1}^{t_2} f(t) x_n(t) dt}{\int_{t_1}^{t_2} x_n^2(t) dt}. \tag{A-3}$$

A mutually orthogonal basis set is complete when the error, $e(t)$, is zero and the basis vectors span the entire space.

The trigonometric Fourier series is expressed in equation 2.1, where the constant terms a_n and b_n have been defined in chapter 2 using equation A-3. It is important to note that $a_{-n} = a_n$, $b_{-n} = -b_n$, and $b_o = 0$. The trigonometric Fourier series is equivalent to

the exponential Fourier series, as is shown:

$$\begin{aligned}
f(t) &= \frac{a_o}{2} + \sum_{n=1}^{\infty}(a_n \cos(n\omega_o t) + b_n \sin(n\omega_o t)) \\
&= \frac{a_o}{2} + \sum_{n=1}^{\infty} a_n \cos(n\omega_o t) + \sum_{n=1}^{\infty} b_n \sin(n\omega_o t) \\
&= \frac{a_o}{2} + \sum_{n=1}^{\infty} \frac{a_n}{2}(e^{in\omega_o t} + e^{-in\omega_o t}) + \sum_{n=1}^{\infty} \frac{-ib_n}{2}(e^{in\omega_o t} - e^{-in\omega_o t}) \\
&= \frac{a_o}{2} + \sum_{n=1}^{\infty} \frac{a_n - ib_n}{2} e^{in\omega_o t} + \sum_{n=1}^{\infty} \frac{a_n + ib_n}{2} e^{-in\omega_o t} \\
&= \frac{a_o}{2} + \sum_{n=1}^{\infty} \frac{a_n - ib_n}{2} e^{in\omega_o t} + \sum_{n=-1}^{-\infty} \frac{a_{-n} + ib_{-n}}{2} e^{-i(-n)\omega_o t} \\
&= \frac{a_o}{2} + \sum_{n=1}^{\infty} \frac{a_n - ib_n}{2} e^{in\omega_o t} + \sum_{n=-1}^{-\infty} \frac{a_n - ib_n}{2} e^{in\omega_o t} \\
&= \sum_{n=0}^{\infty} \frac{a_n - ib_n}{2} e^{in\omega_o t} + \sum_{n=-1}^{-\infty} \frac{a_n - ib_n}{2} e^{in\omega_o t} \\
&= \sum_{n=-\infty}^{\infty} \frac{a_n - ib_n}{2} e^{in\omega_o t} \\
&= \sum_{n=-\infty}^{\infty} d_n e^{in\omega_o t},
\end{aligned} \tag{A-4}$$

where the values for d_n (complex valued) are given by:

$$d_n = \frac{a_n - ib_n}{2} \tag{A-5}$$

(also see equation 2.7), and $n = -\infty, -\infty + 1, ..., \infty - 1, \infty$.

Appendix B

Fourier transform properties

The following is a list of properties of the Fourier transform. The forward Fourier transform is given by:

$$F(\sigma) = \int_{-\infty}^{+\infty} f(z) e^{-i2\pi\sigma z} dz, \tag{B-1}$$

and the inverse Fourier transform is given by:

$$f(z) = \int_{-\infty}^{+\infty} F(\sigma) e^{i2\pi\sigma z} d\sigma. \tag{B-2}$$

The above equations have been listed in the body of the thesis but are repeated here for ease of reference. Rather than displaying the Fourier integral, for clarity, the following notation will be used where the symbol $\Leftrightarrow$ represents transformation between the reciprocal Fourier domains:

$$f(z) \Leftrightarrow F(\sigma) \quad , \quad f_1(z) \Leftrightarrow F_1(\sigma) \quad , \quad \text{and} \quad f_2(z) \Leftrightarrow F_2(\sigma).$$

The two Fourier domains listed in this section are OPD and frequency (cm and cm^{-1}), however the results are equally valid for time and frequency (seconds and Hz), or any other

valid reciprocal Fourier domains. The primary reference for this section is pages 251 - 266 of [31]. Table B.1 summarizes the properties of the Fourier transform discussed in this chapter.

The forward and reverse Fourier transform operations are very similar. For any result or relationship between $f(z)$ and $F(\sigma)$ there exists a dual result or relationship, obtained by interchanging the roles of $f(z)$ and $F(\sigma)$ in the original result (provided that the normalization and sign of the exponential indices has been properly accounted for).

If an interferogram is 'stretched' by a factor a, then the spectrum is 'compressed' by the reciprocal of that factor. Conversely, an interferogram 'compressed' by a $(0 < a < 1)$, will have an 'expanded' spectrum.

The frequency shift property is the reciprocal property to the OPD shift property. As natural apodization due to a finite entrance aperture causes a shift in the spectrum, it could be thought to produce a linear 'phase' in the interferogram although only the real portion of the interferogram is actually measured and recorded.

A multiplication by a function in one domain is equivalent to a convolution by the function's Fourier transform in the reciprocal domain.

Operation	$f(z)$	$F(\sigma)$
Addition	$f_1(z) + f_2(z)$	$F_1(\sigma) + F_2(\sigma)$
Scalar multiplication	$kf(z)$	$kF(\sigma)$
Reversal	$f(-z)$	$F(-\sigma)$
Symmetry	F(z)	$f(-\sigma)$
Scaling (a real)	$f(az)$	$\frac{1}{\lvert a\rvert}F(\frac{\sigma}{a})$
OPD shift	$f(z - z_o)$	$F(\sigma)e^{-i2\pi\sigma z_o}$
Frequency shift (ω_o real)	$f(z)e^{i2\pi\omega_o z}$	$F(\sigma - \sigma_o)$
OPD convolution	$f_1(z) * f_2(z)$	$F_1(\sigma)F_2(\sigma)$
Frequency convolution	$f_1(z)f_2(z)$	$F_1(\sigma) * F_2(\sigma)$
OPD modulation	$f(z) \times \cos(2\pi\sigma_o z)$	$\frac{1}{2}F(\sigma - \sigma_o) + \frac{1}{2}F(\sigma + \sigma_o)$
OPD differentiation	$\frac{d^n f(z)}{dz^n}$	$(i2\pi\sigma)^n F(\sigma)$
OPD integration	$\int_{-\infty}^{z} f(z')dz'$	$\frac{F(\sigma)}{i2\pi\sigma} + \pi F(0)\delta(\sigma)$

Table B.1: Fourier transform properties

Appendix C

Convolution

The term *convolution integral* is a special name given to the function used to determine the zero state response of a system[31]:

$$y(t) = \int_{-\infty}^{+\infty} f(\tau)h(t-\tau)d\tau, \tag{C-1}$$

where $f(t)$ is the input, $h(t)$ is the system impulse response, and $y(t)$ is the zero state response, or in other words the response of a system whose initial conditions are all zero. The convolution function is then abbreviated as follows:

$$y(t) = f(t) * h(t). \tag{C-2}$$

Convolution is applicable to more areas than simply that of time response to signals, however, as convolution is also used with functions of OPD (cm) and frequency (cm^{-1}) in FTS analysis. The convolution property of Fourier transforms states that a multiplication by a function in one domain is equivalent to a convolution of the function's Fourier transform in the reciprocal domain (see appendix B).

Appendix D

Phase uncertainty

Spectral phase is calculated from the real, $B_r(\sigma)$, and imaginary, $B_i(\sigma)$, components of the double-sided spectrum as follows:

$$\phi(\sigma) = \arctan(\frac{B_i}{B_r}). \tag{D-1}$$

Suppose that the double-sided spectrum has uncertainty of δB_r and δB_i in the real and imaginary domains, respectively. The phase uncertainty is expressed in terms of the spectral uncertainty as follows:

$$\partial\phi^2 = \partial B_r^2(\frac{\partial\phi}{\partial B_r})^2 + \partial B_i^2(\frac{\partial\phi}{\partial B_i})^2. \tag{D-2}$$

The partial derivative of ϕ with respect to $B_r(\sigma)$ is:

$$\frac{\partial}{\partial B_r}\phi = \frac{1}{1+(\frac{B_i}{B_r})^2}(\frac{-B_i}{B_r^2}) = \frac{-B_i}{|B|^2}, \tag{D-3}$$

and the partial derivative of ϕ with respect to $B_i(\sigma)$ is:

$$\frac{\partial}{\partial B_i}\phi = \frac{1}{1+(\frac{B_i}{B_r})^2}(\frac{1}{B_r}) = \frac{B_r}{|B|^2}. \tag{D-4}$$

Using the results of equations D-3 & D-4, equation D-2 is simplified as follows:

$$\begin{aligned} \partial\phi(\sigma)^2 &= \partial B_r^2(\frac{-B_i}{|B|^2})^2 + \partial B_i^2(\frac{B_r}{|B|^2})^2 \\ &= \partial B_r^2(\frac{B_i^2}{|B|^4}) + \partial B_i^2(\frac{B_r^2}{|B|^4}). \end{aligned} \tag{D-5}$$

If $\delta B_r = \delta B_i = \delta B$ then:

$$\begin{aligned} \partial\phi(\sigma)^2 &= \partial B^2(\frac{B_i^2}{|B|^4}) + \partial B^2(\frac{B_r^2}{|B|^4}) \\ &= \partial B^2(\frac{B_i^2 + B_r^2}{|B|^4}) \\ &= (\frac{\partial B}{|B|})^2. \end{aligned} \tag{D-6}$$

Therefore, the relation between spectral and phase uncertainty is:

$$\partial\phi(\sigma) = \frac{\partial B(\sigma)}{|B(\sigma)|}. \tag{D-7}$$

Therefore, the phase uncertainty is inversely proportional to the amplitude of the spectrum.

Appendix E

Apodization supplement

Apodization is briefly discussed in section 4.8. The functional and graphical representation of several traditional apodization functions are included in this section[38, 39, 85, 86, 87, 88, 89, 90]. In all representations, z represents OPD and L represents maximum OPD.

$$NB_{weak}(z) = (0.384093) - (0.087577)[1 - (\frac{z}{L})^2] + (0.703484)[1 - (\frac{z}{L})^2]^2. \quad \text{(E-1)}$$

$$NB_{medium}(z) = (0.152442) - (0.136176)[1 - (\frac{z}{L})^2] + (0.983734)[1 - (\frac{z}{L})^2]^2. \quad \text{(E-2)}$$

$$NB_{strong}(z) = (0.045335) + (0.554883)[1 - (\frac{z}{L})^2]^2 + (0.39978)[1 - (\frac{z}{L})^2]^4. \quad \text{(E-3)}$$

$$\text{Forman}(z) = [1 - (\frac{z}{L})^2]^2, \quad \text{note similarity to the NB form[39, 61].} \quad \text{(E-4)}$$

$$\text{Bartlett (i.e. triangular)}(z) = 1 - \frac{z}{L}. \tag{E-5}$$

$$\text{Gaussian}(z) = e^{-(\frac{z}{L})^2}. \tag{E-6}$$

$$\text{Hann}(z) = \frac{1}{2}[1 + \cos(\frac{\pi z}{L})]. \tag{E-7}$$

$$\text{Bohman}(z) = (1 - \frac{z}{L})\cos(\frac{\pi z}{L}) + \frac{1}{\pi}\sin(\frac{\pi z}{L}). \tag{E-8}$$

$$\text{Lanczos (i.e. sinc)}(z) = \frac{\sin(\frac{\pi z}{L})}{\frac{\pi z}{L}}. \tag{E-9}$$

$$\text{Hamming}(z) = 0.54 + 0.46\cos(\frac{\pi z}{L}). \tag{E-10}$$

$$BH_{3-term}(z) = 0.42323 + 0.49755\cos(\frac{\pi z}{L}) + 0.07922\cos(\frac{2\pi z}{L}). \tag{E-11}$$

$$BH_{4-term}(z) = 0.35875 + 0.48829\cos(\frac{\pi z}{L}) + 0.14128\cos(\frac{2\pi z}{L}) + 0.01168\cos(\frac{3\pi z}{L}). \tag{E-12}$$

$$\begin{aligned} BH_{\text{modified 4-term}}(z) \quad = \quad & 0.355766 + 0.487395\cos(\frac{\pi z}{L}) \\ & +0.144234\cos(\frac{2\pi z}{L}) \\ & +0.012605\cos(\frac{3\pi z}{L}). \end{aligned} \tag{E-13}$$

$$D_\alpha(z) = \cos(\frac{\pi z}{2L}) + \alpha\cos(\frac{3\pi z}{2L}), \tag{E-14}$$

where $0 \leq \alpha \leq 1$.

$$E_\alpha(z) = 1 + (1+\alpha)\cos(\frac{\pi z}{L}) + \alpha\cos(\frac{2\pi z}{L}), \tag{E-15}$$

where $0 \leq \alpha \leq 1$.

$$P_{\alpha,p}(z) = 1 + p + (1+\alpha)\cos(\frac{\pi z}{L}) + \alpha\cos(\frac{2\pi z}{L}), \tag{E-16}$$

where $-1 \leq \alpha \leq 1$ and $0 \leq p \leq 1$.

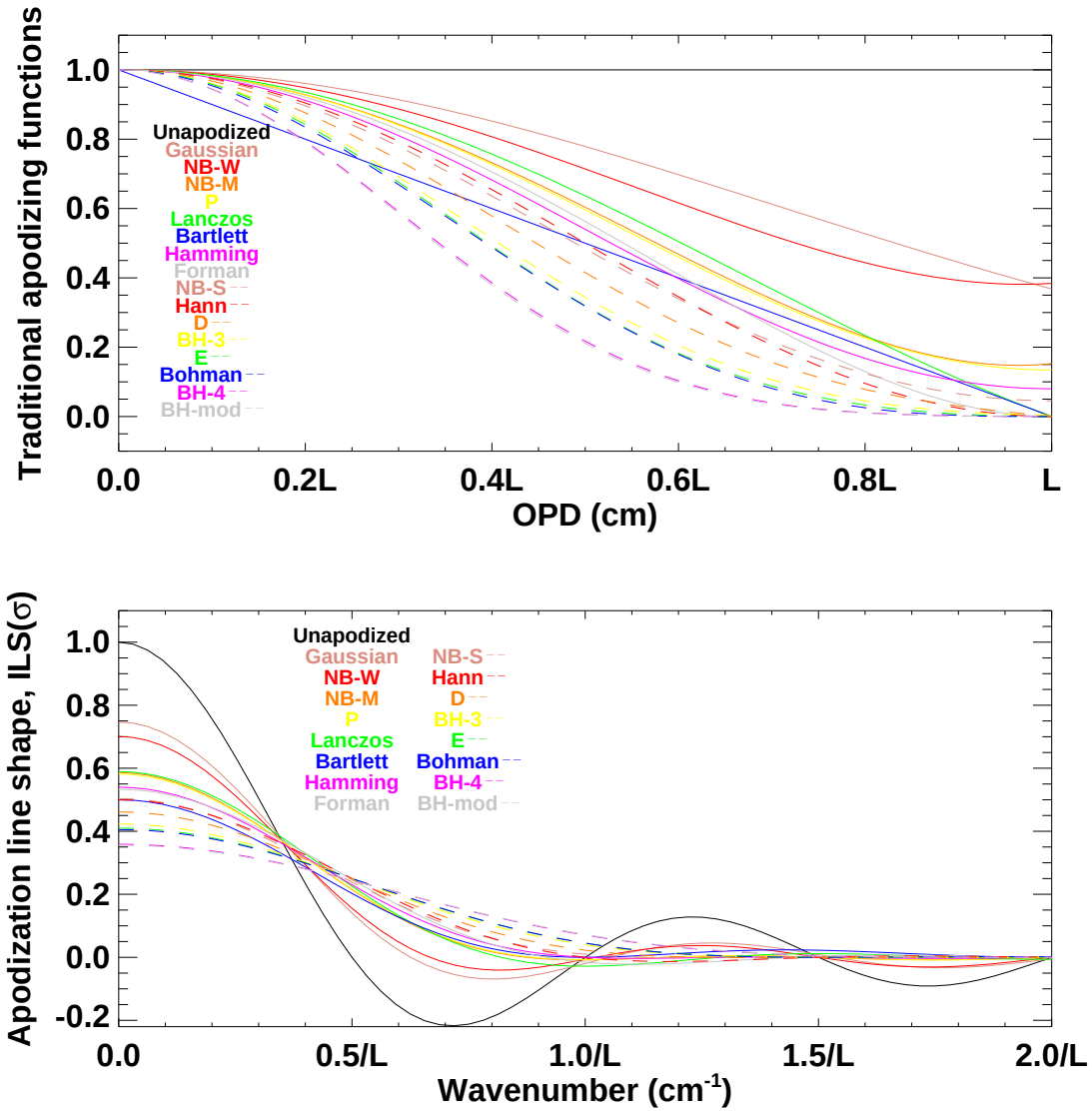

Figure E.1: A variety of common apodization functions with their corresponding ILS.

Apodization function	FWHM of ILS	Normalized FWHM	laregest sidelobe amplitude	sidelobe reduction (%)
Unapodized	1.20728	1.00	−0.2172	0.00
Gaussian	1.40	1.16	−0.0925	57.40
NB[a] weak	1.44	1.20	−0.0581	73.23
NB medium	1.69	1.40	−0.0142	93.44
P	1.70	1.41	−0.0138	93.62
Lanczos	1.73	1.44	−0.0478	77.98
Bartlett	1.77	1.47	0.0471	78.28
Hamming	1.81	1.51	0.0073	96.62
Forman	1.90	1.58	−0.0411	81.08
NB strong	1.93	1.60	0.0037	98.28
Hann	2.00	1.66	−0.0267	87.71
D	2.10	1.75	−0.0020	99.06
BH[b] 3 term	2.27	1.89	−0.0002	99.87
E	2.35	1.95	−0.0006	99.70
Bohman	2.38	1.97	0.0050	97.69
BH 4 term	2.67	2.21	0.0000	99.99
BH modified	2.69	2.23	−0.0000	99.99

[a] Norton-Beer
[b] Blackman-Harris

Table E.1: Table comparing the ILS FWHM and sidelobe reduction of the various apodizing functions. The normalization is done with respect to the unapodized sinc ILS.

Appendix F

Spectral errors due to residual phase

The phase remaining in a spectrum, e.g. phase which a phase correction algorithm failed to remove, is known as residual phase (ϕ_{res}). This chapter illustrates calculations made in order to obtain an approximation of the potential effect of residual phase on spectral parameters (i.e. line centre, FWHM, amplitude, and area). The results presented here are based on several assumptions:

- a relatively simple line shape of the spectral feature in which the errors are analyzed (specific details of the assumed line shape are presented in each section),
- residual phase is the only error contribution, all other contributions such as photon/electrical noise and apodization are omitted,
- the residual phase is bound by a maximum residual phase,

i.e. $-\phi_{max} \leq \phi_{residual}(\sigma) \leq \phi_{max}$,

- for each spectral parameter in question, the residual phase $\phi_{residual}(\sigma)$ varies in such a manner as to affect the spectrum in the most detrimental fashion possible within the ϕ_{max} boundary (specific details provided in each section), and
- calculations performed only include one spectral feature, no investigation of neighboring spectral feature contributions (i.e. sinc sidelobes) on the spectral parameter determination has been performed.

Suppose there is a spectral emission line, $S(\sigma)$. The observed spectral feature, $S_{obs}(\sigma)$, will be different from the actual spectrum due to residual phase unaccounted for in the interferogram data processing as follows:

$$S_{obs}(\sigma) = S(\sigma) \times \cos(\phi_{residual}(\sigma)). \tag{F-1}$$

The spectral feature is scaled by $\cos(\phi_{res}(\sigma))$, leaving the remainder of the spectral energy in the imaginary domain of the spectrum. Depending on the functional form of $\phi_{res}(\sigma)$, the spectral scaling will result in errors in line amplitude, centre, width, and area.

The following sections explore the potential spectral errors resulting from residual phase. The most negative and most positive error cases are investigated in order to place an upper and lower boundary on the spectral parameter error.

F-1 Amplitude error

The amplitude of $S_{obs}(\sigma)$ will never be larger than $S(\sigma)$ due to residual phase because the amplitude of the cosine function never exceeds 1. Negative amplitude error

will be greatest when the entire feature is multiplied by $\cos(\phi_{max})$ (i.e. $\phi_{res}(\sigma) = \phi_{max}$). Figure F.1 illustrates the residual phase profile used to determine the parameter range for line amplitude.

Therefore the amplitude error limits for a given maximum residual phase are:

$$\frac{\delta Amp}{Amp} = [\cos(\phi_{max}) - 1, 0]. \tag{F-2}$$

F-2 FWHM error

Errors in the FWHM of a spectral line result from non-uniform scaling of the spectral line, i.e. the peak is not scaled down while the remainder of the line is, or the peak is scaled down while the remainder of the line is not (see figure F.2).

Negative FWHM error is caused by residual phase affecting the non-central portion of the line (by $\cos(\phi_{max})$) while the line centre remains at full amplitude, thus decreasing the FWHM.

Positive FWHM error is caused by residual phase with the peak of the spectral line reduced by the full amount ($\cos(\phi_{max})$) while the outer regions of the line are not reduced at all. Figure F.2 shows the residual phase profiles used to determine the upper and lower bounds for residual phase induced FWHM error.

For the negative FWHM error case, the amplitude at the original FWHM points $(\frac{\pm Amp}{2})$ will become $\frac{\pm Amp\ \cos(\phi_{max})}{2}$. In order to find the new boundary points for the FWHM, a linear analysis was used. Figure F.3 illustrates both the zero (black) and residual phase (blue) spectra for the narrow FWHM error determination. On this plot are shown both the spectra (solid lines) and the linear functions (broken lines) used in the error

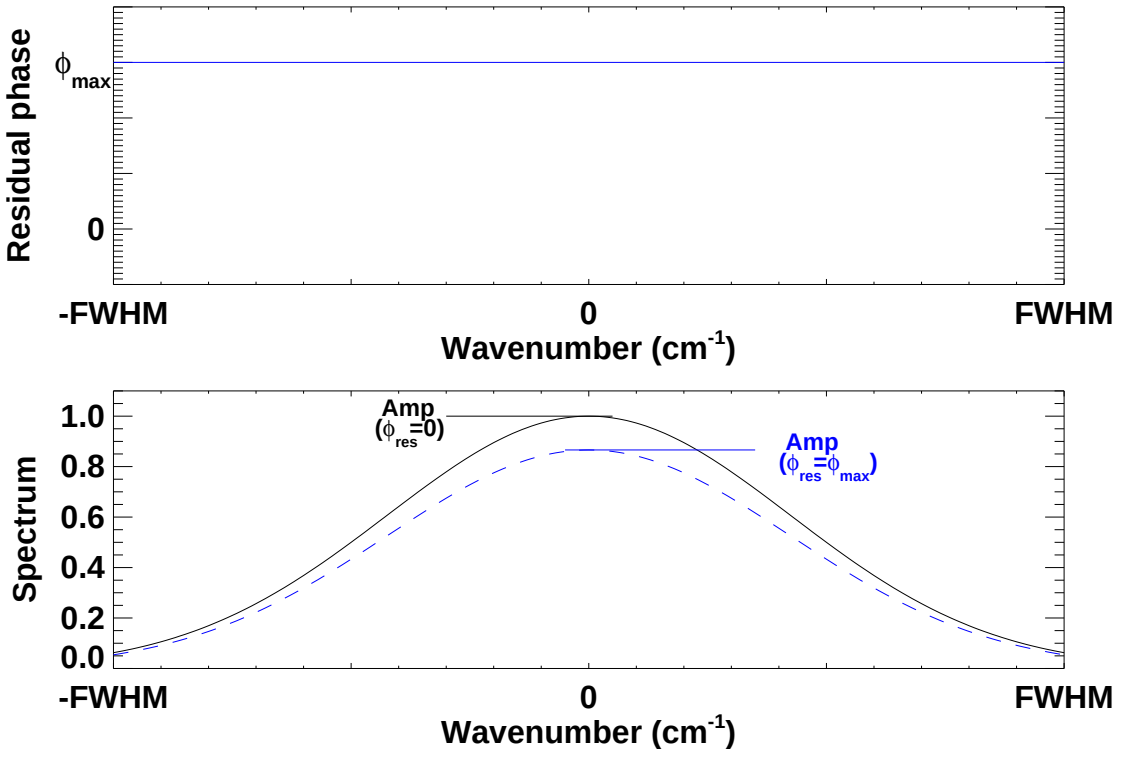

Figure F.1: Approximation of amplitude error resulting from residual spectral phase. The top figure illustrates residual phase for the negative amplitude error case. The bottom figure illustrates the zero phase spectrum (black) and the observed spectrum (blue) due to the residual phase.

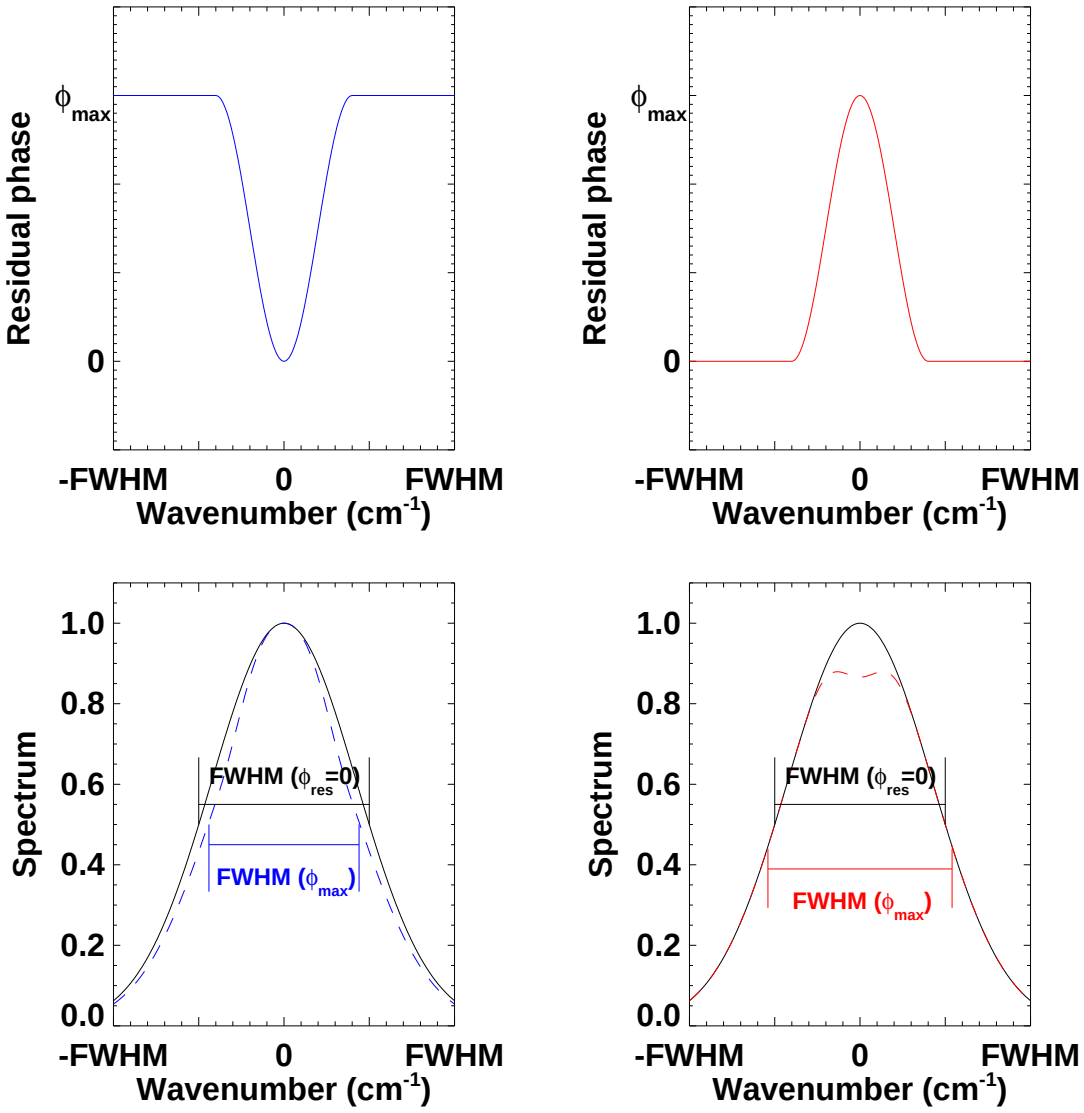

Figure F.2: Negative (left) and positive (right) FWHM error resulting from residual spectral phase. The left column shows the residual phase causing negative FWHM error where the spectral line appears to be more narrow. The right column shows residual phase causing positive FWHM error where the reduced height of the peak causes the line to appear wider.

determination.[1] The difference between the two FWHM locations is denoted as Δ (red). The equation for the linear function relating to the original line is:

$$y = \frac{(Amp)\sigma}{FWHM} + Amp, \tag{F-3}$$

and the equation for the linear function related to the residual line (denoted by the subscript r) is:

$$\begin{aligned} y_r &= \frac{(Amp_r)\sigma}{FWHM_r} + Amp_r \\ &= \frac{Amp_r(1 - \frac{\cos(\phi_{max})}{2})\sigma}{\frac{FWHM}{2}} + Amp_r \\ &= \frac{Amp_r(2 - \cos(\phi_{max}))}{FWHM}\sigma + Amp_r. \end{aligned} \tag{F-4}$$

Both Amp and Amp_r are equivalent in this example because the residual phase at the line centre is zero. At $-\frac{FWHM}{2}$ the original line will have amplitude $\frac{Amp}{2}$. The residual line amplitude will be the same at point $\sigma = -\frac{FWHM}{2} + \Delta$ (see figure F.3). This information allows Δ to be expressed in terms of the original FWHM and ϕ_{max}. Using equation F-4, the following relation is determined:

$$\begin{aligned} y_r &= \frac{Amp(2 - \cos(\phi_{max}))}{FWHM}\sigma + Amp \\ \frac{Amp}{2} &= \frac{Amp(2 - \cos(\phi_{max}))}{FWHM}(-\frac{FWHM}{2} + \Delta) + Amp \\ &\cdots \\ \frac{\Delta}{FWHM} &= \frac{1 - \cos(\phi_{max})}{2(2 - \cos(\phi_{max}))}. \end{aligned} \tag{F-5}$$

The difference between the original and reduced FWHM is 2Δ. Thus, the negative FWHM

[1] The following calculations may be done more precisely for a given line shape, but will vary depending on the line shape used, so a generalized approach is used instead.

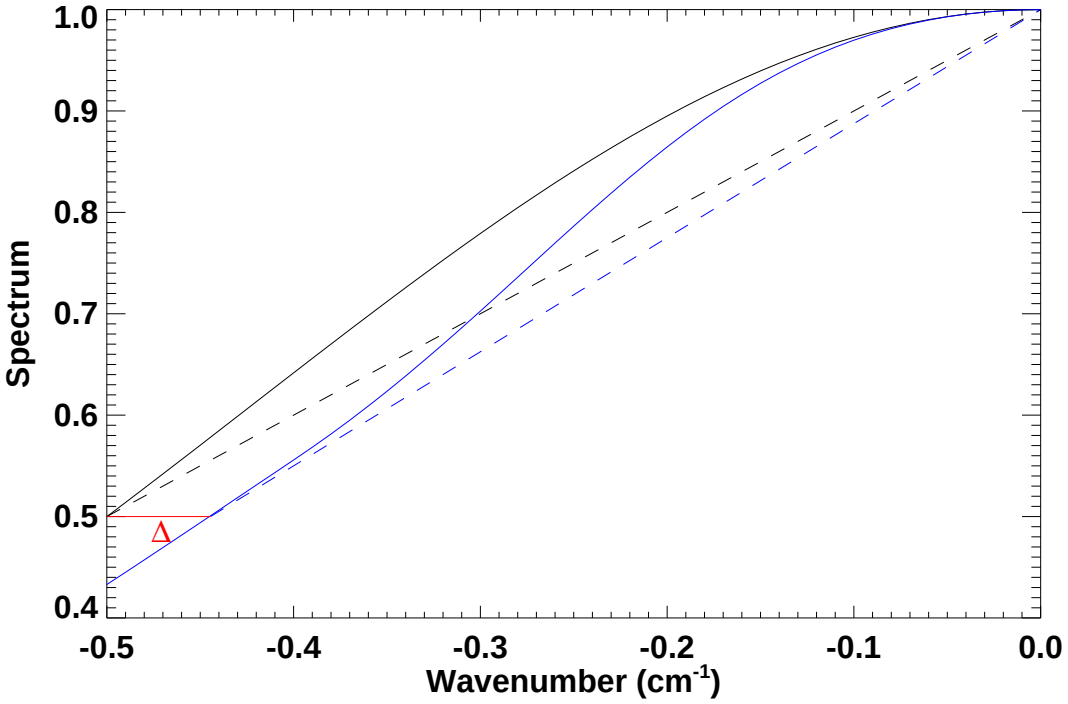

Figure F.3: Negative FWHM error calculation. The difference between the zero phase (black) and residual phase (blue) FWHM is shown by Δ (red). The figures shown are taken from the lower left hand portion of figure F.2.

error ($\frac{-2\Delta}{FWHM}$) can be expressed as:

$$\frac{\delta FWHM}{FWHM} = -2\frac{\Delta}{FWHM} = -\frac{1-\cos(\phi_{max})}{2-\cos(\phi_{max})}. \tag{F-6}$$

Similarly, the positive FWHM error (bottom right section of figure F.2) can be expressed as:

$$\frac{\delta FWHM}{FWHM} = \frac{1-\cos(\phi_{max})}{2\cos(\phi_{max})-1}. \tag{F-7}$$

Thus, the FWHM error limits for a given residual phase limit of ϕ_{max} are:

$$\frac{\delta FWHM}{FWHM} = [\frac{\cos(\phi_{max})-1}{2-\cos(\phi_{max})}, \frac{1-\cos(\phi_{max})}{2\cos(\phi_{max})-1}]. \tag{F-8}$$

F-3 Line centre error

Line centre will appear to shift locations if the residual phase has a profile that causes both ascending and descending halves of the spectral line to be scaled differently. Thus, both positive and negative line centre errors are possible, depending on the nature of $\phi_{res}(\sigma)$. Figure F.4 illustrates the phase profile used to generate the residual phase induced line centre error boundaries.

Near the peak of the line, a parabolic approximation is used.[2] The original line is therefore be expressed as:

$$y = -\frac{2Amp}{FWHM^2}\sigma^2 + Amp. \tag{F-9}$$

The residual phase line is expressed as the product of the original parabola and the residual

[2] i.e. the first few terms of the Taylor expansion of the line profile.

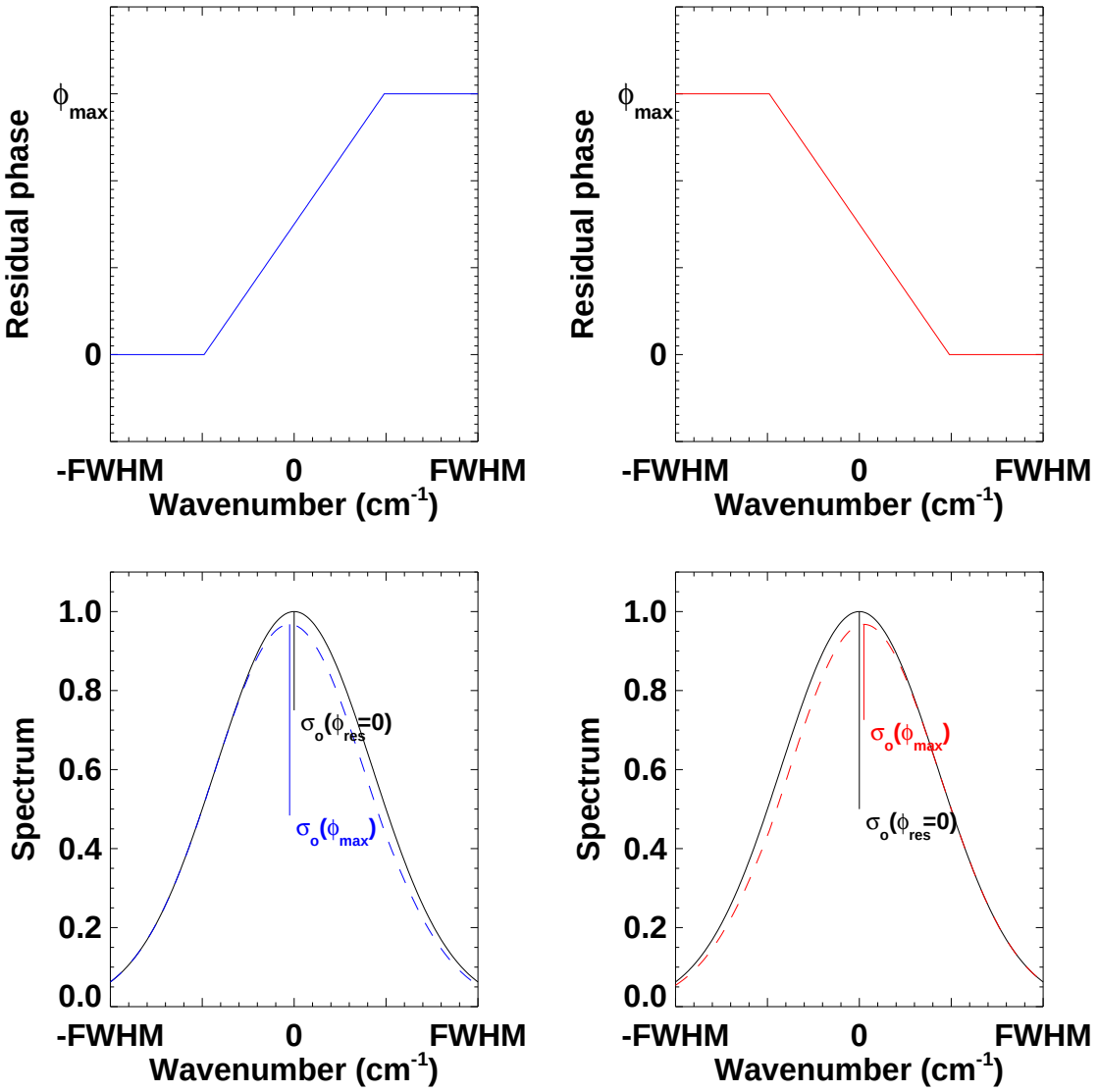

Figure F.4: Line centre error resulting from residual spectral phase. Negative line centre shift is shown in the left column while positive line centre shift is shown in the right column.

phase term, i.e. $\cos(\phi_{res}(\sigma))$ (see the upper half of figure F.4):

$$\begin{aligned} y_r &= (-\frac{2Amp}{FWHM^2}\sigma^2 + Amp) \times (-\frac{1-\cos(\phi_{max})}{FWHM}\sigma + \frac{1+\cos(\phi_{max})}{2}) \\ &= \frac{2Amp\ (1-\cos(\phi_{max}))}{FWHM^3}\sigma^3 - \frac{Amp\ (1+\cos(\phi_{max}))}{FWHM^2}\sigma^2 \\ &\quad -\frac{Amp\ (1-\cos(\phi_{max}))}{FWHM}\sigma + \frac{Amp\ (1+\cos(\phi_{max}))}{2}. \end{aligned} \tag{F-10}$$

The residual line centre, σ_o, can be found through the zero of the first derivative of the function in equation F-10 as follows[3]:

$$\begin{aligned} \frac{dy_r}{dx} &\approx \frac{-2Amp\ (1+\cos(\phi_{max}))}{FWHM^2}\sigma - \frac{Amp\ (1-\cos(\phi_{max}))}{FWHM} \\ 0 &= \frac{-2Amp\ (1+\cos(\phi_{max}))}{FWHM^2}\sigma_o - \frac{Amp\ (1-\cos(\phi_{max}))}{FWHM} \\ &\dots \\ \sigma_o &= -\frac{1-\cos(\phi_{max})}{2(1+\cos(\phi_{max}))}FWHM. \end{aligned} \tag{F-11}$$

Figure F.5 illustrates both the original and residual spectra as well as the quadratic approximations used for the negative residual line centre error determination.

Similarly, the positive line centre shift is determined to be:

$$\sigma_o = \frac{1-\cos(\phi_{max})}{2(1+\cos(\phi_{max}))}FWHM. \tag{F-12}$$

Thus, the line centre error limits for a given residual phase limit of ϕ_{max} are:

$$\frac{\delta\sigma_o}{FWHM} = [\frac{\cos(\phi_{max})-1}{2(1+\cos(\phi_{max}))}, \frac{1-\cos(\phi_{max})}{2(1+\cos(\phi_{max}))}]. \tag{F-13}$$

F-4 Area error

Uncertainty in spectral line area is related to both the amplitude and FWHM errors. The determination of the line area boundaries utilizes the amplitude and FWHM

[3]The σ^3 term was omitted from this calculation for simplicity.

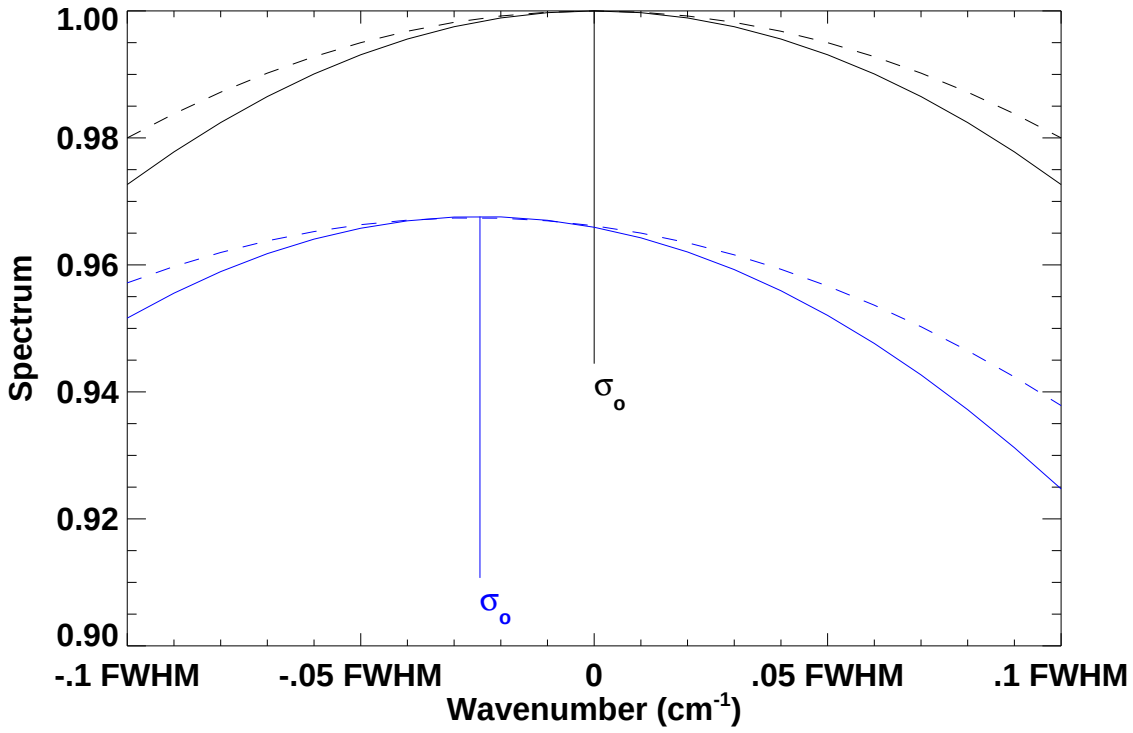

Figure F.5: Spectra used to determine the line centre shift due to residual phase. The original (black) and residual (blue) spectra (solid) and parabolic approximation (broken) figures are shown. The residual phase used to generate the apparent line centre shift is found in the upper left hand side of figure F.4.

errors. If area is assumed to be:

$$Area \approx Amp \times FWHM, \tag{F-14}$$

then the uncertainty in area can be expressed as:

$$\begin{aligned} \partial Area &= \frac{\partial Area}{\partial Amp}\partial Amp + \frac{\partial Area}{\partial FWHM}\partial FWHM \\ &= FWHM\partial Amp + Amp\partial FWHM \\ \frac{\partial Area}{Area} &= \frac{\partial Amp}{Amp} + \frac{\partial FWHM}{FWHM}. \end{aligned} \tag{F-15}$$

For the negative limit, select the negative limits for both amplitude $(\cos(\phi_{max}) - 1)$and FWHM $(\frac{\cos(\phi_{max})-1}{2-\cos(\phi_{max})})$. The area uncertainty can be expressed as:

$$\begin{aligned} \frac{\partial Area}{Area} &= -(1-\cos(\phi_{max})) - \frac{1-\cos(\phi_{max})}{2-\cos(\phi_{max})} \\ &\dots \\ &= \frac{-(3-\cos(\phi_{max}))(1-\cos(\phi_{max}))}{2-\cos(\phi_{max})}. \end{aligned} \tag{F-16}$$

Similarly, the positive area error can be expressed as:

$$\frac{\partial Area}{Area} = \frac{1-\cos(\phi_{max})}{2\cos(\phi_{max})-1}. \tag{F-17}$$

Thus, the area error limits due to a maximum residual phase are:

$$\frac{\delta Area}{Area} = [\frac{-(3-\cos(\phi_{max}))(1-\cos(\phi_{max}))}{2-\cos(\phi_{max})}, \frac{1-\cos(\phi_{max})}{2\cos(\phi_{max})-1}]. \tag{F-18}$$

Appendix G

Rayleigh-Jeans approximation

The Planck law[135] gives the intensity radiated by a blackbody heated to a given temperature (T) as a function of frequency (or wavelength). The blackbody radiates at frequency ν with spectral energy density per unit solid angle ($u_\nu(\Omega)$) given by:

$$u_\nu(\Omega) = \frac{2h}{c^3}\frac{\nu^3}{e^{h\nu/kT}-1}, \tag{G-1}$$

where h is Planck's constant, c is the speed of light, and k is Boltzmann's constant. The flux of energy passing a given surface is given by:

$$\begin{aligned} dE &= u_\nu(\Omega) dA c dt d\Omega d\nu \\ &= I_\nu dA dt d\Omega d\nu, \end{aligned} \tag{G-2}$$

where I_ν is called the specific intensity or brightness. In metres-kilograms-seconds units (MKS), the brightness has units of $\frac{J}{s \times m^2 \times ster \times Hz}$, i.e. energy per unit time per unit area per solid angle per frequency interval. The Planck brightness $B_\nu(T) = I_\nu$ is given by:

$$B_\nu(T) = \frac{2h}{c^2}\frac{\nu^3}{e^{h\nu/kT}-1}, \tag{G-3}$$

which is known as the Planck law.

To express the Planck law per wavelength instead of per unit frequency, the relationship $\nu = \frac{c}{\lambda}$ is required in order to obtain:

$$B_\lambda d\lambda = B_\nu d\nu = B_\nu |d(\frac{c}{\lambda})| = \frac{c}{\lambda^2} B_\nu d\lambda, \tag{G-4}$$

yielding

$$B_\lambda(T) = \frac{2hc^2}{\lambda^5} \frac{1}{e^{hc/\lambda kT} - 1}. \tag{G-5}$$

Similarly, the relation $\nu = c\sigma$ is required in order to determine the brightness per unit wavenumber:

$$B_\sigma d\sigma = B_\nu d\nu = B_\nu |d(c\sigma)| = cB_\nu d\sigma, \tag{G-6}$$

resulting in

$$B_\sigma(T) = \frac{2hc^2\sigma^3}{e^{hc\sigma/kT} - 1}. \tag{G-7}$$

Rayleigh[125] and Jeans[126] derived a classical law approximately describing the intensity of radiation emitted by a blackbody source at a given temperature known as the RJ approximation[136]. The RJ approximation corresponds to Planck's law in the case of small frequencies where $h\nu/kT \ll 1$ allowing the following approximation:

$$e^{h\nu/kT} \approx 1 + \frac{h\nu}{kT} + \dots \ . \tag{G-8}$$

The RJ approximation substituted into Planck's law is given by:

$$\begin{aligned} B_\nu(T) &\approx \frac{2h\nu^3}{c^2}\frac{1}{1+\frac{h\nu}{kT}+\ldots-1} \\ &\approx \frac{2h\nu^3}{c^2}\frac{1}{\frac{h\nu}{kT}+\ldots} \\ B_{\nu,RJ}(T) &= \frac{2\nu^2 kT}{c^2}. \end{aligned} \tag{G-9}$$

For $hc/\lambda kT \ll 1$ in wavelength space,

$$e^{hc/\lambda kT} \approx 1 + \frac{hc}{\lambda kT}, \tag{G-10}$$

and

$$B_{\lambda,RJ}(T) = \frac{2hc^2}{\lambda^5}\frac{\lambda kT}{hc}d\lambda = \frac{2ckT}{\lambda^4}. \tag{G-11}$$

Similarly, for $hc\sigma/kT \ll 1$ in wavenumber space,

$$e^{hc\sigma/kT} \approx 1 + \frac{hc\sigma}{kT}, \tag{G-12}$$

and

$$B_{\sigma,RJ}(T) = 2c\sigma^2 kT. \tag{G-13}$$

Thus, in the RJ region, the σ dependance of the Planck curve is approximated by a parabola. In the RJ region, the temperature dependance of the Planck curve is linear. The highest frequency in any of the SPIRE spectral bands is 50 cm^{-1}. For a blackbody source of 1200^{o}C, such as that used by the TFTS for PLW array CQM qualification tests, $\frac{hc\sigma}{kT} = 0.0488 \ll 1$, which is clearly within the RJ region. Thus, the RJ approximation is valid .

Bibliography

[1] M. K. Tahic and D. A. Naylor. Apodization Functions for Fourier Transform Spectroscopy. In *Fourier transform spectroscopy topical meeting*. Optical Society of America, Feb 2005.

[2] J. W. Cooley and J. W. Tukey. An algorithm for the machine calculation of complex fourier series. *Math. Comput.*, 19:297, 1965.

[3] Interactive Data Language, Research Systems Inc., 2004.

[4] Göran L. Pilbratt. Herschel Mission: status and observing opportunities. In *Optical, Infrared, and Millimeter Space Telescopes, Proc. SPIE*, volume 5487, pages 401 – 412, Jun 2004.

[5] M. F. Kessler, J. A. Steinz, M. E. Anderegg, J. Clavel, G. Drechsel, P. Estaria, J. Faelker, J. R. Riedinger, A. Robson, B. G. Taylor, and S. Ximénez de Ferrán. The infrared space observatory (iso) mission. *Astronomy and Astrophysics*, 315:L27 – L31, 1996.

[6] Göran L. Pilbratt. The ESA FIRST cornerstone mission. In *UV, Optical, and IR*

Space Telescopes and Instruments, Proc. SPIE, volume 4013, pages 142–151, Mar 2000. SPIE symposium, 29-31 March 2000.

[7] http://www.astro.utu.fi/tuorla/new/mirror.shtml.

[8] http://herschel.jpl.nasa.gov/lagrange.shtml.

[9] Matthew J. Griffin, Bruce M. Swinyard, and L. Vigroux. The Herschel - SPIRE instrument. In *Optical, Infrared, and Millimeter Space Telescopes, Proc. SPIE*, volume 5487, pages 413 – 424, Jun 2004.

[10] Douglas Griffin, Matt Griffin, and Bruce Swinyard. Spire design description. Technical Report SPIRE-RAL-PRJ-000620, Rutherford Appleton Laboratory, May 2003.

[11] Bruce M. Swinyard, P. A. R. Ade, M. J. Griffin, K. Dohlen, J. Baluteau, D. Pouliquen, D. Ferand, P. Dargent, G. Michel, J. Martignac, L. Rodriguez, D. Jennings, M. Caldwell, A. Richards, P. Hamilton, and David A. Naylor. The first-spire spectrometer: A novel imaging fts for the sub-millimetre. *SPIE Proceedings: UV, Optical, and IR Space Telescopes and Instruments*, 4013:196–207, 2000.

[12] P. A. R. Ade, P. A. Hamilton, and David A. Naylor. An absolute dual beam emission spectrometer. In *FTS Topical Meeting*, Santa Barbara, California, June 1999. Optical Society of America.

[13] Tanya Lim, Bruce Swinyard, A. A. Aramburu, J. Bock, M. Ferlet, Doug Griffin, Matt J. Griffin, Peter Hargrave, Ken King, Sarah Leeks, David Naylor, Samuel Ronayette, Eric Sawyer, Bernhard Schulz, Sunil Sider, Locke Spencer, Dave Smith, and

Adam Woodcraft. First Results from Herschel - SPIRE performance tests. In *Optical, Infrared, and Millimeter Space Telescopes, Proc. SPIE*, volume 5487, pages 460 – 468, Jun 2004.

[14] Kjetil Dohlen, Alain Origne, and Marc Ferlet. Optical alignment verification of the Herschel - SPIRE instrument. In *Optical, Infrared, and Millimeter Space Telescopes, Proc. SPIE*, volume 5487, pages 448 – 459, Jun 2004.

[15] Locke D. Spencer, David A. Naylor, Bruce M. Swinyard, Asier A. Aramburu, Trevor R. Fulton, Tanya L. Lim, Samuel D. Ronayette, and Ian S. Schofield. A Fourier Transform Spectrometer for Ground Testing of the Herschel/SPIRE Instrument. In *Astronomical Telescopes and Instrumentation*, volume 5487, pages 501 – 512, Jun 2004.

[16] John Lindner, David A. Naylor, and Bruce M. Swinyard. Simulation of the Performance of ESA's Herschel - SPIRE Imaging Fourier Transform Spectrometer. In *Optical, Infrared, and Millimeter Space Telescopes, Proc. SPIE*, volume 5487, pages 469 – 480, Jun 2004.

[17] Bruce Sibthorpe, Adam Woodcraft, Matthew Griffin, and S. Lloyd Watkin. A software simulator for the Herschel - SPIRE imaging photometer. In *Optical, Infrared, and Millimeter Space Telescopes, Proc. SPIE*, volume 5487, pages 491 – 500, Jun 2004.

[18] Matthew Griffin, Bruce Swinyard, and Laurent Vigroux. SPIRE - Herschel's Submillimetre Camera and Spectrometer. In *IR Space Telescopes and Instruments, Proc. SPIE*, volume 4850, pages 686–697, Mar 2003.

[19] Bruce Swinyard, Kjetil Dohlen, Didier Ferand, Jean Paul Baluteau, Dominique Pouliquen, Pascal Dargent, Guy Michel, Jerome Martignac, Peter Ade, Peter Hargrave, Matthew Griffin, Donald Jennings, and Martin Caldwell. The Imaging FTS for Herscel SPIRE. In *IR Space Telescopes and Instruments, Proc. SPIE*, volume 4850, pages 698–709, Mar 2003.

[20] Goutam Chattopadhyay, Jason Glenn, James J. Bock, Brooks Rownd, Martin Caldwell, and Matthew J. Griffin. Feed Horn Coupled Bolometer Arrays for SPIRE: Design, Simulations, and Measurements. *IEEE Transactions on Microwave Theory and Techniques*, 51(10):2139–2146, Oct 2003.

[21] Patrick A. Collins, Peter A. R. Ade, M. Caldwell, M. Ferlet, M. J. Griffin, Pete C. Hargrave, M. R. Harman, Dave L. Smith, and Bruce M. Swinyard. A Ground Calibration Facility for Herschel - SPIRE. In *IR Space Telescopes and Instruments, Proc. SPIE*, volume 4850, Mar 2003.

[22] Matthew Griffin, Bruce Swinyard, and Laurent Vigroux. The SPIRE instrument for FIRST. In *UV, Optical, and IR Space Telescopes and Instruments, Proc. SPIE*, volume 4013, pages 184–195, Mar 2000. SPIE symposium, 29-31 March 2000.

[23] Göran L. Pilbratt. The FIRST ESA Cornerstone Mission. In *UV, Optical, and IR Space Telescopes and Instruments, Proc. SPIE*, volume 3356, pages 452–461, Mar 1998. SPIE symposium, 25-28 March 1998 in Kona, Hawaii.

[24] Matthew Griffin, Laurent Vigroux, Bruce Swinyard, and Colin Cunningham. SPIRE - a bolometer instrument for FIRST. In *Advanced Technology MMW, Radio, and*

Terahertz Telescopes, Proc. SPIE, volume 3357, pages 404–413, Mar 1998. SPIE symposium, 20-28 March 1998 in Kona, Hawaii.

[25] D.A. Naylor, T.R. Fulton, P.W. Davis, I.M. Chapman, B.G. Gom, Locke D. Spencer, J.V. Lindner, N.E. Nelson-Fitzpatrick, M.K. Tahic, and G.R. Davis. Data processing pipeline for a time-sampled imaging fourier transform spectrometer. In *Proc. SPIE Imaging Spectrometry*, page X5546, August 2004.

[26] Locke D. Spencer and D. A. Naylor. Optimization of FTS Phase Correction Parameters. In *Fourier transform spectroscopy topical meeting*. Optical Society of America, Feb 2005.

[27] Brad G. Gom and David A. Naylor. An update on the imaging Fourier transform spectrometer for SCUBA-2. In *Astronomical Telescopes and Instrumentation*, volume 5498. SPIE, Jun 2004.

[28] Ivor Grattan-Guinness. *Joseph Fourier, 1768-1830*. Cambridge: MIT Press, 1972. a survey of his life and work, based on a critical edition of his monograph on the propagation of heat, presented to the Institut de France in 1807.

[29] John Herivel. *Joseph Fourier. The man and the Physicist*. Oxford University Press, 1975.

[30] Eugene Hecht. *Optics*. Addison Wesley, fourth edition, 2002.

[31] B. P. Lathi. *Signal Processing & Linear Systems*. Berkeley-Cambridge Press, Carmichael, 1998.

[32] Albert A. Michelson. *Light Waves and Their Uses*. University of Chicago Press, Chicago, Illinois, 1902.

[33] Albert A. Michelson. Measurement of Jupiter's Satellites by Interference. *Publications of the Astronomical Society of the Pacific*, 3:274–278, September 1891.

[34] Albert A. Michelson. Visibility of interference-fringes in the focus of a telescope. *Philosophical Magazine*, 31:256–259, june 1891.

[35] Fourier transform spectroscopy. *Applied Optics*, 6(4):692, April 1967.

[36] Albert A. Michelson. On the application of interference methods to spectroscopic measurements. *Philosophical Magazine*, 34:280–+, 1892.

[37] R. J. Bell. *Introductory Fourier Transform Spectroscopy*. Academic Press, New York, 1972.

[38] Sumner P. Davis, Mark C. Abrams, and James W. Brault. *Fourier Transform Spectroscopy*. Academic Press, first edition, 2001.

[39] P. R. Griffiths and J. A. Haseth. *Fourier Transform Infrared Spectrometry*. John Wiley and Sons, New York, 1986.

[40] Albert A. Michelson. Determination of Periodicities by the Harmonic Analyzer with an Application to the Sun-Spot Cycle. *Astrophysical Journal*, 38:268–275, October 1913.

[41] A. A. Michelson. Radiation in a Magnetic Field. *Astrophysics Journal*, 7:131–139, February 1898.

[42] H. Rubens and R. W. Wood. Focal isolation of long heat-waves. *Philosophical Magazine*, 21:249–261, 1911.

[43] P. Fellgett. A propos de la theorie du spectrometre interferentiel multiplex. *Journal of Physics Radium*, 19:187, 1958.

[44] P. Jacquinot. New developements in interference spectroscopy. *Rep. Prog. Phys.*, 23:267–312, 1960.

[45] J. Connes, P. Connes, and J. P. Maillard. *Atlas des spectres dans le proche infrarouge de Venus, Mars, Jupiter et Saturn.* Paris: Centre National de la Recherche Scientifique, 1969.

[46] Michael L. Forman. Fast Fourier-Transform Technique and it's Application to Fourier Spectroscopy. *Journal of the Optical Society of America*, 56(7):978, july 1966.

[47] Peter Gustav Lejeune Dirichlet, Richard Dedekind, and John Stillwell. *Lectures on Number Theory.* American Mathematical Society, 1999. translated from original title "Vorlesungen über Zahlentheorie" (1863) compiled and published shortly after Dirichlet's death in 1859.

[48] Eric W. Weisstein. Dirichlet Fourier Series Conditions. From MathWorld–A Wolfram Web Resource. http://mathworld.wolfram.com/ DirichletFourierSeriesConditions.html.

[49] J. S. Walker. *Fourier Analysis.* Oxford University Press, 1988.

[50] E. O. Brigham. *The Fast Fourier Transform.* Prentice-Hall Inc., 1974.

[51] Marc-Antoine Parseval. Mémoire sur les séries et sur l'intégration complète d'une équation aux differences partielle linéaires du second ordre, à coefficiens constans. *Académie des Sciences*, 1806. original submission was 5 April 1799.

[52] M. Born and E. Wolf. *Principles of Optics: Electromagnetic Theory of Propagation, Interference and Diffraction of Light*. Cambridge University Press, 1980.

[53] L. Mertz. Rapid scanning fourier transform spectroscopy. *J. Phys. Coll. C2, Suppl. 3-4*, 28:88, 1967.

[54] L. Mertz. *Transformations in optics*. New York: Wiley, 1965, 1965.

[55] D. A. Naylor, B. G. Gom, P. A. R. Ade, and J. E. Davis. Design and performance of a dual polarizing detector system for broadband astronomical spectroscopy at sub-millimetre wavelengths.

[56] Charles Kittel. *Introduction to Solid State Physics*. John Wiley & Sons, Inc., seventh edition, 1996.

[57] H. Nyquist. Certain topics in telegraph transmission theory. *Transactions of the American Institute of Electrical Engineers*, 47:617 – 644, 1928.

[58] C. E. Shannon. A mathematical theory of communication. *The Bell System Technical Journal*, 27:379 – 423, 1948.

[59] Adel S. Sedra and Kenneth C. Smith. *Microelectronic Circuits*. Oxford University Press, New York, 1998.

[60] L. Mertz. Optical Fourier synthesizer. *Journal of the Optical Society of America*, 46:548–551, 1956.

[61] Michael L. Forman, W. Howard Steel, and George A. Vanasse. Correction of Asymmetric Interferograms Obtained in Fourier Spectroscopy. *Journal of the Optical Society of America*, 56(1):59–63, 1966.

[62] Janine Connes. Computing Problems in Fourier Spectroscopy. In *Aspen International Conference on Fourier Spectroscopy, 1970*, volume AFCRL-71-0019, page 83, Bedford Mass., January 1971.

[63] J. C. Sheamen, W. R. Howell, G. F. Hohnstreiter, and I. Coleman. In *Aspen International Conference on Fourier Spectroscopy*, pages AFCRL–71–0019, 1970.

[64] R. C. M. Learner, A. P. Thorne, I. Wynne-Jones, J. W. Brault, and M. C. Abrams. Phase correction of emission line Fourier transform spectra. *Optical Society of America Journal A*, 12:2165–2171, October 1995.

[65] Thomas P. Sheahen and T. O. McCaney. Phase Discrepencies in Asymmetric Interferograms and Application to Nonlinearities in Fourier Spectroscopy. *Journal of the Optical Society of America*, 65(7):825–828, 1975.

[66] W. H. Press, S. A. Teukolsky, W. T. Vetterling, and B. P. Flannery. *Numerical Recipes in C: The Art of Scientific Computing*. Cambridge University Press, 1992.

[67] D. A. Naylor and T. A. Clark. A mid-infrared astronomical Fourier transform spectrometer. In *Instrumentation in astronomy VI; Proceedings of the Meeting, Tucson,*

AZ, Mar. 4-8, 1986. Part 2 (A87-36376 15-35). Bellingham, WA, Society of Photo-Optical Instrumentation Engineers, 1986, p. 482-490. NSERC-supported research., pages 482–490, 1986.

[68] J. Connes. *Rev. Opt.*, 40:45, 116, 171, 233, 1961. English translation as document AD 409869, Clearinghouse for Federal Scientific and Technical Information, Cameron Station, VA.

[69] Joseph T. Verdeyen. *Laser Electronics*. Prentice Hall, New Jersey, third edition, 1995.

[70] Thomas P. Sheahen. Importance of proper phase analysis in using Fourier transforms. *American Journal of Physics*, 44(1):22–25, 1976.

[71] Louis W. Kunz and David Goorvitch. Combined effects of a converging beam of light and mirror misalignment in michelson interferometry. *Applied Optics*, 13:1077–1079, 1974.

[72] B. Shcröder and R. Geick. The Problem of Nonlinear Phase Errors Introduced by Misalignment of a Michelson Interferometer. *Infrared Physics*, 18:595–605, 1978.

[73] David Goorvitch. Phase correction for a michelson interferometer with misaligned mirrors. *Applied Optics*, 14(6):1387–1390, 1975.

[74] David G. Johnson, Wesley A. Traub, and Kenneth W. Jucks. Phase determination from mostly one-sided interferograms. *Applied Optics*, 35(16):2955–2959, june 1996.

[75] W. Howard Steel and Michael L. Forman. Example of Errors Occurring in Fourier

Spectroscopy Due to Hilbert-Transform Effects. *Journal of the Optical Society of America*, 56:982, 1966.

[76] D. B. Chase. Phase Correction in FT-IR. *Applied Spectroscopy*, 36(3):240–244, 1982.

[77] L. Mertz. Auxiliary Computation for Fourier Spectrometry. *Infrared Physics*, 7:17–23, 1967.

[78] J. W. Brault. High Precision Fourier Transform Spectrometry: The Critical Role of Phase Corrections. *Mikrochimica Acta*, 3:215–227, 1987.

[79] R. B. Sanderson and E. E. Bell. Multiplicative Correction of Phase Errors in Fourier Spectroscopy. *Applied Optics*, 12(2):266–270, 1973.

[80] H. Sakai and G. A. Vanasse. Direct Determination of the Transfer Function of an Infrared Spectrometer. *Journal of the Optical Society of America*, 56(1):131, 1966.

[81] J. C. Pickering, A. P. Thorne, and R. Perez. Oscillator Strengths of Transitions in Ti II in the Visible and Ultraviolet regions. *The Astrophysical Journal Supplement Series*, 132:403–409, February 2001.

[82] R. R. Ernst and W. A. Anderson. Application of fourier transform spectroscopy to magnetic resonance. *Rev. Sci. Instrum.*, 37, 1966.

[83] Edward G. Codding and Gary Horlick. Apodization and Phase Information in Fourier Transform Spectroscopy. *Applied Spectroscopy*, 27(2):85–92, 1973.

[84] H. Sakai, G. A. Vanassse, and M. L. Forman. Spectral recovery in fourier spectroscopy. *Journal of the Optical Society of America*, 58(1):84 – 90, january 1968.

[85] C. Zhu and P. R. Griffiths. Extending the range of beer's law in ft-ir spectrometry. part 2: Theoretical study of continuous apodization functions. *Applied Spectroscopy*, 52:1409 – 1413, 1998.

[86] F. J. Harris. On the use of windows for harmonic analysis with the discrete fourier transform. In *Proceedings of the IEEE*, volume 66, pages 51–83, 1978.

[87] R. H. Norton and R. Beer. Errata. *Journal of the Optical Society of America*, 67:419, 1977.

[88] R. H. Norton and R. Beer. New apodizing functions for fourier spectrometry. *Journal of the Optical Society of America*, 66:259 – 264, 1976.

[89] A. S. Filler. Apodization and interpolation in fourier-transform spectroscopy. *Journal of the Optical Society of America*, 54:762 – 767, 1964.

[90] Margaret K. Tahic. Fourier transform spectroscopy of the orion molecular cloud. Master's thesis, University of Lethbridge, Lethbridge, Alberta, Canada, June 2005.

[91] John R. Taylor. *An Introduction to Error Analysis: The Study of Uncertainties in Physical Measurements*. University Science Books, second edition, 1997.

[92] J. A. Nelder and R. Mead. A simplex method for function minimization.

[93] M. J. D. Powell. A method for minimizing a sum of squares of non-linear functions without calculating derivatives.

[94] 2003. http://www.aerotech.com/products/accessories/mx.html.

[95] http://www.heidenhain.com/Products/ExposedLinear/lip.htm.

[96] Frederic Pinsard. Herschel/SPIRE Detector Control Unit Design Document. Technical Report SPIRE-SAP-PRJ-001243, Rutherford Appleton Laboratories, Feb 2003.

[97] Ian Chapman. The Atmosphere Above Mauna Kea at Mid-Infrared Wavelengths. Master's thesis, University of Lethbridge, Lethbridge, Canada, Dec 2002.

[98] Trevor R. Fulton. Deriving the beamsplitter phase from the data, 2005. Personal communication.

[99] J. C. Pearson, H. M. Pickett, B. J. Drouin, P. Chin, and E. A. Cohen. Microwave, Millimeter, Submillimeter and Far Infrared Spectral Databases. In *NASA Laboratory Astrophysics Workshop*, pages 145–148, November 2002. http://spec.jpl.nasa.gov/.

[100] I. G. Nolt, J. V. Radostitz, G. Dilonardo, K. M. Evenson, D. A. Jennings, K. R. Leopold, M. D. Vanek, L. R. Zink, A. Hinz, and K. V. Chance. Accurate rotational constants of CO, HCl, and HF: Spectral standards for the 0.3 to 6 THz (10 to 200 cm^{-1}) region. *Journal of Molecular Spectroscopy*, 125:274–287, October 1987.

[101] C. H. Townes and A. L. Schawlow. *Microwave Spectroscopy.* McGraw-Hill Book Company, 1955.

[102] Walter Gordy and Robert L. Cook. *Microwave Molecular Spectra.* Techniques of Chemistry. John Wiley & Sons, second edition, 1984.

[103] David J. Griffiths. *Introduction to Quantum Mechanics.* Prentice Hall, New Jersey, 1995.

[104] R. Shankar. *Principles of Quantum Mechanics*. Plenum Publishers, New York, second edition, 1994.

[105] Robin. R. Phillips. *Radiative Transfer Modelling of Star Formation Regions*. PhD thesis, University of Kent at Canterbury, April 1999.

[106] H. Blancher, G. Bachet, and R. Coulon. Frequency shifts of some pure rotational lines in polar mixtures in the far Infrared range. Experiments and theoretical predictions. *The Journal of Chemical Physics*, 85:2498–2501, September 1986.

[107] Jet Propulsion Laboratory, California Institute of Technology, CA, USA.

[108] Laboratoire d'Astronomie Spatiale, Marseille, France.

[109] Douglas Griffin, Matt Griffin, and Bruce Swinyard. Spire design description document. Technical Report SPIRE-RAL-PRJ-000620, Rutherford Appleton Laboratory, 2002.

[110] Trevor R. Fulton. Glitch simulation, 2004. Personal communication.

[111] M. Inguscio, G. Moruzzi, K. M. Evenson, and D. A. Jennings. A review of frequency measurements of optically pumped lasers from 0.1 to 8 THz. *Journal of Applied Physics*, 60:161–194, December 1986.

[112] O. I. Baskakov and J. Demaison. Spectroscopic Study of the v_6=1 and v_8=1 Vibrational States of Formic Acid, HCOOH: New Assignments of Laser Transitions. *Journal of Molecular Spectroscopy*, 211:262–272, February 2002.

[113] Marcel J. E. Golay. Theoretical consideration in heat and infra-red detection, with

particular reference to the pneumatic detector. *Review of Scientific Instruments*, 18(5):347–356, May 1947.

[114] LabVIEW, www.ni.com, National Instruments Inc.

[115] Arianespace Inc. Ariane 5 technical manual. http://www.arianespace.com/.

[116] B. Rownd, J. J. Bock, G. Chattopadhyay, J. Glenn, and M. J. Griffin. Design and performance of feedhorn-coupled bolometer arrays for SPIRE: Design, Simulation, and Measurements. In *Millimeter and Submillimeter Detectors for Astronomy. Edited by Phillips, Thomas G.; Zmuidzinas, Jonas. Proceedings of the SPIE*, volume 4855, pages 510–519, February 2003.

[117] Anthony D. Turner, James J. Bock, Jeffrey W. Beeman, Jason Glenn, Peter C. Hargrave, Voktor V. Hristov, Hien T. Nguyen, Faiz Rahman, Srinivasan Sethuraman, and Adam L. Woodcraft. Silicon nitride micromesh bolometer array for submillimeter astrophysics. *Applied Optics*, 40:4921–31, 2001.

[118] Roger R. Hildebrand. Focal plane optics in far-infrared and submillimeter astronomy. *Optical Engineering*, 25:323 – 330, 1986.

[119] D. A. Harper, R. H. Hildebrand, R. Stiening, and R. Winston. Heat trap: an optimized far infrared field optics system. *Applied Optics*, 15:53 – 60, 1976.

[120] R. H. Hildebrand and R. Winston. Throughput of diffraction-limited field optics systems for infrared and millimetric telescopes. *Applied Optics*, 21:1844 – 1846, 1982.

[121] Roland Winston. Light collection within the framework of geometrical optics. *Journal of the Optical Society of America*, 60:245 – 247, 1970.

[122] Frank J. Low. Low-temperature germanium bolometer. *Journal of the Optical Society of America*, 51:1300 – 1304, 1961.

[123] E. E. Haller. Physics and design of advanced bolometers and photoconductors. *Infrared Physics*, 25:257 – 266, 1985.

[124] Ian. M. Chapman and D. A. Naylor. Development of a Freely-Distributed, Customizable Atmospheric Radiative Transfer Model. In *Fourier transform spectroscopy topical meeting*. Optical Society of America, Feb 2005.

[125] J. W. S. Rayleigh. *Phil. Mag.*, 49, 1900.

[126] J. H. Jeans. *Phil. Mag.*, 10, 1905.

[127] J. C. G. Lesurf. *Millimetre-wave Optics, Devices and Systems*. Adam Hilger, New York, 1990.

[128] L.S. Rothman, D. Jacquemart, A. Barbe, D. Chris Benner, M. Birk, L.R. Brown, M.R. Carleer, C. Chackerian Jr., K. Chance, L.H. Coudert, V. Dana, V.M. Devi, J.-M. Flaud, R.R. Gamache, A. Goldman, J.-M. Hartmann, K.W. Jucks, A.G. Maki, J.-Y. Mandin, S.T. Massie, J. Orphal, A. Perrin, C.P. Rinsland, M.A.H. Smith, J. Tennyson, R.N. Tolchenov, R.A. Toth, J. Vander Auwera, P. Varanasi, and G. Wagner. The hitran 2004 molecular spectroscopic database. *Journal of Quantitative Spectroscopy & Radiative Transfer*, 96:139 – 204, 2005.

[129] Centre spatial de liège. www.csl.ulg.ac.be/Download/PDF/SpaceEnvironmentalTest.pdf.

[130] Spire canada. http://research.uleth.ca/spire/.

[131] The infrared astronomical satellite. http://irsa.ipac.caltech.edu/IRASdocs/iras.html.

[132] David B. Gallagher, William R. Irace, and Michael W. Werner. The development and mission of the space infrared telescope facility (sirtf). In *Optical, Infrared, and Millimeter Space Telescopes, Proc. SPIE*, volume 5487, pages 13 – 25, Jun 2004.

[133] Hiroshi Murakami. ASTRO-F Infrared Sky Survey Mission. In *Optical, Infrared, and Millimeter Space Telescopes, Proc. SPIE*, volume 5487, pages 330 – 337, Jun 2004.

[134] European Space Agency. Herschel science centre home page. http://www.rssd.esa.int/herschel/.

[135] G. Rybicki and A. P. Lightman. *Radiative Processes in Astrophysics*. Wiley-Interscience, New York, 1979. "The Planck Spectrum", pp.3-4 and 20-23.

[136] Eric E. Weisstein. Rayleigh-jeans law. From ScienceWorld–A Wolfram Web Resource. http://scienceworld.wolfram.com/ physics/ Rayleigh-JeansLaw.html.